Modelling Cytosolic Flow and Vesicle Transport in the Growing Pollen Tube

by

James Tyrrell

under the supervision of

Dr. Rosemary Dyson and Prof. Dave Smith

A thesis submitted to the University of Birmingham

for the degree of DOCTOR OF PHILOSOPHY

School of Mathematics

College of Engineering and Physical Sciences

University of Birmingham

February 2019

ABSTRACT

Scientific interest in the mathematical modelling of pollen tube growth has increased steadily over the last few decades. The highly localized and rapid nature of this growth necessitates large–scale actomyosin transport of cellular material throughout the cell cytoplasm. This directed movement of cellular material induces a flow in the cytosol, also known as 'cyclosis'. The extent to which inclusion of this flow is important to modelling the distribution of elements in the cytoplasm is currently unclear, with its effect often conflated with that of actomyosin transport. In this thesis, a finite volume method (FVM) is developed for the numerical evaluation of transport equations describing vesicle distribution in the pollen tube cytoplasm. This is coupled with a novel method of regularized ringlets, derived via analytical azimuthal integration of the regularized Stokeslet, for obtaining numerical solutions to axisymmetric Stokes flows. Using this method of regularized ringlets, we present an axisymmetric velocity profile for cytosolic flow in the pollen tube based on the drag induced by actomyosin vesicle transport. When used in the transport equation for vesicle distribution, we find that recreation of the apical 'inverted vesicle cone' requires the use of an enlarged effective fluid viscosity amongst other results.

ACKNOWLEDGEMENTS

First and foremost, I would like to thank my PhD supervisors Dr Rosemary Dyson and Prof David Smith whose tremendous effort and support was essential to the completion of this thesis.

I further wish to thank Dr Youssef Chebli and Prof Anja Geitmann for their contribution to this work, providing experimental results and consistently insightful feedback.

To my family, friends, and incredibly patient girlfriend Kate, thank you for your endless support.

CONTENTS

1 Introduction **1**

1.1 On the importance of plants 1

1.1.1 Plant cell structure 2

1.1.2 Plant cell growth 3

1.1.3 Diffuse growth versus tip growth 6

1.2 On the role of the pollen tube 8

1.2.1 Pollen tube growth 9

1.3 Motivation for pollen tube research 11

1.3.1 Literature review 12

1.3.2 Inclusion of cytosolic flow in prior models 15

1.4 Summary and outline of Chapters 2 - 5 24

2 Developing numerical methods for solving the advection–diffusion–reaction equation **27**

2.1 Derivation of the advection–diffusion–reaction equation 28

2.2 Developing a finite volume method 30

2.2.1 Mesh generation 31

2.2.2 Construction of control volumes 31

2.2.3 Approximating the integrated advection–diffusion–reaction PDE . 33

2.2.4 Implementing flux limiters 40

2.2.5 Conversion to an axisymmetric 3D geometry 42

2.3 The alternating-direction-implicit method for use on structured grids . . 42

2.4 Error analysis . . . 46
2.5 Chapter summary . . . 54

3 The method of regularized ringlets 56

3.1 Introduction . . . 56
3.2 Singular and regularized Stokeslet solutions . . . 59
3.2.1 Derivation of the regularized ringlet . . . 61
3.2.2 Analytical evaluation of the regularized ringlet . . . 65
3.2.3 On the double layer potential . . . 68
3.3 Simple examples and test cases . . . 69
3.3.1 Resistance problem for the translating unit sphere . . . 70
3.3.2 Resistance problem for the rotating unit sphere . . . 71
3.3.3 Purcell's toroidal swimmer . . . 74
3.4 Further comparisons to other methods . . . 81
3.4.1 Regularized ringlets vs regularized Stokeslets . . . 81
3.4.2 Ringlet vs Stokeslet speed . . . 86
3.4.3 Comparison to singular solutions . . . 88
3.5 Chapter summary . . . 93

4 Tip growth in pollen tubes 95

4.1 Introduction . . . 95
4.2 Vesicle transport model . . . 97
4.2.1 Governing equations . . . 98
4.2.2 Boundary conditions . . . 99
4.2.3 Normal displacement growth assumption . . . 102
4.2.4 Formulation with respect to a moving coordinate system . . . 104
4.2.5 Parameter estimates and nondimensionalization . . . 106
4.2.6 Selecting ε for approximating actin bundle thickness . . . 109
4.3 Cytosolic velocity profiles . . . 110
4.3.1 Generating a velocity profile based on toroidal drag forces . . . 113

4.3.2 Role of the central actin bundle . . . 116
4.3.3 The influence of growth speed . . . 119
4.4 Cytoplasmic vesicle distributions . . . 121
4.4.1 Steady state vesicle distributions . . . 122
4.4.2 FRAP simulations . . . 135
4.4.3 Exocytosis rate . . . 138
4.5 Chapter summary . . . 139

5 Concluding remarks **143**
5.1 Developing new methodology . . . 143
5.2 Biological findings . . . 144
5.3 Future work . . . 147
5.3.1 Modelling other pollen tube species . . . 147
5.3.2 The response of actin filaments to cytosolic flow . . . 150
5.3.3 Coupling growth speed and vesicle deposition for non–steady growth 151
5.3.4 Bending of the tube and asymmetric models of growth . . . 152

Appendices **153**

Chapter 2 Appendices **154**
A.1 Implementation of the finite volume method for the advection - diffusion equation with additional boundary conditions and reaction terms . . . 154
A.1.1 Base case: fluid bulk . . . 155
A.1.2 Inclusion of sources and sinks . . . 157
A.1.3 Inclusion of exocytosis / endocytosis . . . 157

Chapter 3 Appendices **159**
B.1 Regularized Stokeslets in cylindrical coordinates for ringlet evaluation . . . 159
B.2 Evaluating the behaviour of $R^{\varepsilon}_{\alpha\beta}$ as $r_n, r_0 \to 0$ . . . 160
B.3 Evaluating the double layer potential . . . 162

Chapter 4 Appendices **167**

C.1 Materials and methods for experimental FRAP imaging 167
C.2 Mapping experimental tube growth 168

List of References **172**

LIST OF FIGURES

1.1 A simple plant cell. 2

1.2 Typical examples of a plant cell undergoing **(a)** anisotropic diffuse growth, and **(b)** localized tip growth. 6

1.3 Helical microfibril structures of **(a)** small pitch and **(b)** large pitch, as well as **(c)** randomly oriented microfibrils within layers of the plant cell wall. 7

1.4 Diagram of a pistil in a typical angiosperm. 9

1.5 Light micrographs (brightfield microscopy, ×230) of two *Tradescantia virginiana* pollen grains and growing tubes. (Credit: Steer and Steer [109]). 9

1.6 Basic structure of the two myosins (VIII and XI) found in plants. (Credit: Nebenführ and Dixin [93].) 10

1.7 Exo-/endo-cytosis in the apex of the pollen tube. (Credit: Chebli *et al.* [22]). 11

1.8 Dumais' iterative model for tip growth in plant cells. (Credit: Dumais *et al.* [43]). 16

1.9 A diagram of the actin fringe profile used by Kroeger *et al.* [78]. (Credit: Kroeger *et al.* [78]). 20

1.10 Depiction of model for the flow of the plasma membrane along the cell wall. (Credit: Chavarría-Krauser and Yejie [20]). 22

2.1 An example of a control volume surrounding the node A in the vertex-centred method. 32

2.2 An example of a control volume surrounding the boundary node A in the vertex centred method. 33
2.3 Division of control volumes from Figures 2.1 and 2.2 into sub-triangles by drawing (dotted) lines joining each CV vertex to the central node. 34
2.4 The triangle with centroid P containing portions of the control volumes surrounding the nodes A, B, and C. 36
2.5 The edge midpoint M (a vertex of the CV surrounding the node A) does not in general lie on the (dotted) line joining the adjacent triangle centroids, P and P'. 37
2.6 An alternative method for evaluating $\nabla\phi$ along CV edges. 38
2.7 Initial condition $\phi(x, y, 0) = \sin(\pi x)\sin(\pi y)$ for use with Dirichlet boundary conditions. 49
2.8 Initial condition $\phi(x, y, 0) = \cos(\pi x)\cos(\pi y)$ for use with Neumann boundary conditions. 54

3.1 Stokeslet ring in the x-y plane. 61
3.2 The geometry of the toroidal swimmer. Redrawn from Leshansky *et al.* [83]. 75
3.3 Surface velocity and associated force distribution of a toroidal glider with slenderness parameter $s_0 = 2$. 78
3.4 Surface velocity and associated force distribution of an anchored toroidal pump with slenderness parameter $s_0 = 2$. 78
3.5 Scaled propulsion speed $U/u^{(s)}$ versus slenderness parameter s_0 using different numerical schemes. 79
3.6 Streamlines and magnitude of fluid velocity in the region surrounding the force-free toroidal swimmer with slenderness parameter $s_0 = 2$. 80
3.7 ℓ^2 errors for various values of ε using $N = 50$ regularized Stokeslet rings in our discretization of the sphere surface (solid line), plotted against data taken from Cortez *et al.* [33] (dashed line). 83

3.8 ℓ^2 errors for different grid sizes ($N = 25, 50, 100, 200, 400$) in our regularized ring discretization of the sphere surface using fixed $\varepsilon = 0.01$ (solid line), plotted against data taken from Cortez *et al.* (dashed line). 84
3.9 ℓ^2 errors at surface point $(r, z) = (1, 0)$ for various value of ε using $N = 124$ regularized Stokeslet rings in our discretization of the sphere surface (solid line), plotted against data taken from Cortez *et al.* (dashed line). 84
3.10 ℓ^2 errors at fluid point $(r, z) = (1.5, 0)$ for various value of ε using $N = 124$ regularized Stokeslet rings in our discretization of the sphere surface (solid line), plotted against data taken from Cortez *et al.* (dashed line). 85
3.11 Schematic diagram for implementation of the method of fundamental solutions on the unit sphere using singular rings in the r-z plane 89
3.12 Comparison of the magnitude of the singularities present in the Stokeslet (squares) and the Stokeslet ring (circles) in the limit as the source and collocation point coincide. 90

4.1 Suggested mechanism for transport of vesicles in the pollen tube. 101
4.2 Inital configuration for determining growth velocity along the boundary of the apical hemisphere. 102
4.3 Growth velocity of the apical boundary. 104
4.4 Geometric elements of the pollen tube model. 110
4.5 Controlled spreading of force distribution using ϕ_ε with $\varepsilon = 0.05$ 111
4.6 Schematic diagrams for problems in Section 4.3. 112
4.7 Magnitude and direction of apical cytosolic flow induced by drag of myosin-based exocytic vesicle transport along the peripheral actin bundle. 114
4.8 STICS analysis of apical vesicle movement over a 10 s period. (Credit: Chebli *et al.* [22], first published in Bove *et al.* [12]). 117
4.9 Magnitude and direction of apical cytosolic flow in (a) **lab frame**, and (b) **tip frame**, calculated using prescribed velocity of magnitude $0.5\,\mu\mathrm{m\,s^{-1}}$ on the peripheral actin bundle. 119

4.10 Magnitude and direction of apical cytosolic flow in the **lab frame**, calculated using prescribed velocities of magnitude $0.5\,\mu\mathrm{m\,s^{-1}}$ and $1\,\mu\mathrm{m\,s^{-1}}$ on the peripheral and central actin bundles respectively, with varying tube growth speed. 120
4.11 Magnitude and direction of apical cytosolic flow in the **tip frame**, calculated using prescribed velocities of magnitude $0.5\,\mu\mathrm{m\,s^{-1}}$ and $1\,\mu\mathrm{m\,s^{-1}}$ on the peripheral and central actin bundles respectively, with varying tube growth speed. 121
4.12 Volumetric exocytic source σ (shaded area) surrounding terminal location of peripheral actin bundle (thick lines) in the vesicle transport model. Faint lines show increments of $\pi/10$ in polar angle. 123
4.13 Steady state exocytic and endocytic vesicle populations for three different values of the cytosis rate γ. 124
4.14 Steady state combined vesicle populations using cytosis rate $\gamma = 0.1\,\mu\mathrm{m\,s^{-1}}$ for different values of the Péclet numer Pe and different endocytic boundary areas. 126
4.15 Dependence of the viscosity of a $0.033\,\mathrm{mg\,ml^{-1}}$ F-actin solution on the velocity gradient in a Couette viscometer. (Credit: Maruyama *et al.* [88]). 128
4.16 Pulse-chase labelling of membrane material in a tobacco pollen tube, showing mixing of lipophilic dyes as a result of exocytosis and endocytosis. (Credit: Zonia and Munnik [126]). 129
4.17 Fluorescently labelled (using FM4-64FX) apical region of the pollen tube. Part of a series of FRAP experiments conducted by collaborators at McGill University (see Appendix C.1). 131
4.18 False colour fluorescence intensity in the apical region of the tube between 7.500 and 17.144 seconds after photobleaching. 132
4.19 False colour fluorescence intensity in the apical region of the tube between 28.931 and 38.574 seconds after photobleaching. 132

4.20 Similar oscillatory patterns are present in the average growth speed of the pollen tube and the intensity of fluorescence labelling of the extreme APM. 133
4.21 Oscillatory patterns in the growth rate and average fluorescence intensity of the apical region of tobacco pollen tubes. (Credit: Lee *et al.* [81]). . . 133
4.22 Softening/hardening of the apical cell wall precedes an increase/decrease in growth rate by $\approx 10\,\mathrm{s}$ in the *Lilium longiflorum* pollen tube. (Credit: Zerzour *et al.* [124]). 134
4.23 The intensity of fluorescently labelled tip–localized F–actin oscillates out of phase with elongation rate in the *Nicotiana tabacum* pollen tube. (Credit: Fu *et al.* [52]). 134
4.24 FRAP analysis of FM1-43 labelled vesicles in a growing lily pollen tube. (Credit: Bove *et al.* [12]). 136
4.25 FRAP simulation run in Matlab. 137

5.1 Close similarities exist between the (dashed) streamlines of cytosolic flow and the (solid magenta) actin profile of Kroeger *et al.* [78]. 151
C.1 **(a)** An outline of the pollen tube for each frame in the FRAP video we analyze. **(b)** A zoomed–in look at the location of apical points for each frame in the FRAP video. 170
C.2 **(a)** Growth speed between frames in the FRAP video. **(b)** The same data smoothed by averaging over consecutive time points. 171

LIST OF TABLES

1.1 List of symbols used by Dumais *et al.* [43] and their physical meaning. . 18

2.1 Error convergence for the FVM in the purely diffusive case with Dirichlet boundary conditions. Using $\alpha = 1, t_{max} = 0.1, N_t = 201$. 50

2.2 Error convergence for the ADI method in the purely diffusive case with Dirichlet boundary conditions. Using $\alpha = 1, t_{max} = 0.1, N_t = 201$. 50

2.3 Error analysis for the advection–diffusion Dirichlet problem as we approach pure convection. Using $h = 0.02$ and $\beta = 0.8$ (for fixed–β FVM), $N_X = 201$ (for ADI), and $t_{\max} = 0.1$ with $N_t = 201$ (for both). 51

2.4 Error convergence for the fixed–β FVM (with $\beta = 0.8$) and flux–limited FVM in the advective-diffusive case with Dirichlet boundary conditions. Using $\alpha = 1, t_{max} = 0.1, N_t = 201$. 52

2.5 Error convergence for the ADI method in the advective-diffusive case with Dirichlet boundary conditions. Using $\alpha = 1, t_{max} = 0.1, N_t = 201$. 52

2.6 Error convergence for the FVM in the purely diffusive case with Neumann boundary conditions. Using $\alpha = 1, t_{max} = 0.1, N_t = 201$. 53

2.7 Error convergence for the ADI method in the purely diffusive case with Neumann boundary conditions. Using $\alpha = 1, t_{max} = 0.1, N_t = 201$. 54

3.1 Relative errors in the drag calculation for the resistance problem on the translating unit sphere. 71

3.2 Condition numbers of the resistance matrix R^{ε} for the resistance problem on the translating unit sphere. 71

3.3 Relative errors in the drag calculation for the resistance problem on the rotating unit sphere. 74
3.4 Condition numbers of the resistance matrix $\mathsf{R}_\theta^\varepsilon$ for the resistance problem on the rotating unit sphere. 74
3.5 Comparison of computational time (in seconds) for constructing ring matrix R^ε and Stokeslet matrix S^ε using varying numbers of nodes. 86
3.6 Computational time (in seconds) associated with solving the linear system $\mathbf{X} = \mathbf{A} \setminus \mathbf{b}$ for varying sizes of matrix $\mathbf{A}$ and vector $\mathbf{b}$. 87
3.7 Accuracy of the method of regularized ringlets for various values of the regularization parameter ε in the resistance problem on the translating unit sphere. 91
3.8 Accuracy of the method of fundamental solutions using singular ringlets for various values of the separation distance 10^{-b} in the resistance problem on the translating unit sphere. 92

4.1 Summary of boundary conditions for fluid velocity and vesicle flux in the growing pollen tube. 101
4.2 Estimates for values of various parameters related to pollen tube growth. Asterisks $*$ in the 'Reference' column indicate values established in this thesis. 107
4.3 Five different values of the exocytosis rate γ along with the corresponding exocytic, endocytic, and combined average vesicle densities at steady state, as well as the percentage of exocytic material added to the system at each time step that successfully fuses with the apical plasma membrane. . . . 138

5.1 Estimates for values of various parameters related to tobacco pollen tube growth. 148

CHAPTER 1

INTRODUCTION

1.1 On the importance of plants

Throughout history, plants have been essential to our survival. This is a point that is well illustrated in John Lindley's excellent introduction to '*The Vegetable Kingdom*,' [84] in which he writes: "We may assume it as a certain fact that the Vegetable Kingdom was the first to engage the attention of man, for it was more accessible, more easily tuned to useful purposes, and more directly in contact with him than the Animal. Plants must have yielded man his earliest food, his first built habitation; his utensils and his weapons must alike have been derived from the same source." Some of the most important modern uses of plants are as a source of food (both for ourselves and for livestock), as a basis for our clothing (using fibres such as cotton), and as a basis for medicine [46, 111]. Plants are responsible for producing the oxygen we breathe as a product of photosynthesis, helping create the conditions necessary for complex life on Earth [13]. Understanding the mechanisms behind the growth and reproduction of plants is of vital importance if we are to continue exploiting their beneficial uses long into the future.

1.1.1 Plant cell structure

Research into plant growth has been conducted across a wide range of length scales, from molecules to entire ecosystems. Here, we focus on the cellular level. In the simplest of terms, we think of the plant cell in terms of four rudimentary, distinct components: the cell wall, the adjacent plasma membrane, the cytoplasm, and the nucleus (Figure 1.1). The detail provided about these four components here is largely derived from the book '*Biochemistry and molecular biology of plants*' by Buchanan *et al.* [14].

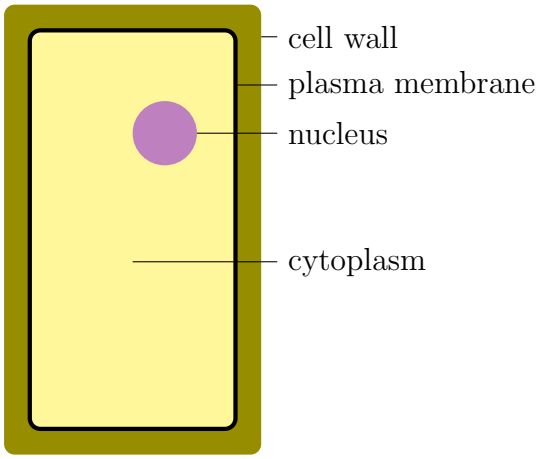

Figure 1.1: A simple plant cell.

The thick, fibrous cell wall is responsible for maintaining the particular shape of the plant cell. Its primary component is usually the polysaccharide cellulose, arranged in longitudinal bundles known as microfibrils. It is the orientation of these cellulose microfibrils that determines the nature of growth (which we define as an increase in the volume of the cell) [105]. In cells that grow by expanding uniformly (i.e. in no oriented direction), microfibrils are arranged in unaligned layers within the wall. For cells that elongate in a single direction, the microfibrils lie in aligned layers within the wall. The alignment of the microfibrils within these layers can be parallel or transverse to the direction of elongation, or in a helical arrangement. The relationship between microfibril orientation and plant cell growth is discussed further in Section 1.1.3.

Encasing the cytoplasm of the cell is the lipid bilayer plasma membrane which is responsible for the uptake of vesicles from the cytoplasm via membrane fusion, as well as the release of vesicles into the cytoplasm via membrane invagination. This plasma

membrane is kept in place, pushed tightly against the cell wall, by the effect of turgor pressure. Proteins in the membrane perform vital functions for the purpose of growth, including enabling the transport of ions and solutes against their concentration gradients by producing an electrochemical potential gradient, promoting the uptake of water to maintain turgidity and structural integrity of the cell, forming physical links to cell wall molecules, and promoting the synthesis and assembly of cell wall polymers.

The cytoplasm houses all the internal contents of the cell besides the nucleus. For the purpose of our modelling, we choose to focus only on the three most relevant components of the cytoplasm: the cytosol, cytoskeleton, and vesicles. The cytosol simply refers to the fluid in which all the other elements and organelles are suspended. The cytoskeleton is a network of filamentous protein polymers, spread throughout the cytosol. These protein polymers come in two forms: actin filaments and tubulin microtubules. Cellular components can be actively transported along the cytoskeleton by the action of motor proteins, giving the cell a degree of motility. Myosin is responsible for transport along actin filaments, whereas dynein and kinesin are responsible for transport along microtubules. In plant cells, actin filaments are the predominant mechanism for the active movement of organelles through the cytosol.

The nucleus contains the majority of the cell's genetic material and is responsible for maintaining cell function, but will not be directly included in our modelling attempts; it is instead grouped with other larger organelles as part of a homogeneous cytoplasmic continuum.

1.1.2 Plant cell growth

The driving mechanism behind plant cell growth was a matter of widespread debate amongst 20th century researchers. In 1965 arguably the earliest widely recognised work

concerning the development of a mathematical model for the growth of plant cells was produced by Lockhart [85], in which the author cites Burström [16] when he writes "it is now generally believed that irreversible elongation of the cell wall is the result of the turgor pressure exerted on the wall." Accordingly, Lockhart posits that the total elongation of a cylindrical plant cell wall is the sum of the change in length due to this irreversible extension and the change in length due to elastic stretching. Using this hypothesis, the following equation is derived,

$$\frac{1}{l}\frac{dl}{dt} = \Psi \cdot (P - Y)H[P - Y], \tag{1.1.1}$$

where l is the length of the cell wall (and thus $\frac{1}{l}\frac{dl}{dt}$ is the relative elongation rate), Ψ is the (constant) extensibility of the cell wall, P is the turgor pressure, and Y is the yielding threshold stress of the wall (corresponding to the critical pressure that P must exceed if irreversible strain is to occur). $H[P-Y]$ denotes the Heaviside step function with values

$$H[P - Y] = \begin{cases} 1 & \text{for } P > Y, \\ 0 & \text{for } P \leq Y, \end{cases} \tag{1.1.2}$$

ensuring elongation is irreversible.

In 1971 Burström himself responded to the work of Lockhart and his peers, criticizing Rayle [101], Ridge [102], Cleland [30] and Green [60] in the succinct '*Wishful thinking of turgor*' [17]. Here, Burstöm argues that "turgor does not cause expansion and is not the driving force," and states that repeated assertions to the contrary have become "dogmatic." Instead, he posits that "expansion is due to water uptake" and "volume changes during growth should be best expressed in terms of water fluxes."

In rebuttal, Ray, Cleland and Green clarified their position in '*Role of turgor in plant cell growth*' [100], stating that "stress relaxation is the primary event in cell enlargement, whereas water uptake, volume increase and extension (strain) of the cell wall are sec-

ondary." This is a small concession; the *in vivo* experiments of Green [60] focus on the *response* of the yield threshold Y to changes in the turgor pressure P (seemingly a consequence of experimental ease), whereas this new statement on stress relaxation makes it clear that it is in fact a *spontaneous* lowering of Y that initiates and precedes growth. During the course of '*Role of turgor...*' the authors also show that an analogous version of the Lockhart equation holds true for the relative rate of volumetric expansion of the cell wall chamber, that is,

$$\frac{1}{V}\frac{dV}{dt} = \Psi \cdot (P - Y)H[P - Y], \tag{1.1.3}$$

where V is the cell wall volume.

The modern understanding of the process by which a cell undergoes enlargement is perhaps best summarised by Cosgrove [37], who writes "cell enlargement begins with a reduction, or relaxation, of wall stress. As a consequence, turgor pressure and water potential are reduced ... and water is drawn into the cell. The result is that the cell enlarges by uptake of water (a reversible process) initiated by yielding of the wall (an irreversible process)." This is, in essence, combining the ideas of Lockhart, Ray and Burström under a single unifying framework and is verified by Cosgrove's earlier experimental work on practical measurements of wall relaxation [34, 36, 35]. This relaxation of the wall is thought to occur on the molecular level, a consequence of "selective loosening and shifting of load–bearing linkages between cellulose microfibrils" [38] that does not itself substantially change wall dimensions.

Although Lockhart [85] mentions elastic stretching of the wall, it is evident that no corresponding term is present in Equation (1.1.1). This is the result of an early assumption of constant turgor pressure ($\frac{dP}{dt} = 0$), eliminating the elastic component. Thus equations (1.1.1) and (1.1.3) essentially model the cell wall as a Bingham plastic [9, 10]. It was not until the work of Ortega [94] that the elastic component was reintroduced, resulting in

the equation,

$$\frac{1}{V}\frac{dV}{dt} = \Psi \cdot (P - Y)H[P - Y] + \frac{1}{\epsilon}\frac{dP}{dt}, \tag{1.1.4}$$

where ϵ is the volumetric elastic modulus of the cell wall (analogous to Young's modulus). This is commonly referred to as the Lockhart–Ortega equation, and models the cell wall as a viscoelastic (or 'Maxwell') material [25]. The inclusion of elasticity is essential for the modelling of plant cells that undergo reversible deformation (e.g. stomatal guard cells [92]).

1.1.3 Diffuse growth versus tip growth

While Equations (1.1.1) - (1.1.4) can be effectively employed to model the uniformly elongating cell, due to the lack of independent spatial variables they do not capture the complexity of localized forms of growth. The difference between uniform and localized growth in plant cells can be seen in Figure 1.2, showing **(a)** an anisotropic diffusely growing cell, and **(b)** a cell undergoing localized tip growth. For the cell undergoing tip growth, elongation is confined to the apex as a result of growth that is approximately normal to the cell surface and shape-preserving in the tip.

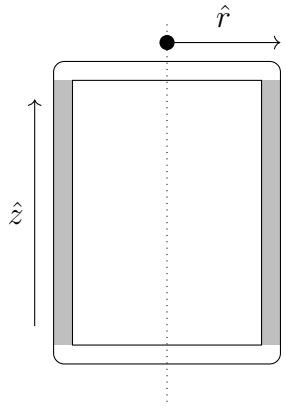

(a) Diffuse growth.

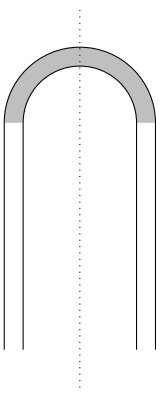

(b) Tip growth.

Figure 1.2: Typical examples of a plant cell undergoing **(a)** anisotropic diffuse growth, and **(b)** localized tip growth. Shaded regions denote regions in which growth occurs. Dotted lines denote central lines of axisymmetry.

The manner in which a plant cell grows is largely dictated by the orientation of cellulose microfibrils within the plant cell wall. These microfibrils lie in stratified layers which span the length of the cell. Fully isotropic wall structures (in which the microfibrils are not layered and are of completely random orientation) are not observed in nature [43]. Within the layers of the cell wall, microfibrils are typically oriented in helices [7] but can also display random orientation. Tightly wound microfibril helices of minimal pitch result in a circumferential microfibril orientation (Figure 1.3a), which yield in the axial $\hat{z}$ direction under significant turgor pressure to produce the longitudinal anisotropic diffuse growth as seen in the shaded region of Figure 1.2a. Loose microfibril helices of large pitch result in a longitudinal microfibril orientation (Figure 1.3b), which typically does not yield under turgor pressure. This orientation is commonly adopted by the static sections of tip–growing cells [21] such as the unshaded region in Figure 1.2b. Random orientation of microfibrils within the wall layers (Figure 1.3c) is often observed in the apical region of tip–growing cells (shaded region in Figure 1.2b).

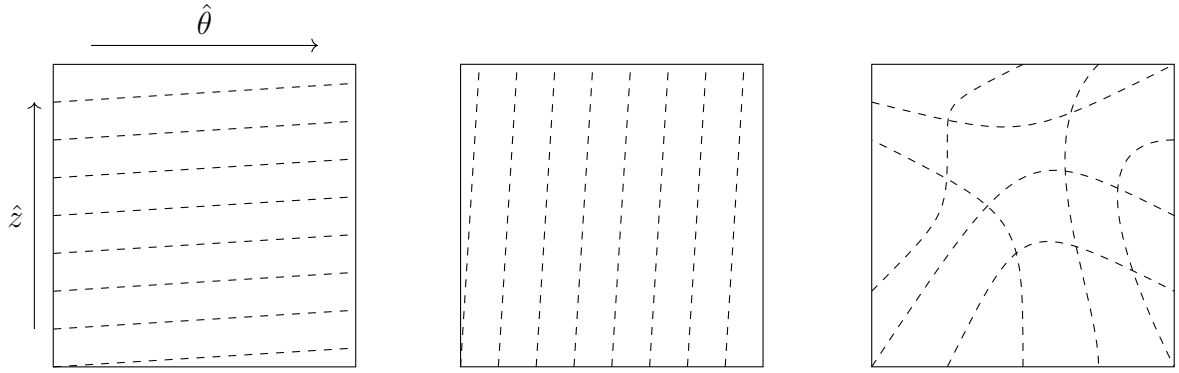

(a) Circumferential **(b)** Longitudinal **(c)** Random

Figure 1.3: Three examples of the possible orientation of cellulose microfibrils (dashed lines) within square sections of wall layers, showing helical microfibril structures of **(a)** small pitch and **(b)** large pitch, as well as **(c)** randomly oriented microfibrils.

In order for localized growth to be sustained in tip–growing cells, membrane and wall materials must be continually delivered to the growing apical region. The coupling of these processes of material deposition and subsequent growth as part of a mathematical model is a non–trivial task and few comprehensive attempts to do so exist. One of the primary goals of this thesis is to investigate the relationship between the internal cytoarchitec-

ture, deposition of new cell wall material, and subsequent growth in a particular type of tip–growing cell, the angiosperm pollen tube, with the aim of producing a mathematical model that can accurately capture this relationship.

1.2 On the role of the pollen tube

Pollen grains are the male gametophyte propagules of seed plants, produced in the anthers of angiosperms (typically referred to as the flowering[1] plants) and responsible for the provision of sperm nuclei for fertilization of the egg cell [109]. Following successful pollination upon a receptive stigma (usually either by animal or by wind [4]), the pollen grain germinates and a tube is produced. According to Malhó [87], the role of the tube can be split into two main functions: to elongate, and to interpret guidance cues from the surrounding tissue. Growth typically occurs quickly but varies between species, with the tube traversing a great distance through the sporophyte tissues (the stigma, style and ovary). Growth ends upon successful penetration of the female gametophyte, the embryo sac, allowing sperm from the pollen grain to travel down the tube and fertilise the egg [51]. A diagram of an angiosperm pistil and a typical journey the pollen tube must take can be seen in Figure 1.4.

Figure 1.5 shows an image taken using brightfield microscopy of an early stage of pollen tube growth *in vitro* for two *Tradescantia virginiana* pollen grains. Together, the vegetative grain and tube constitute a single cell with a remarkable geometry. The sphere-like shape of the grain is markedly different to that of the tube, which displays an extraordinary degree of anisotropy and may have to grow over 30 cm in length (several thousand times its width) at speeds in excess of $1\,\mathrm{cm\,h^{-1}}$ [12].

[1]This description is somewhat vague, since the flower often does not appear as we might expect it to (e.g. in grasses). Presence of the ovary is a more definite classification.

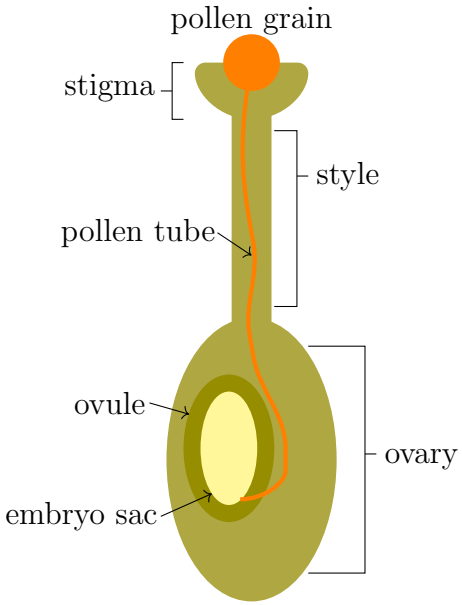

Figure 1.4: Diagram of a pistil in a typical angiosperm.

Figure 1.5: Light micrographs (brightfield microscopy, ×230) of two *Tradescantia virginiana* pollen grains and growing tubes, 15 minutes after being sown on nutrient medium. Image size has not been altered from original publication in order to preserve microscopy scaling. (Credit: Steer and Steer [109].)

1.2.1 Pollen tube growth

In order to sustain the rapid, apical growth of the pollen tube, new cell wall materials (such as phospholipids, polysaccharides, and cell-wall modifying enzymes [22]) must be continually delivered to the growing tip. Prior to delivery these materials are encased within exocytic secretory vesicles, spherical balls of plasma membrane synthesised by the golgi apparatus (a cytoplasmic organelle).

Transport of vesicles occurs along actin filaments (polymers of the globular protein actin), one of the major components of the cytoskeleton. Myosin motor proteins (comprised

of a force–generating globular head domain, an adjoining 'lever arm' neck, and a long coiled–coil tail of amino acid sequences terminating in another globular domain [1]) are responsible for moving the vesicles along these actin filaments. The myosin tail attaches to the vesicle membrane while the myosin head generates a sliding force along an actin filament in an ATP–dependent manner [76], with movement occurring in a single direction (towards the 'positive' barbed end of the actin filament) [115]. A diagram showing the basic structure of the two myosins (VIII) and (XI) found in plants can be seen in Figure 1.6.

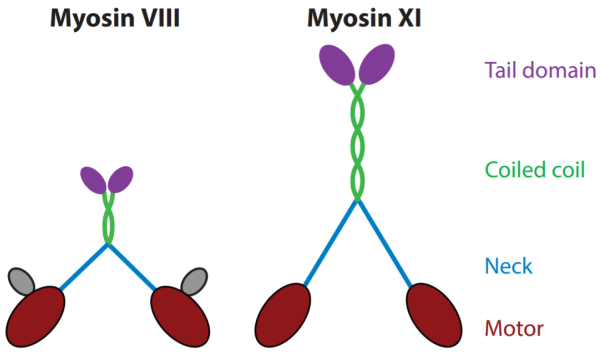

Figure 1.6: Basic structure of the two myosins (VIII and XI) found in plants. (Credit: Nebenführ and Dixin [93].)

In the angiosperm pollen tube, in which actin filaments form bundles running roughly in parallel along the periphery of the tube with their barbed ends pointed towards the apex, actomyosin transport results in the mass movement of exocytic vesicles towards the annular growth region in the subapex. Here, they fuse with the plasma membrane to deliver their contents to the extracellular space. Since the ratio of surface area to volume for spheres is of the order $(\text{radius})^{-1}$, in delivering sufficient wall material for growth the spherical vesicles also typically deliver an excess of membrane material. This is compensated for by the release of endocytic vesicles (containing a significantly smaller proportion of wall materials) from the plasma membrane back into the apical cytoplasm. It is hypothesised that reverse transport of vesicles also occurs on a central actin bundle, which aids in the removal of endocytic vesicles from the apical area. This combination of the anterograde transport of exocytic vesicles and reverse transport of endocytic vesicles produces a drag force that induces a flow in the cytosol, known as 'cytoplasmic streaming'

or ‘cyclosis’ [22]. When viewed as a collective the vesicles form a ‘reverse–fountain’ streaming pattern, a term first attributed to Iwanami [70] by Vidali and Hepler [119]. The distinction between actomyosin based transport of individual vesicles and subsequent bulk vesicle movement in response to the induced flow is often unclear in the literature.

Figure 1.7 presents a closer look at the process of exo–/endo–cytosis, highlighting the presence of peripheral and central actin bundles as well as the ‘inverted vesicle cone’ often observed in the pollen tube apex (or ‘clear zone’). Polarity of actin filaments is denoted by + signs. Arrows show the typical reverse–fountain streaming pattern of vesicles. The peripheral actin bundles extend from the shank into the subapex, stopping just short of the primary site of exocytosis in the shoulder. The central actin bundle is primarily situated in the shank and does not extend as far into the subapex as peripheral actin.

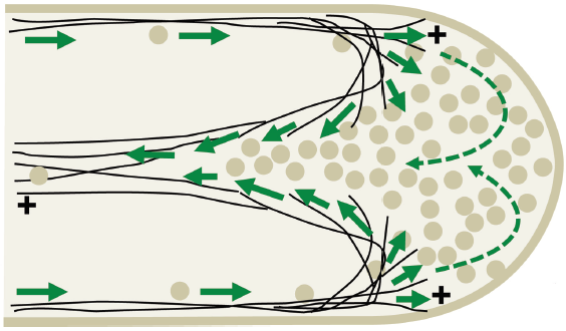

Figure 1.7: Exo-/endo-cytosis in the apex of the pollen tube, showing polarity of actin filaments in the periphery and central bundles as well as the ‘reverse fountain’ pattern of cytoplasmic streaming. (Credit: Chebli *et al.* [22]).

1.3 Motivation for pollen tube research

Mechanisms of growth in the pollen tube are of scientific interest for a number of reasons. The first of these is by virtue of the role of the tube itself; it is a vital part of the fertilization process. Generation of novel hybrid plants with potentially beneficial properties is critically limited by the compatibility between pollen and the pistil [54]. These hybrids

can often display heterosis (or 'hybrid vigor') with increased biomass, growth rate, and yield [24]. As an experimental tool for further study of plant cells in general, the pollen tube exhibits many interesting behaviours. These include highly localized and rapid growth, extreme polarity (with associated calcium gradients) [68], and swift responses to external stimuli (for navigational purposes) [15]. In the following, we provide a detailed overview of some of the arguments for and progress made in the mathematical modelling of pollen tube growth.

1.3.1 Literature review

One of the earliest and strongest arguments for study of the tube was first given in '*Cellular oscillations and the regulation of growth: the pollen tube paradigm*' by Feijó *et al.* in 2001 [50]. Their key assertion is that since the chemical processes concerning tube growth involve many simple inorganic ions (e.g. H^+, Ca^{2+}, K^+, Cl^-) and biomolecules, the combined oscillatory chemical patterns in the tube may represent a class of basic ion oscillator providing insight into the spatial and temporal organisation of many other developing cells. This is supported by the experimental simplicity of handling and observing pollen tubes as well as the clarity of their oscillatory patterns of both structural and temporal features. As a means of highlighting these features, the paper goes on to utilise the theory of deterministic chaos and non-linear phenomena to show that ionic and chemical fluxes within the tube oscillate with the same periodicity as the growth rate with a slight phase shift. This work was instrumental in igniting wider interest in the mathematical modelling of pollen tubes.

Eleven years later in 2012, the most significant results of the previous decade were summarised by Kroeger and Geitmann in '*The pollen tube paradigm revisited*' [77]. They split the various attempts at modelling the pollen tube into three main categories: those that model growth dynamics using physical equations, those that model chemical interac-

tions inside growing tubes, and those that combine the two within "closed-loop feedback models of oscillatory growth." After reviewing the various models that these categories encompass, the authors conclude that while great progress has been made on steady state models of cell morphology, no current model can fully describe phenomena such as actin dynamics, vesicle secretion, and oscillatory or tropic growth.

To elucidate on the progress made in modelling cell morphology in tip–growing cells we refer to the examples of Bartnicki-García *et al.* [6, 5] whose videomicroscopy experiments were able to determine that hyphal growth in the *Rhizoctonia solani* fungus occurs via apical orthogonal cell wall expansion, as well as the work of Goriely *et al.* [55, 56, 57] who modelled the hyphal tip as a two dimensional axisymmetric elastic membrane (later generalised to an elastic shell [58]) which was shown to produce growing tip shapes with a remarkable degree of self-similarity (i.e. the apical tip shape, once established, appears to simply translate as it grows). An alternative formulation in which the cell wall is modelled using a viscous fluid shell is posited by Campàs and Mahadevan [19] who include intracellular processes in the growing cell using just two functions (accounting for local secretion rate and rheology of the wall). The viscoplastic model of Dumais *et al.* [43], initially developed to explain expansion anisotropy in growing *Medicago truncatula* root hairs [42], provides an elegant iterative algorithm connecting wall stresses, wall strains, and the resultant cell geometry through three sets of equations. Finally, Fayant *et al.* [49] used finite element modelling of a viscoelastic shell in order to investigate how changes in parameters such as the elastic moduli, cell wall thickness, turgor pressure and tube radius affected whether a growing tip would undergo self-similar, swelling, or tapering patterns of growth. This finite element modelling also provided the framework for breaking the axisymmetric growth assumption relied upon in all of these works, potentially allowing for phenomena such as the bending of the tube during changes in growth direction to be investigated more thoroughly. To our knowledge, this breaking of axisymmetry has yet to be fully utilised in a tip–growth model.

In addition to results obtained from these largely mechanistic models, significant progress has also been made in establishing links between internal processes in the pollen tube and subsequent cell growth (following the suggestions of Feijó *et al.* [50] and Kroeger and Geitmann [77]). Examples of research focused on these internal processes include the Spatiotemporal Image Correlation Spectroscopy (STICS) and Fluorescence Recovery After Photobleaching (FRAP) experiments of Bove *et al.* [12], quantifying vesicle distribution patterns and movement in the *Lilium longiflorum* pollen tube. Following this work Kroeger *et al.* [78] posed a diffusive mathematical model capable of describing vesicle distribution patterns in a confined apical region. An equation is derived for the orientation of filaments within the steadily-advancing apical actin fringe, based on the tread-milling model for microfilament polymerization [44, 91], with normal vesicle flux along the fringe assumed to be a consequence of filament orientation. Chavarría-Krauser and Yejie [20] derived a series of equations based on a one-dimensional model of the tube, describing rates of exo-/endo-cytosis (with associated vesicle densities and receptor concentrations) and membrane flow velocity along the length of the tube.

Crucially, no prior mathematical model of any element of the pollen tube cytoplasm has (to our knowledge) attempted to fully account for the effects of cytosolic flow in a manner deriving directly from physical principles. One of the primary results of this thesis is the derivation of an axisymmetric model for this flow, which we employ in simulations of vesicle distribution and transport in the tube. Through thorough treatment of the conditions leading to this often simplified cytosolic flow, we are able to produce a model capable of accurately mapping vesicle distribution in axisymmetric 3D space throughout the length of the tube. This method is not limited to modelling vesicle transport; in future work with a different focus (e.g. modelling of cytoplasmic calcium gradients [90]) it is likely that cyclosis will play an important role.

1.3.2 Inclusion of cytosolic flow in prior models

In order to understand how a more complete inclusion of cytosolic flow could be of benefit to the mathematical modelling of pollen tubes, we consider some of the models described above in more detail and highlight the effect of cyclosis in each. All Equations in this Section are credited to their respective sources, namely Dumais *et al.* [43] (Equations (1.3.1) - (1.3.9)), Kroeger *et al.* [78] (Equations (1.3.10) - (1.3.11)), and Chavarría-Krauser and Yejie [20] (Equations (1.3.12) - (1.3.17)).

In '*An anisotropic-viscoplastic model of plant cell morphogenesis*' by Dumais *et al.* [43], an almost purely mechanistic model for pollen tube growth is derived. An overview for this iterative model and a description of the cell geometry can be seen in Figure 1.8, with a full glossary of the symbols used is given in Table 1.1. In the equations that follow, subscripts s, θ, n refer to material property components in the meridional, circumferential, and normal directions respectively (as detailed in Figure 1.8).

Starting from a given axisymmetric cell geometry, the turgor stresses in the wall can be calculated according to the force equilibrium equations

$$\sigma_s = \frac{P}{2\delta\kappa_\theta}, \tag{1.3.1}$$

$$\sigma_\theta = \frac{P}{2\delta\kappa_\theta}\left(2 - \frac{\kappa_s}{\kappa_\theta}\right), \tag{1.3.2}$$

whose derivation follows from arguments concerning forces and stress resultants [75, 117]. Using the turgor stresses, wall strain rates can be calculated according to the constitutive

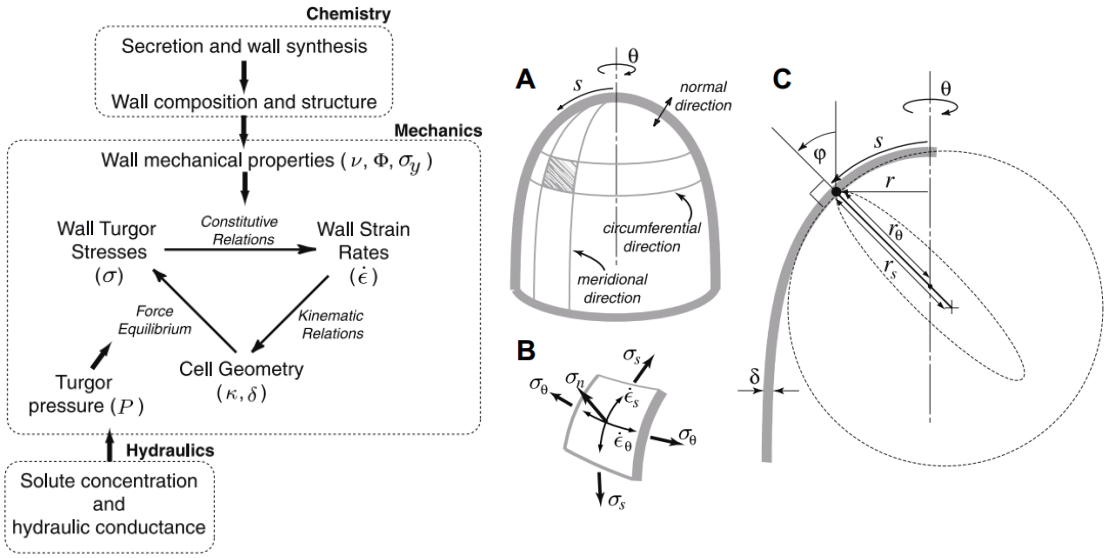

Figure 1.8: Left: Dumais' iterative model for tip growth in plant cells, based on a set of equations governing relations between cell geometry, turgor stresses, and strain rates. Right: (**A**) Principal directions (meridional s, circumferential θ, and normal n) in Dumais' tip growth model. (**B**) Principal stress (σ) and strain rates ($\dot{\epsilon}$) acting on a shell element, in which the normal stress σ_n is considered negligible compared to in-plane wall stresses σ_s and σ_θ. (**C**) Cell wall geometry defined by thickness δ as well as principal first ($r_s = 1/\kappa_s$) and second ($r_\theta = 1/\kappa_\theta$) radii of curvature, defined as functions of meridional distance s. φ denotes angle between surface normal and cell axis. (Credit: Dumais *et al.* [43]).

equations

$$\dot{\epsilon}_s = \Phi(\sigma_e - \sigma_y)\left(\frac{\sigma_s - \nu\sigma_\theta}{K}\right), \tag{1.3.3}$$

$$\dot{\epsilon}_\theta = \Phi(\sigma_e - \sigma_y)\left(\frac{\sigma_\theta - \nu\sigma_s}{K}\right), \tag{1.3.4}$$

$$\dot{\epsilon}_n = \Phi(\sigma_e - \sigma_y)\left(\frac{(\nu - 1)(\sigma_s + \sigma_\theta)}{K}\right), \tag{1.3.5}$$

provided $\sigma_e \geq \sigma_y$, with $\dot{\epsilon}_s = \dot{\epsilon}_\theta = \dot{\epsilon}_n = 0$ otherwise. Here, $K = [\beta\sigma_s^2 + \beta\sigma_\theta^2 + (\beta - 6\nu)\sigma_s\sigma_\theta]^{1/2}$ and $\beta = 2\nu^2 - 2\nu + 2$. The condition $\sigma_e \geq \sigma_y$ requires that the 'effective' stress σ_e in the wall is in excess of a yielding stress σ_y, similar to the model posed by the Lockhart Equation [85]. Equations (1.3.3) – (1.3.5) follow from Hill's yield criterion [67], an anisotropic generalisation of the isotropic von Mises criterion [116]. Their specific form here is a consequence of defining the global yield stress σ_y as the average of in-plane yield stresses (i.e. $\sigma_y = (\sigma_y^{(s)} + \sigma_y^{(\theta)})/2$) and assuming that the expanding cell wall is transversely isotropic ($\sigma_y^{(s)} = \sigma_y^{(\theta)}$). The effective stress under these conditions is given

by

$$\sigma_e = [\nu(\sigma_s - \sigma_\theta)^2 + (1-\nu)(\sigma_\theta - \sigma_n)^2 + (1-\nu)(\sigma_n - \sigma_s)^2]^{1/2}. \tag{1.3.6}$$

Finally, by considering the deformation of the surface of an infinitesimal meridional element over a small time step the following kinematic relations can be used to relate wall strain rates to displacement velocities of the cell surface:

$$\dot{\epsilon}_s = v_n \kappa_s + \frac{\partial v_t}{\partial s}, \tag{1.3.7}$$

$$\dot{\epsilon}_\theta = v_n \kappa_\theta + \frac{v_t \cos\varphi}{r}, \tag{1.3.8}$$

$$\dot{\epsilon}_n = -(\dot{\epsilon}_s + \dot{\epsilon}_\theta) + \frac{D}{\delta} = 0. \tag{1.3.9}$$

Inversion of Equations (1.3.7) and (1.3.8) yields v_t and v_n, the tangential and normal velocities of a point on the cell wall, which can be used to calculate the displacement of material points over a small time step Δt. These displaced points form the outline of the new cell geometry, which is remeshed at each stage before the iterative process is repeated.

While investigating steady growth Dumais *et al.* [43] found that "there is a unique geometry corresponding to a given set of mechanical properties," with tips of differing initial geometries but the same set of wall mechanical properties all converging to the same final configuration after a sufficient number of iterations. Further, in a series of simulations on non–steady growth they showed that spatiotemporal variations in wall mechanical properties could result in a great variety of cell shapes, including those of the oscillatory pollen tube. These variations are attributed to "modifications in either the rate, or the localization of, delivery to the apical dome's cell wall, of secreted agents... that influence the mechanical properties of the wall," although this is not modelled directly by Dumais. Indeed, the secretion of wall agents in Dumais' model is encompassed solely in the variable D, the rate of wall deposition per unit surface area, whose value is fixed by Equation (1.3.9) via an early assumption that "the rate of wall deposition matches the rate of wall thinning due to in–plane expansion." This assumption is based on the

observation of Hejnowicz [66] (amongst others) that the thickness of the cell wall in the growing tip is approximately constant in time. Thus, although Dumais *et al.* [43] emphasize the importance of the cytoplasmic distribution and targeted deposition of wall agents during growth, a mathematical description of these evolving agent populations is not within the remit of their model.

Symbol	Physical meaning
P	turgor pressure
δ	cell wall thickness
κ	curvature
σ	turgor stress
$\dot{\epsilon}$	strain rate
Φ	cell wall extensibility (reciprocal of viscosity)
σ_e	effective stress
σ_y	yield stress
ν	flow coupling (analogous to Poisson's ratio in linear elasticity)
v_n	normal velocity of point on cell wall
v_t	tangential velocity of point on cell wall
D	rate of wall deposition per unit surface area
φ	angle between the normal to the surface and the axis of the cell

Table 1.1: List of symbols used by Dumais *et al.* [43] and their physical meaning. Additional sub/super-scripts s, θ, n refer to meridional, circumferential, and normal directions respectively. All variables are functions of meridional position s.

The question of how secretory vesicles are distributed throughout the cytoplasm was addressed by Kroeger *et al.* in '*Microfilament orientation restricts vesicle flow...*' [78], which focuses on a confined apical region of the tube between the growing wall boundary and an advancing actin fringe. Here, it is posited that vesicles enter and exit this region via actomyosin transport with their direction of movement dictated by filament polarity. The actin fringe is modelled as a single structure spanning the width of the tube, encompassing both the central and peripheral actin bundles as well as the intermediate region. Its leading edge $y(x)$ is defined by the equation

$$y(x) = -\frac{1}{m}\ln(\cos\Theta(x)) - \frac{\lambda}{m}\ln\left(\tan\left(\frac{\pi}{4} + \frac{\Theta(x)}{2}\right)\right). \tag{1.3.10}$$

with $x \in [0, L]$ denoting the radial distance from the centre ($x = 0$) to the boundary

($x = L$) of the tube. The filament angle $\Theta(x)$ between the barbed ends of the filaments and the x axis is given by

$$\Theta(x) = -\frac{\pi}{L}x - \frac{\pi}{2}, \tag{1.3.11}$$

such that there is a linear change from $\Theta(0) = -\frac{\pi}{2}$ at the centre to $\Theta(L) = \frac{\pi}{2}$ at the periphery of the tube, matching the expected polarity of the actin filaments. The parameter $\lambda \approx 1$ is equal to the the profile velocity divided by the maximum filament growth rate, and $m = -\frac{\pi}{L}$ is the slope in the expression $\Theta(x) = mx + b$. Note that $y \to -\infty$ as $x \to 0$, predicting an infinitely long tail for the clear zone parallel to the central actin bundle. Kroeger *et al.* account for this by truncating the range of x used in Equation (1.3.10) to $x \in [L/10, L]$, with the missing part of the profile filled using a quarter circle of radius $L/10$ according to arguments regarding surface tension and capillary effects at the tail end of the cone as outlined in their Supporting Material.

The appearance of this actin profile as well as its approximate location in the tube can be seen in Figure 1.9, in which the vectors $\mathbf{r}, \mathbf{n}$, and $\mathbf{v}$ are the vector normal to the profile, the microfilament orientation vector, and the growth vector of the cytoskeleton respectively. It is assumed that the growth vector has constant magnitude and direction such that $\mathbf{v} = v_p\hat{\mathbf{j}}$ for some growth rate v_p. The shape of the profile is then fixed by $\mathbf{n}$, related to the microfilament angle $\Theta(x)$ by $\mathbf{n} = \hat{\mathbf{i}}\cos\Theta + \hat{\mathbf{j}}\sin\Theta$. The direction of the normal unit vector $\mathbf{r}$ can be deduced from the fact that the angle φ between $\mathbf{n}$ and $\mathbf{r}$ is always equal to the angle θ between $\mathbf{r}$ and $\mathbf{v}$.

The results of Kroeger *et al.* [78] for vesicle flux and distribution match experimental results closely but are associated with a number of simplifications. During the course of the paper, an unusually small Péclet number (the dimensionless ratio of advective to diffusive transport) is calculated for the vesicle transport problem using vesicle radius (rather than the arguably more applicable tube radius) as a typical length scale. The model they use is thus purely diffusive, assuming any advective effects to be negligible. Replacing vesicle radius with tube radius in their calculation yields a Péclet number of

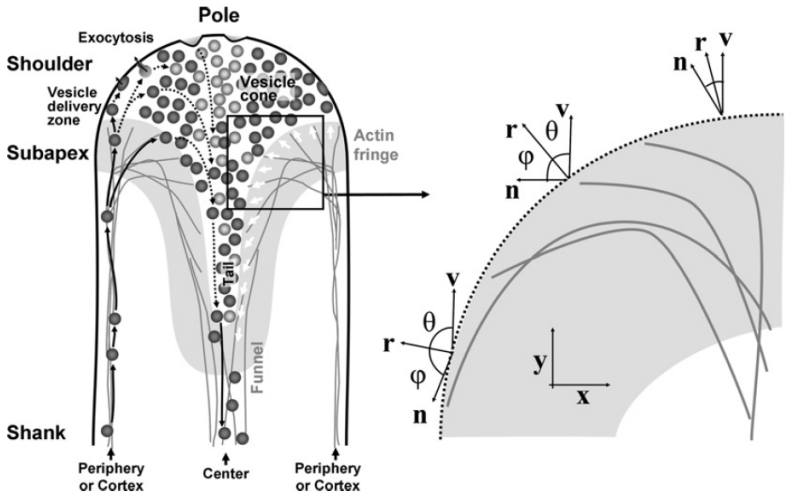

Figure 1.9: A diagram of the actin fringe profile used by Kroeger *et al.* [78]. (Credit: Kroeger *et al.* [78]).

Pe ≈ 5, suggesting advection cannot be ignored. Further, the model is based on the theory that actin acts as a physical barrier to prevent vesicles from leaving the pool except in the central region. While the colocalization of the actin fringe and the vesicle cone appear to provide strong evidence for the action of the fringe as a physical barrier to vesicles, we do not believe this to be the only mechanism responsible for constraining vesicles. Rather, we posit that it is the cytosolic flow (induced by bulk vesicle transport along longitudinal actin cables) that is the primary source of the creation of the distinctive vesicle cone shape, as well as possibly influencing the shape of the fringe itself. This partially explains why the inverted vesicle cone can still be observed in tobacco pollen tubes [81] in spite of the fact that the organization of apical actin is markedly different from that of lily or arabidopsis [52, 119].

Further possible evidence for the role of the cytosolic flow in the creation of the inverted vesicle cone (and its influence on the shape of the actin fringe) can be found in the fluorescence microscopy experiments of Jiang *et al.* [71]. Here, the authors investigate actin structure and vesicle distribution in *adf*10 pollen tube mutants, in which $ADF10$ (a member of the the actin–depolymerizing factor family) ceases to function. ADFs, responsible for the severing of actin filaments, are found throughout the pollen tube but the effect of ADF10 is most pronounced in the apex. In the *adf*10 mutant, the disfunction

of $ADF10$ results in disorganised and longer–living apical actin filaments with a greater tendency to bundle compared to in the wild–type (WT) pollen tube. Interestingly, in spite of the disorganization of apical actin the funnel shaped fringe is still produced but its location is $\approx$ 2 to 4 µm further away from the apex. Similarly, the depth of the inverted vesicle cone is increased by ≈ 2 µm in the *adf*10 mutant. The role of apical actin filaments in preventing the entry of larger organelles into the apical zone is not affected by the changes in the *adf*10 pollen tube. This leads Jiang *et al.* [71] to conclude that, "the two functions of the physical barrier - preventing the backward movement of small vesicles and the apical invasion of large organelles - depend on different properties of the barrier in terms of organization and/or bundling status." We agree with this assessment and further posit that apical actin disorganization affects rearward vesicle movement in the *adf*10 mutant as a result of cytosolic flow being impeded, but the remaining actin structure is still sufficiently dense (in spite of its disorganization) to block entry of larger organelles into the apical area. The preservation of the actin fringe and vesicle cone, albeit in a more basal location where $ADF10$ is less active and directed actomyosin transport can continue, supports the hypothesis that these features of the tube are primarily a consequence of cytosolic flow.

Our argument is somewhat reminiscent of that of early disagreements regarding the role of turgor pressure in growth of the plant cell [85, 17, 100]. In the same way that turgor is essential to growth but preceded by wall softening, we argue that the shape of the actin fringe and its role in constraining vesicles is preceded by the establishment of the cytosolic flow. Later, we will show that this flow is capable of creating the inverted vesicle cone shape without the imposition of any kind of physical barrier but the response of actin orientation to cytosolic flow is not within the remit of this thesis.

The final model we consider is that of Chavarría-Krauser and Yejie [20], in which a more detailed account of the process of exo/endo-cytosis and the balance between the delivery of plasma membrane and cell wall material is presented based on a conceptual flowing

membrane. The tube is modelled in 1D with $x = 0$ at the tip, resulting in growth that seems to move the pollen grain away from the tip (a reversal of the real physical scenario but one that is mathematically valid). The membrane flow v is equal to 0 at $x = 0$ due to symmetry conditions, and equal to the growth velocity of the tube v_g at some point $x = L$ where it is assumed that the membrane is fixed to the wall. The setup for this problem can be seen in Figure 1.10 below.

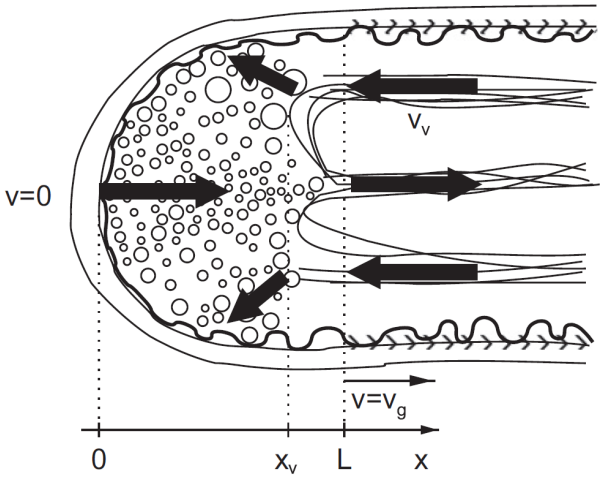

Figure 1.10: Depiction of model for the flow of the plasma membrane along the cell wall. The large bold arrows show direction of vesicle movement. (Credit: Chavarría-Krauser and Yejie [20]).

Using continuity of membrane flow and conservation of momentum, a dimensionless equation system for the membrane flow velocity v and density ρ is derived:

$$\frac{\partial \rho}{\partial t} + \frac{\partial v}{\partial x} = R, \tag{1.3.12}$$

$$\frac{\partial v}{\partial t} + bv + \epsilon \frac{\partial \ln \rho}{\partial x} = 0, \quad \text{for } (x,t) \in [0,1] \times (0,\infty), \tag{1.3.13}$$

where b is the dimensionless friction coefficient, ϵ is small and equal to the reciprocal of the Mach number squared, and R is the cytosis rate. This function R is given by,

$$R(\rho, c_1, c_2, \rho_x) = -\eta \rho c_1 + \chi \rho_x c_2, \tag{1.3.14}$$

where ρ_x is the density of free exocytic membrane, and c_1 and c_2 are membrane receptors for endocytosis and exocytosis regulation respectively with associated rate constants η and

χ. A further distinction is made between active and inactive receptors, with activation described by an exponential activation law (corresponding to activation with an enzyme in which receptor concentration, but not enzyme concentration, is limiting). Cytoplasmic vesicle concentration is also considered, in which individual vesicle motion is attributed to either (diffusive) Brownian motion or (advective) actomyosin transport. The transition between these two movement regimes is modelled using a stochastic distribution $\phi(x)$, such that the fraction of free vesicles (not fixed to actin) is given by $\Phi(x) = \int_x^\infty \phi(z)\,dz$ which yields

$$\rho_x = \tilde{\rho_x}\Phi, \quad \rho_n = \tilde{\rho_n}\Phi, \tag{1.3.15}$$

where $\tilde{\rho_x}, \tilde{\rho_n}$ are the total concentration of exocytic and endocytic vesicles respectively. Conservation laws are then applied such that

$$\frac{\partial \tilde{\rho_x}}{\partial t} - \frac{\partial}{\partial x}\left((1-\Phi)v_v\tilde{\rho_x} + \Phi D_x \frac{\partial \tilde{\rho_x}}{\partial x}\right) = -\chi\tilde{\rho_x}\Phi c_2, \tag{1.3.16}$$

$$\frac{\partial \tilde{\rho_n}}{\partial t} + \frac{\partial}{\partial x}\left((1-\Phi)v_v\tilde{\rho_n} - \Phi D_n \frac{\partial \tilde{\rho_n}}{\partial x}\right) = \eta\rho c_1, \tag{1.3.17}$$

in which D_x, D_n are diffusive coefficients associated with exocytic and endocytic vesicles respectively, and v_v is the speed of vesicles undergoing actomyosin transport. This model does not include the effects of cytosolic flow, assuming all vesicles not undergoing actomyosin transport are part of a purely diffusive regime. This is a significant simplification; spatial differences in flow velocity (greater in the shank than in the apex and greater in the centre of the tube than the periphery [12]) and vesicle distribution (with exocytic vesicles entering the clear zone in the periphery and endocytic vesicles exiting through the centre) suggest a 3D model could yield very different results. Further, the steady state membrane velocity found by Chavarría-Krauser and Yejie [20] reaches speeds of up to $\approx 0.72\,\mu\mathrm{m\,s^{-1}}$, far in excess of any apical cytosolic flow speeds observed experimentally [12] (suggesting issues would arise were the membrane flow velocity to be used as a no–slip boundary condition for internal cytosolic flow). How to reconcile this discrepancy is currently unclear and highlights the necessity for the development of a 3D model of vesicle distribution in the tube that can fully account for spatial differences in cytosolic

velocity.

1.4 Summary and outline of Chapters 2 - 5

In this opening chapter, we began by giving a brief overview of plant cell structure and early attempts at modelling plant cell growth. These models revolve around the Lockhart Equation [85], in which the cell wall is modelled as a viscoplastic (Bingham plastic) material. Later work by Ortega resulted in the Lockhart–Ortega Equation [94], reintroducing the reversible elastic component of growth such that the cell wall is modelled as a viscoelastic (Maxwell) material. We also discussed the ongoing debate throughout the 20th century with regards to the driving mechanism behind growth, through which a general consensus was reached that stress relaxation of the cell wall is the primary event driving growth. Although the Lockhart Equation and its variants effectively describe a diffusely growing cell, their applicability to cells undergoing tip growth is limited. One type of tip growing cell, the pollen tube, has been of particular interest to researchers in the last couple of decades. Attempts at modelling the pollen tube using mechanistic principles have been largely successful (particularly for axisymmetric models such as that of Dumais *et al.* [43]) but significant space in the literature exists for models linking the mechanical process of growth to chemical processes inside the cell. These chemical processes are typically inextricable from the internal cytosolic flow, an often simplified part of many models. This thesis presents the methodology for reintroducing this cytosolic flow to these models within an axisymmetric cylindrical coordinate system.

In Chapter 2, we derive an advection–diffusion–reaction partial–differential–equation (ADR PDE) for mapping chemical concentrations in the pollen tube. This ADR PDE takes the form

$$\frac{\partial \phi(\mathbf{x},t)}{\partial t} + \underbrace{\nabla \cdot (\mathbf{u}(\mathbf{x})\phi(\mathbf{x},t))}_{\text{advection}} = \underbrace{\alpha \nabla^2 \phi(\mathbf{x})}_{\text{diffusion}} + \underbrace{Q(\mathbf{x},t)}_{\text{reaction}}, \tag{1.4.1}$$

in which ϕ denotes chemical (e.g. vesicle) concentration, $\mathbf{u}$ the velocity vector for cytosolic flow, α the chemical diffusivity, and Q a source/sink term (additional reaction terms may appear in the boundary conditions). Numerical methods are developed to find approximate solutions to this PDE. These methods include both a finite volume method (FVM) for use on unstructured grids and irregular geometries, as well as an alternating-direction-implicit (ADI) method for the sake of comparison. Error analysis shows that our two methods generally produce errors of a similar magnitude, with both displaying rapid convergence towards analytical solutions as degrees of freedom are increased.

In Chapter 3, we develop methods for finding numerical solutions to low Reynolds number flow problems (Stokes flow). This is necessary to determine an appropriate form for $\mathbf{u}$, the velocity vector representing cytosolic flow in the pollen tube. We first present an overview of the method of regularized Stokeslets, developed by Cortez *et al.* [31, 33], which forms the basis of our own work. We convert Cortez' 3D Cartesian method to cylindrical coordinates and integrate analytically in the azimuthal direction under the assumption of axisymmetry about the z axis. Our newly derived solutions, termed 'regularized ringlets', exhibit a favourable speed and accuracy compared to the traditional method of regularized Stokeslets as well as to analogous singular Stokeslet methods.

In Chapter 4, we use the method of regularized ringlets to produce cytosolic velocity profiles for the growing pollen tube. A number of different cases are considered, encompassing differing proportions and locations of actomyosin vesicle transport as well as a variety of growth speeds for the tube. Using these velocity profiles in conjunction with the FVM developed in Chapter 2, we model the cytoplasmic vesicle distribution at (and during stages leading to) steady–state. Our modelling yields new results regarding cytoplasmic viscosity and the rates and locations of exo–/endo–cytosis, validated by new experimental imaging (courtesy of our collaborators Dr Chebli and Prof Geitmann at McGill University). These results highlight the importance of including cytosolic fluid velocity in any modelling of cytoplasmic dynamics.

Finally, we conclude with a comprehensive summary of our results and a discussion of future work in Chapter 5.

CHAPTER 2

DEVELOPING NUMERICAL METHODS FOR SOLVING THE ADVECTION–DIFFUSION–REACTION EQUATION

A key requirement to model vesicle distributions in the pollen tube tip is solving the associated advection–diffusion–reaction system. This is particularly challenging as the spatial domain of the tip displays a curved geometry. Here, we develop and test numerical schemes (both finite volume and alternating–direction–implicit methods) for this system, which will be coupled to the method for finding flow field solutions developed in Chapter 3 and applied to the pollen tube in Chapter 4.

2.1 Derivation of the advection–diffusion–reaction equation

We seek an equation to model the concentration of vesicles in the growing pollen tube. Starting from the most general form of the continuity equation, let

$$\frac{\partial \phi(\mathbf{x}, t)}{\partial t} + \nabla \cdot \mathbf{j}(\mathbf{x}, t) = Q(\mathbf{x}, t), \tag{2.1.1}$$

in which ϕ denotes vesicle concentration, $\mathbf{j}$ the total flux, and Q a volumetric source/sink for ϕ. The total flux $\mathbf{j}$ is given by the sum of diffusive (approximated by Fick's first law) and advective components, such that

$$\mathbf{j}_{\text{diff}} = -\alpha \nabla \phi(\mathbf{x}, t), \quad \mathbf{j}_{\text{adv}} = \mathbf{u}(\mathbf{x})\phi(\mathbf{x}, t), \tag{2.1.2}$$

where α is the (constant) coefficient of vesicle diffusivity and $\mathbf{u}$ represents steady cytosolic flow. Substitution of these flux terms into Equation (2.1.1) yields

$$\frac{\partial \phi(\mathbf{x}, t)}{\partial t} + \nabla \cdot (\mathbf{u}(\mathbf{x})\phi(\mathbf{x}, t) - \alpha \nabla \phi(\mathbf{x}, t)) = Q(\mathbf{x}, t). \tag{2.1.3}$$

Under the assumption that $Q = 0$ (as will be often used in the FVM), Equation (2.1.3) reduces to the well known mass conserving form of the advection–diffusion–reaction equation,

$$\frac{\partial \phi}{\partial t} + \nabla \cdot (\mathbf{u}\phi) = \alpha \nabla^2 \phi, \tag{2.1.4}$$

in which $\nabla \cdot \mathbf{u} = 0$ under the assumption of incompressible flow employed throughout this thesis.

The method for evaluating the flow term $\mathbf{u}$ will be detailed in Chapter 3 and applied to the pollen tube in Chapter 4. When choosing suitable boundary conditions for the ADR

PDE, the Robin condition will be frequently employed. This is given by

$$(\mathbf{u}\phi + \alpha\nabla\phi) \cdot \hat{\mathbf{n}} = f(\mathbf{x}, t) \qquad \forall \mathbf{x} \in \boldsymbol{\partial\Omega}, \tag{2.1.5}$$

in which $\hat{\mathbf{n}}$ is the outward pointing unit normal to the boundary $\boldsymbol{\partial\Omega}$ on which the condition is applied, and $f(\mathbf{x}, t)$ determines flux in/out of $\boldsymbol{\partial\Omega}$. The $\mathbf{u}$ here represents the velocity of the fluid relative to the boundary. Thus in the case of an impermeable, static boundary (or any general case where the velocity of the boundary matches that of the fluid), the Robin condition reduces to the Neumann

$$(\alpha\nabla\phi(\mathbf{x}, t)) \cdot \hat{\mathbf{n}} = f(\mathbf{x}, t) \qquad \forall \mathbf{x} \in \boldsymbol{\partial\Omega}. \tag{2.1.6}$$

The Dirichlet condition will also be employed, which can be similarly expressed as

$$\phi(\mathbf{x}, t) = L(\mathbf{x}, t) \qquad \forall \mathbf{x} \in \boldsymbol{\partial\Omega}, \tag{2.1.7}$$

for some function $L(\mathbf{x}, t) \in \mathbb{R}$. This could be used, for example, to maintain a constant population of vesicles in some basal region in order to allow a constant flow of vesicles into the shank.

Precise forms of the boundary conditions simulating removal/addition of vesicles to the apical pool as a result of exo/endocytosis along the growing part of the tube will be considered in Chapter 4.

2.2 Developing a finite volume method

The finite volume method (FVM) is a mathematical technique for representing and evaluating a PDE as a set of algebraic equations in order to obtain a numerical solution to the PDE. This is achieved by discretising the spatial domain of the problem into a set of 'nodes' (each joined to a number of others by non-overlapping 'edges') around which we construct distinct control volumes (CVs) such that the entire domain is covered.

The first step in developing a FVM for the ADR equation is to re–write Equation (2.1.3) in the form

$$\frac{\partial \phi(\mathbf{x},t)}{\partial t} = \nabla \cdot (\alpha \nabla \phi(\mathbf{x},t) - \mathbf{u}(\mathbf{x})\phi(\mathbf{x},t)) + Q(\mathbf{x},t). \tag{2.2.1}$$

By considering the integral of the ADR equation over each CV and by applying Gauss' divergence theorem so that flux terms need only be evaluated at CV surfaces, it is found that

$$\begin{aligned} \int_V \frac{\partial \phi(\mathbf{x},t)}{\partial t}\, dV &= \int_V \left((\nabla \cdot (\alpha \nabla \phi(\mathbf{x},t) - \mathbf{u}(\mathbf{x})\phi(\mathbf{x},t))) + Q(\mathbf{x},t) \right)\, dV, \\ &= \oint_S (\alpha \nabla \phi(\mathbf{x},t) - \mathbf{u}(\mathbf{x})\phi(\mathbf{x},t)) \cdot \hat{\mathbf{n}}\, dS + \int_V Q(\mathbf{x},t)\, dV. \end{aligned} \tag{2.2.2}$$

Application of suitable quadrature rules to each integral then yields a set of algebraic equations (one for each CV) which can be solved simultaneously to give an approximate numerical solution to the PDE. The integral formula (2.2.2) applies both in 3D (with a volume V enclosed by a surface S) and in 2D (with an area V enclosed by a curve S). In the following, we will explain our method for a 2D system with an extension to the axisymmetric 3D case. The formulation for the 3D case without axisymmetry is not considered here but the methodology is similar. In keeping with 3D convention, we will continue to use the terms 'volume' and 'surface' when describing elements of our mesh despite the fact that these are represented graphically as surfaces and lines respectively.

2.2.1 Mesh generation

Due to the number of spatially–dependent terms in (2.2.2) (some of which may have large spatial gradients) it is evident that mesh and CV geometries will have a significant effect on the numerical solution to the PDE. We identify three ideal properties of these geometries, (i) that the mesh should be such that it can be applied to almost any shape, including curved surfaces, (ii) that the CVs should be such that accurate approximations to the variable values can be made along their surfaces by using the values of these variables at the mesh nodes, and (iii) that the accuracy of the numerical solution should increase as the granularity of the mesh is increased. We have used the 'MESH2D' algorithm of Engwirda [45] in MATLAB for this purpose, which constructs a triangular mesh on a given 2D geometry using a Delaunay triangulation algorithm.

2.2.2 Construction of control volumes

Methods of CV construction can be split into two distinct groups, either cell-centred or vertex-centred approaches. For triangular meshes, the CVs in a cell-centred method correspond to the triangles directly with surfaces described by their edges and their centroids essentially forming a dual set of nodes on which the numerical solution is obtained. While this approach seems most natural given the MESH2D output, it is somewhat problematic in practice. In particular, implementing boundary conditions can prove challenging since no dual nodes are present on the domain boundary meaning values of the solution here are not inherently calculated. This is not ideal for situations involving a displacement condition on the boundary (e.g. due to growth). Fallah [48] suggests the use of additional 'line cells' along boundaries of a cell-centred FVM, transferring boundary conditions into the internal adjacent cells. This method was found to be very effective, resulting in smaller errors for cell-centred than vertex-centred FVM for a given mesh but at an unspecified

additional cost. We instead choose to use a vertex-centred method, whereby a CV is constructed around each original node by joining the midpoints of the node's adjacent edges to the centroids of the triangle(s) each edge belongs to. Development of the code for this method is undoubtedly more challenging than it is for the cell-centred method, but the benefits of the vertex-centred approach are substantial. Additional 'line cells' at domain boundaries are not needed in the vertex-centred FVM, with solution values at the boundary easily calculated in a manner similar to internal parts of the domain. Interpolation between vertices to triangle centroids also arguably allows for more consistent and readily available approximations to the values of variables and parameters on the CV surfaces in the vertex-centred approach. An example of a CV for the vertex-centred method can be seen in Figure 2.1. In cases where the central node of the CV lies on the boundary of the domain, the volume is closed by joining the midpoints of the boundary edges to the node itself (Figure 2.2).

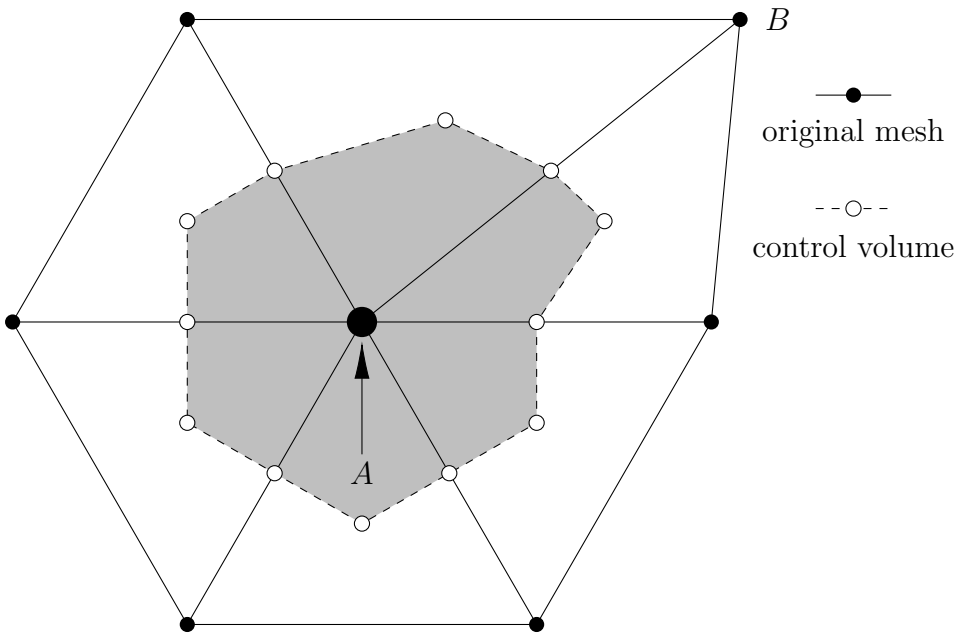

Figure 2.1: An example of a control volume surrounding the node A in the vertex-centred method. The midpoints of the edges adjacent to A are joined to the centroids of the triangle(s) they belong to in order to create the CV. The location of the node B is purposefully irregular to highlight the fact that the midpoint of each edge in the original mesh does not necessarily coincide with the midpoint of the line joining the centroids of the adjacent triangles.

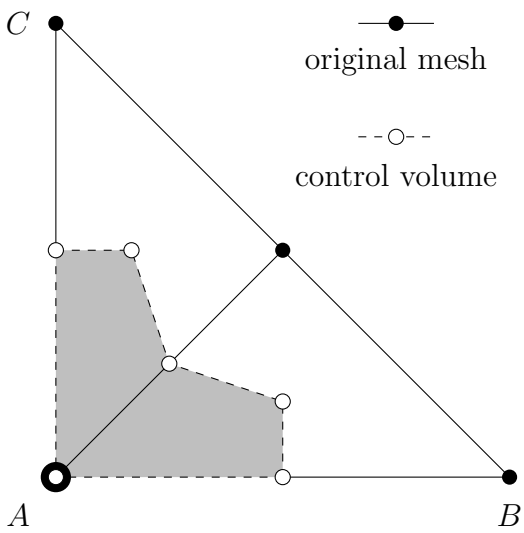

Figure 2.2: An example of a control volume surrounding the boundary node A in the vertex centred method, in which the lines AB and AC are part of the boundary of the domain.

2.2.3 Approximating the integrated advection–diffusion–reaction PDE

Recall that the integrated ADR equation can be expressed as

$$\int_V \frac{\partial \phi(\mathbf{x},t)}{\partial t}\, dV = \oint_S (\alpha \nabla \phi(\mathbf{x},t) - \mathbf{u}(\mathbf{x})\phi(\mathbf{x},t)) \cdot \hat{\mathbf{n}}\, dS + \int_V Q(\mathbf{x},t)\, dV. \tag{2.2.3}$$

The LHS of this equation is easily approximated by using a first forward difference (for the time derivative) and the midpoint method (for the integral) to yield,

$$\int_V \frac{\partial \phi}{\partial t}\, dV \approx \Delta V \frac{\phi_A^{k+1} - \phi_A^k}{\Delta t}, \tag{2.2.4}$$

where ϕ_A^k denotes the kth iterate of ϕ in time, evaluated at the central node A (around which the current control volume has been constructed). The parameters ΔV and Δt are given by the size (area in 2D, volume in 3D) of the current control volume and the size of the time-step respectively. ΔV can be calculated by summing the areas of the 'sub-triangles' created by drawing edges joining each vertex of the CV surface to the

central node A (Figure 2.3). The vertices of each of these sub-triangles are either a node, an edge midpoint, or a triangle centroid in our original mesh and so their positions can be easily calculated. This makes it possible to calculate the area (say, T) of the sub-triangle using Heron's Formula

$$T = \sqrt{s(s-a)(s-b)(s-c)}, \tag{2.2.5}$$

in which a, b, c are the lengths of each side of the sub-triangle and $s = (a+b+c)/2$ is its semiperimeter.

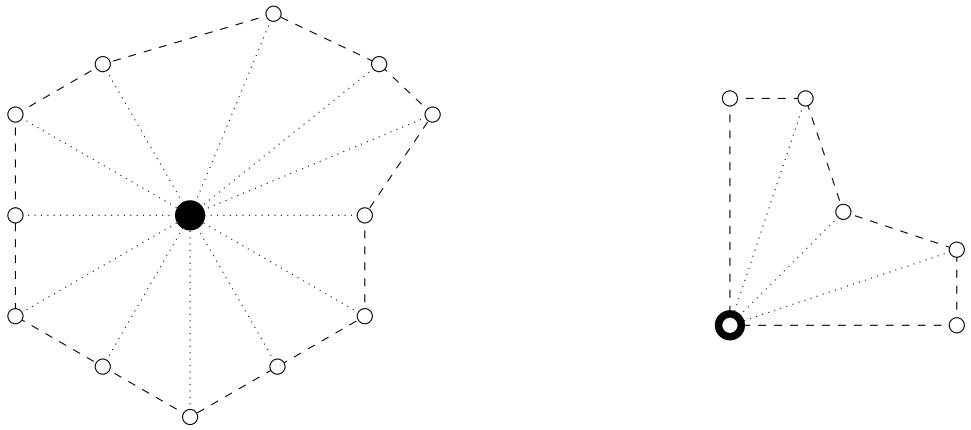

Figure 2.3: Division of control volumes from Figures 2.1 and 2.2 into sub-triangles by drawing (dotted) lines joining each CV vertex to the central node.

For the source/sink term $Q(\mathbf{x}, t)$, the approximation is straightforward and is given by

$$\int_V Q(\mathbf{x}, t)\, dV = \Delta V Q(\mathbf{x}, t). \tag{2.2.6}$$

Additional complexity comes in the form of a proportional sink, that is, when Q takes the form $Q(\mathbf{x}, t) = -\gamma\phi(\mathbf{x}, t)$ for constant γ. In this case, it follows that

$$-\int_V \gamma\phi(\mathbf{x}, t)\, dV = -\frac{1}{2}\Delta V(\phi_A^{k+1} + \phi_A^k), \tag{2.2.7}$$

in which ϕ is averaged over time steps k and $k+1$ such that our discretization method is implicit in time. This averaging of ϕ is employed for all terms in the RHS.

In what follows, we frequently make use of linear interpolation to approximate ϕ (and

later $\mathbf{u}$) at points inside or along the edges of triangles in the original mesh using known values at triangle vertices. For grid size h (corresponding to the approximate length of each triangle edge), this interpolation is associated with an error of $\mathcal{O}(h^2)$ (as can be verified using a Taylor expansion). When other methods are employed that are associated with a larger error value, this is made explicitly clear.

To evaluate the diffusive $\nabla\phi$ term in Equation (2.2.3), it is necessary to calculate the partial derivatives $\frac{\partial\phi}{\partial x}$ and $\frac{\partial\phi}{\partial y}$ at the centroid of each triangle in the mesh. This is achieved using linear extrapolation and a least-squares method. Consider the triangle shown in Figure 2.4 with vertices A, B, C and centroid P, located at $\mathbf{x}_A, \mathbf{x}_B, \mathbf{x}_C$ and $\mathbf{x}_P := \frac{1}{3}(\mathbf{x}_A + \mathbf{x}_B + \mathbf{x}_C)$ respectively. Linear extrapolation for ϕ from its value ϕ_P at centroid P to the vertices yields,

$$\phi_A = \phi_P + (x_A - x_P) \cdot \frac{\partial\phi}{\partial x}\Big|_P + (y_A - y_P) \cdot \frac{\partial\phi}{\partial y}\Big|_P + \mathcal{O}(h^2), \tag{2.2.8}$$

$$\phi_B = \phi_P + (x_B - x_P) \cdot \frac{\partial\phi}{\partial x}\Big|_P + (y_B - y_P) \cdot \frac{\partial\phi}{\partial y}\Big|_P + \mathcal{O}(h^2), \tag{2.2.9}$$

$$\phi_C = \phi_P + (x_C - x_P) \cdot \frac{\partial\phi}{\partial x}\Big|_P + (y_C - y_P) \cdot \frac{\partial\phi}{\partial y}\Big|_P + \mathcal{O}(h^2), \tag{2.2.10}$$

which can be written as a linear system $\mathbf{DX} = \mathbf{F}$, with:

$$\mathbf{X} = \begin{bmatrix} \frac{\partial\phi}{\partial x} \\ \frac{\partial\phi}{\partial y} \end{bmatrix}; \ \mathbf{F} = \begin{bmatrix} \phi_A - \phi_P \\ \phi_B - \phi_P \\ \phi_C - \phi_P \end{bmatrix}; \ \mathbf{D} = \begin{bmatrix} \Delta x_{PA} & \Delta y_{PA} \\ \Delta x_{PB} & \Delta y_{PB} \\ \Delta x_{PC} & \Delta y_{PC} \end{bmatrix} \tag{2.2.11}$$

where $\Delta\mathbf{x}_{PA} := \mathbf{x}_A - \mathbf{x}_P$. This is a system of three equations in two unknowns and so is over-constrained with no solution (in general). By implementing a least squares method, the system can be reduced to two equations which yield an optimal least squares solution that minimises the sum of the squares of the errors in each equation of the original system. This is achieved by multiplying the system by the transpose matrix $\mathbf{D}^T$, which yields

$$\mathbf{D}^T\mathbf{DX} = \mathbf{D}^T\mathbf{F} \Rightarrow \mathbf{X} = (\mathbf{D}^T\mathbf{D})^{-1}\mathbf{D}^T\mathbf{F}, \tag{2.2.12}$$

a solvable system of equations. This process can be applied to each triangle in order to approximate $\nabla\phi$ at each centroid to $\mathcal{O}(h)$ accuracy. For implementation in MATLAB, the vector $\mathbf{F}$ is further decomposed into the product of a matrix $\mathbf{G}$ and vector $\boldsymbol{\phi}^k$ (containing value of ϕ at each node at time $k\Delta t$) so that $(\mathbf{D}^T\mathbf{D})^{-1}\mathbf{D}^T\mathbf{G}$ is a linear operator on $\boldsymbol{\phi}^k$.

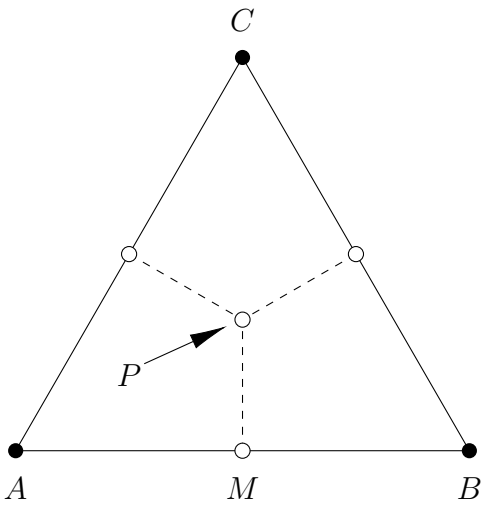

Figure 2.4: The triangle with centroid P containing portions of the control volumes surrounding the nodes A, B, and C. The point M is the midpoint of the line AB.

To evaluate the integral of $\nabla\phi$ along the surface of a CV by using a midpoint method on each of its edges, it is also necessary to find an approximation for $\nabla\phi$ at the midpoint of each edge in the original mesh. Using the portion of the CV around the point A in Figure 2.4 as an example, before evaluating $\oint_S(\alpha\nabla\phi)\cdot\hat{\mathbf{n}}\,ds$ along the line MP using a midpoint method an approximation for $\nabla\phi$ at M is required. This can be achieved by interpolation of $\nabla\phi$ between the two centroids, P and P', of the adjacent triangles to which the point M belongs (as shown in Figure 2.5). However, in the general case the midpoint M of the line AB does not lie on the line PP' so standard linear interpolation is ineffective. Instead, we employ the modified interpolation

$$\nabla\phi_M \approx \frac{dP'\cdot\nabla\phi_P + dP\cdot\nabla\phi_{P'}}{dP+dP'}, \tag{2.2.13}$$

in which

$$dP = |\mathbf{x}_M - \mathbf{x}_P|, \quad dP' = |\mathbf{x}_M - \mathbf{x}_{P'}|. \tag{2.2.14}$$

The error associated with this approximation is a consequence of irregularity of the mesh

and thus difficult to quantify, but for two adjacent equilateral triangles of identical size (the ideal scenario) Equation (2.2.13) reduces to standard linear interpolation with error $\mathcal{O}(h^2)$.

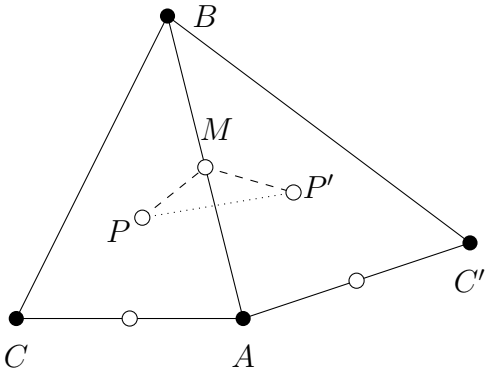

Figure 2.5: The edge midpoint M (a vertex of the CV surrounding the node A) does not in general lie on the (dotted) line joining the adjacent triangle centroids, P and P'. Thus, the value of $\nabla\phi$ at M must be found using a modified version of linear interpolation between P and P'.

Splitting $\nabla\phi$ and $\hat{\mathbf{n}}$ into x and y components, it then follows that

$$\begin{aligned}\int_{MP}(\alpha\nabla\phi)\cdot\hat{\mathbf{n}}\,ds \approx &\frac{1}{4}\Big[\Big(\frac{\partial\phi}{\partial x}\Big|_P+\frac{\partial\phi}{\partial x}\Big|_M\Big)\Delta y_{MP}-\Big(\frac{\partial\phi}{\partial y}\Big|_P+\frac{\partial\phi}{\partial y}\Big|_M\Big)\Delta x_{MP}\Big]^{k+1}\\ &+\frac{1}{4}\Big[\Big(\frac{\partial\phi}{\partial x}\Big|_P+\frac{\partial\phi}{\partial x}\Big|_M\Big)\Delta y_{MP}-\Big(\frac{\partial\phi}{\partial y}\Big|_P+\frac{\partial\phi}{\partial y}\Big|_M\Big)\Delta x_{MP}\Big]^{k},\end{aligned} \tag{2.2.15}$$

in which $\Delta\mathbf{x}_{MP}=\mathbf{x}_P-\mathbf{x}_M$ as before and the outward pointing unit normal is given by $\hat{\mathbf{n}}=(dy,-dx)$. Superscripts k and $k+1$ refer to the time step at which each term is evaluated. Applying this to each edge of the CV yields the total diffusive flux through the surface of the volume. The ordering of the letters MP in the subscripts present in Equation (2.2.15) and the subsequent definition of $\Delta\mathbf{x}_{MP}$ are important; the path of integration *must* be counterclockwise along the surface of the control volume. If the point M lies on an edge on domain boundary, since there is no point P' to use for interpolation the simpler first order approximation

$$\begin{aligned}\int_{MP}(\alpha\nabla\phi)\cdot\hat{\mathbf{n}}\,ds \approx &\frac{1}{2}\left[\frac{\partial\phi}{\partial x}\Big|_P\Delta y_{MP}-\frac{\partial\phi}{\partial y}\Big|_P\Delta x_{MP}\right]^{k+1}\\ &+\frac{1}{2}\left[\frac{\partial\phi}{\partial x}\Big|_P\Delta y_{MP}-\frac{\partial\phi}{\partial y}\Big|_P\Delta x_{MP}\right]^{k},\end{aligned} \tag{2.2.16}$$

is employed instead.

An alternative approach is to use the least squares method outlined in Equations (2.2.8)–(2.2.10) to calculate $\frac{\partial \phi}{\partial x}$ and $\frac{\partial \phi}{\partial y}$ at the midpoint of the line MP directly (as opposed to at the centroids P, P'). In this case, the value of ϕ at the midpoint of the line MP is approximated by $\phi_{MP} \approx \frac{1}{12}(5\phi_A + 5\phi_B + 2\phi_C)$, via linear interpolation of $\phi_M \approx \frac{1}{2}(\phi_A + \phi_B)$ and $\phi_P \approx \frac{1}{3}(\phi_A + \phi_B + \phi_C)$. The benefit of this approach is that all the information necessary for approximating MP is now contained within a single triangle, and there is no additional complexity near the boundary (so the same method can be employed throughout the entire domain). The major drawback is that data must now be stored for the derivatives at 3 points in each triangle (instead of just at the centroid), increasing computational complexity considerably (see Figure 2.6).

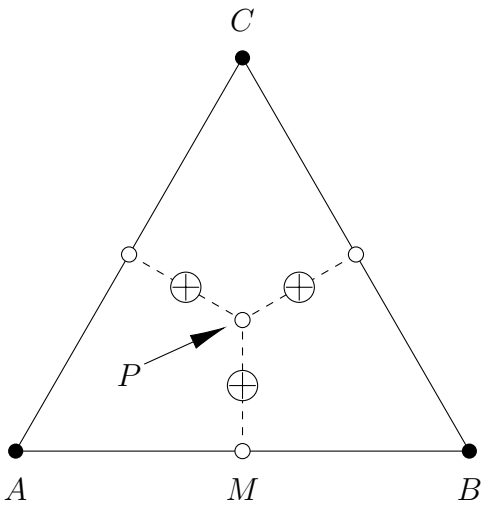

Figure 2.6: Each evaluation point $\oplus$ is located at the midpoint of a line joining the midpoint of one of the triangle edges to the centroid P. It is possible to estimate $\nabla\phi$ directly at these locations with improved accuracy using the least squares method and values for ϕ at A, B, C, but doing so is significantly more computationally expensive than simply estimating $\nabla\phi$ at the triangle centroid.

Evaluating the advective $\mathbf{u}\phi$ term in Equation (2.2.3) requires more careful consideration than the diffusive term. Denoting the separate components of the flow vector $\mathbf{u}$ by $\mathbf{u} = (u, v)$, the integral for the advective term takes the form

$$\int_{MP} (-\mathbf{u}\phi) \cdot \hat{\mathbf{n}}\, ds \approx -\frac{1}{2}(\phi_{MP}^{k+1} + \phi_{MP}^{k}) \left(u_{MP}\Delta y_{MP} - v_{MP}\Delta x_{MP}\right). \tag{2.2.17}$$

Let $\mathbf{u}$ take the value of $\mathbf{u}_{MP} \approx \frac{1}{12}(5\mathbf{u}_A + 5\mathbf{u}_B + 2\mathbf{u}_C)$ at the midpoint of the line MP through repeated use of linear interpolation (as for ϕ_{MP} when estimating the diffusive flux). If the previous (central differencing) choice of $\phi^{\text{cd}}_{MP} := (5\phi_A + 5\phi_B + 2\phi_c)/12$ is used for evaluating the advective flux, it is known that while this yields accurate solutions of 2nd order with respect to grid size it also produces unstable oscillations when the Péclet number (the ratio of advective to diffusive transport rate) is large [82]. The alternative is to use an upwind scheme, such as,

$$\phi^{\text{up}}_{MP} := \begin{cases} \phi_A & \text{if } (\mathbf{u}_{MP} \cdot \hat{\mathbf{n}}) > 0, \\ \phi_B & \text{if } (\mathbf{u}_{MP} \cdot \hat{\mathbf{n}}) < 0. \end{cases} \tag{2.2.18}$$

This choice of ϕ_{MP} provides far superior stability than the linearly interpolated value, but only exhibits 1st order accuracy. Further, the method works best when the flow direction is normal to the surface and the line AB is perpendicular to MP; two conditions that are essentially impossible to guarantee throughout the entirety of the computational domain, incurring an additional unquantifiable error based on mesh irregularity similar to in Equation (2.2.13).

In order to achieve both a sufficient accuracy and stability, it is sensible to implement a mixed scheme of the form

$$\phi_{MP} = \beta\phi^{\text{up}}_{MP} + (1 - \beta)\phi^{\text{cd}}_{MP}, \tag{2.2.19}$$

in which $0 \leq \beta \leq 1$. For the remainder of this thesis, we choose to use the value of $\beta = 0.8$ which yields consistently accurate results in the modelling of problems with smooth ϕ. This is by no means an optimal choice but involves a large enough proportion of upwind differencing that we do not see the emergence of spurious oscillations in our results. A more rigorous formulation for defining β as a linear function that varies in space and minimizes the emergence of spurious oscillations (based on the total variational diminishing (TVD) scheme [65, 122] of Darwish and Moukalled [39] for unstructured

grids) is given in the following Section.

2.2.4 Implementing flux limiters

Following the example of Darwish and Moukalled [39] for implementing a flux limiter in a PDE discretization with unstructured grids, we introduce the scheme

$$\phi_{MP} = \begin{cases} \phi_A + \frac{1}{2}\psi(\phi_B - \phi_A) & \text{if } (\mathbf{u}_{MP} \cdot \hat{\mathbf{n}}) > 0, \\ \phi_B + \frac{1}{2}\psi(\phi_A - \phi_B) & \text{if } (\mathbf{u}_{MP} \cdot \hat{\mathbf{n}}) < 0, \end{cases} \tag{2.2.20}$$

where the flux limiter $0 \leq \beta(\psi) \leq 2$ is a linear function dependent on ψ, the upwind ratio of consecutive gradients of ϕ. This ratio ψ is given by

$$\psi = \frac{\phi_A - \phi_U}{\phi_B - \phi_A}, \qquad \text{for } (\mathbf{u}_{MP} \cdot \hat{\mathbf{n}}) > 0, \tag{2.2.21}$$

for some theoretical node U downwind of A (the case $\mathbf{u}_{MP} \cdot \hat{\mathbf{n}} < 0$ will be addressed shortly).

The value of β dictates the kind of numerical scheme employed, with the most important examples including upwind ($\beta = 0$), downwind ($\beta = 2$), and central differences ($\beta = 1$). Intermediate values of β represent a combination of these schemes. For a flux–limited scheme to have second order accuracy with respect to the grid size it is required that $\beta(1) = 1$, and in order to be total variational diminishing (TVD) we require $0 \leq \beta(\psi) \leq \min[2\psi, 2]$. The term TVD, first introduced by Harten *et al.* [65, 122], refers to a numerical scheme in which the total variation in the solution in the spatial domain $\mathbf{\Omega}$, given by

$$TV = \int_{\mathbf{\Omega}} |\nabla\phi(\mathbf{x})| \, d\mathbf{x}, \tag{2.2.22}$$

is non–increasing in time.

Observe that ψ may be written in the form,

$$\psi = \frac{\phi_A - \phi_U}{\phi_B - \phi_A} = \frac{(\phi_B - \phi_U) - (\phi_B - \phi_A)}{\phi_B - \phi_A} = \frac{\phi_B - \phi_U}{\phi_B - \phi_A} - 1. \tag{2.2.23}$$

Now if we let U be located such that the node A is the midpoint of the line UB, then application of the midpoint method yields,

$$(\phi_B - \phi_U) = \nabla\phi_A \cdot \Delta\mathbf{x}_{UB} = (2\nabla\phi_A \cdot \Delta\mathbf{x}_{AB}), \tag{2.2.24}$$

and so ψ can be expressed solely using values of ϕ at the mesh nodes A and B,

$$\psi = \frac{(2\nabla\phi_A \cdot \Delta\mathbf{x}_{AB})}{\phi_B - \phi_A} - 1. \tag{2.2.25}$$

For $(\mathbf{u}_{MP} \cdot \hat{\mathbf{n}}) < 0$, the new formulation for ψ is found simply by swapping the indices A and B. That is,

$$\psi = \frac{(2\nabla\phi_B \cdot \Delta\mathbf{x}_{BA})}{\phi_A - \phi_B} - 1. \tag{2.2.26}$$

Since $\Delta\mathbf{x}_{AB}/(\phi_B - \phi_A) = \Delta\mathbf{x}_{BA}/(\phi_A - \phi_B)$, the value of ψ may be neatly summarised as,

$$\psi = \begin{cases} \frac{(2\nabla\phi_A \cdot \Delta\mathbf{x}_{AB})}{\phi_B - \phi_A} - 1 & \text{if } (\mathbf{u}_{MP} \cdot \hat{\mathbf{n}}) > 0, \\ \frac{(2\nabla\phi_B \cdot \Delta\mathbf{x}_{AB})}{\phi_B - \phi_A} - 1 & \text{if } (\mathbf{u}_{MP} \cdot \hat{\mathbf{n}}) < 0, \end{cases} \tag{2.2.27}$$

i.e. the direction of flow affects only the location at which we calculate the derivative $\nabla\phi$. Calculation of this derivative can be achieved by application of the least squares method using values of ϕ at all adjacent nodes.

There are many different ways to construct an appropriate flux limiter β using the gradient ratio ψ. The Koren limiter, given by $\beta(\psi) = \max[0, \min(2r, (2 + \psi)/3, 2)]$, is a poplar choice which is third-order accurate for sufficiently smooth data ($\psi \in [2/5, 4]$) [18] and lies within the 2nd order TVD region for all values of ψ [112]. In the limit as $\alpha \to 0$, the flux–limited FVM typically outperforms the fixed–β FVM but the increase

in computational time is significant.

2.2.5 Conversion to an axisymmetric 3D geometry

This Chapter has detailed the key steps in constructing a FVM for solving the diffusion equation on a 2D geometry in Cartesian (x, y) co-ordinates. In order to extend this work to a 3D geometry in cylindrical (r, θ, z) co-ordinates, axisymmetry is assumed about the z axis so that the solution can be described in terms of r and z only. A 2D mesh is generated in exactly the same manner as before, with $x \equiv r$ and $y \equiv z$. The only change necessary is in the ΔV and $\Delta \mathbf{x}$ terms, which must be multiplied by a factor $2\pi r$ to reflect the fact that the spatial domain is now 3D. There is some additional complexity in choosing which value of r to use to represent each control volume, since the position of the enclosed node (the easiest choice) does not correspond to the centroid of the CV in general. In particular, using the value of r at the node may be problematic at the $r = 0$ boundary. Thus, it is sensible to calculate the position of the centroid of each CV and use this as the representative value of r.

2.3 The alternating-direction-implicit method for use on structured grids

In addition to the FVM, we also develop a separate finite difference method for the purpose of comparison of errors (particularly useful in situations where an analytical solution is not readily available). The method we employ is a modification of the original Alternating–Direction–Implicit (ADI) method of Peaceman and Rachford [95] to include the QUICK algorithm of Leonard [82] for the discretization of the advective flux. The standard ADI method for the diffusion equation using central differences is uncondition-

ally stable and second order in both time and space. The QUICK discretization of the advective flux is third order accurate with respect to the spatial grid size. Thus the combination of these two schemes provides a method with remarkable accuracy as well as impressive computational efficiency. Unfortunately, the method is only applicable to structured grids and so lacks the flexibility of the FVM.

When working with a structured grid, it is intuitive to write the ADR equation in Cartesian form:

$$\frac{\partial \phi}{\partial t} + u\frac{\partial \phi}{\partial x} + v\frac{\partial \phi}{\partial y} = \alpha\left(\frac{\partial^2 \phi}{\partial x^2} + \frac{\partial^2 \phi}{\partial y^2}\right), \tag{2.3.1}$$

where u and v are the x and y components of the flow vector $\mathbf{u} = (u, v)$ respectively. The full ADI discretisation of this equation occurs in two stages using an intermediate time step. During the first stage, Equation (2.3.1) is discretized such that its resultant form is explicit in one direction (say x) and implicit in the other (y). That is

$$\frac{\partial \phi}{\partial t} = \frac{\phi_{i,j}^{k+\frac{1}{2}} - \phi_{i,j}^{k}}{(\Delta t/2)}, \tag{2.3.2}$$

$$\frac{\partial^2 \phi}{\partial x^2} = \frac{\phi_{i-1,j}^{k} - 2\phi_{i,j}^{k} + \phi_{i+1,j}^{k}}{(\Delta x)^2}, \tag{2.3.3}$$

$$\frac{\partial^2 \phi}{\partial y^2} = \frac{\phi_{i,j-1}^{k+\frac{1}{2}} - 2\phi_{i,j}^{k+\frac{1}{2}} + \phi_{i,j+1}^{k+\frac{1}{2}}}{(\Delta y)^2}, \tag{2.3.4}$$

$$\frac{\partial \phi}{\partial x} = \begin{cases} \frac{1}{8\Delta x}\left(-3\phi_{i-1,j}^{k} - 3\phi_{i,j}^{k} + 7\phi_{i+1,j}^{k} - \phi_{i+2,j}^{k}\right) & \text{if } u_{i,j} > 0, \\ \frac{1}{8\Delta x}\left(\phi_{i-2,j}^{k} - 7\phi_{i-1,j}^{k} + 3\phi_{i,j}^{k} + 3\phi_{i+1,j}^{k}\right) & \text{if } u_{i,j} < 0, \end{cases} \tag{2.3.5}$$

$$\frac{\partial \phi}{\partial y} = \begin{cases} \frac{1}{8\Delta y}\left(-3\phi_{i,j-1}^{k+\frac{1}{2}} - 3\phi_{i,j}^{k+\frac{1}{2}} + 7\phi_{i,j+1}^{k+\frac{1}{2}} - \phi_{i,j+2}^{k+\frac{1}{2}}\right) & \text{if } v_{i,j} > 0, \\ \frac{1}{8\Delta y}\left(\phi_{i,j-2}^{k+\frac{1}{2}} - 7\phi_{i,j-1}^{k+\frac{1}{2}} + 3\phi_{i,j}^{k+\frac{1}{2}} + 3\phi_{i,j+1}^{k+\frac{1}{2}}\right) & \text{if } v_{i,j} < 0. \end{cases} \tag{2.3.6}$$

In the absence of advection, Equations (2.3.1)–(2.3.4) can be written in the form

$$-c_y\phi_{i,j-1}^{k+\frac{1}{2}} + (1+2c_y)\phi_{i,j}^{k+\frac{1}{2}} - c_y\phi_{i,j+1}^{k+\frac{1}{2}} = c_x\phi_{i-1,j}^{k} + (1-2c_x)\phi_{i,j}^{k} + c_x\phi_{i+1,j}^{k}, \tag{2.3.7}$$

where $c_y = \frac{\alpha \Delta t}{2(\Delta y)^2}$ and $c_x = \frac{\alpha \Delta t}{2(\Delta x)^2}$. Considering the common form of Equation (2.3.7) for all $j = 1, 2, ..., N_y$, it is possible to write

$$\mathbf{A}\boldsymbol{\phi}_i^{k+\frac{1}{2}} = \mathbf{B}_i, \tag{2.3.8}$$

where

- The $N_y \times N_y$ matrix $\mathbf{A}$ is a linear operator between $\boldsymbol{\phi}_i^{k+\frac{1}{2}}$ and $\mathbf{B}_i$ comprised of the coefficients on the LHS of Equation (2.3.7),
- $\boldsymbol{\phi}_i^{k+\frac{1}{2}}$ is the $N_y \times 1$ vector with elements $\phi_{i,j}^{k+\frac{1}{2}}$ for $j = 1, 2, ..., N_y$,
- $\mathbf{B}_i$ is the $N_y \times 1$ vector containing the values of the explicit sums on the RHS of Equation (2.3.7) for $j = 1, 2, ..., N_y$.

For any given $i \in 1, ..., N_x$, following *a priori* calculation of $\mathbf{B}_i$ and by inversion of the matrix $\mathbf{A}$ the solutions $\boldsymbol{\phi}_i^{k+\frac{1}{2}} = \mathbf{A} \backslash \mathbf{B}_i$ may be found. Iteration over all i then yields the complete solution for all $\phi_{i,j}^{k+\frac{1}{2}}$.

It is important to note that while the vector $\mathbf{B}_i$ is different for each i, the matrix $\mathbf{A}$ is not. This is only true for the purely diffusive case. When we also include the advective terms, the diffusive matrix $\mathbf{A}$ must be augmented by an advective matrix $\mathbf{A}'_i$, which is different for each i as a result of changes in $v_{i,j}$ for $i = 1, 2, ..., N_x$. For steady flow each $\mathbf{A}'_i$ need only be calculated once.

During the second stage of the ADI method, we alternate direction so that the equations

are now explicit in y and implicit in x. That is

$$\frac{\partial \phi}{\partial t} = \frac{\phi_{i,j}^{k+1} - \phi_{i,j}^{k+\frac{1}{2}}}{(\Delta t/2)}, \tag{2.3.9}$$

$$\frac{\partial^2 \phi}{\partial x^2} = \frac{\phi_{i-1,j}^{k+1} - 2\phi_{i,j}^{k+1} + \phi_{i+1,j}^{k+1}}{(\Delta x)^2}, \tag{2.3.10}$$

$$\frac{\partial^2 \phi}{\partial y^2} = \frac{\phi_{i,j-1}^{k+\frac{1}{2}} - 2\phi_{i,j}^{k+\frac{1}{2}} + \phi_{i,j+1}^{k+\frac{1}{2}}}{(\Delta y)^2}, \tag{2.3.11}$$

$$\frac{\partial \phi}{\partial x} = \begin{cases} \frac{1}{8\Delta x}\left(-3\phi_{i-1,j}^{k+1} - 3\phi_{i,j}^{k+1} + 7\phi_{i+1,j}^{k+1} - \phi_{i+2,j}^{k+1}\right) & \text{if } u_{i,j} > 0, \\ \frac{1}{8\Delta x}\left(\phi_{i-2,j}^{k+1} - 7\phi_{i-1,j}^{k+1} + 3\phi_{i,j}^{k+1} + 3\phi_{i+1,j}^{k+1}\right) & \text{if } u_{i,j} < 0, \end{cases} \tag{2.3.12}$$

$$\frac{\partial \phi}{\partial y} = \begin{cases} \frac{1}{8\Delta y}\left(-3\phi_{i,j-1}^{k+\frac{1}{2}} - 3\phi_{i,j}^{k+\frac{1}{2}} + 7\phi_{i,j+1}^{k+\frac{1}{2}} - \phi_{i,j+2}^{k+\frac{1}{2}}\right) & \text{if } v_{i,j} > 0, \\ \frac{1}{8\Delta y}\left(\phi_{i,j-2}^{k+\frac{1}{2}} - 7\phi_{i,j-1}^{k+\frac{1}{2}} + 3\phi_{i,j}^{k+\frac{1}{2}} + 3\phi_{i,j+1}^{k+\frac{1}{2}}\right) & \text{if } v_{i,j} < 0, \end{cases} \tag{2.3.13}$$

so that in the absence of advection

$$-c_x\phi_{i-1,j}^{k+1} + (1+2c_x)\phi_{i,j}^{k+1} - c_x\phi_{i+1,j}^{k+1} = c_y\phi_{i,j-1}^{k+\frac{1}{2}} + (1-2c_y)\phi_{i,j}^{k+\frac{1}{2}} + c_y\phi_{i,j+1}^{k+\frac{1}{2}}. \tag{2.3.14}$$

By considering the common form of Equation (2.3.14) for all $i = 1, 2, ..., N_x$, it follows that

$$\mathbf{C}\boldsymbol{\phi}_j^{k+1} = \mathbf{D}_j, \tag{2.3.15}$$

where

- The $N_x \times N_x$ matrix $\mathbf{C}$ is a linear operator between $\boldsymbol{\phi}_j^{k+1}$ and $\mathbf{D}_j$ comprised of the coefficients on the LHS of Equation (2.3.14),
- $\boldsymbol{\phi}_j^{k+1}$ is the $N_x \times 1$ vector with elements $\phi_{i,j}^{k+1}$ for $i = 1, 2, ..., N_x$,
- $\mathbf{D}_j$ is the $N_x \times 1$ vector containing the values of the explicit sums on the RHS of Equation (2.3.14) for $i = 1, 2, ..., N_x$.

The process for finding the complete solution for all $\phi_{i,j}^{k+1}$ and including the advective terms then follows similarly from the first stage, the only difference being iteration over

j instead of i throughout.

2.4 Error analysis

To investigate the accuracy of our numerical methods (both FVM and ADI), consider the 2D advection–diffusion problem

$$\frac{\partial \phi}{\partial t} + \mathbf{u} \cdot \nabla \phi = \alpha \nabla^2 \phi, \qquad x, y \in [0, 1], \tag{2.4.1}$$

with $\phi = 0$ on $x, y = 0, 1$ and $\mathbf{u} = (\sin(\pi x)\cos(\pi y), -\cos(\pi x)\sin(\pi y))$. This choice of flow field is useful since it results in zero normal flow at the boundaries as well as satisfying the continuity equation $\nabla \cdot \mathbf{u} = 0$. The Dirichlet condition on the boundaries is necessary for finding an analytical solution (as will be seen shortly). Employing a separable solution

$$\phi(x, y, t) = F(x, y)T(t), \tag{2.4.2}$$

it follows that

$$\frac{1}{T}\frac{dT}{dt} = \frac{1}{F}(\alpha \nabla^2 F - \mathbf{u} \cdot \nabla F) = -\lambda^2, \tag{2.4.3}$$

for some constant λ (since temporal and spatial dependencies have been successfully split). If it is assumed that the spatial part F of the solution ϕ has sinusoidal form $F = \sin(\pi x)\sin(\pi y)$, then

$$\begin{aligned} \mathbf{u} \cdot \nabla F &= \sin(\pi x)\cos(\pi y)\frac{\partial F}{\partial x} - \cos(\pi x)\sin(\pi y)\frac{\partial F}{\partial y}, \\ &= \sin(\pi x)\cos(\pi y)[\pi \cos(\pi x)\sin(\pi y)] - \cos(\pi x)\sin(\pi y)[\pi \sin(\pi x)\cos(\pi y)], \\ &= 0, \end{aligned} \tag{2.4.4}$$

and so the advective term disappears completely. This choice of F dictates why Dirichlet boundary conditions must be employed, since it is incompatible with Neumann conditions. Solving the remaining part of the equation for F to find λ then yields $\lambda^2 = 2\alpha\pi^2$, and so

$$\frac{dT}{dt} = -2\alpha\pi^2 T \Rightarrow T = e^{-2\alpha\pi^2 t}. \tag{2.4.5}$$

Thus the analytical solution for ϕ is

$$\phi(x, y, t) = e^{-2\alpha\pi^2 t} \sin(\pi x) \sin(\pi y), \tag{2.4.6}$$

with initial condition implicitly defined as

$$\phi(x, y, 0) = \sin(\pi x) \sin(\pi y). \tag{2.4.7}$$

As a result of the disappearance of the advective term, this solution holds for both $\mathbf{u} = \mathbf{0}$ and $\mathbf{u} = (\sin(\pi x)\cos(\pi y), -\cos(\pi x)\sin(\pi y))$. Note that in spite of the fact that $\mathbf{u}\cdot\nabla\phi = 0$ in the analytical solution, advection is included in the FVM through approximation of surface flux through each CV (i.e. $\int_S (\mathbf{u}\phi) \cdot \hat{\mathbf{n}}\, dS$) which is in general non-zero over each individual surface. Thus, while an analytical solution in which advection does not disappear would perhaps be preferable, the forthcoming tests should still prove to be a reasonable measure of the accuracy of the FVM and ADI method in tackling advection.

It is now possible to run MATLAB code and compare the magnitude of the absolute errors for FVM and ADI.

Test 1: Pure diffusion with Dirichlet boundary conditions

The two methods are first tested in the purely diffusive case (i.e. in the absence of advection) with Dirichlet boundary conditions. The diffusive constant $\alpha = 1$ is fixed

while mesh size is varied, showing that the magnitude of the errors is decreasing for increasing degrees of freedom (number of grid points used for meshing). The speed of convergence of the errors towards zero is approximately quadratic with respect to the grid size h. For the FVM with uniform meshing (which we have used here), this h represents the approximate length of each triangle edge. For the ADI method, h represents the exact spacing between any two adjacent points. Results can be seen in Tables 2.1 (for FVM) and 2.2 (for ADI), where the ADI method has been tested using finer grids due to its superior computational speed. The parameter t_{max} refers to the dimensionless final time of the simulation whereas N_t denotes the total number of (uniformly spaced) time steps, implicitly defining step size Δt via $N_t - 1 = t_{max}/\Delta t$. The value N_p in the FVM calculations is equal to the total number of nodes used (implicitly chosen by h). The value N_X in the ADI calculations is equal to the total number of nodes used to discretize each axis (implicitly choosing h). The errors listed in these tables are given by:

$$\text{max norm error} = \max|\phi_{num} - \phi_{ana}|, \tag{2.4.8}$$

$$\text{max percentage error} = \frac{\max|\phi_{num} - \phi_{ana}|}{\max|\phi_{ana}|}, \tag{2.4.9}$$

where ϕ_{num} and ϕ_{ana} refer to numerical and analytical solutions for ϕ respectively and the maximum is evaluated using all grid points. Notice that for the percentage error we use separate max functions in the numerator and denominator (instead of just a single max function encompassing the whole fraction) to avoid the possibility of dividing by a number numerically close to 0.

Test 2: Diffusion with advection and Dirichlet boundary conditions

With the introduction of the advective field $\mathbf{u} = (\sin(\pi x)\cos(\pi y), -\cos(\pi x)\sin(\pi y))$, the analytical solution to the Dirichlet problem remains the same. In the following, the

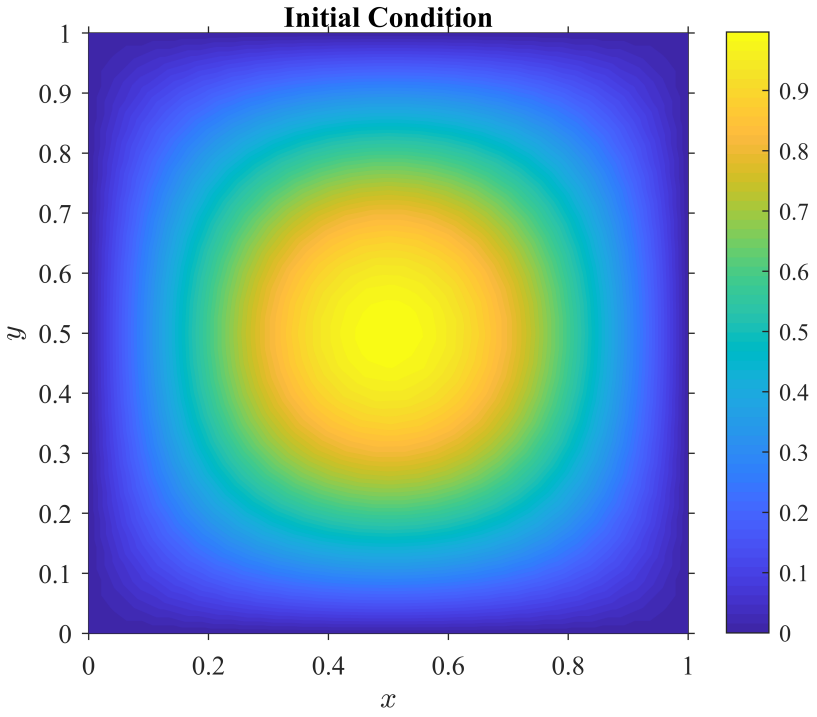

Figure 2.7: Initial condition $\phi(x, y, 0) = \sin(\pi x)\sin(\pi y)$ for use with Dirichlet boundary conditions.

value of α is varied without changing the mesh size to investigate the accuracy of the methods while approaching pure advection. FVM is split into two methods here: the fixed–β and flux–limited schemes. Results are given in Table 2.3. The accuracy of the ADI method begins to deteriorate rapidly near $\alpha = 10^{-4}$ (since QUICK is numerically unstable for pure advection), whereas the fixed–β FVM is surprisingly resilient despite the use of a large value of $\beta = 0.8$ (tending towards the unstable central differencing). The flux–limited FVM outperforms all other methods tested for small α.

We also repeat the Test 1 with the inclusion of advection, using $\alpha = 1$ (for a Péclet number approximately equal to 1) and varying h. The results in Tables 2.4 and 2.5 show that all of our methods readily cope with the introduction of advection, with no method showing any significant deterioration in accuracy from the results of Test 1. The increase in accuracy for small h is more pronounced for the fixed–β FVM than the flux–limited FVM for this choice of $\alpha = 1$.

h	N_p	max norm error	max percentage error
0.1	136	$3.8296 \cdot 10^{-3}$	2.8046
0.09	162	$2.8973 \cdot 10^{-3}$	2.1054
0.08	193	$2.5523 \cdot 10^{-3}$	1.8388
0.07	258	$1.9995 \cdot 10^{-3}$	1.4397
0.06	368	$1.2753 \cdot 10^{-3}$	$9.2061 \cdot 10^{-1}$
0.05	507	$9.0392 \cdot 10^{-4}$	$6.5268 \cdot 10^{-1}$
0.04	780	$5.8542 \cdot 10^{-4}$	$4.2226 \cdot 10^{-1}$
0.03	1354	$3.3712 \cdot 10^{-4}$	$2.4276 \cdot 10^{-1}$
0.02	2996	$1.4149 \cdot 10^{-4}$	$1.0192 \cdot 10^{-1}$

Table 2.1: Error convergence for the FVM in the purely diffusive case with Dirichlet boundary conditions. Using $\alpha = 1, t_{max} = 0.1, N_t = 201$.

h	N_X	max norm error	max percentage error
0.02	51	$8.9669 \cdot 10^{-5}$	$6.4551 \cdot 10^{-2}$
0.01	101	$2.1997 \cdot 10^{-5}$	$1.5835 \cdot 10^{-2}$
0.005	201	$5.0816 \cdot 10^{-6}$	$3.6582 \cdot 10^{-3}$
0.0025	401	$8.5306 \cdot 10^{-7}$	$6.1410 \cdot 10^{-4}$

Table 2.2: Error convergence for the ADI method in the purely diffusive case with Dirichlet boundary conditions. Using $\alpha = 1, t_{max} = 0.1, N_t = 201$.

	max norm error			max percentage error		
α	FVM (fixed–β)	FVM (flux–limited)	ADI	FVM (fixed–β)	FVM (flux–limited)	ADI
1	$6.1452 \cdot 10^{-5}$	$1.4025 \cdot 10^{-4}$	$5.1169 \cdot 10^{-6}$	$4.4267 \cdot 10^{-2}$	$1.0103 \cdot 10^{-1}$	$3.6836 \cdot 10^{-3}$
10^{-1}	$8.8880 \cdot 10^{-4}$	$1.2906 \cdot 10^{-4}$	$3.3605 \cdot 10^{-6}$	$1.0835 \cdot 10^{-1}$	$1.5733 \cdot 10^{-2}$	$4.0938 \cdot 10^{-4}$
10^{-2}	$1.2542 \cdot 10^{-3}$	$2.6262 \cdot 10^{-4}$	$6.8083 \cdot 10^{-6}$	$1.2800 \cdot 10^{-1}$	$2.6803 \cdot 10^{-2}$	$6.9440 \cdot 10^{-4}$
10^{-3}	$1.4026 \cdot 10^{-3}$	$4.9002 \cdot 10^{-4}$	$5.4476 \cdot 10^{-5}$	$1.4063 \cdot 10^{-1}$	$4.9131 \cdot 10^{-2}$	$5.4584 \cdot 10^{-3}$
10^{-4}	$1.6792 \cdot 10^{-3}$	$5.3149 \cdot 10^{-4}$	$3.3593 \cdot 10^{-1}$	$1.6806 \cdot 10^{-1}$	$5.3194 \cdot 10^{-2}$	33.5991

Table 2.3: Error analysis for the advection–diffusion Dirichlet problem as we approach pure convection. Using $h = 0.02$ and $\beta = 0.8$ (for fixed–β FVM), $N_X = 201$ (for ADI), and $t_{\max} = 0.1$ with $N_t = 201$ (for both).

		max norm error		max percentage error	
h	N_p	fixed–β	flux–limited	fixed–β	flux–limited
0.1	136	$2.8846 \cdot 10^{-3}$	$3.5768 \cdot 10^{-3}$	2.1125	2.6195
0.09	162	$2.1014 \cdot 10^{-3}$	$2.7323 \cdot 10^{-3}$	1.5270	1.9855
0.08	193	$1.8074 \cdot 10^{-3}$	$2.4111 \cdot 10^{-3}$	1.3022	1.7371
0.07	258	$1.3253 \cdot 10^{-3}$	$1.9201 \cdot 10^{-3}$	$9.5425 \cdot 10^{-1}$	1.3825
0.06	368	$7.2491 \cdot 10^{-4}$	$1.2344 \cdot 10^{-3}$	$5.2331 \cdot 10^{-1}$	$8.9114 \cdot 10^{-1}$
0.05	507	$4.5550 \cdot 10^{-4}$	$8.8075 \cdot 10^{-4}$	$3.2890 \cdot 10^{-1}$	$6.3596 \cdot 10^{-1}$
0.04	780	$2.2882 \cdot 10^{-4}$	$5.7477 \cdot 10^{-4}$	$1.6505 \cdot 10^{-1}$	$4.1458 \cdot 10^{-1}$
0.03	1354	$7.1700 \cdot 10^{-5}$	$3.3332 \cdot 10^{-4}$	$5.1631 \cdot 10^{-2}$	$2.4003 \cdot 10^{-1}$
0.02	2996	$6.1452 \cdot 10^{-5}$	$1.4025 \cdot 10^{-4}$	$4.4267 \cdot 10^{-2}$	$1.0103 \cdot 10^{-1}$

Table 2.4: Error convergence for the fixed–β FVM (with $\beta = 0.8$) and flux–limited FVM in the advective-diffusive case with Dirichlet boundary conditions. Using $\alpha = 1, t_{max} = 0.1, N_t = 201$.

h	N_X	max norm error	max percentage error
0.02	51	$9.0677 \cdot 10^{-5}$	$6.5277 \cdot 10^{-2}$
0.01	101	$2.2140 \cdot 10^{-5}$	$1.5938 \cdot 10^{-2}$
0.005	201	$5.1169 \cdot 10^{-6}$	$3.6836 \cdot 10^{-3}$
0.0025	401	$8.7480 \cdot 10^{-7}$	$6.2975 \cdot 10^{-4}$

Table 2.5: Error convergence for the ADI method in the advective-diffusive case with Dirichlet boundary conditions. Using $\alpha = 1, t_{max} = 0.1, N_t = 201$.

Test 3: Pure Diffusion with Neumann boundary conditions

It is also possible to find an analytical solution to the diffusive Neumann problem

$$\frac{\partial \phi}{\partial t} = \alpha \nabla^2 \phi, \qquad x, y \in [0, 1], \tag{2.4.10}$$

with

$$\frac{\partial \phi}{\partial x} = 0 \qquad \text{on } x = 0, 1, \tag{2.4.11}$$

$$\frac{\partial \phi}{\partial y} = 0 \qquad \text{on } y = 0, 1. \tag{2.4.12}$$

This has solutions of the form

$$\phi_{mn}(x, y, t) = C_{mn} e^{-\lambda_{mn}^2 t} \cos m\pi x \cos n\pi y, \tag{2.4.13}$$

where $\lambda_{mn}^2 = \alpha\pi^2(m^2 + n^2)$. Solutions can be combined to give a total solution of the form

$$\phi(x, y, t) = \sum_{m=1}^{\infty} \sum_{n=1}^{\infty} \phi_{mn}, \tag{2.4.14}$$

in which the constants C_{mn} can be determined via the initial condition. We take the alternative approach of choosing the constants to be such that

$$C_{mn} = \begin{cases} 1 & \text{if } m = n = 1, \\ 0 & \text{otherwise,} \end{cases} \tag{2.4.15}$$

defining the initial condition $\phi(x, y, 0) = \cos(\pi x)\cos(\pi y)$ implicitly. This condition is particularly challenging for the Neumann FVM, since it creates sharp gradients near the boundaries (where the accuracy is reduced as we have to rely on a first order approximation for the diffusive flux along any CV edge with precisely one vertex on the boundary). Our results in Tables 2.6 and 2.7 show rapid improvements in accuracy as $h \to 0$ for both FVM and ADI.

h	N_p	max norm error	max percentage error
0.1	136	$6.6101 \cdot 10^{-3}$	4.7585
0.09	162	$4.7432 \cdot 10^{-3}$	3.4145
0.08	193	$5.9746 \cdot 10^{-3}$	4.3010
0.07	258	$3.3139 \cdot 10^{-3}$	2.3856
0.06	368	$3.4013 \cdot 10^{-3}$	2.4486
0.05	507	$2.7243 \cdot 10^{-3}$	1.9612
0.04	780	$1.5728 \cdot 10^{-3}$	1.1322
0.03	1354	$1.2753 \cdot 10^{-3}$	$9.1809 \cdot 10^{-1}$
0.02	2996	$7.4040 \cdot 10^{-4}$	$5.3300 \cdot 10^{-1}$

Table 2.6: Error convergence for the FVM in the purely diffusive case with Neumann boundary conditions. Using $\alpha = 1, t_{max} = 0.1, N_t = 201$.

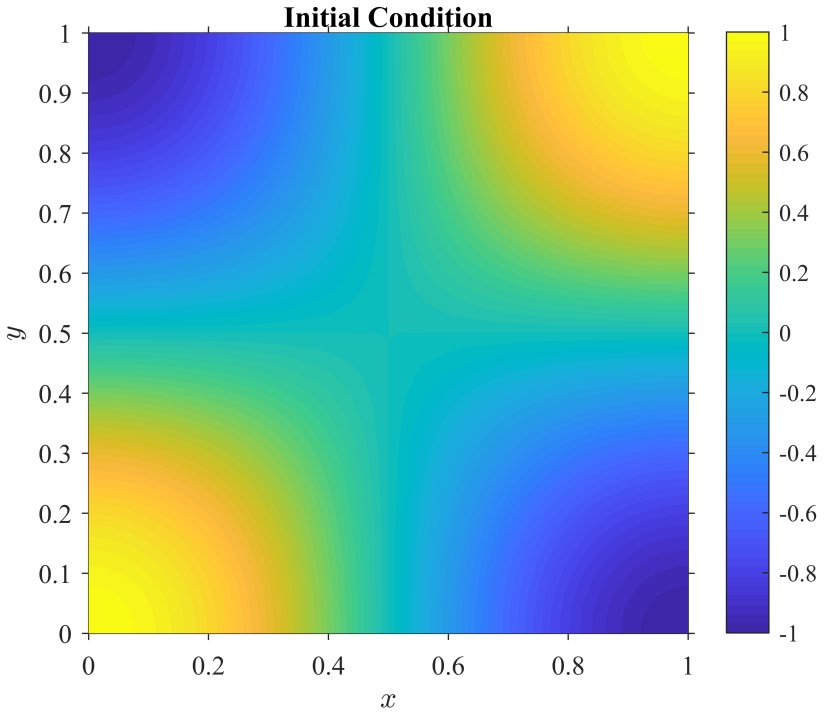

Figure 2.8: Initial condition $\phi(x, y, 0) = \cos(\pi x)\cos(\pi y)$ for use with Neumann boundary conditions.

h	N_X	max norm error	max percentage error
0.02	51	$8.9669 \cdot 10^{-5}$	$6.4551 \cdot 10^{-2}$
0.01	101	$2.1997 \cdot 10^{-5}$	$1.5835 \cdot 10^{-2}$
0.005	201	$5.0816 \cdot 10^{-6}$	$3.5682 \cdot 10^{-3}$
0.0025	401	$8.5306 \cdot 10^{-7}$	$6.1410 \cdot 10^{-4}$

Table 2.7: Error convergence for the ADI method in the purely diffusive case with Neumann boundary conditions. Using $\alpha = 1, t_{max} = 0.1, N_t = 201$.

2.5 Chapter summary

Starting from the most general form of the continuity equation, a generalized advection–diffusion–reaction partial–differential–equation was derived for use in a model describing chemical concentrations in the pollen tube cytoplasm. Since this PDE yields analytical solutions only in specific cases, methods were developed for solving the ADR PDE numerically.

The first of these methods was the FVM, purposefully constructed to be as general as

possible and applicable to any domain geometry using an unstructured triangular mesh. An extensive account of the numerical approximations used for discretizing each term of the ADR PDE using this method was also given.

In addition to developing a novel FVM, we also presented an outline of the alternating–direction– implicit method for use on structured meshes. Capable of providing numerical solutions to PDEs using only the principles of finite differences, the ADI method typically results in smaller errors than the FVM. This is offset by the need to employ a structured grid, limiting the use of the ADI to computational domains with a regular geometry.

To conclude this Chapter, we conducted an error analysis for both FVM and ADI in 3 test cases on the unit square with known analytical solutions: both i) pure diffusion and ii) advection–diffusion with Dirichlet boundary conditions, as well as iii) pure diffusion with Neumann conditions.

CHAPTER 3

THE METHOD OF REGULARIZED RINGLETS

In Chapter 2 we developed numerical schemes for advection–diffusion–reaction equations for use with a given velocity profile. Here, we derive the novel method of 'regularized ringlets' – axisymmetric rings of regularized Stokeslets which can be used to determine the cytoplasmic flow induced by the motion of vesicles along actin bundles. We verify and demonstrate the method by application to some simple test cases before combining with the FVM from Chapter 2 and applying to the pollen tube in Chapter 4.

3.1 Introduction

The Stokes equations for incompressible flow at zero Reynolds number are used extensively to model the viscous-dominated regime of microscale flows, particularly biological flows associated with cilia-driven transport, and the motility and feeding of flagellated cells such as bacteria, spermatozoa, algae and choanoflagellates. For an overview, see Lauga and Powers [80]. The fundamental solution of the Stokes flow equation, which corresponds to the flow driven by a single spatially-concentrated force is often referred to

as the Oseen tensor or Stokeslet. The linearity of the Stokes flow equations enables the construction of solutions to problems involving moving boundaries with complex geometry through integral sums of Stokeslets, forming the basis for the method of fundamental solutions, slender body theory and boundary integral methods. The latter numerical method has the principle major advantage of avoiding the need to mesh the fluid volume, which has enabled highly accurate and efficient simulation of biological flow systems for several decades [96, 99, 106]. Indeed more approximate methods based on line distributions of Stokeslets and higher order singularities also enabled major progress in this area before the present era of computationally-intensive research. For review see the earlier work of Chwang, Wu and co-authors [29], who also explore a wide range of applications as part of a series of papers on low-Reynolds number flow [28, 26, 27, 73, 69].

Nevertheless, two implementational issues arise with methods based on singular solutions. The first is that boundary integrals of solutions with a $1/r$-type singularity can be technically complex to evaluate on or near the boundary. Line integrals associated with models of slender bodies such as cilia and flagellar are 'more singular', and can require careful distinction between the inside and outside of the body. Moreover, there are cases in which immersed forces due to, e.g. many suspended moving particles, are desired to be modelled by an immersed volumetric force. Cortez *et al.* developed the method of regularized Stokeslets [31, 33] based on the exact, divergence-free solution to the Stokes flow equations due to a concentrated but spatially-smoothed (regularized) force. This approach has enabled the use of Stokeslet methods in a wider range of applications, such as those in which an inducing force is present in the interior of the fluid domain (as either a point in $\mathbb{R}^2$ or a point/curve in $\mathbb{R}^3$).

While conceptually elegant, the standard implementation of the method of regularized Stokeslets is computationally expensive, motivating the development of boundary element discretization [107], line integration [32], and meshless interpolation [108] among other approaches. Many diverse biological flow problems of interest exhibit rotational symmetry,

examples including spherical 'squirmer' swimmers [11], the conceptual toroidal swimmer of Purcell [98], and cytosolic flow in elongating pollen tubes [22]. Thus motivated, we study axisymmetric Stokes flows in which the singular and regularized Stokeslets can be integrated azimuthally to yield an axisymmetric ring of point forces. The singular solution to this problem is already known [97]; the regularized solution, which we term the 'regularized ringlet', is newly derived. This solution forms the basis for an efficient axisymmetric method of regularized Stokeslets.

We begin in Section 3.2 by introducing the singular and regularized Stokeslets, and review their application in solving the resistance problem for a rigid body translating in a viscous fluid. This is followed by the derivation of the regularized ringlet, whose analytical solution is given in terms of complete elliptic integrals of the first and second kind. The double layer potential (DLP), relevant to bodies undergoing volume-changing deformation, is also considered, with analytical evaluation of the azimuthal integral in the DLP given in B.3. In Section 3.3 we consider some simple cases of motion, applying the method of regularized ringlets to the resistance problem for the translating and rotating unit sphere. We further consider the case of Purcell's toroidal swimmer [98, 83], in which the method of regularized ringlets enables the calculation of propulsion speeds which are in excellent agreement with analytical results for both slender and non-slender tori. Section 3.4 encompasses some further examples on the unit sphere, with a thorough comparison between regularized ringlets and Cortez' method of regularized Stokeslets [33] covering both absolute errors and computational speed as well as a comparison to results obtainable using the singular method of fundamental solutions.

3.2 Singular and regularized Stokeslet solutions

For the viscous–dominated very low Reynolds number flow associated with microscopic length scales and slow velocities, incompressible Newtonian flow is well–approximated by the steady Stokes flow equations

$$\mu\nabla^2\mathbf{u} = \nabla p - \mathbf{F}, \tag{3.2.1}$$

$$\nabla \cdot \mathbf{u} = 0, \tag{3.2.2}$$

where μ is dynamic viscosity, p the pressure, $\mathbf{u}$ the velocity, and $\mathbf{F}$ the applied force per unit volume. If we let $\mathbf{F}$ be a singular force of the form $\mathbf{F}(\mathbf{x}_0) = \mathbf{g}^p\delta(\mathbf{x}_0 - \mathbf{x})$ for arbitrary strength $\mathbf{g}^p$, arbitrary point $\mathbf{x}$ at which the singularity is located, and where δ is the Dirac delta function, then the fundamental solution [47, 123] for $\mathbf{u}$ is given by

$$u_i(\mathbf{x}_0) = \frac{1}{8\pi\mu}S_{ij}(\mathbf{x}_0, \mathbf{x})g_j^p, \tag{3.2.3}$$

where

$$S_{ij}(\mathbf{x}_0, \mathbf{x}) = \frac{\delta_{ij}}{|\mathbf{x}_0 - \mathbf{x}|} + \frac{(x_{0,i} - x_i)(x_{0,j} - x_j)}{|\mathbf{x}_0 - \mathbf{x}|^3}, \tag{3.2.4}$$

is known as the Stokeslet.

The singularity in the Stokeslet solution can be eliminated without loss of incompressibility by regularization of the force $\mathbf{F}$, as described by Cortez and colleagues [31, 33]. The Dirac delta function is replaced with $\mathbf{F}(\mathbf{x}_0) = \mathbf{g}^p\phi_\varepsilon(\mathbf{x}_0 - \mathbf{x})$ where ϕ_ε is a radially symmetric, smooth 'cutoff' function with the property $\int_{\mathbb{R}^3}\phi_\varepsilon(\mathbf{x})\,d\mathbf{x} = 1$. This is in essence applying the force over a small ball, varying smoothly from a maximum at its centre to ≈ 0 sufficiently far away, instead of using an infinite point force as in the classical Stokeslet solution. The numerical parameter ε dictates the radius of support of the force, and as $\varepsilon \to 0$ we recover the classical solution. Solutions for $\mathbf{u}$ using regularized Stokeslets appreciably differ from those found using the singular Stokeslet only near the point where

the force is applied. Following Cortez *et al.* [33] we take

$$\phi_\varepsilon(\mathbf{x}_0 - \mathbf{x}) = \frac{15\varepsilon^4}{8\pi(|\mathbf{x}_0 - \mathbf{x}|^2 + \varepsilon^2)^{7/2}}, \tag{3.2.5}$$

which yields,

$$S_{ij}^\varepsilon(\mathbf{x}_0, \mathbf{x}) = \delta_{ij}\frac{|\mathbf{x}_0 - \mathbf{x}|^2 + 2\varepsilon^2}{(|\mathbf{x}_0 - \mathbf{x}|^2 + \varepsilon^2)^{3/2}} + \frac{(x_{0,i} - x_i)(x_{0,j} - x_j)}{(|\mathbf{x}_0 - \mathbf{x}|^2 + \varepsilon^2)^{3/2}}. \tag{3.2.6}$$

By considering a solid body D moving through the fluid, it can be shown that [33],

$$\int_{\mathbb{R}^3} u_i(\mathbf{x})\phi_\varepsilon(\mathbf{x}_0 - \mathbf{x})\, dV(\mathbf{x}) = \frac{1}{8\pi\mu}\int_{\partial D} S_{ij}^\varepsilon(\mathbf{x}_0, \mathbf{x}) g_j^a\, dS(\mathbf{x}), \tag{3.2.7}$$

where $\mathbf{g}^a$ is the force per unit area exerted by the body surface (denoted ∂D) on the surrounding fluid. The above equation is exact; replacing the left hand side with the velocity $u_i(\mathbf{x}_0)$ such that

$$u_i(\mathbf{x}_0) = \frac{1}{8\pi\mu}\int_{\partial D} S_{ij}^\varepsilon(\mathbf{x}_0, \mathbf{x}) g_j^a\, dS(\mathbf{x}), \tag{3.2.8}$$

introduces an error $\mathcal{O}(\varepsilon^p)$ where $p = 1$ on or near the body surface, and $p = 2$ sufficiently far away.

Discretising Equation (3.2.8) using N Stokeslets on the surface of the solid body D enables the approximation of the fluid velocity at any point $\mathbf{x}_0$ via a numerical quadrature formula

$$u_i(\mathbf{x}_0) = \frac{1}{8\pi\mu}\sum_{n=1}^{N} S_{ij}^\varepsilon(\mathbf{x}_0, \mathbf{x}_n) g_{n,j}^a W_n, \tag{3.2.9}$$

where $g_{n,j}^a$ denotes the jth component of the force per unit area applied at the point x_n (a Stokeslet location) and W_n is the quadrature weight associated with the nth particle. The value of W_n is dependent on the geometry of the body surface ∂D and in Cortez and colleagues' work has units of area.

3.2.1 Derivation of the regularized ringlet

Consider a specific case of Equation (3.2.8) using a cylindrical (r, θ, z) coordinate system in which the body D exhibits rotational symmetry about the z axis. This symmetry enables analytical integration azimuthally, reducing the surface discretisation to a line discretisation and increasing accuracy. In doing so, we are effectively placing 'rings' of regularized Stokeslets at positions $\mathbf{x}_n = (r_n, \theta, z_n)$ for $n = 1, ..., N$, and $\theta \in [0, 2\pi)$ (see Figure 3.1 for a diagram of a single ring). This is analogous to covering the surface of the body in 'strips' instead of the patches used in a standard 3D Cartesian discretisation. With a surface parametrization $\mathbf{x}(s, \theta)$ where $0 \leq s \leq \ell$ denotes arclength and $0 \leq \theta \leq 2\pi$, the boundary integral Equation (3.2.8) reads

$$u_i(\mathbf{x}_0) = \frac{1}{8\pi\mu} \int_{\partial D} S_{ij}^{\varepsilon}(\mathbf{x}_0, \mathbf{x}) g_j^a(\mathbf{x})\, dS(\mathbf{x}) = \frac{1}{8\pi\mu} \int_{s=0}^{\ell} \left(\int_{\theta=0}^{2\pi} S_{ij}^{\varepsilon}(\mathbf{x}_0, \mathbf{x}(s,\theta)) g_j^a(s,\theta)\, r(s)\, d\theta \right) ds. \tag{3.2.10}$$

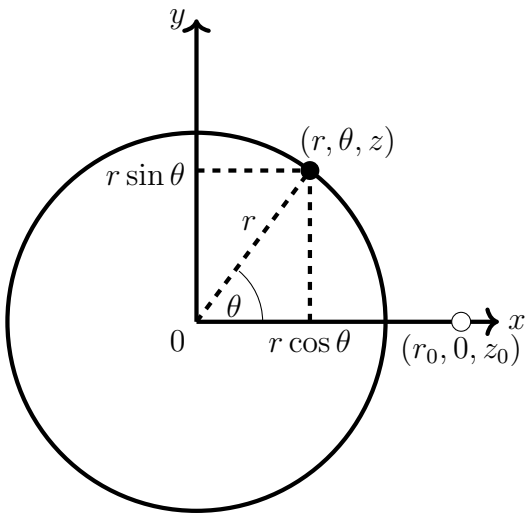

Figure 3.1: Stokeslet ring in the x-y plane. Note that the fluid point (open circle) and points on the ring (closed circle) do not necessarily both lie in the plane of the page (i.e. $z = z_0$ is not required).

Converting to cylindrical polar coordinates, we introduce the transformation matrix

$$\Theta(\theta) = \begin{pmatrix} \cos\theta & -\sin\theta & 0 \\ \sin\theta & \cos\theta & 0 \\ 0 & 0 & 1 \end{pmatrix}. \tag{3.2.11}$$

Letting indices i, j, k and α, β, γ correspond to Cartesian and cylindrical polar bases respectively (such that $i = 1, 2, 3$ and $\alpha = 1, 2, 3$ correspond to x, y, z and r, θ, z respectively, with Einstein summation convention employed for both sets), it follows that $g_j^a = \Theta_{j\alpha}(\theta) g_\alpha^a$. Assuming that velocity is evaluated at fluid point $\mathbf{x}_0 = (r_0, \theta_0, z_0)$ in cylindrical polars, it further follows that $u_i = \Theta_{i\alpha}(\theta_0) u_\alpha$. Recognizing that $\Theta^{-1} = \Theta^T$, substitution of the cylindrical forms of the velocity and force vectors into Equation (3.2.10) thus yields

$$\begin{aligned} u_\alpha(r_0, \theta_0, z_0) &= \Theta_{\alpha i}(\theta_0) u_i(x_0, y_0, z_0) \\ &= \frac{1}{8\pi\mu} \Theta_{\alpha i}(\theta_0) \int_0^\ell \int_0^{2\pi} S_{ij}^\varepsilon(\mathbf{x}_0, \mathbf{x}(s, \theta)) \Theta_{j\beta}(\theta) g_\beta^a(s)\, r(s)\, d\theta\, ds. \end{aligned} \tag{3.2.12}$$

Under the assumption of axisymmetry, it is sufficient to only consider cases $y_0 = \theta_0 = 0$. This results in the Cartesian $x - z$ and the cylindrical polar $r - z$ planes coinciding, such that the transformation matrix with $\theta_0 = 0$ simply yields the identity matrix (written as $\delta_{\alpha i} = 1$ when $\alpha = i$ and 0 otherwise in the summation) and Equation (3.2.12) reduces to,

$$u_\alpha(r_0, z_0) = \frac{1}{8\pi\mu} \int_0^\ell g_\beta^a(s) \left[\delta_{\alpha i} r(s) \int_0^{2\pi} S_{ij}^\varepsilon(\mathbf{x}_0, \mathbf{x}(s, \theta)) \Theta_{j\beta}(\theta)\, d\theta \right] ds, \tag{3.2.13}$$

$$= \frac{1}{8\pi\mu} \int_0^\ell g_\beta^a(s) R_{\alpha\beta}^\varepsilon(\mathbf{x}_0, \mathbf{x}(s))\, ds, \tag{3.2.14}$$

in which the 'ringlet' kernel

$$R_{\alpha\beta}^\varepsilon(\mathbf{x}_0, \mathbf{x}(s)) := \delta_{\alpha i} r(s) \int_0^{2\pi} S_{ij}^\varepsilon(\mathbf{x}_0, \mathbf{x}(s, \theta)) \Theta_{j\beta}(\theta)\, d\theta, \tag{3.2.15}$$

is implicitly defined. Unlike the Stokeslet which has the symmetric property $S_{ij}^\varepsilon(\mathbf{x}_0, \mathbf{x}) \equiv$

$S_{ij}^{\varepsilon}(\mathbf{x}, \mathbf{x}_0)$, ordering of arguments in the ringlet is important; the first and second arguments in $R_{\alpha\beta}^{\varepsilon}(\mathbf{x}_0, \mathbf{x})$ denote the fluid point and ring location respectively, with the ring radius $r(s)$ being the crucial non-symmetric term.

The various terms in the Stokeslet S_{ij}^{ε} can be evaluated in cylindrical polar coordinates via

$$(x_{0,1} - x_1) = r_0 - r\cos\theta, \tag{3.2.16}$$

$$(x_{0,2} - x_2) = -r\sin\theta, \tag{3.2.17}$$

$$(x_{0,3} - x_3) = z_0 - z, \tag{3.2.18}$$

$$|\mathbf{x}_0 - \mathbf{x}|^2 = (r_0 - r\cos\theta)^2 + (r\sin\theta)^2 + (z_0 - z)^2. \tag{3.2.19}$$

The resulting form of each S_{ij}^{ε} is given in B.1 and used in the evaluation of $R_{\alpha\beta}^{\varepsilon}$ in Equation (3.2.15). These integrals $R_{\alpha\beta}^{\varepsilon}$ yield the regularized fundamental solution for an axisymmetric ring of concentrated force (the regularized ringlet). Analytical evaluation reveals that $R_{r\theta}^{\varepsilon} = R_{z\theta}^{\varepsilon} = R_{\theta r}^{\varepsilon} = R_{\theta z}^{\varepsilon} = 0$ such that the rotational problem for g_θ^a decouples from g_r^a and g_z^a. The remaining nonzero $R_{\alpha\beta}^{\varepsilon}$ yield the equations

$$\begin{pmatrix} u_r(\mathbf{x}_0) \\ u_z(\mathbf{x}_0) \end{pmatrix} = \frac{1}{8\pi\mu}\int_0^{\ell} \begin{bmatrix} R_{rr}^{\varepsilon}(\mathbf{x}_0, \mathbf{x}(s)) & R_{rz}^{\varepsilon}(\mathbf{x}_0, \mathbf{x}(s)) \\ R_{zr}^{\varepsilon}(\mathbf{x}_0, \mathbf{x}(s)) & R_{zz}^{\varepsilon}(\mathbf{x}_0, \mathbf{x}(s)) \end{bmatrix} \begin{pmatrix} g_r^a(s) \\ g_z^a(s) \end{pmatrix} ds, \tag{3.2.20}$$

and

$$u_\theta(\mathbf{x}_0) = \frac{1}{8\pi\mu}\int_0^{\ell} R_{\theta\theta}^{\varepsilon}(\mathbf{x}_0, \mathbf{x}(s)) g_\theta^a(s)\, ds. \tag{3.2.21}$$

Utilising Equations (3.2.20) – (3.2.21) in tandem models axisymmetric problems with or without azimuthal rotation, in which the fluid experiences a constant force in each principal direction $(\hat{\mathbf{r}}, \hat{\boldsymbol{\theta}}, \hat{\mathbf{z}})$ at points along which the ringlet is located. This could be used, for example, to model the flow around a mobile axisymmetric body rotating about an axis defined by its direction of translation.

Approximating the integrals in Equations (3.2.20) – (3.2.21) numerically using a series of N rings yields a system of equations of the form

$$\begin{pmatrix} u_r(\mathbf{x}_0) \\ u_z(\mathbf{x}_0) \end{pmatrix} = \frac{1}{8\pi\mu} \sum_{n=1}^{N} \begin{bmatrix} R^{\varepsilon}_{rr}(\mathbf{x}_0, \mathbf{x}_n) & R^{\varepsilon}_{rz}(\mathbf{x}_0, \mathbf{x}_n) \\ R^{\varepsilon}_{zr}(\mathbf{x}_0, \mathbf{x}_n) & R^{\varepsilon}_{zz}(\mathbf{x}_0, \mathbf{x}_n) \end{bmatrix} \begin{pmatrix} g^a_r(\mathbf{x}_n) \\ g^a_z(\mathbf{x}_n) \end{pmatrix} w_n, \tag{3.2.22}$$

$$u_\theta(\mathbf{x}_0) = \frac{1}{8\pi\mu} \sum_{n=1}^{N} R^{\varepsilon}_{\theta\theta}(\mathbf{x}_0, \mathbf{x}_n) g^a_\theta(\mathbf{x}_n) w_n, \tag{3.2.23}$$

where $g^a_r(\mathbf{x}_n), g^a_\theta(\mathbf{x}_n), g^a_z(\mathbf{x}_n)$ are the radial, azimuthal, and axial components of the forces per unit area applied at ringlet location $\mathbf{x}_n$ respectively, and w_n is the quadrature weight associated with $\mathbf{x}_n$ for numerical integration over s. The quantity w_n has units of length unlike its counterpart W_n in Cortez' work (units of length squared). It is also possible to combine the force per unit area $\mathbf{g}^a$ and quadrature weight w_n into a force per unit length $\mathbf{g}^l$, such that Equations (3.2.22) and (3.2.23) can alternatively represent the fluid velocity induced by a series of rings.

By considering the fluid velocity at each individual ringlet location, an invertible system can be produced. In the zero-azimuthal-flow case ($u_\theta \equiv 0$), this takes the block matrix form,

$$\mathsf{G}^l = 8\pi\mu \underbrace{\begin{bmatrix} \mathsf{R}^{\varepsilon}_{rr} & \mathsf{R}^{\varepsilon}_{rz} \\ \mathsf{R}^{\varepsilon}_{zr} & \mathsf{R}^{\varepsilon}_{zz} \end{bmatrix}^{-1}}_{\mathsf{R}^{\varepsilon}} \mathsf{U}, \tag{3.2.24}$$

where,

$$\mathsf{G}^l = \begin{bmatrix} g^l_r(\mathbf{x}_1) \\ \vdots \\ g^l_r(\mathbf{x}_N) \\ g^l_z(\mathbf{x}_1) \\ \vdots \\ g^l_z(\mathbf{x}_N) \end{bmatrix}, \quad \mathsf{U} = \begin{bmatrix} u_r(\mathbf{x}_1) \\ \vdots \\ u_r(\mathbf{x}_N) \\ u_z(\mathbf{x}_1) \\ \vdots \\ u_z(\mathbf{x}_N) \end{bmatrix}, \tag{3.2.25}$$

and,

$$\mathsf{R}^{\varepsilon}_{\alpha\beta} = \begin{bmatrix} R^{\varepsilon}_{\alpha\beta}(\mathbf{x}_1,\mathbf{x}_1) & R^{\varepsilon}_{\alpha\beta}(\mathbf{x}_1,\mathbf{x}_2) & \dots & R^{\varepsilon}_{\alpha\beta}(\mathbf{x}_1,\mathbf{x}_N) \\ R^{\varepsilon}_{\alpha\beta}(\mathbf{x}_2,\mathbf{x}_1) & R^{\varepsilon}_{\alpha\beta}(\mathbf{x}_2,\mathbf{x}_2) & \dots & R^{\varepsilon}_{\alpha\beta}(\mathbf{x}_2,\mathbf{x}_N) \\ \vdots & \vdots & \ddots & \vdots \\ R^{\varepsilon}_{\alpha\beta}(\mathbf{x}_N,\mathbf{x}_1) & R^{\varepsilon}_{\alpha\beta}(\mathbf{x}_N,\mathbf{x}_2) & \dots & R^{\varepsilon}_{\alpha\beta}(\mathbf{x}_N,\mathbf{x}_N) \end{bmatrix}. \tag{3.2.26}$$

Hence, the forces needed to induce a given prescribed velocity in the fluid may be found (the resistance problem). This works for both a series of translating rings and a translating axisymmetric body, with the force per unit length $\mathbf{g}^l$ essentially 'absorbing' both the force per unit area $\mathbf{g}^a$ and the quadrature weight w_n in the latter case. Inclusion of azimuthal-flow involves the formulation of a similar invertible system for Equation (3.2.23) which can be solved separately.

3.2.2 Analytical evaluation of the regularized ringlet

The nonzero elements of the regularized ringlet can be expressed in the form

$$R^{\varepsilon}_{rr}(\mathbf{x}_0,\mathbf{x}_n) = r_n(-r_0 r_n I_0 + (2\tau - (z_0-z_n)^2)I_1 - 3r_0 r_n I_2), \tag{3.2.27}$$

$$R^{\varepsilon}_{rz}(\mathbf{x}_0,\mathbf{x}_n) = r_n(z_0-z_n)(r_0 I_0 - r_n I_1), \tag{3.2.28}$$

$$R^{\varepsilon}_{zr}(\mathbf{x}_0,\mathbf{x}_n) = r_n(z_0-z_n)(-r_n I_0 + r_0 I_1), \tag{3.2.29}$$

$$R^{\varepsilon}_{zz}(\mathbf{x}_0,\mathbf{x}_n) = r_n((\tau + (z_0-z_n)^2 + \varepsilon^2)I_0 - 2r_0 r_n I_1), \tag{3.2.30}$$

$$R^{\varepsilon}_{\theta\theta}(\mathbf{x}_0,\mathbf{x}_n) = r_n(r_0 r_n I_0 + (\tau+\varepsilon^2)I_1 - 3r_0 r_n I_2), \tag{3.2.31}$$

in which $\tau := r_0^2 + r_n^2 + (z_0-z_n)^2 + \varepsilon^2$, and

$$I_n := \int_0^{2\pi} \frac{\cos^n\theta}{(\tau - 2r_0 r_n\cos\theta)^{3/2}}\,d\theta, \tag{3.2.32}$$

$$= \frac{4k^3}{(4r_0 r_n)^{3/2}} \int_0^{\frac{\pi}{2}} \frac{(2\cos^2\theta - 1)^n}{(1-k^2\cos^2\theta)^{3/2}}\,d\theta, \tag{3.2.33}$$

with $k^2 := 4r_0r_n/(\tau + 2r_0r_n)$. Equation (3.2.33) is found by using the double angle formula for $\cos\theta$ as well as symmetry arguments about $\pi/2$. Following the example of Pozrikidis [97], the integrals I_n can be computed by first expanding the numerator of the integrand in Equation (3.2.33) to obtain a series of polynomial integrals with respect to $\cos\theta$. Letting

$$I'_n := 2^n \left(\frac{4k^3}{(4r_0r_n)^{3/2}}\right) \int_0^{\frac{\pi}{2}} \frac{\cos^{2n}\theta}{(1-k^2\cos^2\theta)^{3/2}}\, d\theta, \tag{3.2.34}$$

it follows that

$$I_0 = I'_0, \quad I_1 = I'_1 - I_0, \quad I_2 = I'_2 - 2I'_1 + I_0. \tag{3.2.35}$$

The individual integrals I'_n can be expressed in terms of complete elliptic integrals of the first and second kind, which are respectively defined

$$F = F(k) := \int_0^{\frac{\pi}{2}} \frac{d\theta}{(1-k^2\sin^2\theta)^{1/2}} \quad \text{and} \quad E = E(k) := \int_0^{\frac{\pi}{2}} (1-k^2\sin^2\theta)^{1/2}\, d\theta. \tag{3.2.36}$$

The solutions for each I'_n (as can be found in Section 2.58 of Gradshteyn and Ryzhik [59]) are given by

$$I'_0 = \frac{4k^3}{(4r_0r_n)^{3/2}} \left(\frac{1}{1-k^2}E\right), \tag{3.2.37}$$

$$I'_1 = \frac{8k^3}{(4r_0r_n)^{3/2}} \left(\frac{1}{k^2(1-k^2)}E - \frac{1}{k^2}F\right), \tag{3.2.38}$$

$$I'_2 = \frac{16k^3}{(4r_0r_n)^{3/2}} \left(\frac{2-k^2}{k^4(1-k^2)}E - \frac{2}{k^4}F\right), \tag{3.2.39}$$

from which it follows that

$$I_0 = \frac{4k^3}{(4r_0r_n)^{3/2}} \left(\frac{1}{1-k^2}E\right), \tag{3.2.40}$$

$$I_1 = \frac{4k^3}{(4r_0r_n)^{3/2}} \left(\frac{2-k^2}{k^2(1-k^2)}E - \frac{2}{k^2}F\right), \tag{3.2.41}$$

$$I_2 = \frac{4k^3}{(4r_0r_n)^{3/2}} \left(\frac{k^4-8k^2+8}{k^4(1-k^2)}E - \frac{4(2-k^2)}{k^4}F\right). \tag{3.2.42}$$

Substitution of Equations (3.2.40) – (3.2.42) back into Equations (3.2.27) – (3.2.31) yields the complete solution for the regularized ringlet,

$$R^{\varepsilon}_{rr}(\mathbf{x}_0,\mathbf{x}_n) = \frac{k}{r_0 r_n}\left(\frac{r_n}{r_0}\right)^{\frac{1}{2}}\left[(\tau+(z_0-z_n)^2)F + \frac{4r_0^2r_n^2-\tau(\tau+(z_0-z_n)^2)}{\tau-2r_0r_n}E\right], \quad (3.2.43)$$

$$R^{\varepsilon}_{rz}(\mathbf{x}_0,\mathbf{x}_n) = k\frac{(z_0-z_n)}{r_0}\left(\frac{r_n}{r_0}\right)^{\frac{1}{2}}\left[F + \frac{2r_0^2-\tau}{\tau-2r_0r_n}E\right], \quad (3.2.44)$$

$$R^{\varepsilon}_{zr}(\mathbf{x}_0,\mathbf{x}_n) = -k\frac{(z_0-z_n)}{(r_0r_n)^{\frac{1}{2}}}\left[F + \frac{2r_n^2-\tau}{\tau-2r_0r_n}E\right], \quad (3.2.45)$$

$$R^{\varepsilon}_{zz}(\mathbf{x}_0,\mathbf{x}_n) = 2k\left(\frac{r_n}{r_0}\right)^{\frac{1}{2}}\left[F + \frac{(z_0-z_n)^2+\varepsilon^2}{\tau-2r_0r_n}E\right], \quad (3.2.46)$$

$$R^{\varepsilon}_{\theta\theta}(\mathbf{x}_0,\mathbf{x}_n) = \frac{k}{r_0 r_n}\left(\frac{r_n}{r_0}\right)^{\frac{1}{2}}\left[(2\tau-\varepsilon^2)F + \frac{8r_0^2r_n^2+\tau(\varepsilon^2-2\tau)}{\tau-2r_0r_n}E\right]. \quad (3.2.47)$$

The solutions given by Equations (3.2.43) – (3.2.47) can be readily evaluated except when $r_0 = 0$ or $r_n = 0$. In the limit as $r_n \to 0$ (zero ring radius), all $R^{\varepsilon}_{\alpha\beta} \to 0$. In the limit as $r_0 \to 0$ (central fluid point), both R^{ε}_{zr} and R^{ε}_{zz} tend to finite values while $R^{\varepsilon}_{rr}, R^{\varepsilon}_{rz}, R^{\varepsilon}_{\theta\theta} \to 0$. This behaviour is described in detail in B.2.

The form of the ringlet solutions $R^{\varepsilon}_{\alpha\beta}$ is similar to those for the ring of singular Stokeslets (as detailed by Pozrikidis in [97] with the exception of the newly derived $R^{0}_{\theta\theta}$),

$$R^{0}_{rr}(\mathbf{x}_0,\mathbf{x}_n) = \frac{k}{r_0 r_n}\left(\frac{r_n}{r_0}\right)^{\frac{1}{2}}\left[(r_0^2+r_n^2+2(z_0-z_n)^2)F - \frac{2(z_0-z_n)^4+3(z_0-z_n)^2(r_0^2+r_n^2)+(r_0^2-r_n^2)^2}{(z_0-z_n)^2+(r_0-r_n)^2}E\right], \quad (3.2.48)$$

$$R^{0}_{rz}(\mathbf{x}_0,\mathbf{x}_n) = k\frac{(z_0-z_n)}{r_0}\left(\frac{r_n}{r_0}\right)^{\frac{1}{2}}\left[F + \frac{r_0^2-r_n^2-(z_0-z_n)^2}{(z_0-z_n)^2+(r_0-r_n)^2}E\right], \quad (3.2.49)$$

$$R^{0}_{zr}(\mathbf{x}_0,\mathbf{x}_n) = -k\frac{(z_0-z_n)}{(r_0r_n)^{\frac{1}{2}}}\left[F - \frac{r_0^2-r_n^2+(z_0-z_n)^2}{(z_0-z_n)^2+(r_0-r_n)^2}E\right], \quad (3.2.50)$$

$$R^{0}_{zz}(\mathbf{x}_0,\mathbf{x}_n) = 2k\left(\frac{r_n}{r_0}\right)^{\frac{1}{2}}\left[F + \frac{(z_0-z_n)^2}{(z_0-z_n)^2+(r_0-r_n)^2}E\right], \quad (3.2.51)$$

$$R^{0}_{\theta\theta}(\mathbf{x}_0,\mathbf{x}_n) = \frac{k}{r_0 r_n}\left(\frac{r_n}{r_0}\right)^{\frac{1}{2}}\left[2(r_0^2+r_n^2+(z_0-z_n)^2)F - \frac{4(z_0-z_n)^4+4(z_0-z_n)^2(r_0^2+r_n^2)+2(r_0^2-r_n^2)^2}{(z_0-z_n)^2+(r_0-r_n)^2}E\right], \quad (3.2.52)$$

and in the limit as $\varepsilon \to 0$ our solutions are equivalent to their singular counterparts. This can be verified by substitution of $\varepsilon = 0$ into $R^{\varepsilon}_{\alpha\beta}$ and is a result of the cutoff function ϕ_ε approaching a delta distribution as $\varepsilon \to 0$.

Equations (3.2.20) – (3.2.21) and (3.2.43) – (3.2.47) provide the solution (to within regularization error) for the fluid velocity at any point due to the drag force per unit area on the surface of a generalized axisymmetric body. Using Equations (3.2.22) – (3.2.23) in place of (3.2.20) – (3.2.21) yields the numerical solution based on discretization over the arclength s. In the case of a single ring, removing the integral over s and replacing the force per unit area $\mathbf{g}^a$ with a force per unit length $\mathbf{g}^l$ yields the solution for the fluid velocity induced by the force acting along the ring in 3D space.

3.2.3 On the double layer potential

A more complete formulation of Equation (3.2.7) for the fluid velocity induced by a translating body D is given by

$$\int_{\mathbb{R}^3} u_j(\mathbf{x})\phi_\varepsilon(\mathbf{x}_0 - \mathbf{x})\, dV(\mathbf{x}) = \frac{1}{8\pi\mu}\int_{\partial D} S^{\varepsilon}_{ij}(\mathbf{x}_0, \mathbf{x}) g^a_i(\mathbf{x})\, dS(\mathbf{x}) + \frac{1}{8\pi}\int_{\partial D} u_i(\mathbf{x}) T^{\varepsilon}_{ijk}(\mathbf{x}_0, \mathbf{x}) n_k(\mathbf{x})\, dS(\mathbf{x}), \quad (3.2.53)$$

where the first and second integrals on the right hand side are known as the single layer potential (SLP) and the double layer potential (DLP) respectively. The stress tensor T^{ε}_{ijk} present in the DLP is given by

$$T^{\varepsilon}_{ijk}(\mathbf{x}_0, \mathbf{x}) = -6\frac{(x_{0,i} - x_i)(x_{0,j} - x_j)(x_{0,k} - x_k)}{(|\mathbf{x}_0 - \mathbf{x}|^2 + \varepsilon^2)^{5/2}} - 3\varepsilon^2 \frac{(x_{0,i} - x_i)\delta_{jk} + (x_{0,j} - x_j)\delta_{ik} + (x_{0,k} - x_k)\delta_{ij}}{(|\mathbf{x}_0 - \mathbf{x}|^2 + \varepsilon^2)^{5/2}}. \quad (3.2.54)$$

Thus far, it has been possible to neglect the contribution of the DLP by only considering the movement of rigid bodies, in which case the DLP disappears as a result of the zero-deformation condition on D and the continuity of velocity on ∂D (see Cortez [33, Section II.B]). However, other cases also exist in which it is possible to eliminate the DLP without relying on the body being rigid. Following the method outlined by Pozrikidis [97, Chapter 2.3], for any closed boundary ∂D if

$$\int_{\partial D} \mathbf{u} \cdot \hat{\mathbf{n}} \, dS = 0, \tag{3.2.55}$$

as is the case throughout this thesis, then it is always possible to eliminate the DLP by using a modified value for the force per unit area $\mathbf{g}^a$ in the SLP. Whether this is deemed acceptable depends on whether the exact value of $\mathbf{g}^a$ is of particular consequence to results, but this certainly allows for a wider range of applications.

Analytical integration of the DLP in the azimuthal direction is also possible, although the resulting equations are somewhat unwieldy (see B.3).

3.3 Simple examples and test cases

In Section 3.2 the expression for the regularized fundamental solution for an axisymmetric ring of concentrated forces, the regularized ringlet, was derived. In the following, we demonstrate the validity of the method through application to simple cases of motion.

The first two cases concern the translation and rotation of the unit sphere in a Stokesian fluid, treated independently in Sections 3.3.1 and 3.3.2 respectively. In Section 3.3.3 a more complicated example is considered: the propulsion of 'Purcell's toroidal swimmer' [98, 83], powered by tank treading of the torus surface. In considering these different

cases, it is shown that the method of regularized ringlets can be used to model the surface motion of axisymmetric bodies in each principal direction $\hat{\mathbf{r}}, \hat{\boldsymbol{\theta}}, \hat{\mathbf{z}}$ in a cylindrical coordinate system.

3.3.1 Resistance problem for the translating unit sphere

The validity of the regularized ringlet method is illustrated by solving the resistance problem for the translating unit sphere. Given a prescribed surface velocity $(-\hat{\mathbf{z}})$, Equation (3.2.14) yields a Fredholm first kind integral equation for the unknown force distribution [108]. The method of regularized ringlets (implemented here via Matlab) can be used to solve this problem.

The sphere is parametrized in the r-z plane by $\mathbf{p} = \cos\varphi\,\hat{\mathbf{r}} + \sin\varphi\,\hat{\mathbf{z}}$ for $\varphi \in [-\pi/2, \pi/2]$, then discretized as

$$\varphi_n = \pi\frac{n-1/2}{N} - \frac{\pi}{2} \quad \text{for } n = 1, \ldots, N. \tag{3.3.1}$$

The velocity boundary condition $\mathbf{u} = -\hat{\mathbf{z}}$ is prescribed at each $\mathbf{x}_n := \mathbf{p}(\varphi_n)$, and the resulting linear system is solved to yield the required force densities $\mathbf{g}^l$ at each of these locations. The total drag is then calculated as

$$-\sum_{n=1}^{N}\int_{\theta=0}^{2\pi} g_z^l(\mathbf{x}_n)\, r(\mathbf{x}_n) d\theta = -2\pi\sum_{n=1}^{N} r(\mathbf{x}_n) g_z^l(\mathbf{x}_n), \tag{3.3.2}$$

which is compared with the Stokes law value of 6π. The relative errors are given for various values of N and regularization parameter ε in Table 3.1 alongside the condition number of the resistance matrix R^ε in Table 3.2.

For given N, excessively small ε results in the drag error becoming non–monotonic in ε. For larger values of N we see that the error in the total drag is approximately of order ε, similar to the regularization error associated with fluid velocity $\mathbf{u}$ in transitioning from

ε	$N = 25$	51	101	201	401
0.01	$-1.4689 \cdot 10^{-2}$	$-2.0609 \cdot 10^{-3}$	$1.6439 \cdot 10^{-3}$	$2.4053 \cdot 10^{-3}$	$2.5104 \cdot 10^{-3}$
0.005	$-2.4754 \cdot 10^{-2}$	$-7.2086 \cdot 10^{-3}$	$-1.1116 \cdot 10^{-3}$	$7.6816 \cdot 10^{-4}$	$1.2056 \cdot 10^{-3}$
0.001	$-4.7242 \cdot 10^{-2}$	$-1.8774 \cdot 10^{-2}$	$-7.0948 \cdot 10^{-3}$	$-2.3160 \cdot 10^{-3}$	$-5.1183 \cdot 10^{-4}$

Table 3.1: Relative errors in the drag calculation for the resistance problem on the translating unit sphere.

ε	$N = 25$	51	101	201	401
0.01	$4.6282 \cdot 10^{1}$	$1.5857 \cdot 10^{2}$	$7.1602 \cdot 10^{2}$	$7.0167 \cdot 10^{3}$	$4.0767 \cdot 10^{5}$
0.005	$3.3089 \cdot 10^{1}$	$9.6186 \cdot 10^{1}$	$3.1303 \cdot 10^{2}$	$1.4181 \cdot 10^{3}$	$1.3947 \cdot 10^{4}$
0.001	$1.9973 \cdot 10^{1}$	$4.9332 \cdot 10^{1}$	$1.2386 \cdot 10^{2}$	$5.7653 \cdot 10^{2}$	$1.0449 \cdot 10^{3}$

Table 3.2: Condition numbers of the resistance matrix R^{ε} for the resistance problem on the translating unit sphere.

Equation (3.2.7) to (3.2.8). For given ε, increasing N eventually ceases to result in a further reduction in the relative error. This is often the case with regularized Stokeslet methods (eg. see Figure 3.7, Figure 3.8, and references Cortez *et al.* [33], Gallagher *et al.* [53]).

A thorough comparison of our results for the translating unit sphere with those of Cortez *et al.* [33] can be found in Section 3.4.1. A further comparison to results obtainable using the axisymmetric method of fundamental solutions (a singular Stokeslet method) is given in Section 3.4.3.

3.3.2 Resistance problem for the rotating unit sphere

The solution for the steady motion of a Stokesian fluid surrounding a solid sphere rotating uniformly about a central axis is well known and can be found in e.g. *Hydrodynamics* by Lamb [79, Chapter XI]. If the sphere rotates around its z axis in an (r, θ, z) cylindrical coordinate system with an angular velocity $\boldsymbol{\Omega} = \omega_0 \hat{\mathbf{z}}$, the resulting angular velocity of the fluid is given by $\boldsymbol{\omega} = (a/\gamma)^3 \omega_0 \hat{\boldsymbol{\theta}}$ where $\gamma = \sqrt{r^2 + z^2}$. This can be written in terms of

the linear velocity (more readily usable in the Stokeslet formulae) over the entire domain as,

$$\mathbf{u} = \begin{cases} r\left(\frac{a}{\gamma}\right)^3 \omega_0 \hat{\boldsymbol{\theta}} & \forall \gamma \geq a, \\ r\omega_0 \hat{\boldsymbol{\theta}} & \forall \gamma < a, \end{cases} \tag{3.3.3}$$

where $\gamma \geq a$ corresponds to the surrounding fluid velocity and $\gamma < a$ to the solid body rotation of the sphere respectively. The zero Reynolds number torque on this sphere is given by,

$$\mathbf{T} = -8\pi\mu a^3 \boldsymbol{\Omega}, \tag{3.3.4}$$

the derivation of which can be found in [104]. This torque is associated with a drag force per unit area on the surface of the sphere given by $\mathbf{f} = -3\mu\omega_0(r/a)\hat{\boldsymbol{\theta}} = -\mathbf{g}^a$, which can be verified by considering the identity

$$\mathbf{T} = \iint_S \mathbf{x} \times \mathbf{f}\, dS, \tag{3.3.5}$$

where S denotes the sphere surface. Multiplication by $\hat{\mathbf{z}}$ yields,

$$\hat{\mathbf{z}} \cdot \mathbf{T} = -8\pi\mu a^3 \omega_0, \tag{3.3.6}$$

for the LHS of Equation (3.3.5). For the RHS, using $\mathbf{f} = -3\mu\omega_0(r/a)\hat{\boldsymbol{\theta}}$ it follows that

$$\begin{aligned} \hat{\mathbf{z}} \cdot (\mathbf{x} \times \mathbf{f}) &= \hat{\mathbf{z}} \cdot ((r\hat{\mathbf{r}} + \theta\hat{\boldsymbol{\theta}} + z\hat{\mathbf{z}}) \times (-3\mu\omega_0(r/a)\hat{\boldsymbol{\theta}})) \\ &= -3\mu\omega_0(r/a)\hat{\mathbf{z}} \cdot (r\hat{\mathbf{z}} - z\hat{\mathbf{r}}) \\ &= -3\mu\omega_0(r^2/a). \end{aligned} \tag{3.3.7}$$

Converting to a spherical system (r, θ, φ) in which θ denotes the azimuthal angle and φ the polar angle, we substitute $r^2 = a^2 \sin^2 \varphi$ and $dS = a^2 \sin \varphi \, d\theta d\varphi$ to find

$$\begin{aligned} \hat{\mathbf{z}} \cdot \iint_S \mathbf{x} \times \mathbf{f} \, dS &= -3\mu a^3 \omega_0 \int_{\theta=0}^{2\pi} \left(\int_{\varphi=0}^{\pi} \sin^3 \varphi \, d\varphi \right) d\theta, \\ &= -6\pi\mu a^3 \omega_0 \int_{\varphi=0}^{\pi} \sin^3 \varphi \, d\varphi, \\ &= -6\pi\mu a^3 \omega_0 \cdot \frac{4}{3} = -8\pi\mu a^3 \omega_0, \end{aligned} \tag{3.3.8}$$

such that $\hat{\mathbf{z}} \cdot \mathbf{T} = \hat{\mathbf{z}} \cdot \iint_S \mathbf{x} \times \mathbf{f} \Rightarrow \mathbf{T} = \iint_S \mathbf{x} \times \mathbf{f}$ as required.

Thus, the force per unit length used in the method of regularized ringlets takes form

$$g_\theta^l = g_\theta^a \frac{\pi}{N} = \left(\frac{3\pi\mu}{N} \right) \left(\frac{r}{a} \right) \omega_0, \tag{3.3.9}$$

although for the resistance problem this is not prescribed.

As before, the sphere surface is parametrized in the r-z plane by $\mathbf{p} = \cos\varphi \, \hat{\mathbf{r}} + \sin\varphi \, \hat{\mathbf{z}}$ for $\varphi \in [-\pi/2, \pi/2]$, with $\mathbf{p}$ discretized using N ringlets at uniformly-spaced locations $\mathbf{x}_n$. Letting $\omega_0 = -1$, the velocity $\mathbf{u}(\mathbf{x}_n) = -r(\mathbf{x}_n)\hat{\boldsymbol{\theta}}$ is prescribed at each $\mathbf{x}_n$ and the resistance matrix is constructed to yield the required force densities $\mathbf{g}^l$ at each of these locations. The torque is then calculated as

$$-\sum_{n=1}^{N} \int_{\theta=0}^{2\pi} g_\theta^l(\mathbf{x}_n) \, r^2(\mathbf{x}_n) d\theta = -2\pi \sum_{n=1}^{N} r^2(\mathbf{x}_n) g_\theta^l(\mathbf{x}_n), \tag{3.3.10}$$

in which $r(\mathbf{x}_n)$ is squared since the torque is a moment, the product of distance and force. Comparing to the value 8π, relative errors are given for various values of N and regularization parameter ε in Table 3.3 alongside the condition number of the resistance matrix $\mathsf{R}_\theta^\varepsilon$ in Table 3.4.

These results are similar to those of the translating unit sphere, although for given ε, N the relative error in the drag is generally slightly larger and the condition number of

ε	$N = 25$	51	101	201	401
0.01	$-6.6820 \cdot 10^{-2}$	$-1.3919 \cdot 10^{-2}$	$3.1012 \cdot 10^{-3}$	$7.1409 \cdot 10^{-3}$	$7.5502 \cdot 10^{-3}$
0.005	$-1.0168 \cdot 10^{-1}$	$-3.3360 \cdot 10^{-2}$	$-7.2206 \cdot 10^{-3}$	$1.5183 \cdot 10^{-3}$	$3.5556 \cdot 10^{-3}$
0.001	$-1.7339 \cdot 10^{-1}$	$-7.5656 \cdot 10^{-2}$	$-3.0238 \cdot 10^{-2}$	$-1.0422 \cdot 10^{-2}$	$-2.6879 \cdot 10^{-3}$

Table 3.3: Relative errors in the drag calculation for the resistance problem on the rotating unit sphere.

ε	$N = 25$	51	101	201	401
0.01	7.7965	$2.1678 \cdot 10^{1}$	$7.1174 \cdot 10^{1}$	$3.4925 \cdot 10^{2}$	$4.2212 \cdot 10^{3}$
0.005	6.2313	$1.5492 \cdot 10^{1}$	$4.2389 \cdot 10^{1}$	$1.4119 \cdot 10^{2}$	$6.9613 \cdot 10^{2}$
0.001	4.4051	9.5164	$2.1792 \cdot 10^{1}$	$5.4064 \cdot 10^{1}$	$1.4690 \cdot 10^{2}$

Table 3.4: Condition numbers of the resistance matrix $\mathsf{R}_\theta^\varepsilon$ for the resistance problem on the rotating unit sphere.

the resistance matrix slightly smaller than for the results using the same ε, N on the translating unit sphere.

3.3.3 Purcell's toroidal swimmer

The torus is the simplest geometry capable of describing self–propelled organisms [114]. Purcell's toroidal swimmer [98, 113] describes one such organism, the geometry of which can be seen in Figure 3.2. Inward rotation of the torus surface produces a net force in the direction of motion of the outermost surface (against which the torus is propelled). The magnitude of this net force (and resultant propulsion speed of the torus) is dependent on the speed with which the surface of the torus rotates as well as the slenderness of the torus. Three modes of locomotion are considered by Leshansky and Kenneth [83], corresponding to tank treading of (a) an incompressible surface, in which the tangential surface velocity is largest on the inner surface, (b) a weakly compressible surface, in which the tangential surface velocity is constant, (c) a highly compressible surface, in which the tangential surface velocity is largest on the outer surface. In the following, we restrict ourselves to looking at the case of constant tangential surface velocity.

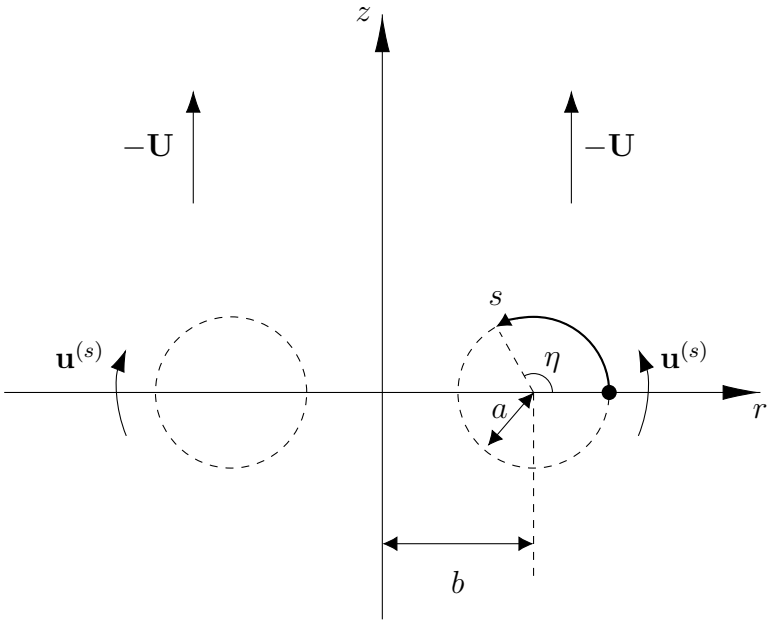

Figure 3.2: The geometry of the toroidal swimmer, whose cross section in the r-z plane is given by the dashed lines. Rotation around the z axis produces the complete torus. The torus moves with velocity $\mathbf{U}$ in the direction opposing outer surface motion (such that in the given frame of reference in which the torus remains stationary, the surrounding fluid appears to move with velocity $-\mathbf{U}$). Redrawn from Leshansky *et al.* [83].

The torus geometry is reduced to a single slenderness parameter $s_0 = b/a$, where b and a refer to the major and minor radii of the torus respectively. The torus surface is parametrized in terms of angle $\eta \in [0, 2\pi)$ in the r-z plane such that $ds = a\, d\eta$ and $\eta = 0$ corresponds to the outermost radial point on the surface of the torus, traversed in an anticlockwise direction. For the free swimming torus, the rigid body translation $\mathbf{U}$ and rotation $\mathbf{u}^{(s)}$ of the torus surface ∂D are related to the force per unit area $\mathbf{g}^a$ exerted by the torus on the surrounding fluid by,

$$U_\alpha(\mathbf{x}_0) + u_\alpha^{(s)}(\mathbf{x}_0) = \frac{1}{8\pi\mu} \int_{s=0}^{\ell} R_{\alpha\beta}^{\varepsilon}(\mathbf{x}_0, \mathbf{x}) g_\beta^a(\mathbf{s})\, ds \quad \forall \mathbf{x}_0 \in \partial D \tag{3.3.11}$$

subject to the condition of zero net force in the $\hat{\mathbf{z}}$ direction,

$$\int_{\partial D} \mathbf{g}_z^a(\mathbf{x})\, dS(\mathbf{x}) = 0, \tag{3.3.12}$$

where s is the arclength parametrization of the cross section of the torus surface ∂D in the r-z plane. We note that the additional free swimming conditions of zero net force

in $\hat{\mathbf{r}}$ and zero total moment (as outlined by Phan–Thien *et al.* [96]) are automatically satisfied by axisymmetry and $g^a_\theta \equiv 0$ respectively.

The propulsion speed $U := |\mathbf{U}|$ of the rotating torus for any given value of s_0 and rotation speed $u^{(s)} := \mathbf{u}^{(s)}$ can be determined by considering two separate situations: one in which motion is purely translational in the $\hat{\mathbf{z}}$ direction (the toroidal glider with $\mathbf{U} = \hat{\mathbf{z}}, \mathbf{u}^{(s)} \equiv \mathbf{0}$) and one in which motion is purely rotational (the anchored toroidal pump with $\mathbf{U} \equiv \mathbf{0}, \mathbf{u}^{(s)} = \hat{\boldsymbol{\eta}}$ where $\hat{\boldsymbol{\eta}}$ is the unit vector whose direction varies over s, pointing tangential to the surface in the anticlockwise direction at all points). The glider and pump have associated force distributions $\mathbf{g}^{\text{gld}}$ and $\mathbf{g}^{\text{pmp}}$ respectively. Using the regularized ringlet, surface motions can be prescribed (Figures 3.3a & 3.4a) in order to compute the associated force distributions (Figures 3.3b & 3.4b) responsible for producing each motion. For the toroidal glider the radial force is assumed to be zero ($g^{\text{gld}}_r \equiv 0$) such that

$$U_r(\mathbf{x}_0) = \frac{1}{8\pi\mu}\int_{\eta=0}^{2\pi} R^{\varepsilon}_{rz}(\mathbf{x}_0,\mathbf{x}) g^{\text{gld}}_z(\mathbf{x})\, a\, d\eta = 0 \quad \forall\, \mathbf{x}_0 \in \partial D, \tag{3.3.13}$$

$$U_z(\mathbf{x}_0) = \frac{1}{8\pi\mu}\int_{\eta=0}^{2\pi} R^{\varepsilon}_{zz}(\mathbf{x}_0,\mathbf{x}) g^{\text{gld}}_z(\mathbf{x})\, a\, d\eta = 1 \quad \forall\, \mathbf{x}_0 \in \partial D, \tag{3.3.14}$$

which, after solving for the unknown force distribution $\mathbf{g}^{\text{gld}}_z$, yields the net axial $\hat{\mathbf{z}}$ force

$$G^{\text{gld}} = \int_{\partial D} g^{\text{gld}}_z(\mathbf{x})\, dS(\mathbf{x}), \tag{3.3.15}$$

which is nonzero. For the anchored toroidal pump the surface velocity is given by $\mathbf{u}^{(s)} = \hat{\boldsymbol{\eta}} = (-\sin\eta, \cos\eta)$ in (r, z) coordinates. It follows that

$$u^{(s)}_r(\mathbf{x}_0) = \frac{1}{8\pi\mu}\int_{\eta=0}^{2\pi} R^{\varepsilon}_{r\beta}(\mathbf{x}_0,\mathbf{x}) g^{\text{pmp}}_\beta(\eta)\, a\, d\eta = -\sin\eta, \quad \forall\, \mathbf{x}_0 \in \partial D, \tag{3.3.16}$$

$$u^{(s)}_z(\mathbf{x}_0) = \frac{1}{8\pi\mu}\int_{\eta=0}^{2\pi} R^{\varepsilon}_{z\beta}(\mathbf{x}_0,\mathbf{x}) g^{\text{pmp}}_\beta(\eta)\, a\, d\eta = \cos\eta, \quad \forall\, \mathbf{x}_0 \in \partial D, \tag{3.3.17}$$

from which it can be determined that the net axial $\hat{\mathbf{z}}$ force is given by

$$G^{\text{pmp}} = \int_{\partial D} g_z^{\text{pmp}}(\eta)\, dS(\mathbf{x}). \tag{3.3.18}$$

By linearity of the Stokes flow equations we may subtract the gliding solution from the pump solution so that with $\mathbf{g}^a = \mathbf{g}^{\text{pmp}} - (G^{\text{pmp}}/G^{\text{gld}})g_z^{\text{gld}}\hat{\mathbf{z}}$, then

$$u_r^{(s)}(\mathbf{x}_0) = \frac{1}{8\pi\mu}\int_{\eta=0}^{2\pi} R_{r\beta}^{\varepsilon}(\mathbf{x}_0,\mathbf{x})g_\beta^a(\eta)\, a\, d\eta, \quad \forall\, \mathbf{x}_0 \in \partial D, \tag{3.3.19}$$

$$-\frac{G^{\text{pmp}}}{G^{\text{gld}}} + u_z^{(s)}(\mathbf{x}_0) = \frac{1}{8\pi\mu}\int_{\eta=0}^{2\pi} R_{z\beta}^{\varepsilon}(\mathbf{x}_0,\mathbf{x})g_\beta^a(\eta)\, a\, d\eta, \quad \forall\, \mathbf{x}_0 \in \partial D, \tag{3.3.20}$$

in which the net force is equal to

$$\int_{\partial D} g_z^a(\eta)\, dS(\mathbf{x}) = 0, \tag{3.3.21}$$

as required for the free–swimmer. The propulsion velocity of the swimming torus is thus given by $\mathbf{U} = -(G^{\text{pmp}}/G^{\text{gld}})\hat{\mathbf{z}}$, opposing the direction of outer surface motion. The speed U is dependent on both the rotation speed $u^{(s)}$ and the slenderness ratio s_0, so both G^{gld} and G^{pmp} must be computed whenever one of these parameters is changed. However, Leshansky and Kenneth [83] were able to show that the propulsion speed depends linearly on the rotation speed, such that by considering the scaled propulsion speed $U/u^{(s)}$ it is only necessary to vary s_0 to be able to consider all possible propulsion speeds resulting from a given constant rotational surface velocity.

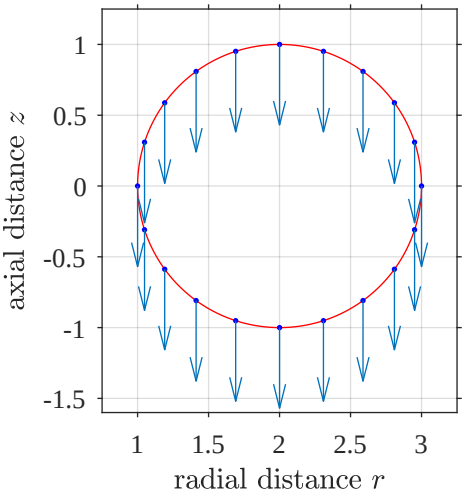

(a) Broadwise translation of the torus.

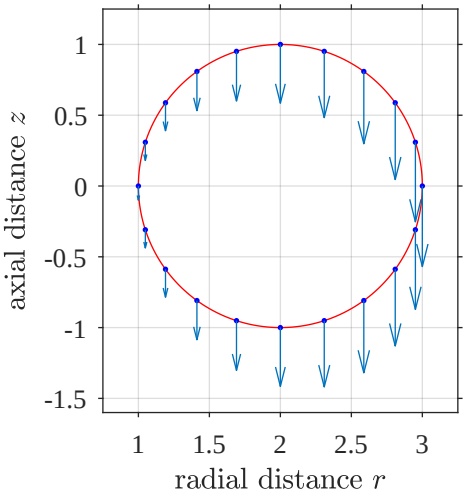

(b) Associated force distribution.

Figure 3.3: Surface velocity and associated force distribution of a toroidal glider with slenderness parameter $s_0 = 2$.

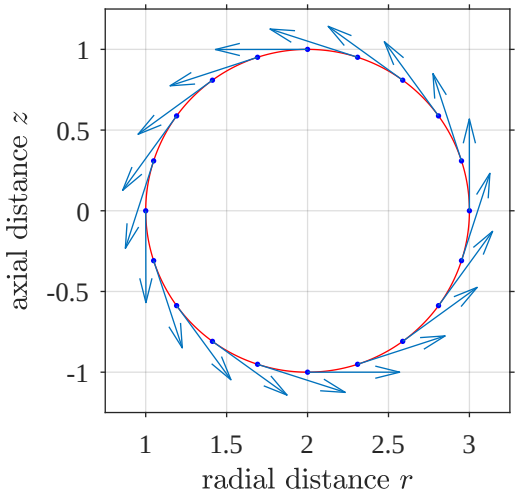

(a) Anticlockwise surface rotation of the torus.

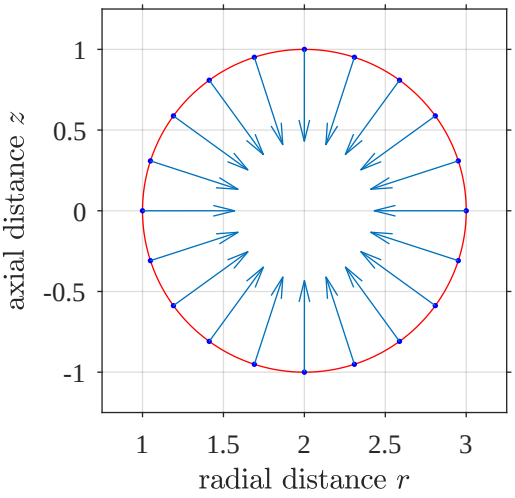

(b) Associated force distribution.

Figure 3.4: Surface velocity and associated force distribution of an anchored toroidal pump with slenderness parameter $s_0 = 2$.

Our results for the scaled propulsion velocity found using a discretization of the torus surface using $N = 100$ regularized ringlets are compared with those obtained by Leshansky and Kenneth [83], who tackled the same problem using a line distribution of rotlets at the torus centreline (inaccurate as $s_0 \to 1$) and an exact series solution via expansion in toroidal harmonics. A plot of the results for each of these solution methods can be seen

in Figure 3.5. Of particular note, in the limit as $s_0 \to 1$ it is found that using $N = 100$ rings with $\varepsilon = 0.01$ in the regularized ringlet method yields a scaled propulsion velocity of 0.6684, representing just a 0.513% error when compared to the series solution value of 0.665. This error can be reduced to $< 0.1\%$ by using $N = 1000$ rings, at which point the value of the scaled propulsion velocity as calculated by the method of regularized ringlets is 0.6656. This is a significant improvement over the solution found using a line distribution of rotlets, in which the error is $> 1\%$ for all $s_0 \leq 6$.

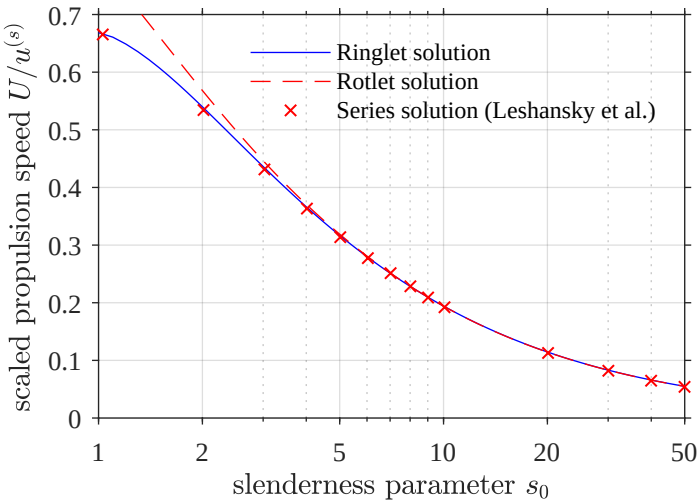

Figure 3.5: Scaled propulsion speed $U/u^{(s)}$ versus slenderness parameter s_0 using different numerical schemes. **Solid blue line** shows regularized ringlet solution using $N = 100$ rings (method derived in this paper). **Dashed red line** shows rotlet solution as detailed in [83]. **Red crosses** denote values of the exact series solution, obtained from Figure 7 of Leshansky *et al.* [83] using MathWorks' grabit function [72] in Matlab.

In addition to giving values for the scaled propulsion speed that are in excellent agreement with the series solution of Leshansky and Kenneth [83], the regularized ringlet solution also provides the force required at each point on the torus surface to produce the swimming motion. The series and rotlet solutions do not yield this information, with the propulsion speed instead being calculated according to the net drag force on the toroidal glider in these methods. This, in combination with Figures 3.3a & 3.3b, highlights why the centreline rotlet solution is inaccurate for small values of s_0; as slenderness decreases, the difference between the magnitude of the force required at the inner- and outer-most surfaces to produce rigid body translation of the torus grows large. In Figure 3.3b (in which $s_0 = 2$), the drag force on the outer surface is approximately 5.7 times larger than

that on the inner surface. The constant centreline force associated with the rotlet cannot account for this discrepancy, whereas the full discretization of the torus surface using regularized ringlets can.

Figures 3.6a & 3.6b show the streamlines and magnitude of the fluid velocity in a region near the force–free toroidal swimmer with slenderness parameter $s_0 = 2$, undergoing uniform anticlockwise surface rotation with unit angular velocity. This results in propagation of the torus in the direction $-\hat{\mathbf{z}}$. Fluid passing through the central hole of the torus is caught in closed streamlines, in agreement with the results of Leshansky and Kenneth [83].

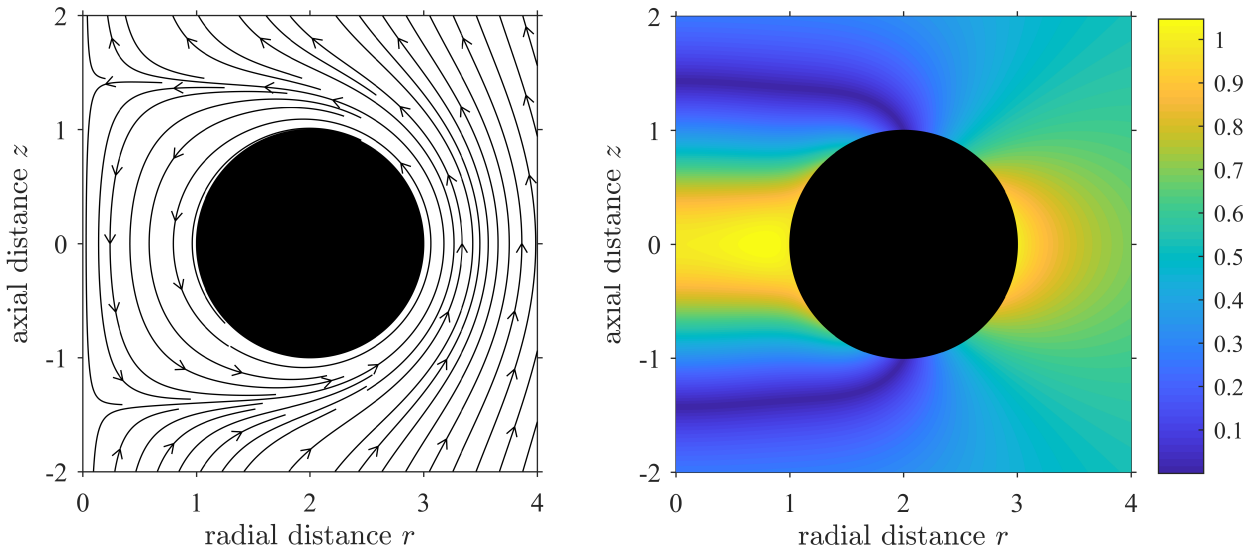

(a) Streamlines of fluid velocity.

(b) Magnitude of fluid velocity.

Figure 3.6: Streamlines and magnitude of fluid velocity in the region surrounding the force-free toroidal swimmer with slenderness parameter $s_0 = 2$, undergoing uniform anticlockwise surface rotation with unit angular velocity. The torus propagates in direction $-\hat{\mathbf{z}}$ and the frame of reference moves with the swimmer.

3.4 Further comparisons to other methods

Here, we conduct detailed comparisons between the method of regularized ringlets and other alternative methods of evaluating Stokes flows, including both Cortez' method of regularized Stokeslets [33] in Sections 3.4.1 – 3.4.2 and the method of fundamental solutions for the singular ringlet in Section 3.4.3.

3.4.1 Regularized ringlets vs regularized Stokeslets

Following the example of Cortez [33], consider the translating unit sphere with velocity $\mathbf{u} = -\hat{\mathbf{z}}$. As before, the sphere surface is parametrized in the r-z plane by $\mathbf{p} = \cos\varphi\,\hat{\mathbf{r}} + \sin\varphi\,\hat{\mathbf{z}}$ for $\varphi \in [-\pi/2, \pi/2]$, with $\mathbf{p}$ discretized using N ringlets at uniformly-spaced locations $\mathbf{x}_n$. Assuming the sphere experiences zero azimuthal spin, the fluid velocity at any point $\mathbf{x}_0$ can be approximated using the N ringlets via Equation (3.2.22). Using intervals of equal size, the quadrature weight associated with numerical integration over $\mathbf{p}$ is simply $w_n = \frac{\pi}{N}\,\forall n$. Now considering the velocity evaluated at the location of each ring in the r-z plane yields a system of equations which can be written in matrix form,

$$\mathsf{u} = \frac{1}{8N\mu}\begin{bmatrix} \mathsf{R}^{\varepsilon}_{rr} & \mathsf{R}^{\varepsilon}_{rz} \\ \mathsf{R}^{\varepsilon}_{zr} & \mathsf{R}^{\varepsilon}_{zz} \end{bmatrix}\mathsf{G}^{a}, \tag{3.4.1}$$

as outlined in Equations (3.2.24) - (3.2.26). By setting,

$$g^{a}_{r}(\mathbf{x}_i) = 0, \quad g^{a}_{z}(\mathbf{x}_i) = -\frac{3\mu}{2a}U, \quad \forall i = 1, \ldots, N, \tag{3.4.2}$$

where μ, a, U are the fluid viscosity, sphere radius, and sphere speed (in z) respectively, the classical solution for Stokes flow

$$u_r(\mathbf{x}_i) = 0, \quad u_z(\mathbf{x}_i) = U, \quad \forall i = 1, \dots, N, \tag{3.4.3}$$

should follow. Note that this calculation is independent of the value of μ by cancellation (besides the implicit requirement that $\mathrm{Re} = UL/\mu \ll 1$ for the Stokes equations to be valid), and that we use $a = 1$, $U = -1$ as described in the outline of the problem.

The first test involves using $N = 50$ regularized rings so that the grid size is given by $\pi/50 \approx 0.065$. This is chosen such that the minimum distance between adjacent rings in the axisymmetric discretisation of the sphere surface is approximately the same as the distance between adjacent points in Cortez' discretization using $3N^2/2$ regularized Stokeslets. The regularization parameter ε is varied between 0.005 and 0.1, and the error in the ℓ^2 norm for the z component of the flow field is recorded in each case. This error is defined as,

$$|u_z + 1|_2 := \sqrt{\frac{\sum_{i=1}^{N}(u_z(\mathbf{x}_i) + 1)^2}{N}}. \tag{3.4.4}$$

Division by N is necessary for the sake of comparison of errors with later tests where the value of N will change in order to alter the grid size. Initial results using regularized ringlets are shown in Figure 3.7 and are favourable compared to those of Cortez. The regularized ringlet method appears to be optimal for a lower value of ε than Cortez's method, with a minimal error found at $\varepsilon \approx 0.015$ with our method and $\varepsilon \approx 0.025$ with that of Cortez, as well as being slightly more accurate for almost all values of ε tested. Interestingly, the magnitude of the errors using the two methods briefly appear to coincide near the point at which Cortez' error is minimized.

The second test involves varying the grid size for a fixed value of $\varepsilon = 0.01$. Regularized ringlet results are shown in Figure 3.8 and again compare very favourably to the results of Cortez. For larger grid sizes our errors are significantly reduced compared to those

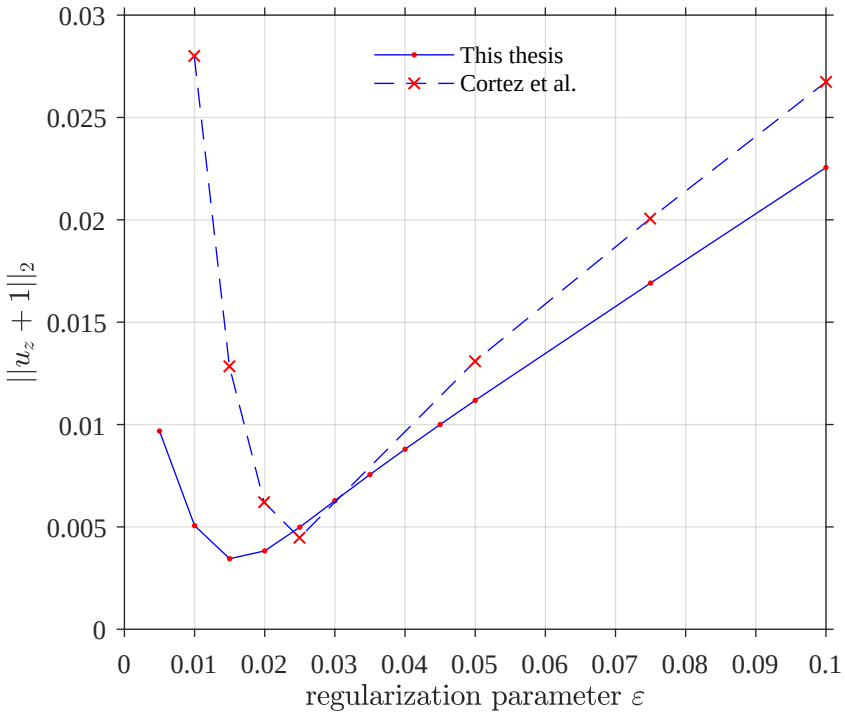

Figure 3.7: ℓ^2 errors for various values of ε using $N = 50$ regularized Stokeslet rings in our discretization of the sphere surface (solid line), plotted against data taken from Cortez *et al.* [33] (dashed line).

of Cortez. This is at least in part a result of the ringlet method being better suited to handling the small value of $\varepsilon = 0.01$. With both methods, the error eventually stops decreasing as the grid size tends towards 0 since in this regime the regularization error dominates.

The final test again looks at the effect of varying the value of ε on the magnitude of the numerical error, this time using $N = 124$ ringlets for a grid size approximately equal to 0.026. Note that we do not use $N = 125$ ringlets to avoid placing a ring at the point $(r, z) = (1, 0)$, which would result in a singular velocity when $\varepsilon = 0$. The velocity error is compared at two distinct points: $(r, z) = (1, 0)$ lying on the surface of the sphere, and $(r, z) = (1.5, 0)$ lying a distance of half the sphere radius away. Ringlet results are shown in Figures 3.9 & 3.10, and once more match the results of Cortez very closely. The magnitude of the error is linear with respect to ε on the surface of the sphere and quadratic a sufficient distance away.

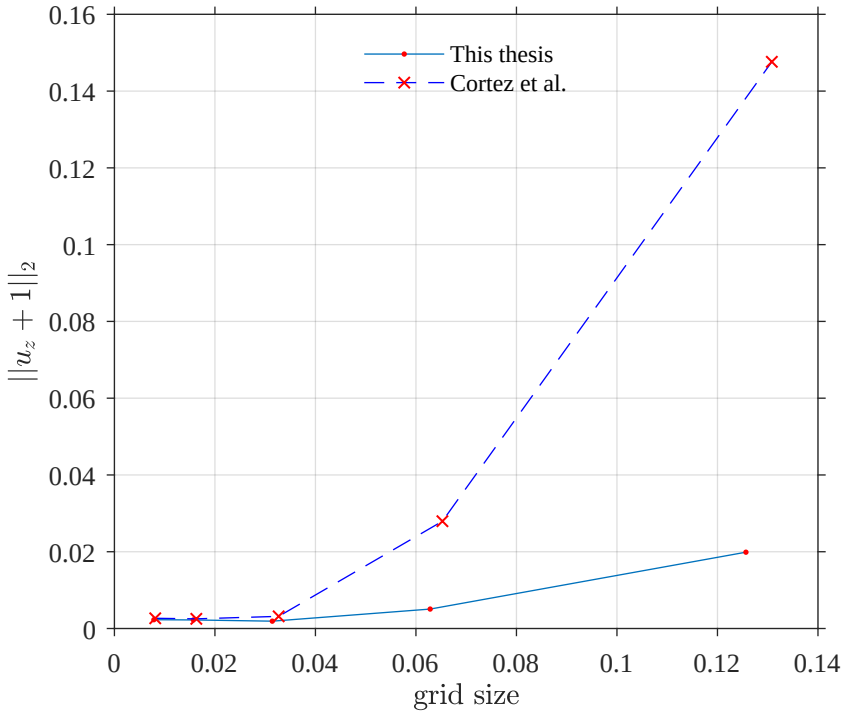

Figure 3.8: ℓ^2 errors for different grid sizes ($N = 25, 50, 100, 200, 400$) in our regularized ring discretization of the sphere surface using fixed $\varepsilon = 0.01$ (solid line), plotted against data taken from Cortez *et al.* (dashed line).

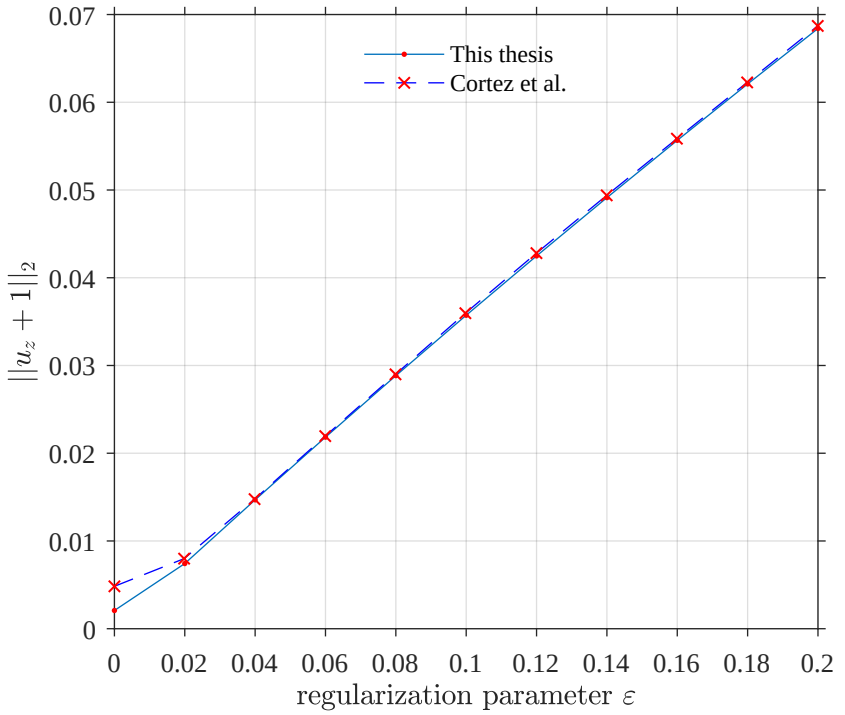

Figure 3.9: ℓ^2 errors at surface point $(r, z) = (1, 0)$ for various value of ε using $N = 124$ regularized Stokeslet rings in our discretization of the sphere surface (solid line), plotted against data taken from Cortez *et al.* (dashed line).

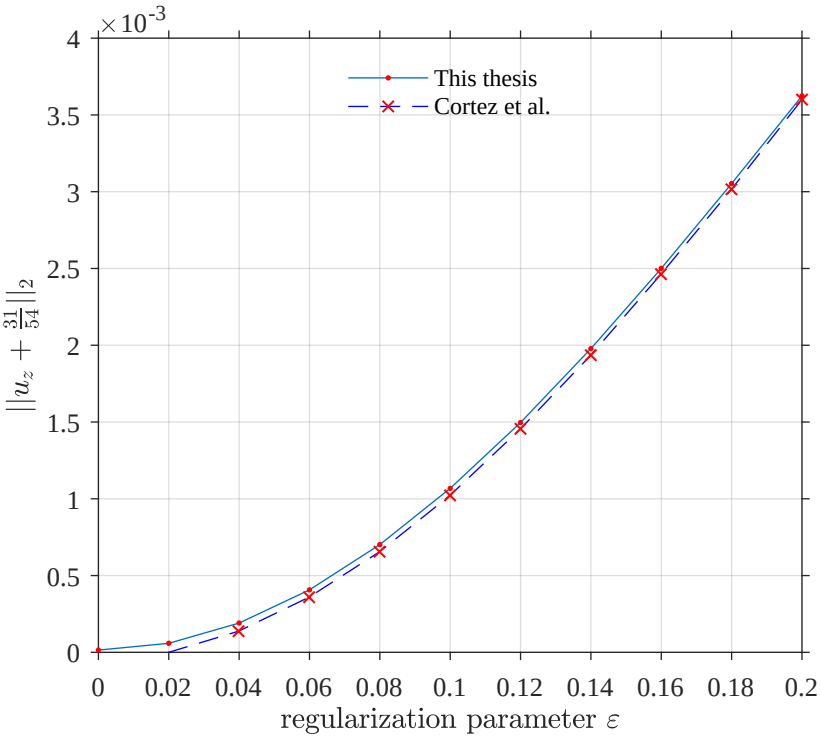

Figure 3.10: ℓ^2 errors at fluid point $(r, z) = (1.5, 0)$ for various value of ε using $N = 124$ regularized Stokeslet rings in our discretization of the sphere surface (solid line), plotted against data taken from Cortez *et al.* (dashed line). Value of $-31/54$ corresponds to analytical solution for u_z at location $(r, z) = (1.5, 0)$.

3.4.2 Ringlet vs Stokeslet speed

Table 3.5 shows a comparison of the computational times t_R and t_S (measured in seconds), associated with constructing the $2N \times 2N$ ringlet matrix R^ε (in the zero-azimuthal-flow case) and the $3N \times 3N$ Stokeslet matrix S^ε respectively. The increase in computational time for computing R^ε is a result of needing to compute the complete elliptic integrals $F(k)$ and $E(k)$ for all combinations of ring locations $(\mathbf{x}_m, \mathbf{x}_n) \forall\, m, n \in 1, ..., N$, which requires the construction of two further $2N \times 2N$ matrices E and F. The computational time needed for this isolated operation, t_e is also listed in Table 3.5. The total additional time needed to construct R^ε is modest, typically between 10% and 20% of the time needed for S^ε.

The computational time associated with F and E (and by extension, R^ε) can be reduced by evaluating $F(k)$ and $E(k)$ to a lower degree of accuracy; the Matlab function `ellipke(k,TOL)` calculates $F(k)$ and $E(k)$ to the accuracy defined by TOL, which has a default value of $2^{-52} \approx 2.2 \cdot 10^{-16}$ (double-precision accuracy). This is a far greater accuracy than we are typically able to achieve using regularized Stokeslet methods, suggesting a larger value of TOL will suffice.

	number of nodes N					
	1000	2000	3000	4000	5000	6000
t_e	0.1029	0.4100	0.9208	1.6228	2.5303	3.6553
t_R	0.2863	1.1182	2.4406	4.4124	6.9682	9.9643
t_S	0.2380	0.9396	2.1676	3.7562	6.0355	8.9524

Table 3.5: Comparison of computational time (in seconds) for constructing ring matrix R^ε and Stokeslet matrix S^ε using varying numbers of nodes.

We note that by consideration of the size of the matrices involved and the typically small value of t_e, we should hypothetically be able to achieve $t_R = (4/9)t_S + t_e < t_S$ for any given value of N. In practice, this is not the case. The elements S^ε_{ij} for $i, j \in \{1, 2, 3\}$ share a common form that enables them to be encoded in matrix form S^ε very efficiently. The same is not true of the elements $R^\varepsilon_{\alpha\beta}$ for $\alpha, \beta \in \{r, z\}$, hence why $t_R > t_S \forall\, N$ in

Table 3.5.

Inclusion of azimuthal-flow (such that an additional $N \times N$ matrix must be constructed for $\mathsf{R}_\theta^\varepsilon$ incurs an additional cost of small value, approximately equal to $(t_R - t_e)/4$ for any given value of N. We divide by 4 under the assumption that the cost associated with constructing the additional $N \times N$ matrix $\mathsf{R}_\theta^\varepsilon$ is one quarter of the cost associated with constructing the zero-azimuthal $2N \times 2N$ matrix R^ε.

The true value of working with ringlets can be seen by by evaluating the cost of inverting the matrices $\mathsf{R}_\theta^\varepsilon$ and R^ε versus S^ε (as is necessary in the resistance problem for evaluating the force associated with a given boundary velocity). These matrices are of size $N \times N$, $2N \times 2N$ and $3N \times 3N$ respectively. We investigate the cost of solving a linear system $\mathbf{X} = \mathbf{A} \setminus \mathbf{b}$ in which $\mathbf{A}$ and $\mathbf{b}$ are a $M \times M$ matrix and a $M \times 1$ vector of normally distributed random data respectively, with $M \in \{N, 2N, 3N\}$. We denote the time taken to solve this system by t_N, t_{2N}, and t_{3N} in each case. The results are given in Table 3.6, in which it is clear to see that t_{3N} is significantly larger than the sum of t_N and t_{2N} for all values of N tested. In practice, this means that using a 3D Stokeslet implementation with S^ε for solving an axisymmetric resistance problem will always be significantly more costly than our 2D ringlet implementation with $\mathsf{R}^\varepsilon, \mathsf{R}_\theta^\varepsilon$.

	number of nodes N					
	1000	2000	3000	4000	5000	6000
t_N	0.0178	0.1119	0.2986	0.6377	1.2263	2.0053
t_{2N}	0.1018	0.7139	2.0614	5.1004	9.3121	15.7495
t_{3N}	0.2978	2.3084	6.7434	15.1372	30.0496	50.7495

Table 3.6: Computational time (in seconds) associated with solving the linear system $\mathbf{X} = \mathbf{A} \setminus \mathbf{b}$ for varying sizes of matrix $\mathbf{A}$ and vector $\mathbf{b}$.

As well as producing smaller resistance matrices with a reduced associated computational cost for *a given number of nodes*, our axisymmetric ringlet method also *requires far fewer nodes* in order to achieve the same level of accuracy as the traditional regularized Stokeslet method. In 3.4.1 we show that for the case of the translating unit sphere our axisymmetric

discretization of the sphere surface with N rings produces results that are consistently more accurate than the traditional 3D patch discretization using $3N^2/2$ nodes. The result using 1000 ringlets in 2D (computational time $\approx 0.1\,\mathrm{s}$) thus corresponds to using $1,500,000$ regularized Stokeslets in 3D (computational time ≈ 500 days, extrapolating from data in Table 3.6 and assuming that $t_{3N} \propto N^{2.6}$ such that doubling N corresponds to a sixfold increase in t_{3N}) – a drastic improvement in computational efficiency.

3.4.3 Comparison to singular solutions

Regularized solutions for Stokes flow have the advantage of being simple to implement and readily usable without needing to worry about the presence of singularities in the computational domain. This does not mean that singular solutions cannot be used, however; so long as the appropriate care is taken to deal with the singularities in some way, singular solutions can also yield excellent results. The method of fundamental solutions [123, 2] is a popular choice for implementing singular Stokeslet solutions, in which a fictitious boundary is placed outside of the computational domain and adjacent to the physical boundary of the problem considered. Stokeslets (or 'source points') are placed on this fictitious boundary and are associated with collocation points (typically of an equal number) on the physical boundary, with the force density for each Stokeslet being calculated using the resistance matrix such that the physical boundary conditions are satisfied. What the appropriate distance between the fictitious and physical boundaries should be is difficult to determine *a priori*, and in some sense this distance can be regarded as a regularization parameter for the singular problem [3]. If the separation distance is too small, the proximity between the Stokeslet singularities and the physical boundary may lead to inaccurate solutions, whereas if the distance is too large the resistance matrix may become ill-conditioned [23]. In some cases, placement of the fictitious boundary may also be constrained by the geometry of the problem itself, leading to solutions that are far from optimal. The difficulty in balancing all of these factors is one of the reasons for

the popularity of regularized methods.

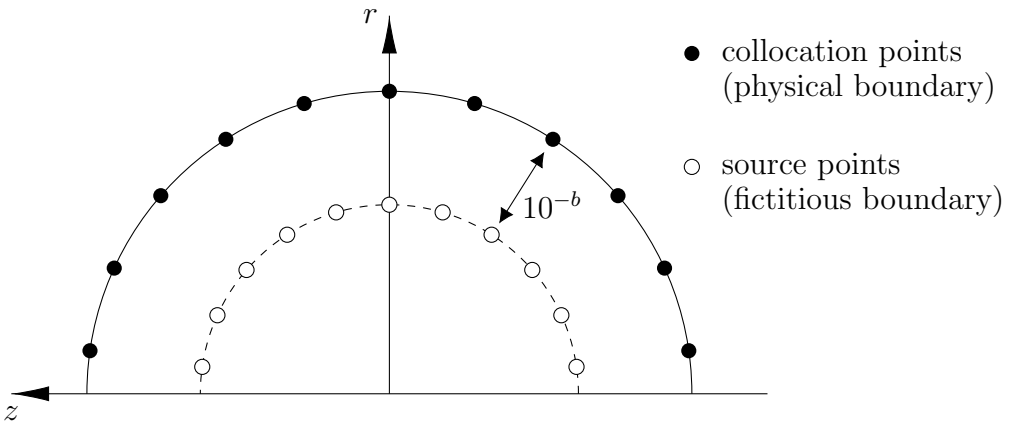

Figure 3.11: Schematic diagram for implementation of the method of fundamental solutions on the unit sphere using singular rings in the r-z plane. Separation distance 10^{-b} is exaggerated for the sake of clarity.

In the case of the axisymmetric ring of singular Stokeslets, some interesting behaviour occurs in the limit as the source and collocation points coincide. In this limit, k tends to unity from which it follows that $F \to \infty$ and $E \to 1$ in Equations (3.2.48) – (3.2.52). By employing the asymptotic expansion $F \approx -\ln \rho + \ldots$ in which $\rho = |\mathbf{x}_0 - \mathbf{x}_n|$, we find that $R^0_{\theta\theta} \approx 2R^0_{rr} \approx 2R^0_{zz} \approx -4 \ln \rho + \ldots$ which all tend to infinity as $\rho \to 0$ but at a significantly slower rate than the individual Stokeslet ($\approx \rho^{-1}$). The matrix elements R^0_{rz} and R^0_{zr} are similarly divergent but typically take values in the range $[-1, 1]$. Figure 3.12 shows a comparison of the magnitude of the singularities as $\rho \to 0$ for $R^0_{rr}, R^0_{zz} \approx -2 \ln \rho$ (circles) versus $S^0_{ij} \approx 2\rho^{-1}$ for $i = j$ (squares). A log-log plot must be employed due to the speed with which the Stokeslet singularity increases for small ρ.

As a result of the slow rate with which the singularity in the axisymmetric Stokeslet ring approaches infinity, the method of fundamental solutions can be employed with a separation distance between the fictious and physical boundaries that is several orders of magnitude smaller than is possible using individual Stokeslets. This allows for the discovery of accurate solutions with a well-conditioned underlying resistance matrix. We illustrate this by once again conducting Matlab simulations for the resistance problem on the translating unit sphere (velocity $-\hat{\mathbf{z}}$) using both regularized and singular Stokeslet

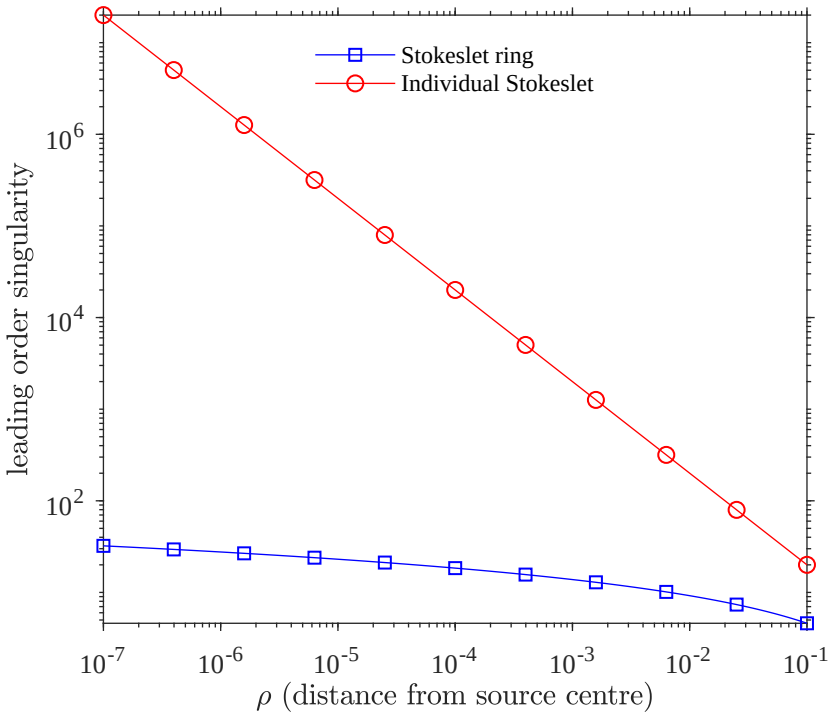

Figure 3.12: Comparison of the magnitude of the singularities present in the Stokeslet (squares) and the Stokeslet ring (circles) in the limit as the source and collocation point coincide.

rings.

As before, the sphere surface is parametrized in the r-z plane by $\mathbf{p} = \cos\varphi\,\hat{\mathbf{r}} + \sin\varphi\,\hat{\mathbf{z}}$ for $\varphi \in [-\pi/2, \pi/2]$, with $\mathbf{p}$ discretized using N ringlets at uniformly-spaced locations $\mathbf{x}_n$. For the method of regularized ringlets, these $\mathbf{x}_n$ denote ringlet locations. The velocity $\mathbf{u}(\mathbf{x}_n) = -\hat{\mathbf{z}}$ is prescribed at all ringlet locations and the resistance matrix is constructed to yield the required force densities $\mathbf{g}^l(\mathbf{x}_n)$. The condition number of the resistance matrix R^ε is determined using the `cond` function in Matlab. The analytical solution for the drag on the unit sphere with unit velocity $-\hat{\mathbf{z}}$ is known to be equal to $(3/2)\hat{\mathbf{z}}$, so that the mean relative error for the calculation of the force term resulting from the resistance matrix is given by

$$e(g_z^a) = \frac{1}{N}\sum_{n=1}^{N}\left|\frac{g_z^a(\mathbf{x}_n) + 3/2}{-3/2}\right|, \tag{3.4.5}$$

in which we recall that $\mathbf{g}^a$ is the force per unit area exerted by the sphere on the fluid and so has opposite sign to the drag. The fluid velocity at the near– and far–field locations

$(r, z) = (0, 1.1), (0, 1.5)$ is evaluated using the force densities $\mathbf{g}^a$ according to Equation (3.2.22). The relative error in these velocities is given by

$$e(1.1) = \left| \frac{u_z(0, 1.1) + 1315/1331}{-1315/1331} \right|, \quad e(1.5) = \left| \frac{u_z(0, 1.5) + 23/27}{-23/27} \right|, \tag{3.4.6}$$

based on the analytical solution given by Cortez *et al.* [33]. Table 3.7 shows a summary of the results obtained for each of these four metrics for various values of regularization parameter ε.

ε	$e(g_z^a)$	$e(1.1)$	$e(1.5)$	Cond
.1	5.3	$4.0 \cdot 10^{-3}$	$1.7 \cdot 10^{-2}$	$1.1 \cdot 10^{19}$
.05	$1.8 \cdot 10^{-2}$	$2.5 \cdot 10^{-3}$	$8.4 \cdot 10^{-3}$	$8.6 \cdot 10^{15}$
.025	$9.7 \cdot 10^{-3}$	$1.4 \cdot 10^{-4}$	$4.1 \cdot 10^{-3}$	$2.9 \cdot 10^{10}$
.01	$4.3 \cdot 10^{-3}$	$5.8 \cdot 10^{-4}$	$1.6 \cdot 10^{-3}$	$4.2 \cdot 10^{5}$
.005	$2.5 \cdot 10^{-3}$	$2.2 \cdot 10^{-4}$	$7.6 \cdot 10^{-4}$	$1.4 \cdot 10^{4}$
.0025	$2.1 \cdot 10^{-3}$	$2.3 \cdot 10^{-4}$	$1.1 \cdot 10^{-4}$	$2.8 \cdot 10^{3}$
.001	$2.5 \cdot 10^{-3}$	$1.0 \cdot 10^{-3}$	$7.4 \cdot 10^{-4}$	$1.0 \cdot 10^{3}$

Table 3.7: Accuracy of the method of regularized ringlets for various values of the regularization parameter ε in the resistance problem on the translating unit sphere. Columns refer to relative errors in total drag on the sphere $e(g_z^a)$, fluid velocity at the point $(r, z) = (0, 1.1)$ denoted $e(1.1)$ and analogous error at $(0, 1.5)$, and finally the condition number of the underlying resistance matrix.

For the method of fundamental solutions, let $\mathbf{x}_n$ denote collocation points on the sphere surface. N source points are placed at positions $\mathbf{x}_s = (1 - 10^{-b}) \cdot \mathbf{x}_c$ where b is a parameter that represents the separation distance between the physical and fictitious boundaries (Figure 3.11). The velocity $\mathbf{u}(\mathbf{x}_n) = -\hat{\mathbf{z}}$ is prescribed at all collocation points and the resistance matrix is constructed to yield the required force densities $\mathbf{g}^l(\mathbf{x}_s)$ at each source point. The accuracy and applicability of the method is measured using the same four metrics as for the method of regularized ringlets. Table 3.8 shows a summary of results for various values of separation distance 10^{-b}, analogous to the results in the regularized case from Table 3.7.

Similar results are achievable using both methods, although the singular method generally yields more well-conditioned resistance matrices and can produce relative errors of a

b	$e(g_z^a)$	$e(1.1)$	$e(1.5)$	Cond
1	$4.8 \cdot 10^{1}$	$1.5 \cdot 10^{-13}$	$3.5 \cdot 10^{-14}$	$1.1 \cdot 10^{19}$
2	$1.6 \cdot 10^{-2}$	$1.6 \cdot 10^{-6}$	$3.8 \cdot 10^{-7}$	$9.5 \cdot 10^{6}$
3	$4.3 \cdot 10^{-3}$	$9.5 \cdot 10^{-4}$	$6.3 \cdot 10^{-4}$	$2.5 \cdot 10^{3}$
4	$5.4 \cdot 10^{-4}$	$3.0 \cdot 10^{-3}$	$2.5 \cdot 10^{-3}$	$4.4 \cdot 10^{2}$
5	$7.3 \cdot 10^{-3}$	$5.1 \cdot 10^{-3}$	$4.6 \cdot 10^{-3}$	$2.4 \cdot 10^{2}$
6	$9.4 \cdot 10^{-3}$	$7.2 \cdot 10^{-3}$	$6.7 \cdot 10^{-3}$	$1.6 \cdot 10^{2}$
7	$1.1 \cdot 10^{-2}$	$9.3 \cdot 10^{-3}$	$8.8 \cdot 10^{-3}$	$1.2 \cdot 10^{2}$

Table 3.8: Accuracy of the method of fundamental solutions using singular ringlets for various values of the separation distance 10^{-b} in the resistance problem on the translating unit sphere. Columns refer to relative errors in total drag on the sphere $e(g_z^a)$, fluid velocity at the point $(r, z) = (0, 1.1)$ denoted $e(1.1)$ and analogous error at $(0, 1.5)$, and finally the condition number of the underlying resistance matrix.

smaller magnitude for the drag calculation and fluid velocities. It should however be noted that it is not possible to minimize each error in the singular calculation concurrently (as the smallest values for $e(1.1)$ and $e(1.5)$ are generally associated with larger values for the condition number and $e(g_z^a)$). Despite axisymmetry enabling a drastic reduction of the separation distance for the singular problem, the question of what distance is considered 'optimal' still persists. This is not an issue for the regularized ringlet, in which case each error achieves a minimal value for similar values of ε (≈ 0.0025 to 0.005). For excessively small ε (< 0.05), the error becomes non–monotonic as is often the case with regularized Stokeslet methods (eg. see Figure 3.7, Cortez *et al.* [33], Gallagher *et al.* [53]). The same is also true for small b in the singular case. For both regularized and singular methods, reduction of regularization parameter ε or b always appears to result in a reduction of the condition number of the resistance matrix.

Although the singular method can be tuned to give smaller relative errors in either the fluid velocity or total drag separately, it cannot do so simultaneously; regularized ringlets display more satisfactory convergence properties and are the more effective method to minimize errors in both fluid velocity and total drag.

3.5 Chapter summary

In this chapter, we have derived the regularized fundamental solution for the velocity (single layer potential) and stress (double layer potential) due to an axisymmetric ring of smoothed point forces, the 'regularized ringlet', expanding on the work of Cortez [31, 33]. The velocity solution, written in the form of complete elliptic integrals of the first and second kind, tends to the singular solution of Pozrikidis [97] in the limit as the regularization parameter ε tends to 0.

The applicability of the regularized ringlet to fluid flow problems involving motion in all principal $(\hat{\mathbf{r}}, \hat{\boldsymbol{\theta}}, \hat{\mathbf{z}})$ directions was established in the resistance problems on the unit sphere and the example of Purcell's toroidal swimmer. Ringlets perform very favourably on the unit sphere, as was detailed in the comparison with Cortez' method of regularized Stokeslets [33]. Using the collocation method for evaluating boundary integrals with just N regularized Stokeslet rings on a 2D parametrization of the sphere surface, we are able to produce consistently more accurate results than are achievable using the same collocation method with $3N^2/2$ regularized Stokeslets on the 3D surface for any given value of the regularization parameter ε.

Using the method of regularized ringlets, we were also able to reproduce Leshansky and Kenneth's [83] results for the scaled propulsion velocity of the toroidal swimmer, propelled by surface tank treading against the direction of motion of its outer surface. Our results show a significant improvement over the asymptotic solution found by integrating a centre-line distribution of rotlets in the limit as slenderness decreases ($s_0 \to 0$). The use of regularized ringlets also yields the drag force at all points on the torus surface for the toroidal swimmer, information that is not readily available using the series or rotlet solutions.

Discounting the modest cost involved in evaluating the complete elliptic integrals, this

new method for solving problems involving axisymmetric Stokes flows presents a significant improvement in accuracy as well as a reduction in both computational time and memory usage over non–axisymmetric methods.

In the following Chapter, the vital nature of the further benefits of regularization (namely, the ability to place Stokeslet points directly in the fluid and use the regularization parameter ε to control the spreading of the force) will be highlighted in the determination of a velocity profile for cytosolic fluid flow in the angiosperm pollen tube.

CHAPTER 4

TIP GROWTH IN POLLEN TUBES

Chapters 2 and 3 develop the numerical methods necessary for modelling of cytosolic flow and vesicle transport. In this Chapter, we now model vesicle transport in the growing pollen tube in detail.

4.1 Introduction

For the rapid elongation of the pollen tube to be sustained, the addition of new membrane and wall material to the growing apex is essential. This material is delivered via secretory vesicles, the motion of which can occur via a number of different mechanisms. Myosin–based transport along actin bundles is used to direct long–distance vesicle motion, which in turn induces a flow in the cytosol that further directs vesicle movement. In regions of reduced flow (such as near the extreme apex), vesicle motion is thought to be predominantly Brownian in nature. Uptake and secretion of vesicles by the cortical plasma membrane via exo–/endo–cytosis is also essential to the understanding of vesicle distribution patterns. Comprehensive models including all of these mechanisms

are difficult to find in the literature. In particular, the effect of cytosolic flow is rarely comprehensively considered and is typically conflated with that of actomyosin transport. The extent to which this is an issue is an open question. Based on the regularized ringlet method derived in Chapter 3, we are able to consider the cytosolic flow induced by drag forces resulting from actomyosin transport of vesicles. This can be coupled with the FVM of Chapter 2 to solve an ADR PDE for vesicle motion (to be derived shortly), yielding new results concerning the internal dynamics of pollen tube growth.

In the absence of direct measurements of pollen tube cytosolic flow fields, researchers have employed a variety of models. In the following, we expand upon the diffusive vesicle distribution model of Kroeger *et al.* [78] by extending the numerical domain from the apex into the distal region and incorporating advective effects. In doing so, we see the apical 'inverted vesicle cone' emerge naturally without reliance on prescribed flux along the actin fringe. Our choice of boundary conditions for vesicle flux (corresponding to apical exo/endo–cytosis) yield comparisons with the work of Chavarría-Krauser and Yejie [20].

We begin in Section 4.2 by deriving two ADR PDEs for vesicle motion (one for the exocytic population and one for the endocytic) along with accompanying boundary conditions for the growing tube. We establish the orthogonal growth velocity needed along the apical hemisphere to result in a steady, self-similar geometry. A transition is made to a moving coordinate system following the tip of the growing tube for the sake of simplifying our numerical procedure. We introduce the parameter values we will be using for the majority of the rest of our work and use these to nondimensionalize the advection–diffusion–reaction and Stokes equations. An appropriate value for the regularization parameter ε in the method of regularized ringlets is determined such that the area over which the majority of the force is applied approximates the region occupied by the peripheral actin bundle.

In Section 4.3, we seek a complete velocity profile for cytosolic flow in the apex, subapex, and adjacent shank using relations between the drag induced by the actomyosin vesicle

transport and the effect on the surrounding fluid. This is achieved using the method of regularized ringlets, derived in Chapter 3, in conjunction with the STICS imaging of Bove *et al.* [12]. We aim to answer three key questions during the course of this work:

- Section 4.3.1: What proportion of the exocytic vesicle population undergoes actomyosin based transport on the peripheral actin bundle?
- Section 4.3.2: What is the role of the central actin bundle and does actomyosin vesicle transport occur here?
- Section 4.3.3: What effect does growth speed have on the cytosolic flow in the tube?

In Section 4.4, the velocity profiles derived using the method of regularized ringlets are used in conjunction with the two ADR PDEs to model the spatial distribution of 'free' (i.e. not 'fixed' to actin) exocytic and endocytic vesicles at steady state. The two PDEs are solved using the finite volume method developed in Chapter 2 in Matlab. The parameter values necessary for the emergence of the 'inverted vesicle cone' in the apex highlight the importance of the cytosolic flow. We conclude with some exploratory work on determining an accurate value for the exocytosis rate at the apical plasma membrane, as well as running Fluorescence Recovery After Photobleaching (FRAP) simulations in Matlab with results closely agreeing with the FRAP experiments of Bove *et al.* [12].

4.2 Vesicle transport model

We consider two populations of free vesicles - one exocytic and one endocytic. These are modelled using advection–diffusion–reaction equations, with the advective term corresponding to the cytosolic flow induced by actomyosin transport.

4.2.1 Governing equations

The Reynolds number for fluid flow in the pollen tube can be evaluated using the typical flow speed ($\approx 1\,\mu\mathrm{m\,s^{-1}}$), tube radius ($\approx 8.13\,\mu\mathrm{m}$) and the kinematic viscosity of water ($\approx 10^9\,\mu\mathrm{m^2\,s^{-1}}$) to find $\mathrm{Re} \approx 8.13 \times 10^{-5}$, firmly in the regime of Stokes flow. Although pollen tube growth can be oscillatory, acceleration and deceleration are small compared to growth speed itself enabling the use of the steady Stokes equations

$$\mu\nabla^2\mathbf{U} - \nabla p + \mathbf{F} = 0, \tag{4.2.1}$$

$$\nabla \cdot \mathbf{U} = 0. \tag{4.2.2}$$

Starting from a general differential continuity equation in a static 'lab frame' co-ordinate system for the flux $\mathbf{j}$ and generation Σ of free vesicles Φ,

$$\frac{\partial\Phi(\mathbf{x},t)}{\partial t} + \nabla \cdot \mathbf{j} = \Sigma(\mathbf{x},t), \tag{4.2.3}$$

we define $\mathbf{j}$ to be the sum of diffusive and advective fluxes,

$$\mathbf{j} = \mathbf{U}(\mathbf{x},t)\Phi(\mathbf{x},t) - \alpha\nabla\Phi(\mathbf{x},t), \tag{4.2.4}$$

where $\mathbf{U}$ represents cytosolic flow and α is the coefficient of diffusivity. Relying on continuity of incompressible flow $\nabla \cdot \mathbf{U} = 0$, we may then write,

$$\frac{\partial\Phi(\mathbf{x},t)}{\partial t} = \alpha\nabla^2\Phi(\mathbf{x},t) - \mathbf{U}(\mathbf{x},t) \cdot [\nabla\Phi(\mathbf{x})] + \Sigma(\mathbf{x},t). \tag{4.2.5}$$

Since we consider two separate vesicle populations, we denote the exocytic population

$\Phi^{(x)}$ and the endocytic population $\Phi^{(n)}$. Using (4.2.5), we then have

$$\frac{\partial \Phi^{(x)}}{\partial t} = \alpha^{(x)} \nabla^2 \Phi^{(x)} - \mathbf{U} \cdot \nabla \Phi^{(x)} + \Sigma, \tag{4.2.6}$$

$$\frac{\partial \Phi^{(n)}}{\partial t} = \alpha^{(n)} \nabla^2 \Phi^{(n)} - \mathbf{U} \cdot \nabla \Phi^{(n)}. \tag{4.2.7}$$

No source term is present for the endocytic population, since these are instead added to the system via a boundary condition at the apical wall, whilst the exocytic source term Σ represents release of vesicles from actin within the domain.

4.2.2 Boundary conditions

We model the pollen tube in cylindrical (r, θ, z) coordinates with axisymmetry about the axial $\hat{z}$ axis. The shape of the tube is given by a cylindrical shank capped by a hemispherical apex. We consider a region ranging from the extreme apex to a point equal to 6 tube radii distal where the domain is artificially truncated. In dimensionless values, the extreme apex is thus given by $(r, z) = (0, 6)$ with $z = 0$ being the distal truncation line. The central line of axisymmetry is given by $r = 0$, with $r = 1$ denoting the peripheral boundary in the shank. The hemispherical apex is the upper–right quarter circle of radius 1, centred at $(0, 5)$.

The domain boundary is initially split into five distinct sections[1] (see Figure 4.1), with a different condition applied on each. Steady growth occurs along the apical boundary such that the shape of the apical hemisphere is conserved (discussed in Section 4.2.3).

We first consider the conditions placed on the fluid velocity. On the three physical cell wall boundaries $\mathbf{\Omega}_{\text{imp,in,out}}$, we employ the 'no-slip' condition such that $\mathbf{U} = \mathbf{0}$ on $\mathbf{\Omega}_{\text{imp}}$ and

[1]The $\mathbf{\Omega}_{\text{in}}$ boundary will later be extended to cover the entire apical hemisphere, overlapping with $\mathbf{\Omega}_{\text{out}}$ and $\mathbf{\Omega}_{\text{imp}}$. When this happens, the endocytic flux condition on $\mathbf{\Omega}_{\text{in}}$ and the exocytic flux condition on $\mathbf{\Omega}_{\text{out}}$ take priority over all other conditions.

$\mathbf{U} = \mathbf{u}_g$ on $\mathbf{\Omega}_{\text{in,out}}$ where $\mathbf{u}_g$ is the growth velocity of the apical wall. On the symmetry boundary $\mathbf{\Omega}_{\text{sym}}$ at $r = 0$ we have zero radial fluid flow ($U_r = 0$) as well as $\frac{\partial U_z}{\partial r} = 0$, both of which are automatically satisfied by ringlets. No restriction is placed on the fluid velocity at the basal boundary $\mathbf{\Omega}_{\text{bas}}$, since this is an artificial boundary we must impose for the sake of computing a numerical solution rather than a physical boundary in our problem.

Conditions must also be applied to the vesicle flux through each boundary. For the impermeable and symmetric boundaries $\mathbf{\Omega}_{\text{imp,sym}}$, we have zero normal flux ($\mathbf{j} \cdot \hat{\mathbf{n}} = 0$) for both vesicle populations. On the basal boundary $\mathbf{\Omega}_{\text{bas}}$, we have zero diffusive flux ($[\alpha \nabla \Phi] \cdot \hat{\mathbf{n}} = 0$) by numerical necessity but allow both populations to freely leave the domain via advective flux. On the two remaining boundaries, our exocytic and endocytic populations are treated differently. On the flux boundary $\mathbf{\Omega}_{\text{out}}$ at the subapical wall, we have zero normal endocytic flux ($\mathbf{j}^{(n)} \cdot \hat{\mathbf{n}} = 0$) and normal exocytic flux proportional to exocytic concentration ($\mathbf{j}^{(x)} \cdot \hat{\mathbf{n}} = -\gamma \Phi^{(x)}$ for some velocity γ). On the flux boundary $\mathbf{\Omega}_{\text{in}}$ at the apical wall, we have zero normal exocytic flux ($\mathbf{j}^{(x)} \cdot \hat{\mathbf{n}} = 0$) and normal endocytic flux proportional to exocytic flux through the $\mathbf{\Omega}_{\text{out}}$ boundary ($\mathbf{j}^{(n)} \cdot \hat{\mathbf{n}} = \zeta \frac{N_{\text{out}}}{A_{\text{in}}}$). Here, $N_{\text{out}} = \gamma \int_{\mathbf{\Omega}_{\text{out}}} \Phi^{(x)} \, dS$ is the total number of exocytic vesicles taken up through the $\mathbf{\Omega}_{\text{out}}$ boundary per unit time, $A_{\text{in}} = \int_{\mathbf{\Omega}_{\text{in}}} dS$ is the area of the surface $\mathbf{\Omega}_{\text{in}}$, and ζ is the recycling fraction, a dimensionless constant representing the number of endocytic vesicles that must be secreted by the apical plasma membrane as a fraction of the number of successful exocytic fusions in order for the correct balance of wall material and plasma membrane to be achieved. These apical flux conditions are consistent with the theory that exo- and endo-cytosis are active processes, mediated by vesicle associated membrane proteins (VAMPs) as has been suggested in the literature [61, 62].

For a complete summary, we have,

fluid velocity	vesicle flux		boundary
$\mathbf{U} = \mathbf{u}_g$,	$\mathbf{j}^{(x)} \cdot \hat{\mathbf{n}} = -\gamma \Phi^{(x)}$,	$\mathbf{j}^{(n)} \cdot \hat{\mathbf{n}} = 0$,	on $\mathbf{\Omega}_{\text{out}}$,
$\mathbf{U} = \mathbf{u}_g$,	$\mathbf{j}^{(x)} \cdot \hat{\mathbf{n}} = 0$,	$\mathbf{j}^{(n)} \cdot \hat{\mathbf{n}} = \zeta \frac{N_{\text{out}}}{A_{\text{in}}}$	on $\mathbf{\Omega}_{\text{in}}$,
$\mathbf{U} = \mathbf{0}$,	$\mathbf{j}^{(x)} \cdot \hat{\mathbf{n}} = 0$,	$\mathbf{j}^{(n)} \cdot \hat{\mathbf{n}} = 0$,	on $\mathbf{\Omega}_{\text{imp}}$,
$U_r = \frac{\partial U_z}{\partial r} = 0$,	$\mathbf{j}^{(x)} \cdot \hat{\mathbf{n}} = 0$,	$\mathbf{j}^{(n)} \cdot \hat{\mathbf{n}} = 0$,	on $\mathbf{\Omega}_{\text{sym}}$,
	$[\alpha^{(x)} \nabla \Phi^{(x)}] \cdot \hat{\mathbf{n}} = 0$,	$[\alpha^{(n)} \nabla \Phi^{(n)}] \cdot \hat{\mathbf{n}} = 0$,	on $\mathbf{\Omega}_{\text{bas}}$.

Table 4.1: Summary of boundary conditions for fluid velocity and vesicle flux in the growing pollen tube.

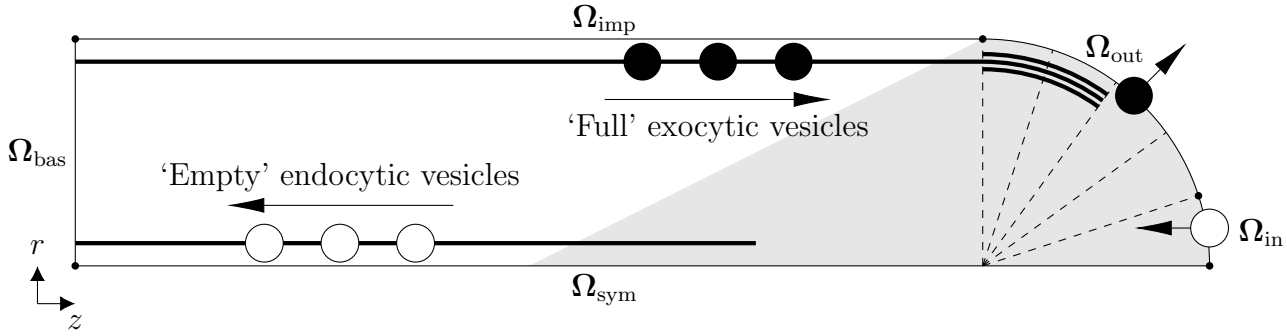

Figure 4.1: Suggested mechanism for transport of vesicles in the pollen tube, showing actin bundles (thick interior lines) and dense, apical actin fringe running parallel to the peripheral wall, as well as pooling of apical vesicles and shape of the 'inverted vesicle cone' (shaded area). The location of each of the five boundaries of our domain are also shown. Dashed lines show increments of $\pi/10$ in polar angle.

In Figure 4.1, the shape and location of the perhiperal and central actin bundles are drawn to match results from the experimental imaging of Lovy-Wheeler *et al.* [86]; the confined location of apical endocytosis (i.e. the $\mathbf{\Omega}_{\text{in}}$ boundary) corresponds to the endocytic region suggested by Bove *et al.* [12].

4.2.3 Normal displacement growth assumption

In order to be able to apply these boundary conditions, we must determine the form of the growth velocity $\mathbf{u}_g$. In accordance with our understanding of tip growth, we set $\mathbf{U} = \mathbf{0}$ on $\boldsymbol{\Omega}_{\text{imp}}$ (the wall of the shank). In the hemispherical apex, we define $\mathbf{u}_g \coloneqq \mathbf{u}_g(\varphi)$ where φ is the angle between the outward-pointing surface normal and the positive r axis, varying from 0 at the point where the hemisphere joins the shank to $\frac{\pi}{2}$ at the extreme apex. Let the point $(0, z_0)$ be the centre of the hemisphere and ℓ its radius, such that for any arbitrary point (r_1, z_1) on its surface we have,

$$\ell^2 = {r_1}^2 + (z_1 - z_0)^2. \tag{4.2.8}$$

The problem setup can be seen in Figure 4.2.

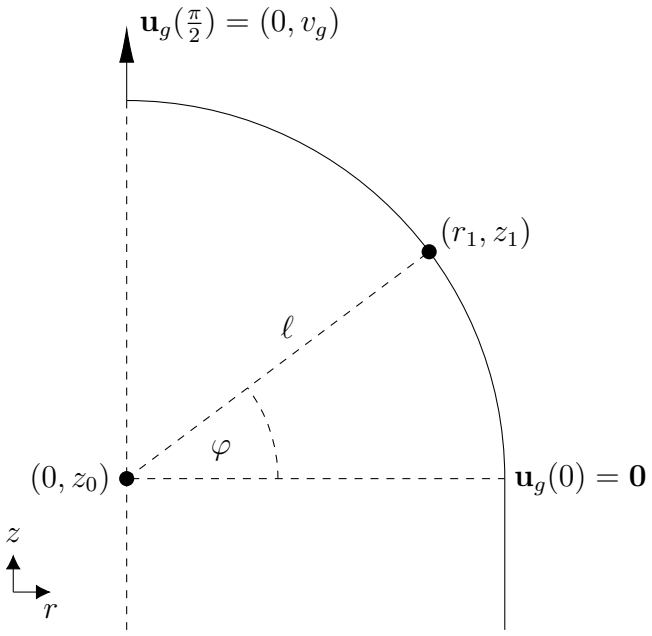

Figure 4.2: Inital configuration for determining growth velocity along the boundary of the apical hemisphere. We assume maximal growth occurs at the extreme apex ($\varphi = \pi/2$) with velocity $v_g\hat{\mathbf{z}}$, decreasing continuously to a zero velocity at the point at which the hemispherical apex joins the shank ($\varphi = 0$). By assuming growth always occurs normal to the boundary surface, we are able to derive the shape-preserving growth velocity $\mathbf{u}_g(\varphi) = v_g \sin\varphi(\cos\varphi, \sin\varphi)$.

Now for the hemispherical shape to be preserved (as is necessary under our assumption of a steady apical geometry) we require $d\ell/dt \equiv 0$. Differentiating Equation (4.2.8) with respect to time thus yields,

$$r_1 \frac{dr_1}{dt} + (z_1 - z_0)\frac{d}{dt}(z_1 - z_0) = 0, \tag{4.2.9}$$

that is,

$$r_1 \frac{dr_1}{dt} + (z_1 - z_0)\left(\frac{dz_1}{dt} - v_g\right) = 0, \tag{4.2.10}$$

where we have used the fact that $d(z_0)/dt \equiv v_g$ in order for shape to be preserved. Now following the steady state analysis of Dumais *et al.* [43], we assume that the growth velocity is normal to the cell surface for all $\varphi \in [0, \pi/2]$. This gives,

$$\frac{dz_1}{dt} = \frac{dr_1}{dt}\tan\varphi, \tag{4.2.11}$$

which upon substitution into Equation (4.2.10) yields,

$$\frac{dr_1}{dt} = \frac{v_g(z_1 - z_0)}{r_1 + (z_1 - z_0)\tan\varphi}. \tag{4.2.12}$$

Letting $r_1 = \ell\cos\varphi$ and $(z_1 - z_0) = \ell\sin\varphi$ (i.e. expressing everything in terms of φ) then gives,

$$\mathbf{u}_g(\varphi) = \left(\frac{v_g\sin\varphi}{\cos\varphi + \sin\varphi\tan\varphi}, \frac{v_g\sin\varphi\tan\varphi}{\cos\varphi + \sin\varphi\tan\varphi}\right), \tag{4.2.13}$$

which reduces to $\mathbf{u}_g(\varphi) = \left(v_g\sin\varphi\cos\varphi, v_g\sin^2\varphi\right) = v_g\sin\varphi(\cos\varphi, \sin\varphi)$. This is the vector normal to the cell surface with magnitude $v_g\sin\varphi$ (varying from v_g at the extreme apex to 0 at the point where the hemisphere joins the shank) as one might intuitively expect. An example of how the growth of the boundary thus varies over the apical hemisphere (radius 8.13 µm) can be seen in Figure 4.3, where the maximum growth speed v_g is equal to 0.1 µm s^{-1} and the wall velocity in the adjacent shank (not pictured) is equal to zero.

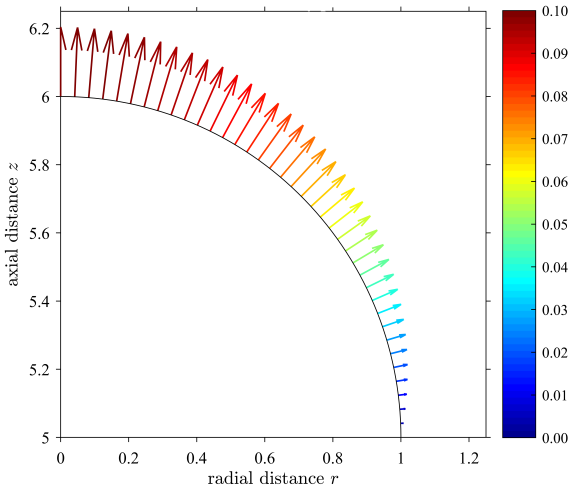

Figure 4.3: Growth velocity of the apical boundary, normal to the cell surface and varying from a maximum at the extreme apex to zero at the point where the apical hemisphere joins the adjacent shank. Velocities are scaled by the speed of vesicles on actin ($1\,\mu\mathrm{m\,s^{-1}}$), with lengths scaled by the radius of the tube ($8.13\,\mu\mathrm{m}$).

4.2.4 Formulation with respect to a moving coordinate system

The formulation given in Sections 4.2.1 - 4.2.3 outlines the equations for vesicle transport and associated boundary conditions with respect to a static 'lab frame' coordinate system. In this system the domain of interest will grow, necessitating frequent re-meshing operations during numerical evaluation. It is thus intuitive to consider the vesicle transport equation with respect to a moving frame of reference following the tip ('tip frame'), such that the domain does not need to be remeshed and the steady Stokes equations must only be evaluated once. In doing so, we lose information about regions distal to the apex as we iterate through time and our domain moves forwards, but so long as the domain is sufficiently large this should have little to no affect on the vesicle distribution in the apex.

Consider the full form of Equation (4.2.5) given in axisymmetric cylindrical coordinates,

$$\frac{\partial \Phi(r,z,t)}{\partial t} = \alpha \left(\frac{1}{r}\frac{\partial}{\partial r}\left(r\frac{\partial \Phi(r,z,t)}{\partial r}\right) + \frac{\partial^2 \Phi(r,z,t)}{\partial z^2}\right) - U_r(r,z,t)\frac{\partial \Phi(r,z,t)}{\partial r} - U_z(r,z,t)\frac{\partial \Phi(r,z,t)}{\partial z} + \Sigma(r,z,t). \quad (4.2.14)$$

If the growth speed of the tube is given by v_g, we define the moving coordinate system using $(r', z', t') = (r, z - v_g t, t)$, such that,

$$\phi(r', z', t') = \Phi(r, z, t), \quad (4.2.15)$$

$$u_r(r', z') = U_r(r, z, t), \quad (4.2.16)$$

$$u_z(r', z') = U_z(r, z, t) - v_g, \quad (4.2.17)$$

$$\sigma(r', z') = \Sigma(r, z, t), \quad (4.2.18)$$

where the fluid velocities u_r and u_z are now invariant in time (convenient for numerical evaluation of the steady Stokes equations) under the assumption that tube geometry remains steady in the advancing fluid region we consider. Under this transformation, Equation (4.2.5) becomes

$$\frac{\partial \phi(\mathbf{x}', t')}{\partial t'} = \alpha \nabla'^2 \phi(\mathbf{x}', t') - \mathbf{u}(\mathbf{x}', t') \cdot [\nabla' \phi(\mathbf{x}', t')] + \sigma(\mathbf{x}', t), \quad (4.2.19)$$

which is consistent with our original formulation. Rewriting this in terms of two separate exocytic and endocytic populations yields,

$$\frac{\partial \phi^{(x)}}{\partial t'} = \alpha^{(x)} \nabla'^2 \phi^{(x)} - \mathbf{u} \cdot \nabla' \phi^{(x)} + \sigma, \quad (4.2.20)$$

$$\frac{\partial \phi^{(n)}}{\partial t'} = \alpha^{(n)} \nabla'^2 \phi^{(n)} - \mathbf{u} \cdot \nabla' \phi^{(n)}. \quad (4.2.21)$$

Linearity of the Stokes flow equations (4.2.1)–(4.2.2) implies that they remain unchanged

under this change of coordinate system, such that

$$\mu\nabla^2\mathbf{u} - \nabla p + \mathbf{F} = 0, \tag{4.2.22}$$

$$\nabla \cdot \mathbf{u} = 0. \tag{4.2.23}$$

Boundary conditions on the fluid velocity are now given by $\mathbf{u} = \mathbf{u}_g - v_g\hat{\mathbf{z}}$ on $\mathbf{\Omega}_{\text{out,in}}$, $\mathbf{u} = -v_g\hat{\mathbf{z}}$ on $\mathbf{\Omega}_{\text{imp}}$, and $u_r = \frac{\partial u_z}{\partial r} = 0$ on $\mathbf{\Omega}_{\text{sym}}$. The conditions on vesicle flux remain unchanged (since fluid velocity matches boundary velocity in both frames of reference).

We have thus reformulated the problem in terms of a moving coordinate system, in which the domain geometry, the fluid velocity, and the exocytic source σ are all steady in time. The 'growing' problem has essentially been reduced to a static one in which the moving coordinate system takes the form of a standard cylindrical coordinate system. From this point onwards, we drop the apostrophe $'$ notation with the understanding that we will continue to work within this new coordinate system.

4.2.5 Parameter estimates and nondimensionalization

Pollen tubes from different plant species can exhibit significant differences in growth-related parameters (eg. growth velocity, tube radius, vesicle radius etc.). For this reason it is intuitive to nondimensionalize our problem, generalising our equations for multiple plant species and allowing efficient comparison between them. In our work, we use parameter values from a number of sources based on measurements taken experimentally in lily pollen tubes, as outlined in Table 4.2.

Parameter	Value	Reference
Radius of pollen tube (R_0)	$8.13\,\mu m$	[12]
Average vesicle radius (R_v)	$0.085\,\mu m$	[12]
Vesicle velocity on actin (U_a)	$1\,\mu m\,s^{-1}$	[40, 119]
Rate of vesicle supply into clear zone	$400\,s^{-1}$	[12]
Cytoplasmic viscosity (μ)	$10^{-3}\,Pa\,s$	[78]
Recycling fraction (ζ)	5/6	[12]
Cytoplasm temperature (T)	$300\,K$	
Boltzmann constant (k_B)	$1.4 \times 10^{-23}\,m^2\,kg\,K^{-1}\,s^{-2}$	
Diffusivity (α)	$2.6\,\mu m^2\,s^{-1}$	*
Cytosis rate (γ)	$0.1\,\mu m\,s^{-1}$	*

Table 4.2: Estimates for values of various parameters related to pollen tube growth. Asterisks $*$ in the 'Reference' column indicate values established in this thesis.

We note that the diffusivity α has been calculated using the Stokes-Einstein relation, $\alpha = k_B T/(6\pi\mu R_v) \approx 2.6\,\mu m^2\,s^{-1}$, which in turn yields a Péclet number of $\mathrm{Pe} = R_0 U_a/\alpha = 3.15$. Our current results use the same average vesicle radius, diffusivity, and Péclet number for both exocytic and endocytic populations in accordance with the results from [12]. This can be easily adjusted in future simulations with a different focus.

For the nondimensionalization of our governing equations, we scale,

- Lengths using shank radius R_0,
- Fluid velocity using average vesicle velocity on actin U_a,
- Time using advective timescale $T = R_0/U_a$,
- Concentration (number of vesicles per unit volume) using scale $\phi_0 = (\frac{4}{3}\pi R_v^3)^{-1}$ such that the dimensionless ϕ^* represents an approximate volume fraction.

Using asterisks * to denote dimensionless variables, we thus have,

$$\mathbf{x} = R_0\mathbf{x}^*, \quad \nabla = \frac{1}{R_0}\nabla^*, \quad \mathbf{u} = U_a\mathbf{u}^*, \quad t = \frac{R_0}{U_a}t^*, \quad \phi = \phi_0\phi^*, \quad \sigma = \frac{U_a\phi_0}{R_0}\sigma^*. \tag{4.2.24}$$

The governing transport equations (4.2.20) - (4.2.21) nondimensionalize to

$$\frac{\partial\phi^{(x)^*}}{\partial t^*} = \frac{1}{\mathrm{Pe}^{(x)}}\nabla^{*2}\phi^{(x)^*} - \mathbf{u}^*\cdot\nabla^*\phi^{(x)^*} + \sigma^*, \tag{4.2.25}$$

$$\frac{\partial\phi^{(n)^*}}{\partial t^*} = \frac{1}{\mathrm{Pe}^{(n)}}\nabla^{*2}\phi^{(n)^*} - \mathbf{u}^*\cdot\nabla^*\phi^{(n)^*}, \tag{4.2.26}$$

where $\mathrm{Pe}^{(i)} = U_aR_0/\alpha^{(i)}$. For the apical boundary conditions, we also require,

$$\gamma = U_a\gamma^*, \quad N_{\mathrm{out}} = (U_a\phi_0R_0^2)N_{\mathrm{out}}^*, \quad A_{\mathrm{in}} = R_0^2A_{\mathrm{in}}^*. \tag{4.2.27}$$

Then for the exocytic flux on $\mathbf{\Omega}_{\mathrm{out}}$ we find,

$$\frac{1}{\mathrm{Pe}}(\nabla^*\phi_x^*)\cdot\hat{\mathbf{n}} = -\gamma^*\phi_x^*. \tag{4.2.28}$$

Similarly, for the endocytic flux on the $\mathbf{\Omega}_{\mathrm{in}}$ boundary we have,

$$\frac{1}{\mathrm{Pe}}(\nabla^*\phi_x^*)\cdot\hat{\mathbf{n}} = \zeta\frac{N_{\mathrm{out}}^*}{A_{\mathrm{in}}^*}. \tag{4.2.29}$$

Nondimensionalization of the remaining flux conditions on the boundaries is trivial and follows similarly.

For the Stokes equations and their regularized Stokeslet solutions (see Chapter 3), we further employ,

$$p = \frac{\mu U_a}{R_0}p^*, \quad \mathbf{F} = \frac{\mu U_a}{R_0^2}\mathbf{F}^*, \tag{4.2.30}$$

With these scalings, the dimensional equation,

$$\mu\nabla^2\mathbf{u} - \nabla p + \mathbf{F} = 0, \tag{4.2.31}$$

reduces to the dimensionless,

$$\nabla^{*2}\mathbf{u}^* - \nabla^* p^* + \mathbf{F}^* = 0. \tag{4.2.32}$$

4.2.6 Selecting ε for approximating actin bundle thickness

The peripheral actin bundle is considered to be adjacent to the pollen tube wall (see Figure 4.4), with its width equal to one fifth of the pollen tube radius (0.2) and extending at an angle $\varphi = \pi/5$ into the apical hemisphere in accordance with the confocal microscopy imaging of Lovy-Wheeler *et al.* [86]. By placing rings of regularized Stokeslets in series along the centre line of the peripheral actin bundle, it is possible to carefully select an appropriate value for the regularization parameter ε such that the region over which the majority of the force distribution is applied is approximately the same as the bundle thickness. The same procedure is employed for the central actin bundle, only with individual regularized Stokeslets rather than ringlets since the centreline coincides with $r = 0$. Using $\varepsilon = 0.05$ it is found that $\approx 93\%$ of the total applied force is contained within a region of radius 0.1 which corresponds well to the approximate thickness of the actin bundles. This is shown in Figure 4.5 where $\rho = |\mathbf{x}_0 - \mathbf{x}_n|$ denotes distance from ring location (in the r-z plane) and the maximal value of ϕ_ε has been scaled to 1 for the sake of clarity. Smaller values of ε result in a larger percentage of the total force being contained within $0 \leq \rho \leq 0.1$ but are increasingly skewed towards $\rho = 0$.

We note that our modelling ignores the presence of a third f-actin structure, the short actin bundles observed in the extreme apex [52]. This is on account of the fact that these bundles are transient and significantly less dense than the thick peripheral and central actin bundles. Further, due to their proximity to the growing tube wall, any effect that these short actin bundles may have on the fluid velocity is likely insignificant compared to the effect of the growth of the wall.

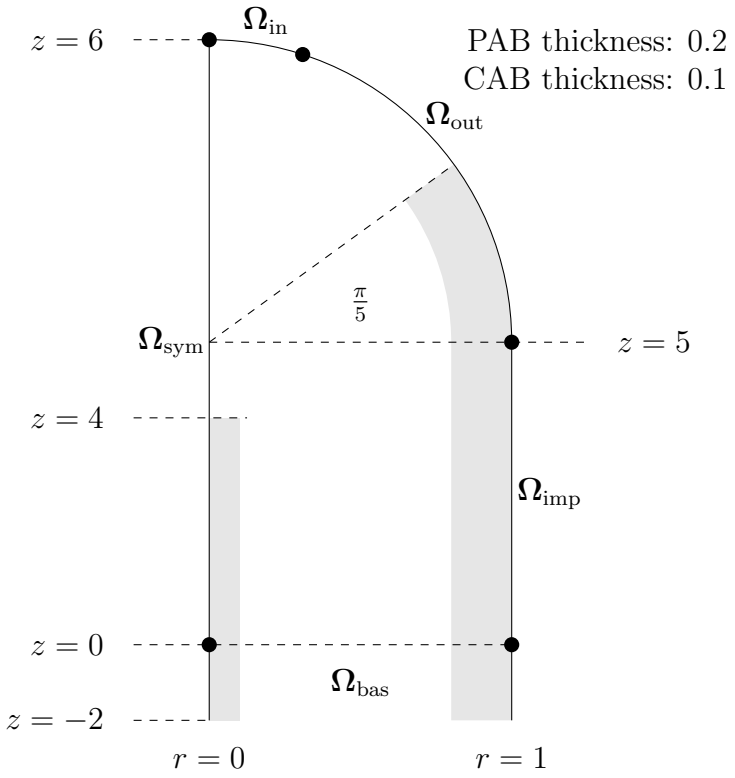

Figure 4.4: Geometric elements of the pollen tube model. PAB and CAB refer to peripheral actin bundle and central actin bundle respectively, with CAB thickness half that of PAB by axisymmetry. Image not drawn to scale in $\hat{z}$.

4.3 Cytosolic velocity profiles

Here, we employ the method of regularized ringlets derived in Chapter 3 alongside our knowledge of cytoplasmic dynamics to produce velocity profiles for internal cytosolic flow in the growing pollen tube. Schematic diagrams for the problems considered are given in Figure 4.6.

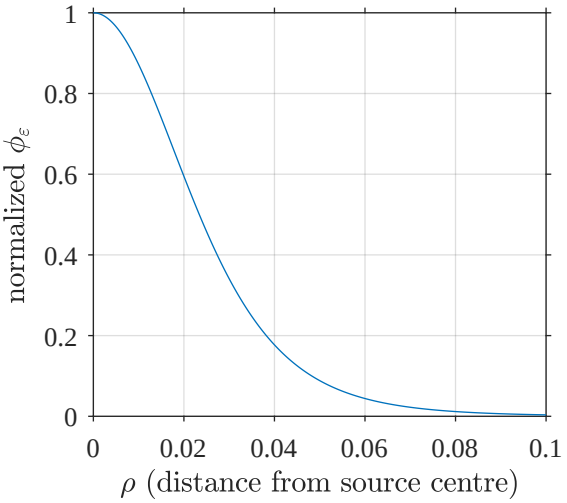

Figure 4.5: Controlled spreading of force distribution using ϕ_ε with $\varepsilon = 0.05$

.

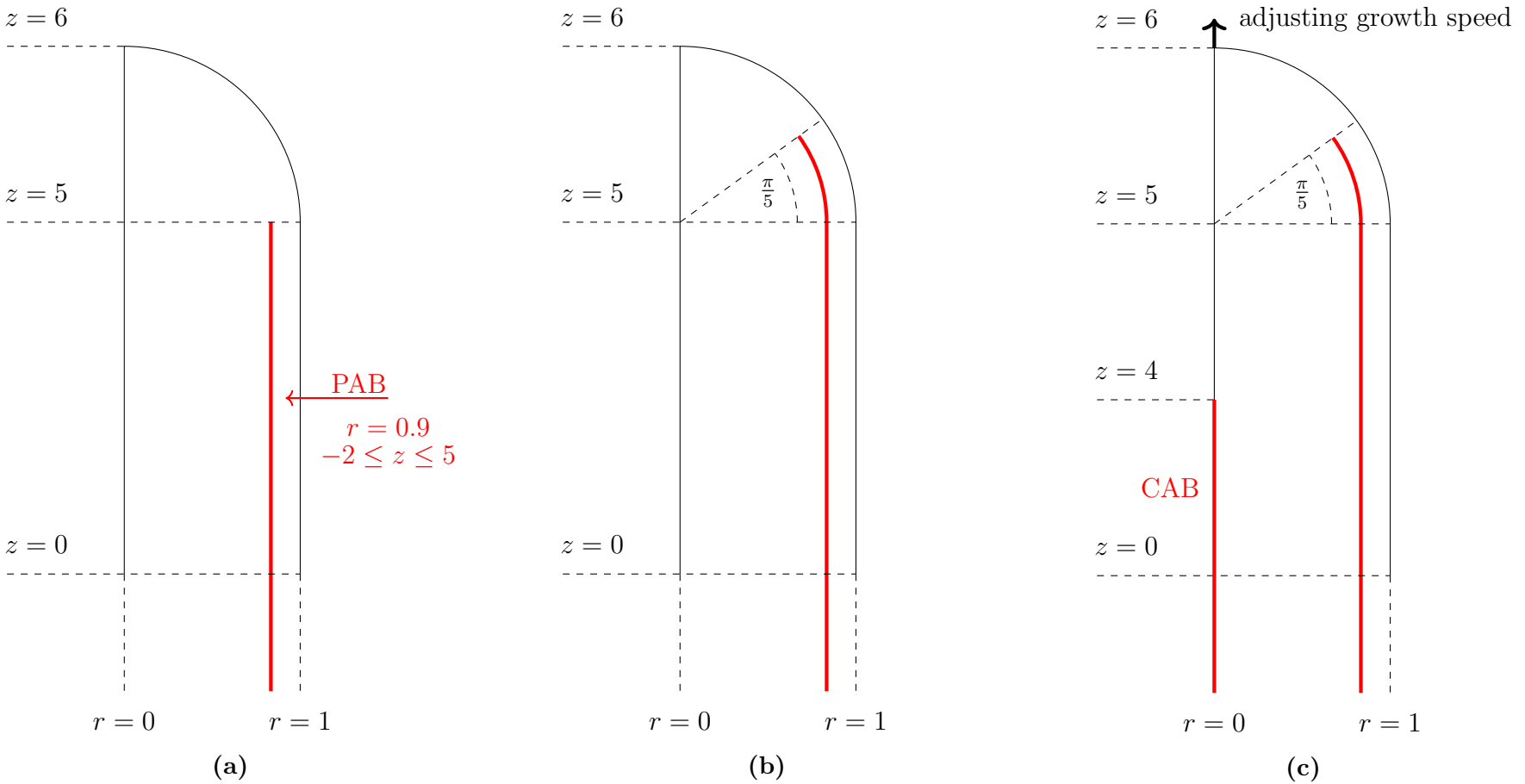

Figure 4.6: Schematic diagrams for problems in Section 4.3. **(a)** In 4.3.1, a force is applied along the peripheral actin bundle (PAB) corresponding to drag induced by the actomyosin transport of exocytic vesicles. **(b)** In 4.3.2, fluid velocity is prescribed along the PAB (extended further into the apical hemisphere) to investigate the resulting magnitude of central fluid velocity. **(c)** In 4.3.3, fluid velocities are prescribed along both the PAB and central actin bundle (CAB) while we determine the effect of adjusting the tube growth speed on the internal cytosolic flow.

4.3.1 Generating a velocity profile based on toroidal drag forces

For the first velocity profile to be produced, it is assumed that the movement of exocytic vesicles in the periphery of the tube is entirely dictated by actomyosin transport (i.e. all exocytic vesicles are fixed to actin with none freely flowing in the cytosol). Based on the STICS images in Figure 4.8, as well as results from De Win [40] and Vidali *et al.* [119], we make the conservative estimate that vesicle velocity on actin is given by $0.5\,\mu\mathrm{m\,s^{-1}}$ (note that this is smaller than the value listed in Table 4.2). We further assume that exocytic vesicles undergoing actomyosin transport are arranged in axisymmetric rings, such that their shape can be approximated by that of a torus with minor radius equal to exocytic vesicle radius R_v and major radius equal to the perpendicular distance from the centre of the tube to the centre of the peripheral actin bundle, $0.9R_0$. Letting each vesicle torus be represented by a single Stokes ringlet, the force per (azimuthal) unit length exerted by the moving torus on the surrounding fluid is given by,

$$\mathbf{g}^l = \frac{4\pi\mu U_a}{\log\left(8/\kappa\right) + \frac{1}{2}}\hat{\mathbf{z}}, \tag{4.3.1}$$

as derived by Johnson and Wu [73], where $\kappa = R_v/0.9R_0$ is the 'slenderness parameter' for the torus (minor radius divided by major radius). Based on the calculations of Bove *et al.* [12], we assume that a tube growing with speed $0.1\,\mu\mathrm{m\,s^{-1}}$ requires the delivery of 400 vesicles per second to the growing apical region[1]. We calculate the number of vesicles that it is possible to pack into a single torus to be equal to $(0.9R_0)\pi/R_v \approx 270$, such that the maximum separation distance between the centres of adjacent tori must be $(270\,U_a/400) \approx 0.338\,\mu\mathrm{m}$ in order to maintain the constant delivery rate. Placing Stokeslet rings in series along the centreline of the peripheral actin bundle ($r = 0.9R_0$) using this separation distance of $0.338\,\mu\mathrm{m}$ (0.0416 in dimensionless terms) and the force per unit length $\mathbf{g}^l$ from Equation (4.3.1) yields the velocity profiles seen in Figure 4.7. Note that the peripheral actin bundle is not modelled as extending beyond $z = 5$ in this

[1]This is a small overestimate, since this number actually applies for a tube growing with speed $7\,\mu\mathrm{m\ min^{-1}}$ or $0.117\,\mu\mathrm{m\,s^{-1}}$.

case, and a force along the peripheral boundary of the tube is also applied *a posteriori* such that the boundary conditions are satisfied.

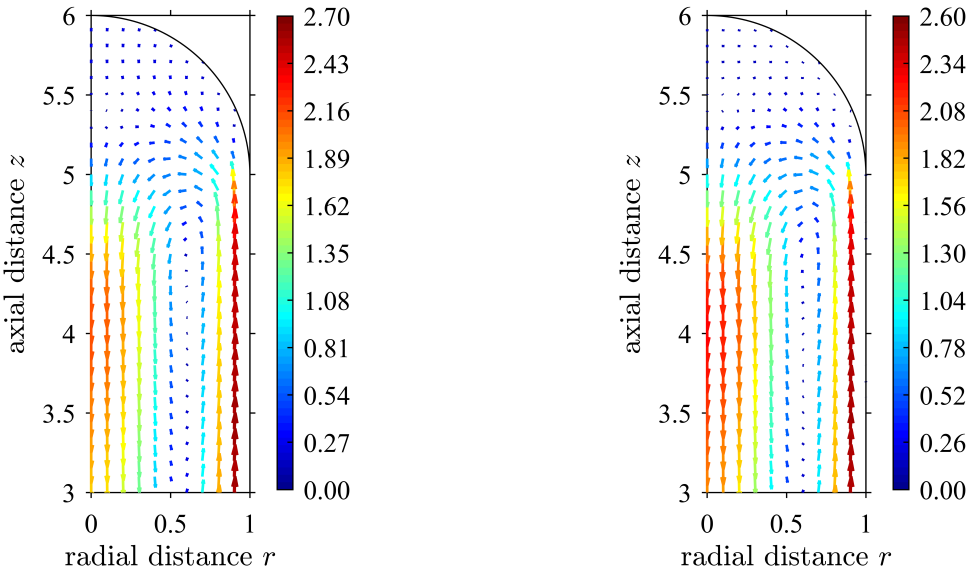

(a) Lab frame. **(b)** Tip frame.

Figure 4.7: Magnitude and direction of apical cytosolic flow induced by drag of myosin-based exocytic vesicle transport along the peripheral actin bundle. Velocities are scaled by the speed of vesicles on actin ($0.5\,\mu\mathrm{m\,s^{-1}}$), with lengths scaled by the radius of the tube ($8.13\,\mu\mathrm{m}$).

Clearly, the combination of these applied drag forces is too large since the speed of the cytosol exceeds vesicle speed along actin (an 'unphysical' situation, given that vesicle movement along actin is responsible for inducing the flow). This appears to suggest that it may not be necessary for the entire exocytic vesicle population to be transported via actin-myosin in order for a sufficiently large cytosolic flow to be induced. There are some simple and immediate counterarguments against this, which we address in turn.

The first possible counterargument is that the arrangement of vesicles in axisymmetric rings represents a highly idealised orientation unlikely to ever be observed naturally in the pollen tube. While true, arranging the vesicles in tori in this idealised configuration also results in a larger separation distance in the axial direction $\hat{\mathbf{z}}$ than would otherwise be possible, theoretically limiting the 'overlap' of adjacent drag forces. In fact, if the total drag force produced by the moving torus, $2\pi(0.9R_0)|\mathbf{g}^l|$, is compared to that of 270

individual vesicles, $270 \cdot (6\pi\mu R_v U_a)$, the combined drag of the individual vesicles is over 5 times larger than that of the torus. This suggests that the axisymmetric case actually vastly underestimates the contribution of vesicles undergoing actin-myosin transport to cytosolic flow.

The second counterargument we foresee is that these calculations do not take into account the larger combined vesicle population or the presence of other organelles in the tube, which may impede the speed of cytosolic flow. This is valid criticism and is not easy to address since a rigorous implementation of these potential flow obstacles in any model is nontrivial. A quick calculation of the volume fraction occupied by exocytic vesicles in the peripheral region yields,

$$\frac{400}{U_a}\frac{4\pi R_v^3}{3}\frac{1}{\pi(R_0^2-(0.8R_0)^2)} = 2.75\%, \tag{4.3.2}$$

an order of magnitude smaller than the space occupied by the total vesicle population, other organelles, and the actin filaments themselves. A simple way in which these flow obstacles could be included is through the use of an 'effective viscosity', essentially treating the cytoplasm as a homogeneous continuum with an effective viscosity larger than cytosolic viscosity. Cytosolic viscosity could continue to be used for the toroidal drag calculation in Equation (4.3.1) under the assumption that the fluid region local to any given exocytic vesicle is largely free of other obstacles, but effective viscosity would be employed in the calculation of fluid velocity based on Equation (3.2.22). This calculation is further complicated by the fact that filamentous actin networks also contribute to an increased local viscosity.

In light of these results, it seems clear that only a relatively small proportion of the total vesicle population needs to be undergoing actomyosin transport in order for cytosolic flow to attain a similar speed to vesicle velocity on actin. The assumption that the movement of exocytic vesicles is entirely dictated by actomyosin transport is likely false. This makes sense given that bulk vesicle movement in the periphery of the tube doesn't

exceed $\approx 0.5\,\mu m\,s^{-1}$ in the SpatioTemporal Image Correlation Spectroscopy results of Bove *et al.* [12], but the speed of individual organelles in the tube is known to reach values as large as $2\,\mu m\,s^{-1}$ [40, 119]. The exact proportion of the vesicle population undergoing actin-myosin transport is linked to the heightened effective viscosity of the cytoplasm, representing the strength with which free flowing vesicles and other organelles resist the cytosolic flow. As vesicles accumulate in a region, the effective viscosity is increased further due to hydrodynamic interactions between them. For example, the effective viscosity of a fluid containing a uniform suspension of spherical particles at 15% volume fraction (the approximate density of vesicles in the clear zone [78]) is known to be anywhere from ≈ 1.7 to ≈ 2 that of the fluid viscosity absent the particles [8, 64]. This effect can also be seen in the *Escherichia coli* bacterium where the small size of the cell ($< 1\,\mu m^3$) means that the effective viscosity of the cytoplasm is altered by the size of the probe used in measurements. The effective viscosity here varies from ≈ 1.1 times that of water at the smallest scale to ≈ 26000 times at the largest [74]. Without being able to quantify the effective viscosity of the cytoplasm or the proportion of vesicles undergoing actomyosin transport in the pollen tube, it is not possible to produce an accurate cytosolic velocity profile based on toroidal drag forces.

4.3.2 Role of the central actin bundle

For the next velocity profile, the role of the central actin bundle in the cycling of vesicles to and from the apical region is considered. Direct observation of actomyosin vesicle transport is often hindered by the small size of vesicles (typically below the resolution limit of conventional confocal microscopes). Higher resolution imaging methods such as evanescent wave microscopy have been used to observe long-range vesicle movement (presumably a result of actomyosin transport) in the periphery of the tube [120], but the limited penetration depths available in these methods ($\leq 400\,nm$) do not allow for imaging of the central region. Thus although it has long been hypothesised that the

central bundle must aid vesicle transport, this has never been directly observed. In the STICS analysis of Bove *et al.* [12] directed vesicle movement in the periphery of the tube is not seen to exceed speeds of $\approx 0.5\,\mu\mathrm{m\,s^{-1}}$, smaller than the $\approx 0.8\,\mu\mathrm{m\,s^{-1}}$ observed in the centre. By using the method of regularized ringlets and prescribing fluid velocity only along the peripheral bundle and tube boundary, the resulting fluid velocity in the centre should give us some insight into whether the central bundle participates in vesicle transport.

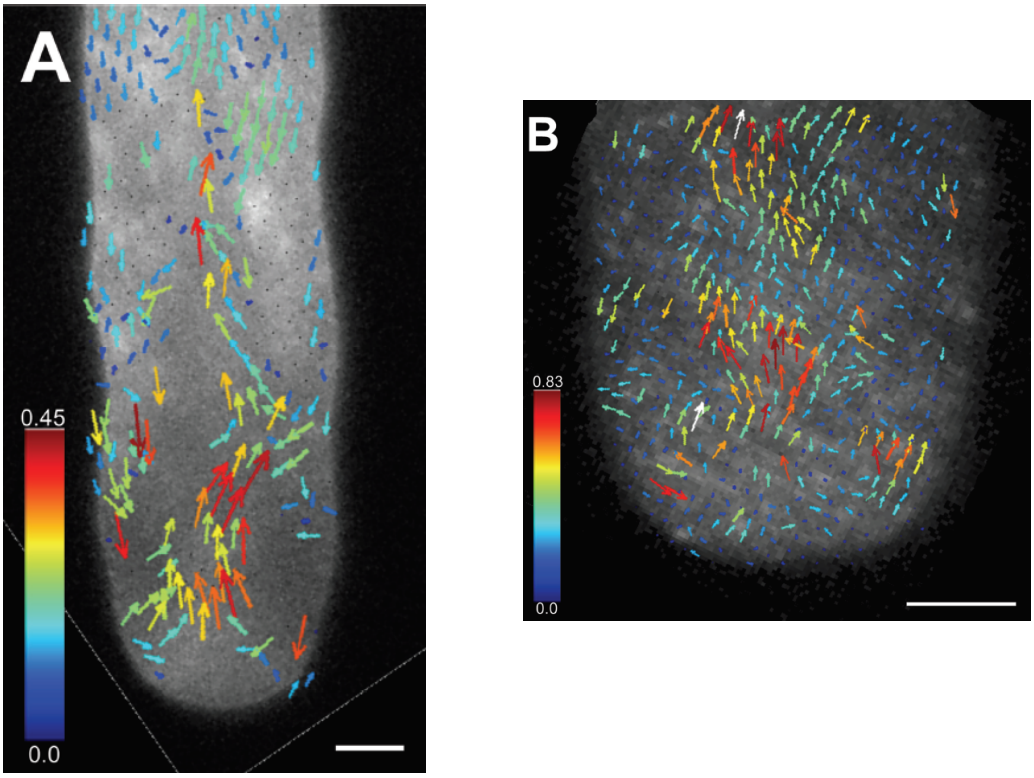

Figure 4.8: STICS analysis of apical vesicle movement over a 10 s period. The size of the analysis window is increased in the image on the right, revealing individual waves of vesicle motion of greater magnitude. Velocities are measured in $\mu\mathrm{m\,s^{-1}}$ with scale bar = 5 µm. (Credit: Chebli *et al.* [22], first published in Bove *et al.* [12])

The results of this investigation can be seen in Figure 4.9. The centreline of the peripheral actin bundle is modelled using the union of the straight line extending from $(r, z) = (0.9, -2)$ to $(0.9, 5)$ and the curve $(r, z) = (0.9\cos\varphi, 5 + 0.9\sin\varphi)$ for $\varphi \in [0, \pi/5]$. The regularized ringlet placement is extended to $z = -2$ to ensure the velocity profile at $z = 0$ is consistent with the rest of the tube. The fluid velocity on the straight line is given by $(U_r, U_z) = (0, 0.5)$ with the fluid velocity on the curve being tangential and of constant

magnitude, that is, $(U_r, U_z) = 0.5(\sin\varphi, \cos\varphi)$ for $\varphi \in [0, \pi/5]$. On the peripheral wall (again extended to $z = -2$), the velocity is $\mathbf{0}$ in the shank and prescribed according to the growth speed v_g of the tube in the apical hemisphere using the velocity function $\mathbf{u}_g(\varphi) = v_g \sin\varphi(\cos\varphi, \sin\varphi)$ for $\varphi \in [0, \pi/2]$. We do **not** prescribe fluid velocity on the central actin bundle. A regularisation parameter of $\varepsilon = 0.05$ is chosen throughout and the Stokeslets are linearly spaced a distance approximately 0.025 apart, resulting in a smooth velocity profile. The flow velocity for $z < 3$ (not pictured) matches the flow velocity at $z = 3$ almost exactly, with no further change occurring in the $\hat{\mathbf{z}}$ direction.

The shape of the velocity profile in Figure 4.9 is in excellent agreement with the STICS analysis of Bove *et al.* [12], with a wider band of basal flow through the centre than apical flow in the periphery. However, despite an arguably exaggerated prescribed peripheral fluid velocity of $0.5\,\mu\mathrm{m\,s^{-1}}$, fluid velocity in the centre does not achieve speeds of $0.8\,\mu\mathrm{m\,s^{-1}}$. This is a strong indication that the central bundle must also participate in the transport of vesicles, particularly considering that the current implementation of the Stokes equations does not account for variations in local fluid viscosity (known to be larger in the presence of filamentous actin networks [121], reducing the fluid velocity induced by any given force). The increased flow speed through the centre of the tube can be easily accounted for by inclusion of additional drag from actomyosin vesicle transport (known to reach speeds of up to $2\,\mu\mathrm{m\,s^{-1}}$ [119, 40]) along the central bundle, with the largest velocities being observed at the very centre as a result of the reduced cytosolic volume in this region.

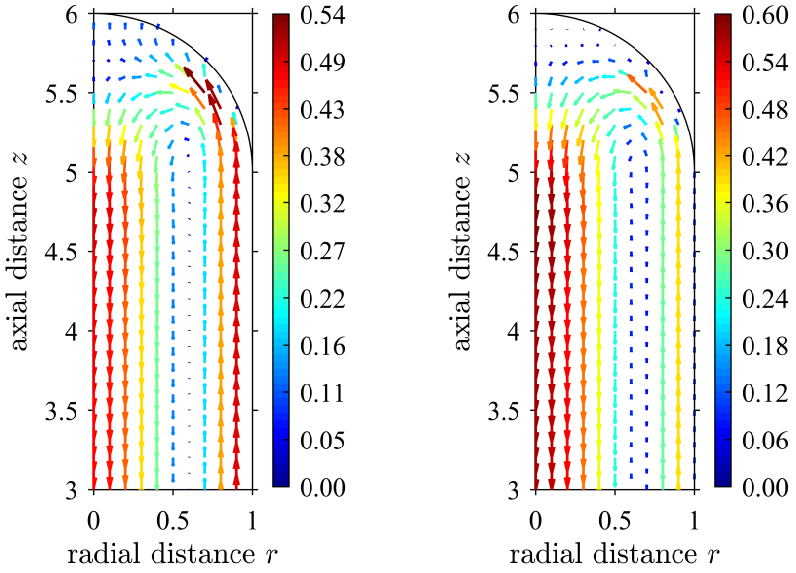

(a) Lab frame. **(b)** Tip frame.

Figure 4.9: Magnitude and direction of apical cytosolic flow in (a) **lab frame**, and (b) **tip frame**, calculated using prescribed velocity of magnitude $0.5\,\mu\mathrm{m\,s^{-1}}$ on the peripheral actin bundle, as well as a prescribed normal velocity with maximum magnitude equal to the growth speed $0.1\,\mu\mathrm{m\,s^{-1}}$ at the apical boundary. Velocities are scaled by the speed of vesicles on actin ($1\,\mu\mathrm{m\,s^{-1}}$), with lengths caled by the radius of the tube ($8.13\,\mu\mathrm{m}$).

4.3.3 The influence of growth speed

A further 3 new velocity profiles are produced, based on 3 different growth speeds for the tube ($0, 0.1,$ and $0.2\,\mu\mathrm{m\,s^{-1}}$). These speeds (approximately) correspond to that of a static tube, the typical growth rate cited in Bove *et al.* [12], and the average growth rate measured by Vidali *et al.* [119] for the *Lilium longiflorum* species. Fluid velocity along the peripheral actin bundle is kept constant at $0.5\,\mu\mathrm{m\,s^{-1}}$ in each of these profiles, based on the observation that streaming rates are typically independent of pollen tube growth rates [119]. In this and all future scenarios, fluid velocity is also prescribed along the centreline of the central actin bundle, given by $r = 0$ for $-2 \leq z \leq 4$. It is assumed that vesicles are sufficiently closely packed on this bundle that the fluid velocity at its centre can be approximated by the speed of vesicles on actin, giving $(U_r, U_z) = (0, -1)$. Since

these node locations are at $r = 0$, standard regularized Stokeslets must be used here.

Figure 4.10 shows the velocity profiles for each of these 3 tube growth speeds in the **lab frame**. Significant differences can be seen between the three profiles, both in the magnitude and direction of the fluid velocity. In particular, at larger growth speeds there is a wider band of cytosolic flow in the positive $\hat{\mathbf{z}}$ direction in the peripheral region, and the central band of basal flow is both narrower and of a reduced magnitude. This is an expected consequence of mass conservation, since in a tube with a faster growth speed more fluid must flow towards the apical region to fill the increasing space.

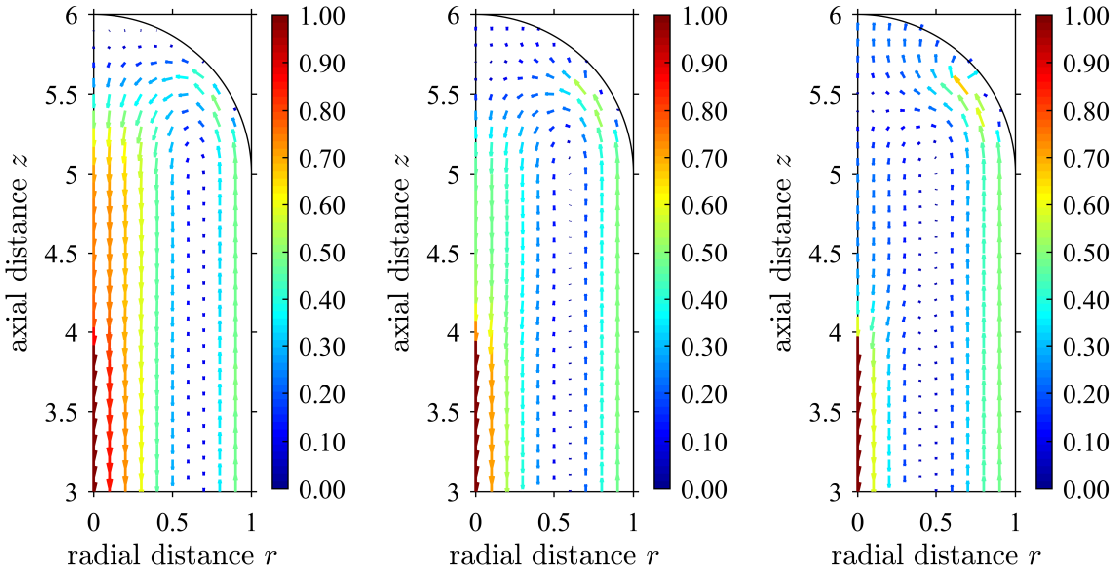

(a) $0\,\mu\mathrm{m\,s^{-1}}$. **(b)** $0.1\,\mu\mathrm{m\,s^{-1}}$. **(c)** $0.2\,\mu\mathrm{m\,s^{-1}}$.

Figure 4.10: Magnitude and direction of apical cytosolic flow in the **lab frame**, calculated using prescribed velocities of magnitude $0.5\,\mu\mathrm{m\,s^{-1}}$ and $1\,\mu\mathrm{m\,s^{-1}}$ on the peripheral and central actin bundles respectively, as well as a prescribed normal velocity with maximum magnitude equal to the growth speed (a) $0\,\mu\mathrm{m\,s^{-1}}$, (b) $0.1\,\mu\mathrm{m\,s^{-1}}$, (c) $0.2\,\mu\mathrm{m\,s^{-1}}$, at the apical boundary. Velocities are scaled by the speed of vesicles on actin ($1\,\mu\mathrm{m\,s^{-1}}$), with lengths scaled by the radius of the tube ($8.13\,\mu\mathrm{m}$).

Figure 4.11 shows the velocity profiles for each of the 3 tube growth speeds in the **tip frame**. Here, the growth speed of the tube has been subtracted from the $\hat{\mathbf{z}}$ component of the fluid velocity for each corresponding velocity profile in the lab frame. Interestingly, the differences between the velocity profiles are significantly less pronounced in this frame of reference. Differences in the magnitude of the fluid velocity still persist, but the overall

shape of the profiles bear a striking similarity. The persistent shape of the velocity profiles seen in Figure 4.11 could help explain the observed similarities in the distribution of the apical vesicle population and other elements of the cytoplasm across multiple pollen tube species and throughout different phases of oscillatory growth.

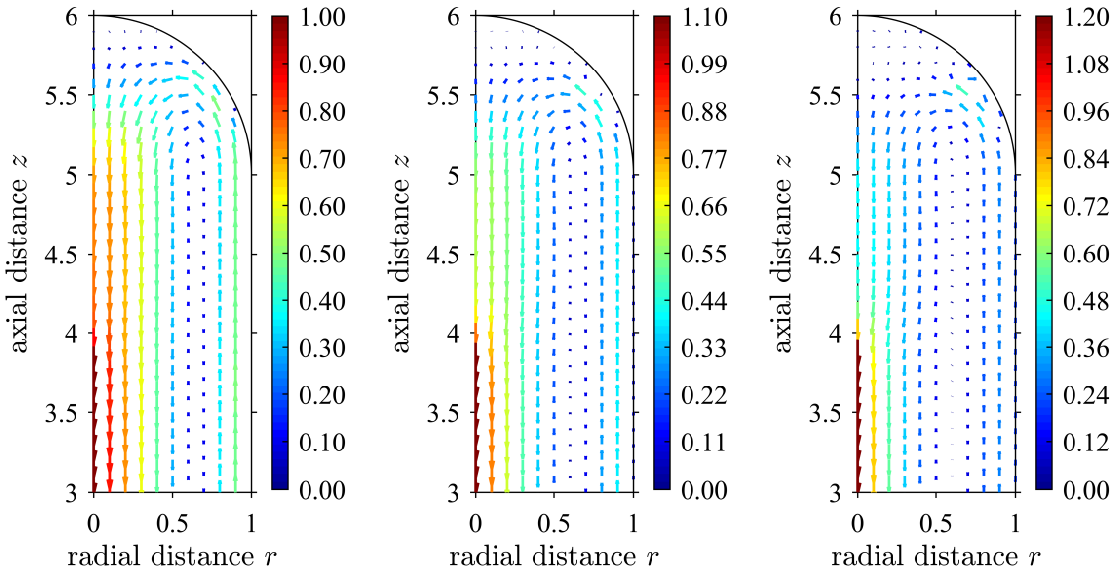

(a) $0\,\mu m\,s^{-1}$. **(b)** $0.1\,\mu m\,s^{-1}$. **(c)** $0.2\,\mu m\,s^{-1}$.

Figure 4.11: Magnitude and direction of apical cytosolic flow in the **tip frame**, calculated using prescribed velocities of magnitude $0.5\,\mu m\,s^{-1}$ and $1\,\mu m\,s^{-1}$ on the peripheral and central actin bundles respectively, as well as a prescribed normal velocity with maximum magnitude equal to the growth speed (a) $0\,\mu m\,s^{-1}$, (b) $0.1\,\mu m\,s^{-1}$, (c) $0.2\,\mu m\,s^{-1}$, at the apical boundary. Velocities are scaled by the speed of vesicles on actin ($1\,\mu m\,s^{-1}$), with lengths scaled by the radius of the tube ($8.13\,\mu m$).

4.4 Cytoplasmic vesicle distributions

Following our determination of a qualitatively accurate cytosolic velocity profile for the growing *Lilium longiflorum* pollen tube, we return to the governing equations for vesicle distribution and consider the conditions under which we see the emergence of the inverted vesicle cone at steady state.

4.4.1 Steady state vesicle distributions

Using the velocity profile from Figure 4.11b (for boundary growth $0.1\,\mu\mathrm{m\,s^{-1}}$), we find numerical solutions to the governing equations (4.2.25) – (4.2.26) for $\phi^{(x)}$ and $\phi^{(n)}$ via the FVM of Chapter 2 implemented in Matlab. Starting from a zero concentration initial condition, exocytic vesicles are added to the system at a rate of 400 per second via a source area extending one fifth of tube radius R_0 from the plasma membrane into the cytoplasm for $\varphi \in [\frac{\pi}{10}, \frac{3\pi}{10}]$ (see Figure 4.12). Prior simulations run using a more distal source point did not yield the desired initial accumulation patterns of exocytic vesicles seen in the FRAP images from [12], hence our decision to place the source point close to the apical membrane under the assumption that vesicles are deposited here directly by actin. We run this until the system is at steady state (change in maximum total vesicle concentration appreciably 0). We label each of our sets of results 'Exo', 'Endo', or 'Combo' depending on whether they show the exocytic, endocytic, or combined vesicle population respectively. The results for the exocytic and endocytic populations can be seen in Figure 4.13, where the exocytosis rate γ at the apical wall is altered in each plot.

The shape of the region of largest exocytic vesicle accumulation matches our exocytic source area and is consistent with the initial accumulation of labelled vesicles in the FRAP images from Bove *et al.* [12]. We also note that larger values of the cytosis rate γ appear to result in a smaller exocytic vesicle concentration in the extreme apex compared to the rest of the apical hemisphere, matching the lower fluorescence intensity observed in this area during the early stages of the same FRAP experiments (when the labelled material is assumed to be exocytic in nature, or at the very least not originating from the plasma membrane).

The shape of each endocytic vesicle population distribution profile is largely identical, with the only differences being in the magnitude of the vesicle concentration in each. For both $\gamma = 0.1\,\mu\mathrm{m\,s^{-1}}$ and $\gamma = 1\,\mu\mathrm{m\,s^{-1}}$ the endocytic population dominates. This

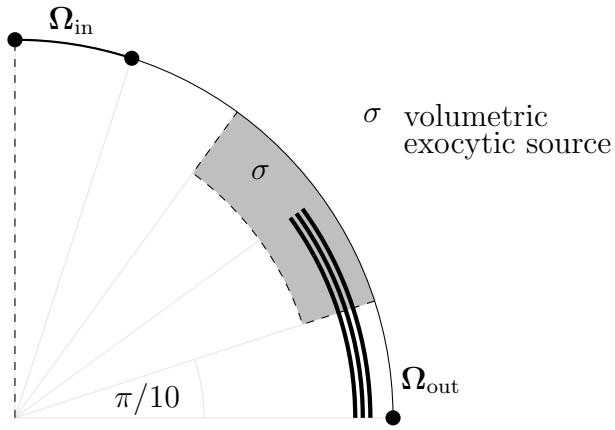

Figure 4.12: Volumetric exocytic source σ (shaded area) surrounding terminal location of peripheral actin bundle (thick lines) in the vesicle transport model. Faint lines show increments of $\pi/10$ in polar angle.

is in agreement with the results of Zonia and Munnik [126], who used high-resolution refraction-free time lapse DIC micrographs of five pollen tubes to measure the various sizes of objects in the tube and found the apical population to be predominantly endocytic. We are also able to extract from our simulation the percentage of exocytic material added to the system at each time step that successfully fuses with the wall (to be discussed in more detail in Section 4.4.3), which for $\gamma = 0.1\,\mu\text{m}\,\text{s}^{-1}$ is 84.52% at steady state, a near-perfect result for our required vesicle uptake of $\approx 340\,\text{s}^{-1}$ (using our parameter values from Table 4.2 and following the calculation in [12]) given our source rate of $400\,\text{s}^{-1}$. It is clear from Figures 4.13a - 4.13c however, that we have not managed to find the correct vesicle distribution pattern in any of these cases. In addition to this, images of the exocytic population during the first 100s (not pictured) show the population to be simply too diffuse, spreading out rapidly from the source area and not reflecting distinct accumulation patterns seen in the FRAP imaging of Bove *et al.* [12].

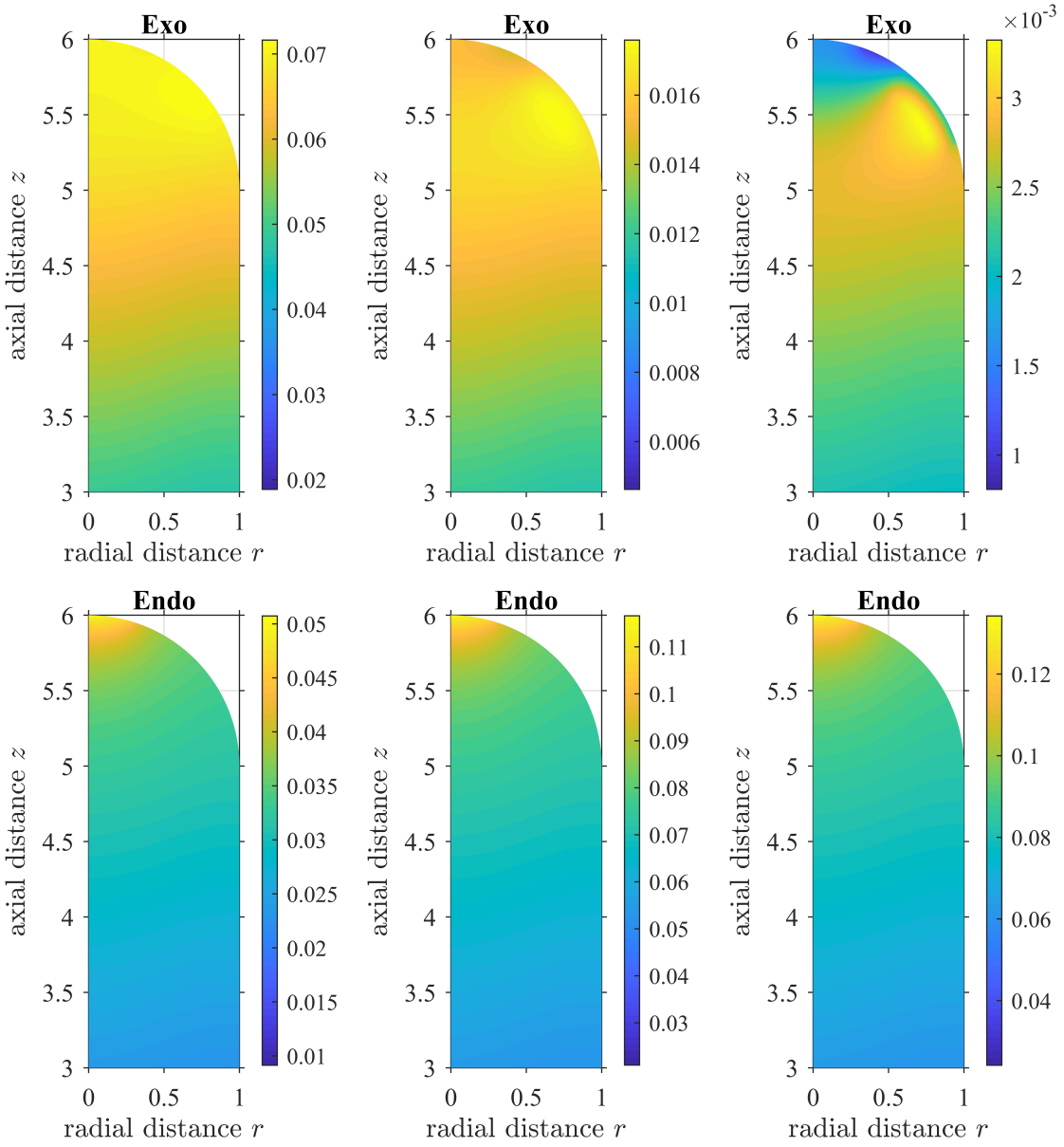

(a) $\gamma = 0.01\,\mu\mathrm{m\,s^{-1}}$ **(b)** $\gamma = 0.1\,\mu\mathrm{m\,s^{-1}}$ **(c)** $\gamma = 1\,\mu\mathrm{m\,s^{-1}}$

Figure 4.13: Steady state exocytic and endocytic vesicle populations for three different values of the cytosis rate γ. Values on the colourbar are given by the product of number density of vesicles and average vesicle volume, giving an approximate volume fraction. Lengths are scaled by the tube radius R_0.

Figure 4.14 shows the combined vesicle population distribution at steady state under four different regimes, in which both the value of the Péclet number and the area over which endocytosis occurs are varied. Figure 4.14a uses the original parameters with endocytosis confined to the boundary region corresponding to $\varphi \in [2\pi/5, \pi/2]$ along the apical hemisphere. Figure 4.14b shows the result of increasing the Péclet number by a factor of 10, with a large accumulation of vesicles in the extreme apex. We note that the maximum value of the volume fraction (almost 0.5) is very large in this case, particularly given that the density of a packing of congruent spheres (as our vesicles have been modelled using here) in three dimensions can never be never greater than $\pi/18 \approx 0.74$ [63]. Figure 4.14c shows the result of extending the area over which endocytosis occurs to occupy the entire boundary of the apical hemisphere (using standard Pe). Finally, Figure 4.14d shows the result of using 10 times the Péclet number and the extended endocytosis area. The shape of the distribution profile is in excellent agreement with the expected inverted vesicle cone [12, 78]. The occupied volume fraction in the cone is found to be ≈ 0.15, a close match to the average vesicle density of $62\,\mu\text{m}^{-3}$ (corresponding to a volume fraction of 0.1595) calculated in Kroeger *et al.* [78].

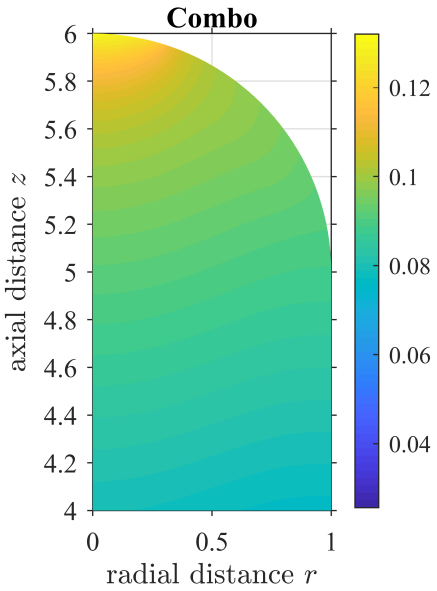

(a) Standard Pe, apical endocytosis.

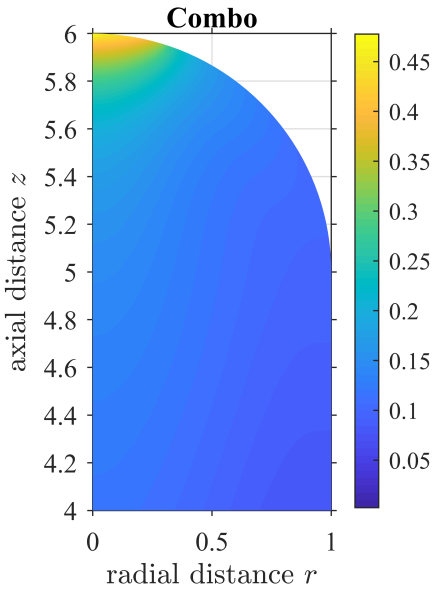

(b) 10Pe, apical endocytosis.

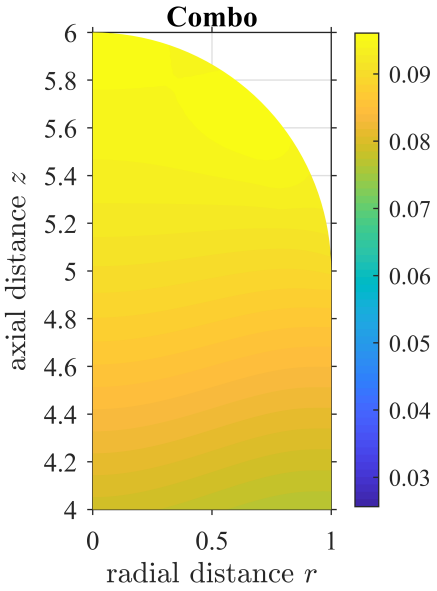

(c) Standard Pe, extended endocytosis.

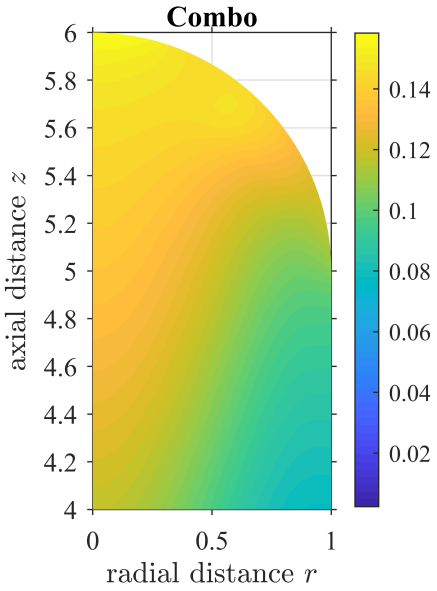

(d) 10Pe, extended endocytosis.

Figure 4.14: Steady state combined vesicle populations using cytosis rate $\gamma = 0.1\,\mu\mathrm{m\,s}^{-1}$ for different values of the Péclet numer Pe and different endocytic boundary areas. Values on the colourbar are given by the product of number density of vesicles and average vesicle volume, giving an approximate volume fraction. Lengths are scaled by the tube radius R_0.

These results are somewhat surprising, but not entirely. Experimental evidence exists for the use of a diffusive coefficient that is smaller (using conventional parameters) than the result of the Stokes-Einstein equation, suggesting the need to use a larger Péclet

number. Kroeger *et al.* [78] calculate a value of $0.625\,\mu m^2\,s^{-1}$ based on the experimental STICS results of Bove *et al.* [12] which is significantly smaller than the S-E value of $2.929\,\mu m^2\,s^{-1}$ found using the parameters in the rest of their work. Alternatively, since viscosity is approximately inversely proportional to diffusivity this could be considered evidence of the need to employ a larger effective cytoplasmic viscosity as previously mentioned in Section 4.3.1. Increasing the Péclet number by a factor of 10 corresponds to our effective viscosity having a value roughly 10 times that of water. Whether this is applicable in the clear zone of the pollen tube is debatable, although we note that the resulting diffusivity of $\alpha = 0.26\,\mu m^2\,s^{-1}$ does not differ significantly from that of Kroeger *et al.* [78] (whose calculation appears to be based on graphical information from [12], allowing some margin for error) and the volume fraction occupied by the vesicles suggests the need to use an effective viscosity of at least 2 times that of water [64].

In distal regions, given the crowded internal architecture of the tube and the abundant presence of F-actin, the use of a smaller diffusive coefficient (or larger viscosity) is more easily justified. Maruyama *et al.* [88] conducted experiments using a Couette viscometer on an F-actin solution of concentration $0.033\,mg\,ml^{-1}$ and found the viscosity of the solution varied from a value ≈ 10 to > 100 times that of water depending on the velocity gradient (see Figure 4.15). The velocity gradient is given by the range of the flow speed ($\approx 0.5\,\mu m\,s^{-1}$ in the periphery of the pollen tube) divided by the distance over which it varies ($\approx 0.8\,\mu m$, corresponding to the distance between the centre of the peripheral actin bundle and the static wall). The velocity gradient for the pollen tube is thus $< 1\,s^{-1}$, resulting in an effective viscosity in excess of our suggested $10^{-2}\,Pa\,s$. This is exacerbated by the fact that Maruyama *et al.* [88] also showed that the viscosity of the solution increases with increased F–actin concentration. In the immunoquantification experiments of Vidali and Hepler [118] the intracellular concentration of total actin (comprising both F–actin and G–actin) in the pollen tube was found to be $\approx 1.76\,mg\,ml^{-1}$, significantly more concentrated than the $0.033\,mg\,ml^{-1}$ solution used by Maruyama *et al.* [88] and suggesting that the effective viscosity of the pollen tube cytoplasm could be even greater

than the values we have considered. Crucially, it is unclear what the effect of proteins like profilin, responsible for the restructuring of actin filaments [118], has on the viscosity of the solution.

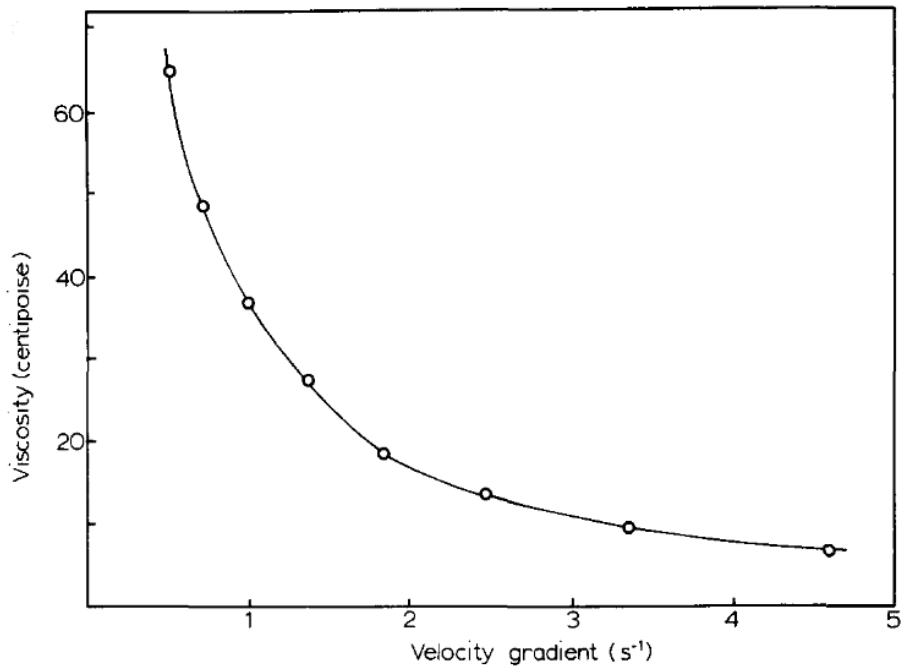

Figure 4.15: Dependence of the viscosity of a $0.033\,\mathrm{mg\,ml^{-1}}$ F-actin solution on the velocity gradient in a Couette viscometer. (Credit: Maruyama *et al.* [88]).

Perhaps of greater interest, in extending the endocytic boundary to encompass the entirety of the apical hemisphere and employing a uniform endocytosis rate throughout, we have implicitly defined endocytosis to vary from a maximum at the distal region of the hemisphere (where surface area is largest) to zero at the extreme apex (following a cosine distribution along the meridian line). This is in disagreement with a number of other results such as those of Chavarrìa-Krauser and Yejie [20], where endocytosis occurs maximally at the extreme apex. It could be argued that our endocytosis profile represents a redistribution of clathrin–mediated endocytosis in the shank ($z < 5$) across the apical hemisphere (focused near the point where the two join), remedying this disparity between our work and others' somewhat.

Alternatively, it could simply be the case that the uniform endocytosis rate we employ

is the best realistic approximation to apical endocytosis and the biological situation is less complex than had previously been believed. Experimental evidence for the extreme apex being the primary site of endocytosis appears to be a result of reduced relative fluorescence intensity after photobleaching in this region [12], but other FRAP studies are less clear on this. Fluorescence intensity in the apical plasma membrane (APM) is found to recover most quickly in the extreme tip of tobacco pollen tubes in [81] (suggesting increased exocytic or endocytic activity here), but the difference in recovery time and final intensity is arguably insignificant compared to results in the adjacent shoulder. Fluorescence intensity also appears to be greatest in the extreme APM even prior to photobleaching in these results and recovery in the first 30s is mostly uniform across the entirety of the APM. This suggests heightened final fluorescence intensity of the extreme APM can not be attributed solely to increased endocytosis. Further to this, the yellow band of fluorescence across the APM in Figure 4.16 (taken from Zonia and Munnik [126]) also suggests significant endocytic activity across the entirety of the APM. This yellow band represents a mixing of the green-labelled vesicles in the cytoplasm and the red-labelled plasma membrane, presumably a consequence of endocytosis. Also shown in Figure 4.16 is what appears to be a combination of distal endocytosis and exocytosis (discussed in more detail in 5.3.)

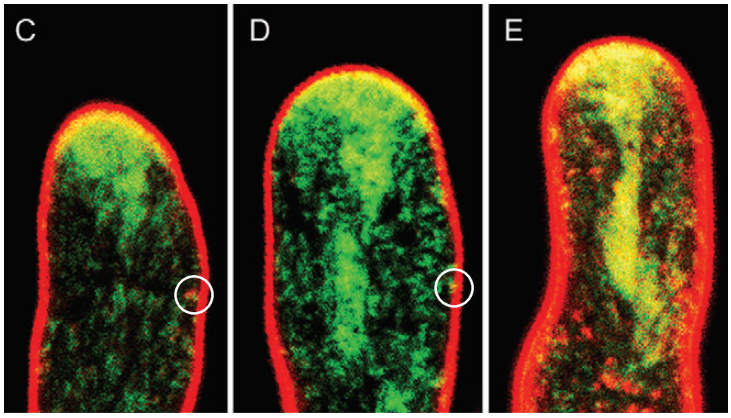

Figure 4.16: Pulse-chase labelling of membrane material in a tobacco pollen tube, showing mixing of lipophilic dyes as a result of exocytosis and endocytosis after (C) 1 min, (D) 3 min, (E) 10 min. A yellow band of dye is clearly visible along the apical plasma membrane, indicating a mixing of green and red dyes as a result of apical exo-/endo-cytosis. The white circles (added by me) show the release of red dye into the cytosol (distal endocytosis) in (C), followed by a yellowing of the plasma membrane (distal exocytosis) in (D). (Credit: Zonia and Munnik [126]).

FRAP images (collected by our collaborators Dr Youssef Chebli and Prof Anja Geitmann at McGill University, analyzed and edited by JT) using laser scanning confocal microscopy with Camellia pollen tubes clearly show uniform initial fluorescence recovery across the majority of the apical membrane (Figure 4.17), indicative of a flat rate of endocytosis. A greater intensity in the extreme apex can be observed starting at around $t = 7.5\,\mathrm{s}$ but this behaviour is not maintained and has ceased by $t = 17.5\,\mathrm{s}$ (Figure 4.18). Oscillatory patterns of increased fluorescence activity originating in the extreme apex and generally lasting for $\approx$ 10 seconds are visible throughout the duration of our FRAP time lapse series. We posit that this is the result of oscillatory growth behaviour not accounted for in our model. A further example of this change in apical fluorescence intensity at a later point in time can be seen in Figure 4.19. This increased fluorescence intensity in the extreme APM is often considered evidence of increased endocytic activity since faster fluorescence recovery indicates a more rapid removal of unlabelled plasma membrane (and subsequent replacement by labelled membrane). However, if the increased fluorescence of the extreme APM is an oscillatory feature rather than a permanent one (as our FRAP series suggests), this line of thinking appears inconclusive.

This oscillatory change in fluorescence appears to be linked to the rate of growth, as can be seen in Figure 4.20 where an increase in fluorescence intensity of the extreme APM precedes the increase in growth speed by $\approx$ 10 seconds. This matches closely to the correlation between vesicle accumulation in the apical region and growth rate of the tube previously observed by Lee *et al.* [81] (Figure 4.21) in tobacco pollen tubes, and is perhaps linked to the oscillatory fluctuations in both apical cellular stiffness (Zerzour *et al.* [124], Figure 4.22) as well as in the concentration of tip-localised F-actin (Fu *et al.* [52], Figure 4.23). Zerzour *et al.* [124] observe a softening of the cell wall $\approx$ 10 seconds prior to an increase in the growth rate, with the magnitude of the softening affecting the magnitude of the increase in growth. It is posited that this could be the result of the local secretion of highly methyl-esterified pectins into the wall prior to the growth event. It seems plausible that our observed oscillatory increase in fluorescence in the

APM is evidence of exactly this process occurring. Finally, in FRAP simulations we run using Matlab in Section 4.4.2, we will see that the reduced fluorescence intensity in the cytoplasm of the extreme apical region (as observed in [12]) is a natural consequence of the velocity profile we use and is consistent with our uniform endocytosis rate.

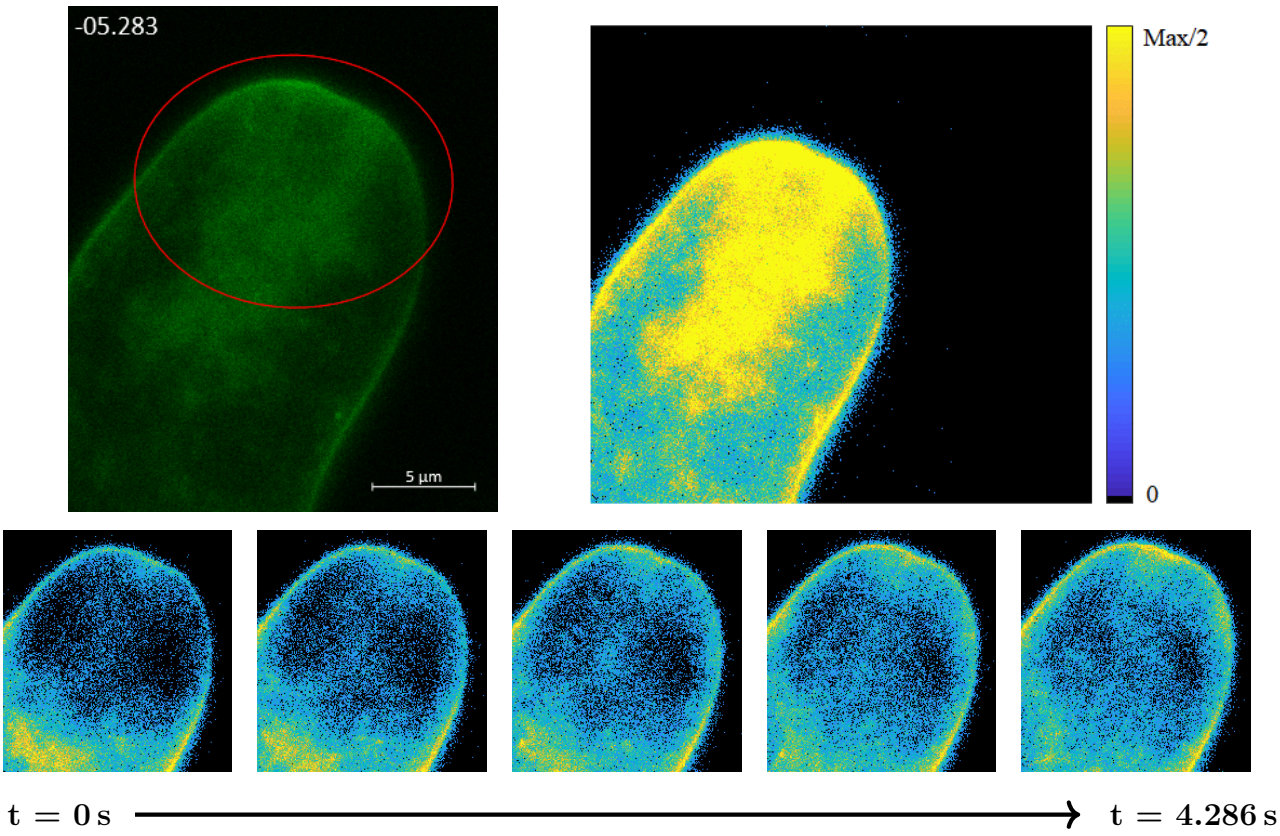

Figure 4.17: **Top left**: Fluorescently labelled (using FM4-64FX) apical region of the pollen tube prior to photobleaching, showing area to bleached. The number in the image refers to time relative to photobleaching in seconds. **Top right**: false colour version of the top left image. The colour bar here (and for the images in the bottom row) is scaled such that the maximal value corresponds to half the maximum fluorescence intensity observed in the tube throughout the duration of the experiment. **Bottom row**: False colour fluorescence labelling of the apical region of the tube, from 0 to 4.286 seconds after photobleaching (left to right). Images are taken roughly 1.07 seconds apart. These experiments were conducted by collaborators at McGill University (see Appendix C.1).

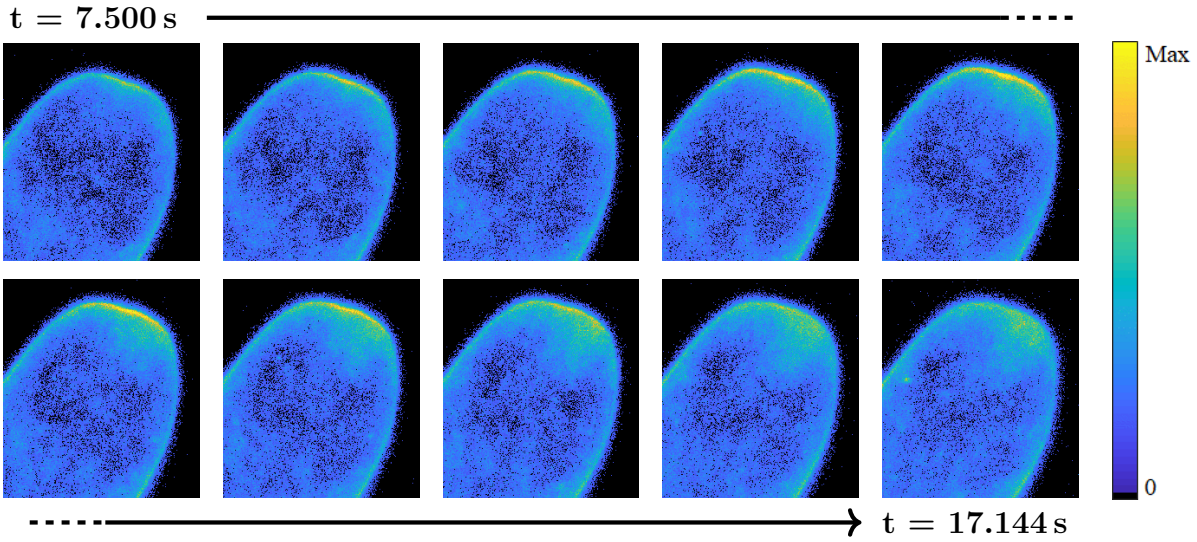

Figure 4.18: False colour fluorescence intensity in the apical region of the tube between 7.500 and 17.144 seconds after photobleaching (left to right, top to bottom). Images are taken 1.07 seconds apart. The colour bar is scaled such that the maximal value corresponds to the maximum fluorescence intensity observed in the tube throughout the duration of the experiment. These experiments were conducted by collaborators at McGill University (see Appendix C.1).

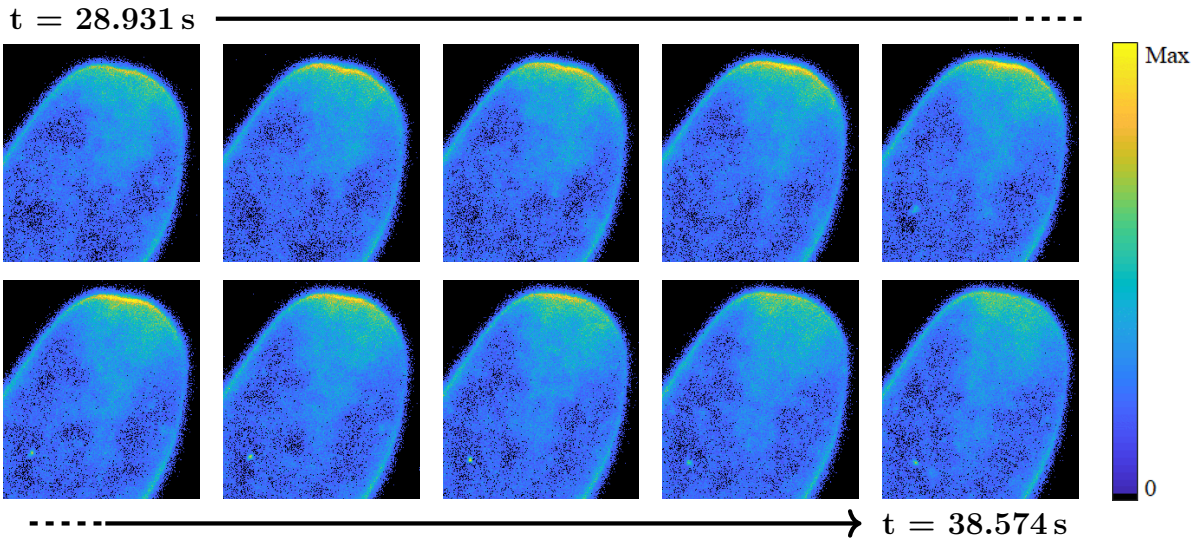

Figure 4.19: False colour fluorescence intensity in the apical region of the tube between 28.931 and 38.574 seconds after photobleaching (left to right, top to bottom). Images are taken 1.07 seconds apart. The colour bar is scaled such that the maximal value corresponds to the maximum fluorescence intensity observed in the tube throughout the duration of the experiment. These experiments were conducted by collaborators at McGill University (see Appendix C.1).

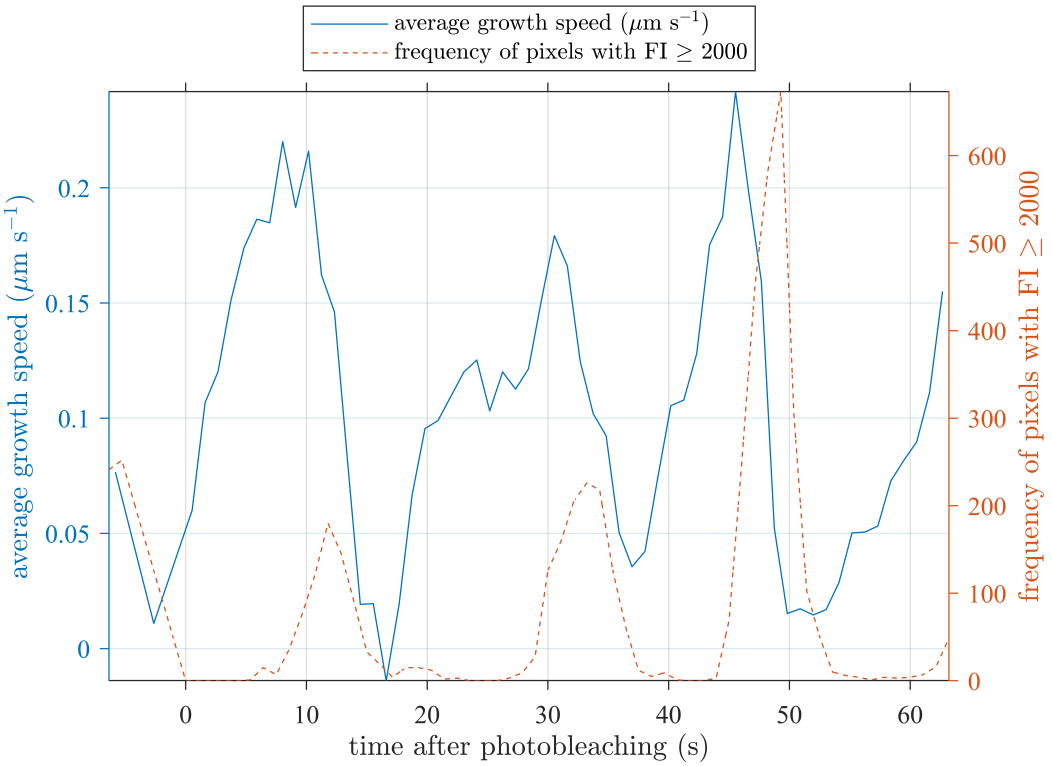

Figure 4.20: Similar oscillatory patterns are present in the average growth speed of the pollen tube and the intensity of fluorescence labelling of the extreme APM. Data for this graph is taken from the time–lapse FRAP series provided by collaborators at McGill University (see Appendix C.1) with growth measurements calculated according to the methodology described in Appendix C.2.

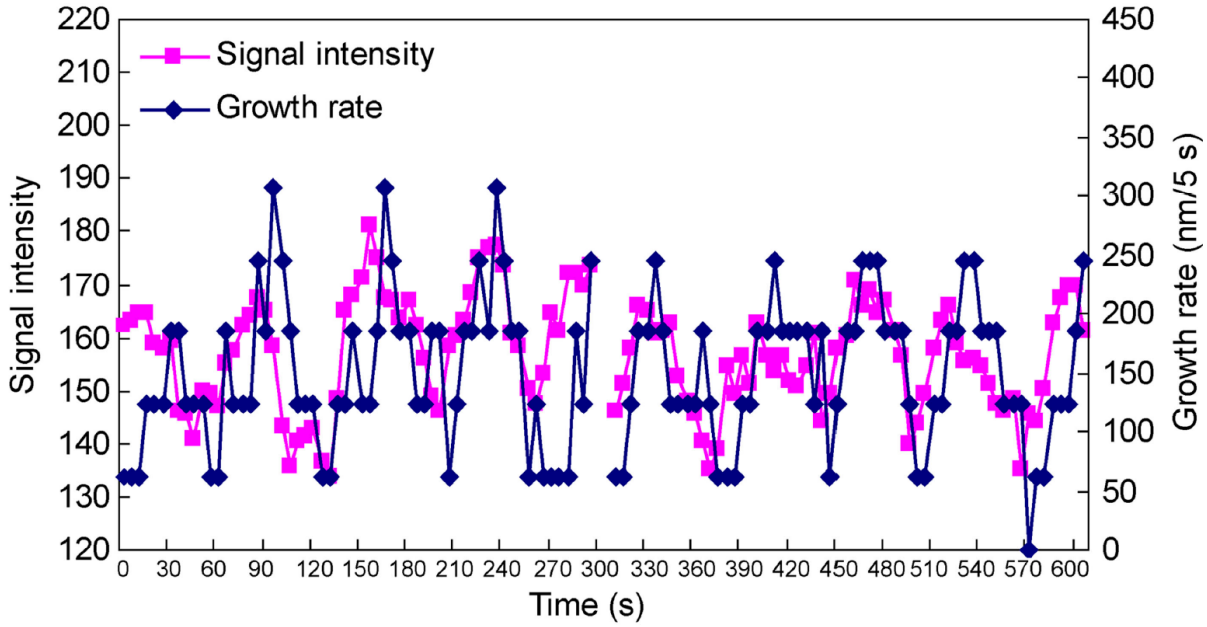

Figure 4.21: Oscillatory patterns in the growth rate and average fluorescence intensity of the apical region of tobacco pollen tubes. (Credit: Lee *et al.* [81]).

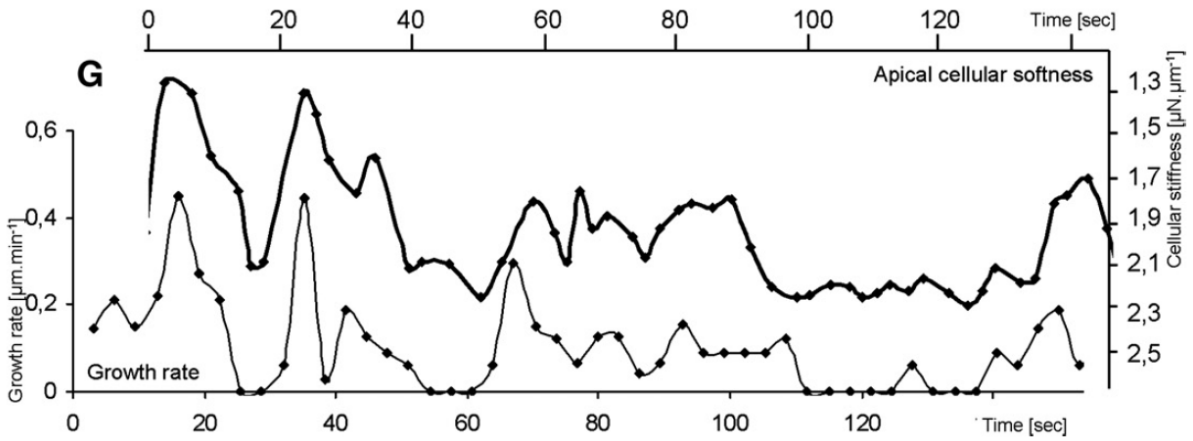

Figure 4.22: Softening/hardening of the apical cell wall precedes an increase/decrease in growth rate by $\approx 10\,\mathrm{s}$ in the *Lilium longiflorum* pollen tube, with the magnitude of the change in cellular softness affecting the magnitude of the change in growth speed. (Credit: Zerzour *et al.* [124]).

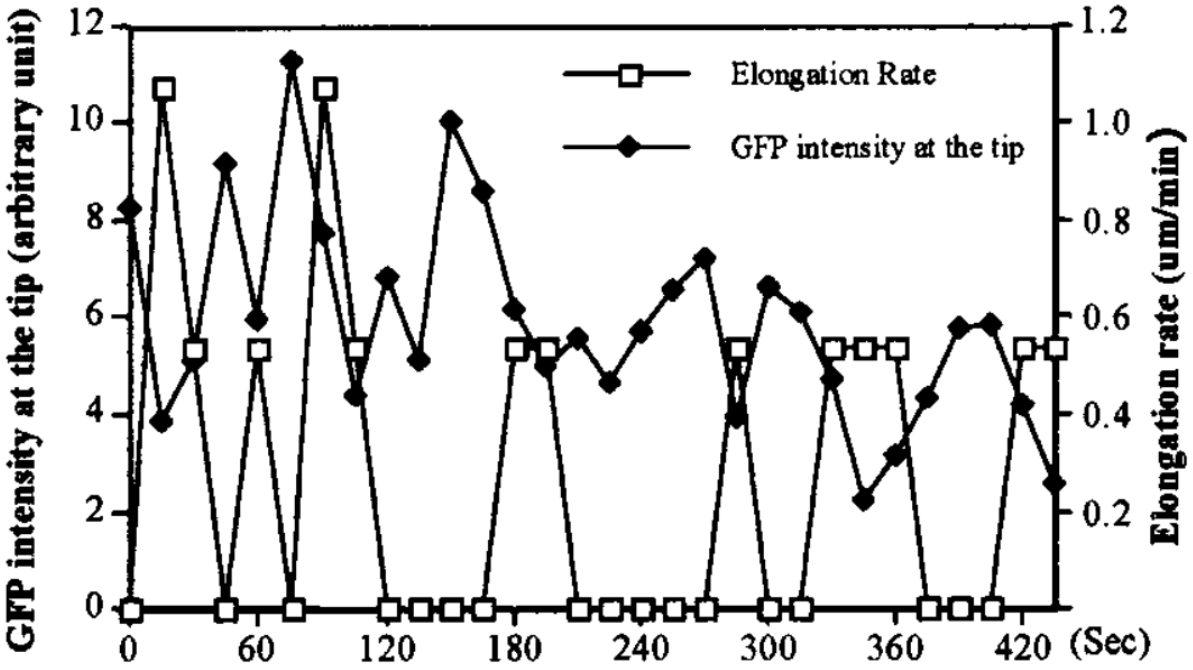

Figure 4.23: The intensity of fluorescently labelled tip–localized F–actin oscillates out of phase with elongation rate in the *Nicotiana tabacum* pollen tube. (Credit: Fu *et al.* [52]).

4.4.2 FRAP simulations

Figure 4.25 shows a simulation of FRAP experiments, conducted using Matlab, over a period of 160 s. All values for time in this section are given in dimensional terms. This simulation is run by taking the steady-state profile found by solving the governing equations for $\phi^{(x)}$ and $\phi^{(n)}$ numerically via the FVM and setting both vesicle concentrations to zero in a region corresponding to two tube radii distal to the extreme apex ($z \geq 4$). This is then used as the initial condition for the same system, which is run until a return to steady state. One adjustment is made to the system, with endocytosis being suppressed until $t \approx 14$ s. This corresponds to the approximate time by which the entire apical membrane should be replaced by labelled exocytic material, after which it is assumed that any material being endocytosed is similarly labelled. The results appear to qualitatively match biological results, with exocytic material initially accumulating in the shoulder prior to fusion with the plasma membrane, with small quantities beginning to advect and diffuse in central and rearward directions (Figures 4.25a - 4.25b). Once sufficient material has fused with the membrane, endocytosis of labelled material begins to occur (Figures 4.25c - 4.25d). Some time later, fluorescence intensity in the extreme apex begins to achieve a similar intensity to the rest of the apical hemisphere (Figure 4.25e) before the accumulation and distal flow of central material finally results in the emergence of the inverted vesicle cone (Figure 4.25f).

Notably, the time scales for this simulation are slow compared to the experimental results found using FRAP; after 160s the average vesicle density in the apical hemisphere is only 62.40% of the steady state value. This rises to 77.24% after 400s and 86.83% after 800s. This is an issue others' have faced before, notably in Bove *et al.* [12] (from which many of our parameter choices are taken) in which the theoretical turnover time of apical vesicles they calculate is considerably slower than the time needed for fluorescence recovery. We posit that this could be accounted for with the inclusion of more exocytic and endocytic events (i.e. a higher source rate) and a distal sink (representing a degradative pathway

for excess vesicle material), increasing the speed with which material is added to the system without significantly increasing the final average density at steady state.

We also note that in spite of the use of a flat endocytosis rate throughout the boundary of the apical hemisphere, the extreme apical area still contains the largest density of endocytic vesicles at steady state. This is perhaps indicative of the fact that the heightened concentration of endocytic vesicles in this small, extreme apical region can be explained by the axisymmetric geometry of the tube rather than increased localised endocytic activity.

The pattern of fluorescence recovery observed in our Matlab simulation closely resembles the experimental results of Bove *et al.* [12] (some of which can be seen in Figure 4.24) besides the sluggish speed of recovery. Unlike in our FRAP simulations in which the extreme apex eventually becomes the location of greatest vesicle accumulation, the FRAP experiments in [12] show a sustained reduction in fluorescence intensity in this area compared to the adjacent shoulder. This is likely the result of our steady growth assumption being an idealised situation not often seen in experiments; the extreme apical vesicle population doesn't exceed that of the adjacent regions in our FRAP simulations until relatively late ($t \approx 100\,\mathrm{s}$), by which point changes in growth direction or small perturbations away from steady growth would likely have altered the location of the extreme apex in an experimental setup (limiting the steady accumulation of vesicles here).

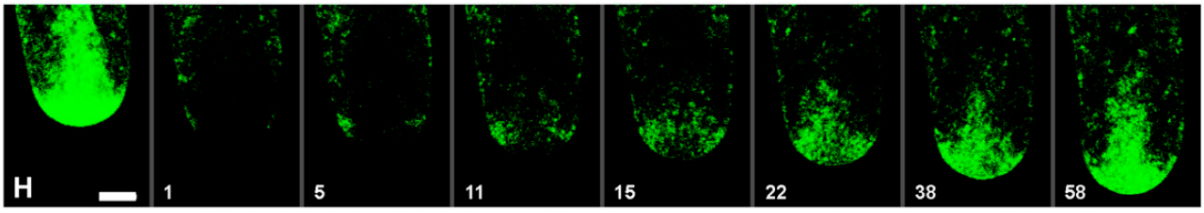

Figure 4.24: FRAP analysis of FM1-43 labelled vesicles in a growing lily pollen tube. Numbers represent time in seconds after photobleaching, with the first frame 'H' being immediately prior to bleaching. Besides the difference in recovery speed, the qualitative vesicle dynamics strongly resemble those found using our Matlab simulation. (Credit: Bove *et al.* [12]).

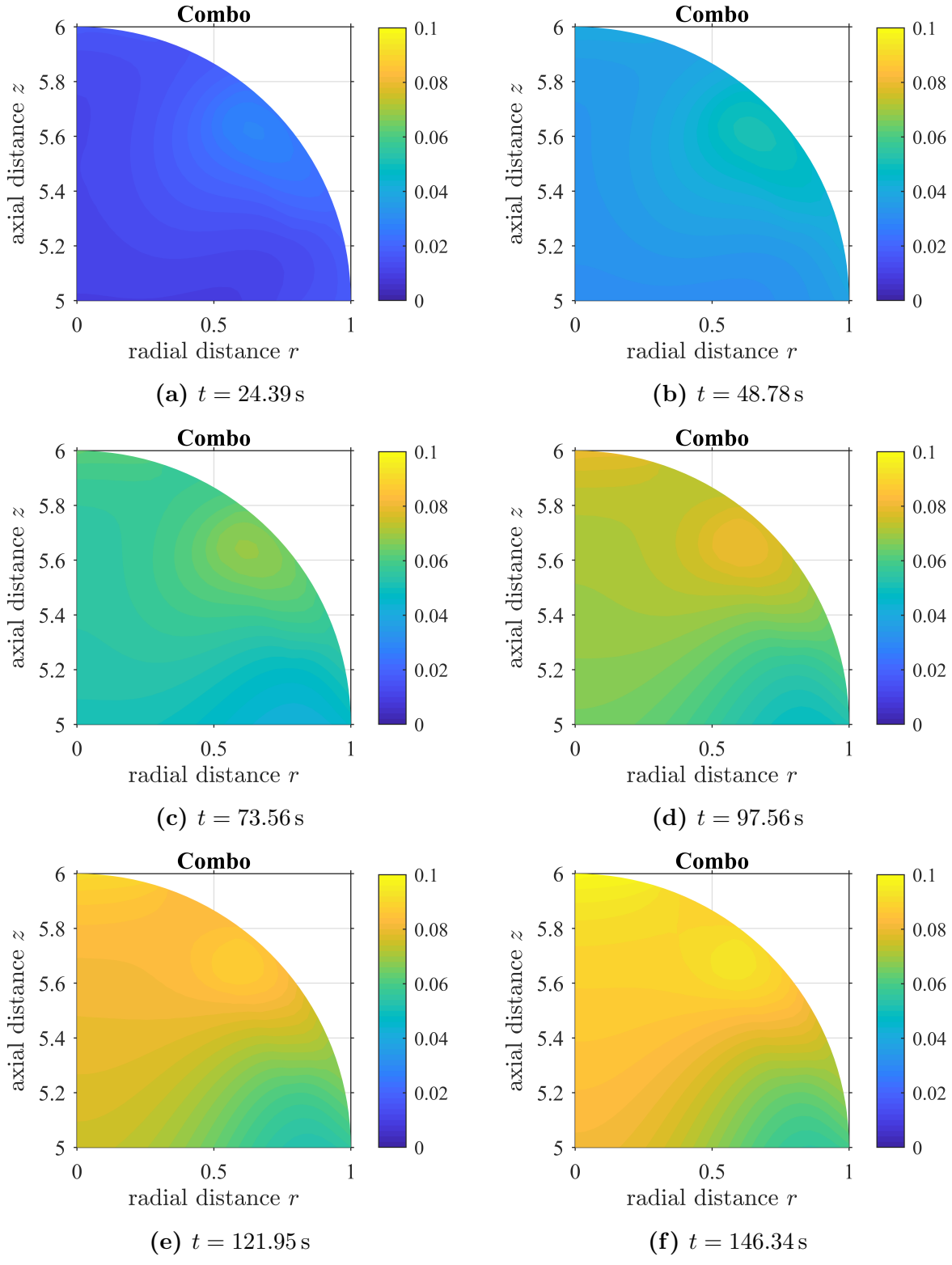

(a) $t = 24.39\,\mathrm{s}$ **(b)** $t = 48.78\,\mathrm{s}$

(c) $t = 73.56\,\mathrm{s}$ **(d)** $t = 97.56\,\mathrm{s}$

(e) $t = 121.95\,\mathrm{s}$ **(f)** $t = 146.34\,\mathrm{s}$

Figure 4.25: FRAP simulation run in Matlab. Exocytic vesicles are added to the system at a rate of 400 s^{-1}, with endocytosis of labelled material beginning at $t \approx 14$ s. The Péclet number is given by $\mathrm{Pe} = 31.46$ with endocytosis occurring at a flat rate across the entire apical hemisphere plasma membrane. Values on the colourbar are given by the product of number density of vesicles and average vesicle volume, giving an approximate volume fraction. Lengths are scaled by the tube radius R_0.

4.4.3 Exocytosis rate

We now investigate more fully the effect of varying the cytosis rate γ. Table 4.3 lists five different values of the cytosis rate, along with associated values for average vesicle densities in the apical hemisphere at steady state and exocytic vesicle uptake.

	Exocytosis rate γ ($\mu m\, s^{-1}$)				
	0.025	0.050	0.100	0.200	1.000
Exocytic vesicle density	0.0513	0.0335	0.0220	0.0154	0.0095
Endocytic vesicle density	0.0829	0.0978	0.1074	0.1129	0.1178
Combined vesicle density	0.1342	0.1313	0.1294	0.1283	0.1274
Exocytic uptake percentage	65.34	76.98	84.52	88.90	92.76

Table 4.3: Five different values of the exocytosis rate γ along with the corresponding exocytic, endocytic, and combined average vesicle densities at steady state, as well as the percentage of exocytic material added to the system at each time step that successfully fuses with the apical plasma membrane. Exocytic vesicles are added to the system at a rate of 400 s^{-1}. The Péclet number is given by Pe= 31.46 with endocytosis occurring at a flat rate across the entire apical hemisphere plasma membrane.

Following the work of Bove *et al.* [12], we calculate that with a source rate of 400 s^{-1} we require an uptake rate of 85.71% (or 6/7) for our growth rate of 0.1 $\mu m\, s^{-1}$ to be maintained. With an exocytosis rate of 0.1 $\mu m\, s^{-1}$, we are very close to achieving this. The ratio of exocytic to endocytic vesicles is also a good qualitative match to the results of Zonia and Munnik [126], who found the apical hemisphere to contain primarily endocytic vesicles with a significantly smaller exocytic population. The combined vesicle density of 0.1294 is slightly smaller than the average vesicle density of 62 μm^{-3} (corresponding to 0.1595 using our density measurement) calculated by Kroeger *et al.* [78], although this is partially a result of their measurement being confined to the inverted vesicle cone (whereas we measure across the entire apical hemisphere ($z \geq 5$) and thus also include a peripheral area of lower vesicle density).

The results from Table 4.3 also hint at a possible reason for the minimal concentration of F–actin in the extreme apex of the pollen tube. Given that $\gamma = 1\, \mu m\, s^{-1}$ would correspond to a cytosis rate equal to our vesicle velocity on actin, our results suggest

that a direct supply of exocytic vesicles to the apical plasma membrane via the peripheral actin bundle isn't necessary; so long as the bundle supplies vesicles to a sufficiently close region, a reduced cytosis rate (perhaps corresponding to a sparser, transient apical actin structure) such as that of $\gamma = 0.1\,\mu\mathrm{m\,s}^{-1}$ is 'good enough' to yield a similar total uptake of exocytic vesicles as we approach steady state. At the very least, we can clearly see that increasing the exocytosis rate yields diminishing returns with respect to the percentage uptake of exocytic vesicles. Relying on a small exocytosis rate with a sub-optimal uptake percentage and compensating with a higher source rate may be the most efficient method of growing for the tube.

4.5 Chapter summary

A novel mathematical model of vesicle distribution in the pollen tube has been developed, including both diffusive and advective effects. This is made possible through the application of the method of regularized ringlets, derived in Chapter 3, in conjunction with the FVM developed in Chapter 2.

Three questions were posed which could be answered using the method of regularized ringlets and our knowledge of the pollen tube:

- What proportion of the exocytic vesicle population undergoes actomyosin based transport on the peripheral actin bundle?
- What is the role of the central actin bundle and does actomyosin vesicle transport occur here?
- What effect does growth speed have on the cytosolic flow in the tube?

In producing a velocity profile based on the toroidal drag force induced by the actomyosin

transport of the entire exocytic vesicle population (a common assumption in the literature), we found that the resultant cytosolic flow speed was far in excess of biological observations. This drew our attention to the need to either employ a larger effective viscosity for the cytosol or reduce the proportion of the vesicle population undergoing actomyosin transport. The use of a heightened effective viscosity is supported by theory concerning the viscosity of particulate suspensions at high volume fraction [8, 64], as well as experimental evidence on the increased viscosity of F–actin solutions [88] and other examples in nature (such as the *E. coli* bacterium [74]) where a small cell size and crowded cytoplasm can lead to enlarged effective viscosities.

In prescribing internal fluid velocities only along the peripheral actin bundle based on the STICS imaging of Bove *et al.* [12], it was observed that cytosolic velocity in the centre of the tube was smaller than experimental values. This suggests that the central actin bundle must also partake in actomyosin vesicle transport, a hypothesis often assumed true but difficult to verify experimentally.

By varying the growth speed of the tube, it was shown that in the frame of reference moving with the tip growth speed has very little effect on the shape of the cytosolic flow profile. This result is based on the assumption that the rate of actin polymerization matches the growth speed of the tube, a reasonable assumption given that the location of the peripheral actin fringe with respect to the extreme apex is typically fairly consistent across multiple tubes [86].

In our FVM solution to the ADR PDEs corresponding to vesicle distribution, we were able to account for the apical pooling or 'inverted cone' of vesicles seen in experimental imaging. This requires the use of an enlarged Péclet number (again indicative of the need for a larger effective fluid viscosity) and a flat endocytosis rate across the entirety of the apical hemisphere, in contrast to prior results suggesting an endocytosis rate with a maximum at the extreme apex. Experimental FRAP evidence for the extreme apex

being the primary site of endocytosis [12] has been disputed by other studies [81, 126] as well as our own findings, and can likely be explained solely by the axisymmetric geometry of the tube.

In analyzing FRAP experiments on *Camellia japonica* pollen tubes we observed that initial fluorescence recovery across the apical membrane was largely uniform, supporting our claim of a flat rate of endocytosis. The increased fluorescence intensity in the extreme apex was identified as an oscillatory feature of the tube, preceding growth by $\approx 10\,\mathrm{s}$. Due to the close temporal proximity between this increased fluorescence and apical increases in cellular softness of the *Lilium longiflorum* tube [124], these events appear to be indicative of the deposition of new apical membrane by exocytosis. This is further supported by the increased concentration of F–actin $\approx 15\,\mathrm{s}$ to $30\,\mathrm{s}$ prior to growth in the *Nicotiana tabacum* tube [52], presumably aiding in targeted exocytosis, although some care must be taken when collating results taken from different plant species.

FRAP simulations of vesicle distributions conducted in Matlab are a good qualitative match to the experimental results of Bove *et al.* [12]. With the exception of a small difference in recovery time and an increased vesicle density in the extreme apical region (likely a result of our steady growth assumption), the distribution of vesicles in our FRAP simulations match the experimental results closely.

The value of the exocytosis rate required at the apical plasma membrane in order to provide sufficient material for growth was also considered. We found that provided exocytic vesicles are delivered close to the area of exocytosis on the apical membrane (within $1.6\,\mu\mathrm{m}$ in our simulations) a relatively small (compared to vesicle speed on actin) exocytosis rate such as $0.1\,\mu\mathrm{m\,s^{-1}}$ is sufficient to achieve a successful vesicle fusion rate of $> 80\%$ at steady state. This provides some insight into the minimal F–actin concentrations present in the apical clear zone; a combination of a constant vesicle supply from the peripheral actin fringe and vesicle uptake by short, transient actin filaments anchored to

the apical plasma membrane is all that is needed to achieve an almost 100% success rate for exocytic vesicle fusion.

In conjunction with the close similarity between the shape of apical actin organisation and the inverted vesicle cone, we cannot rule out the possibility that the maintenance of the heightened population of apical vesicles is still mediated by actin to a larger degree than our model currently accounts for. We posit that it is likely that these cytoskeletal elements do play an additional role, perhaps aiding in the cycling of exocytic vesicles that fail to fuse with the plasma membrane on their 'first pass' back into the apical pool [22] or acting as a semi–permeable vesicle barrier. Inclusion of these ideas in our model may allow for the use of a smaller effective viscosity without compromising the shape of the inverted vesicle cone, likely reducing the time it would take for our model to return to steady state during FRAP simulations (one of the key issues we currently face). Alternatively, since some of the actin microfilaments in the dense, apical fringe are known to curve inwards towards the central core of the tube [86], it could be that the similarity between the shape of apical actin and the inverted vesicle cone is simply a result of both tending to follow the shape governed by cytosolic streaming. The true situation is likely a combination of all of these factors.

CHAPTER 5

CONCLUDING REMARKS

Growth of the pollen tube involves complex interactions between many different systems, in which the chemical dynamics and hydraulics of the cytoplasm are inextricable from the mechanical properties and yielding of the cell wall. This presents a great challenge for researchers intent on modelling tube growth, usually necessitating the use of simplifying assumptions. One of the most commonly employed assumptions regards the nature of cytosolic flow in the tube, the relative importance of which has proved difficult to quantify given the challenges in modelling the flow. This thesis details our method of evaluating the cytosolic flow induced by drag from the myosin–based transport of vesicles along actin, as well as the implementation of this flow within a model for vesicle distribution throughout the tube cytoplasm.

5.1 Developing new methodology

Finding numerical solutions to the vesicle transport equations required the development of a novel finite volume method capable of application to unstructured triangular meshes

on irregular geometries (described in detail in Chapter 2). Numerical testing against known analytical solutions on simple geometries highlighted the stability and accuracy of the FVM. This method showed particular promise in finding the numerical solution for the highly–advective transport equation, where the use of a flux–limiter aided in the minimization of the absolute numerical error.

For the evaluation of Stokes flows in an axisymmetric domain, we modified the method of regularized Stokeslets [31, 33] using analytical integration around the axis of symmetry. This modification yields the method of regularized ringlets, a fast, accurate, and easy–to–implement means of evaluating highly–viscous axisymmetric flows. This method has applications beyond the pollen tube, with the examples considered in Chapter 3 encompassing mobile spheres and toroidal swimmers.

5.2 Biological findings

Detailed modelling of the pollen tube began in Chapter 4, in which our investigation into cytosolic flow using the method of regularized ringlets revealed that:

- To obtain cytosolic flow speeds in line with experimental observations or physically realistic expectations, it is necessary to employ an 'effective viscosity' for the homogeneous cytoplasm that is an order of magnitude larger than the value typically used (the viscosity of water).

- The fraction of vesicles undergoing actomyosin based transport may be smaller than the common assumption (the entire exocytic population), but this fraction is proportional to the effective viscosity of the cytoplasm.

- The central actin bundle likely participates in the actomyosin based transport of vesicles, aiding in their removal from the apical region. Forces induced by vesicle transport on the peripheral actin bundle alone cannot account for the larger central cytosolic flow speeds observed experimentally.

- Altering the growth speed of the tube appears to have very little effect on the cytosolic velocity profile relative to the growing tip, influencing magnitude but not direction of flow. This is reliant on the assumption that the rate at which actin bundles are polymerized matches the growth speed of the tube.

Evidence for these assertions is drawn from a number of sources. Calculation of the drag induced by actomyosin transport of vesicles uses the slender body theory of Johnson and Wu [73] (for the toroidal arrangement of vesicles) in addition to Stokes Drag Law [110] (for disordered vesicles), both of which have been widely employed in the modelling of microscale biological flows. The number of exocytic vesicles used in this calculation corresponds to the minimum quantity required for maintaining the thickness of the apical cell wall. The use of a heightened effective viscosity is supported by theory concerning particulate solutions of large volume fraction [8, 64], experimental observations of the heightened viscosity of F–actin solutions [88], as well as other examples in nature such as the cytoplasm of the *E. coli* bacterium [74]. That a reduced population of vesicles undergoing actomyosin transport is sufficient to induce cyclosis and direct subsequent bulk vesicle movement follows from the STICS imaging of Bove *et al.* [12], in which observed speeds of bulk vesicle motion are slower than the speed of individual organelles on actin [40, 119]. The role of the central actin bundle in the transport of vesicles is not a new result, but one that has proved difficult to verify experimentally and which our model presents new supporting evidence for. The assumption that the elongation rate of actin bundles matches the growth speed of the tube has been employed by other researchers [78, 20] and is supported by experimental observations [86].

In our subsequent modelling of cytoplasmic vesicle distribution, using both the method of regularized ringlets and the FVM for solving the ADR PDEs for vesicle transport, we were further able to show that:

- A cytosis rate of $\gamma = 0.1\,\mu\mathrm{m\,s}^{-1}$ is sufficient to ensure a large proportion of exocytic vesicles ($\approx 85\%$) successfully fuse with the apical membrane at steady state and yields a ratio of exo– to endo–cytic vesicles in close qualitative agreement with the results of Zonia and Munnik [126].

- Confining endocytosis to the extreme apex does not yield the correct apical vesicle distribution patterns. Closest agreement with experimental results was achieved using a flat rate of endocytosis over the entirety of the apical hemisphere. FRAP images provided by our collaborators at McGill University appear to show this flat endocytosis rate, as well as an oscillatory pattern of increased fluorescence in the extreme apical plasma membrane preceding growth.

- The use of a flat endocytosis rate and an enlarged Péclet number (perhaps corresponding to a heightened cytoplasmic viscosity) results in the emergence of the 'inverted vesicle cone' without the need for actin to act as a physical barrier.

- Simulations we ran of FRAP experiments are an excellent qualitative match to the results of Bove *et al.* [12] but simulated fluorescence recovery takes over twice as long as experimental observations. This difference in fluorescence recovery times is very similar to the difference in theoretical and experimental 'turnover times' of the apical vesicle pool calculated by Bove *et al.* [12].

These results again suggest the importance of employing a heightened effective viscosity for modelling the cytoplasm, particularly with regards to the emergence of inverted vesicle cone. The alternative explanation, in which apical vesicle motion is largely diffusive

and the cone is a result of actin acting as a physical barrier, does not yield the correct initial vesicle accumulation patterns in FRAP simulations. This does not preclude the possibility of the existence of the actin barrier, but the evidence for the use of a heightened viscosity appears strong. In fact, we posit that this heightened viscosity is itself at least partially responsible for the shape of the actin fringe described by Kroeger *et al.* [78] although producing direct evidence for this is confined to future work. If this heightened cytoplasmic viscosity is to be accepted, the flat endocytosis rate across the apical hemisphere must surely follow; steady state vesicle distributions using a heightened viscosity with endocytosis confined to the extreme apex resulted in wildly irregular results.

5.3 Future work

We conclude with a brief discussion of future avenues of research following our progress thus far, including some preliminary results.

5.3.1 Modelling other pollen tube species

The majority of the modelling conducted in this thesis has been applied to pollen tubes belonging to the lily species, often used in experimental studies as a result of their large radius, fast growth rate, and relative resilience. The tobacco plant is another species frequently used in pollen tube studies, owing to their large vesicle radius (beneficial in imaging). Here, we repeat some of the calculations we have conducted thus far using parameter values for tobacco pollen tubes to ascertain the applicability of our results to multiple pollen tube species.

Using the parameter values from Table 5.1, we can repeat the calculation of Bove *et al.*

Parameter	Value	Reference
Inner radius of pollen tube	$4\,\mu m$	[89, 103]
Outer radius of pollen tube	$4.1\,\mu m$	[89, 103]
Growth rate	$0.1\,\mu m\,s^{-1}$	[89, 125]
Average exocytic vesicle radius	$0.3\,\mu m$	[126]
Average endocytic vesicle radius	$0.15\,\mu m$	[126]

Table 5.1: Estimates for values of various parameters related to tobacco pollen tube growth.

[12] to find the ratio of endocytic to exocytic events needed to maintain a constant cell wall volume and membrane area is $\approx 8/135$ (far below the value of 5/6 observed in lily tubes). This is in stark contrast to the experimental results of Zonia and Munnik [126] who found significant endocytic activity taking place at the apical plasma membrane (as well as in more distal locations), resulting in an apical vesicle population that is largely endocytic in nature. How can we explain this disparity?

One possible explanation is the need to transport cellular material other than just cell wall polysaccharides towards the apex. As the pollen tube elongates, stationary points on the plasma membrane (and associated proteins) appear to move rearward relative to the tip. Distal endocytosis could therefore be used to recycle large actin-binding proteins, essential to the de novo formation of actin filaments [41], forwards towards the subapical cell cortex from which the peripheral actin fringe originates. We posit that in order for local plasma membrane density to be maintained, this process would necessitate both the addition of membrane back into the distal wall (via distal exocytosis) as well as release from the apical membrane. Evidence supporting this theory can be seen in Figure 4.16, where distal endocytosis (the addition of red-labelled material to the cytoplasm) appears to be followed by exocytosis shortly after (yellowing of the plasma membrane). The necessity of this additional exocytic and endocytic activity could help explain the difference between the theoretical and experimental turnover times of the apical vesicle pool found by Bove *et al.* [12], with the need to recycle proteins throughout the membrane and maintain local membrane density resulting in far more fusion activity than their theoretical calculation suggests.

We further consider how a change in parameter values from lily to tobacco pollen tubes may affect the steady state distribution of vesicles. Recall the nondimensional advection–diffusion–reaction equations for exocytic and endocytic vesicle populations:

$$\frac{\partial \phi^{(x)^*}}{\partial t^*} = \frac{1}{\mathrm{Pe}^{(x)}} \nabla^{*2} \phi^{(x)^*} - \mathbf{u}^* \cdot \nabla^* \phi^{(x)^*} + \sigma^*, \tag{5.3.1}$$

$$\frac{\partial \phi^{(n)^*}}{\partial t^*} = \frac{1}{\mathrm{Pe}^{(n)}} \nabla^{*2} \phi^{(n)^*} - \mathbf{u}^* \cdot \nabla^* \phi^{(n)^*}. \tag{5.3.2}$$

Due to the linearity of these PDEs, the source rate σ^* influences the magnitude of the final steady-state populations but not their shape (assuming the source location remains unchanged). Since the apical endocytic population is known to dominate the exocytic population, the shape of the inverted vesicle cone is largely a result of the endocytic population only. This leaves just two terms that could influence the shape of final vesicle distribution: the endocytic Péclet number $\mathrm{Pe}^{(n)}$ and the advective flow $\mathbf{u}^*$. From the results of de Win in Chapter 3 of 'Quantitative analysis of organelle movements in pollen tubes' [40], it is known that the magnitude of the average cytosolic flow in tobacco tubes is approximately the same as for lily pollen tubes ($\approx 0.5\,\mu\mathrm{m\,s}^{-1}$). Since this flow is induced by vesicle movement along peripheral and central actin bundles, the organisation of which is known to be similar between lily and tobacco tubes [86], we thus deduce that any difference in the dimensionless advective term $\mathbf{u}^*$ between the two species will likely be very minor. The endocytic Péclet number $\mathrm{Pe}^{(n)}$ is found by taking the product of the pollen tube radius and the average vesicle velocity on actin divided by the diffusivity of endocytic vesicles. This again is almost entirely unchanged between species, a result of the pollen tube radius and diffusivity of endocytic vesicles (proportional to the inverse of the vesicle radius) in tobacco tubes both being approximately half that of lily tubes. Preservation of the Péclet number in the pollen tube in both plant species helps explain the striking similarity between the shape of apical vesicle pooling in each.

Further investigation into the possible similarity of the Péclet number between multiple pollen tube species could yield vital information on the cytoplasmic conditions necessary for pollen tube growth. Unfortunately, accurate values for relevant parameters are typically difficult to acquire for any given species, hence our need to sometimes conflate values from multiple sources.

5.3.2 The response of actin filaments to cytosolic flow

A more challenging extension of our work would involve the modelling of actin filaments in response to the cytosolic flow. Close similarity between the direction / streamlines of the flow and the shape of the actin profile derived by Kroeger *et al.* [78] can be observed in Figure 5.1. The orientation of actin filaments within this profile is derived such that local elastic stress between adjacent filaments is minimized but does not consider shear stress incurred by the cytosolic flow. This could become large if the fluid viscosity is similarly large, suggesting that filaments at the leading edge of the profile could orient themselves parallel to the flow. If the barbed end of one such filament was attached to the cortical plasma membrane (where it hypothesised that the formation of new actin filaments takes place), this could account for the cycling of vesicles from the tail end of the inverted vesicle cone towards the peripheral shoulder as has been observed in experimental studies [12, 22]. The method of regularized ringlets provides the framework within which this problem could be studied further.

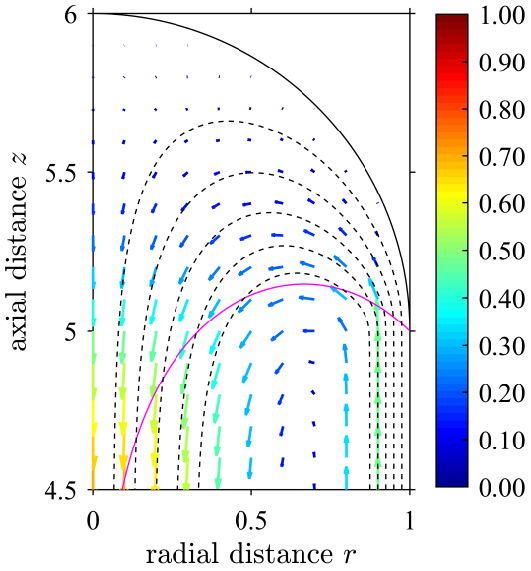

Figure 5.1: Close similarities exist between the (dashed) streamlines of cytosolic flow and the (solid magenta) actin profile of Kroeger *et al.* [78], formulated such that elastic stress between adjacent actin filaments is minimized and the profile advances at a steady rate.

5.3.3 Coupling growth speed and vesicle deposition for non–steady growth

In its current incarnation, our model of the vesicle transport problem assumes the tube grows steadily (with the growth speed of the tube being incorporated within apical boundary conditions and used to define the moving coordinate system). This is generally sufficient for studying steady–state vesicle distributions but does not capture the complexities of non–steady growth. A more refined model would be capable of coupling the rate of vesicle deposition to the growth speed of the tube (under the assumption that the deposition of new material always precedes growth), such that it would be possible to consider cases of non–steady growth. Increased fluorescence intensity in the extreme apex of FRAP imaging preceding growth suggests that employing a pulsatile exocytic source rate in this refined model could lead to cases of oscillatory growth, a phenomenon we have not been able to model thus far. The difficulty in implementing this coupled model lies in the need to frequently recalculate the cytosolic flow based on the changing growth speed of the tube. Provided the acceleration/deceleration in the growth rate are sufficiently small, the steady Stokes Equations could continue to be used for this purpose. Here, the rapid

nature of the method of regularized ringlets would prove to be of a huge benefit to the modelling procedure.

5.3.4 Bending of the tube and asymmetric models of growth

Our ultimate ambition is to be able consider asymmetric deposition of wall material and the bending of the tube on its path through the pistil. In order to do this, it seems inevitable that we will have to remove the assumption of axisymmetry and move into a fully 3D modelling system. Generalising our finite volume method for use in 3D would be somewhat challenging, but the development of the method was conducted in such a way that the 2D and 3D cases are conceptually very similar. Modelling of the cytosolic flow can be achieved using the standard method of regularized Stokeslets as outlined by Cortez *et al.* [33], with our method of regularized ringlets no longer applicable. A finite element model of the tube allowing for the possibility of asymmetric growth has been developed by Fayant *et al.* [49], although axisymmetric conditions are applied throughout their work. It is our hope that the results put forth in this thesis will be of significant use in future models capable of coupling vesicle transport and material deposition to asymmetric growth of the tube.

Appendices

CHAPTER 2 APPENDICES

A.1 Implementation of the finite volume method for the advection - diffusion equation with additional boundary conditions and reaction terms

Consider a domain D in cylindrical (r, z) coordinates in which axisymmetry about the z axis is assumed. Let this domain encompass

- a mass source $\omega(\mathbf{x})$ located in the region D_{source},
- a volumetric sink $\chi(\mathbf{x})$ located in the region D_{sink},
- a symmetry boundary Ω_{sym} and an impermeable boundary Ω_{imp} on which there is zero normal flux,
- an advective boundary Ω_{bas} on which only negative normal advective flux is considered (i.e. no diffusive flux, no positive normal advective flux),
- a flux boundary Ω_{out} on which there is prescribed normal flux $(\nabla\phi)\cdot\hat{\mathbf{n}} = -\frac{\gamma}{\alpha}\phi$ for some diffusive rate γ,
- a flux boundary Ω_{in} on which there is prescribed normal flux $(\nabla\phi)\cdot\hat{\mathbf{n}} = \frac{\zeta}{\alpha}\frac{Q_{\text{out}}}{A_{\text{in}}}$. Here, $0 \leq \zeta \leq 1$ respresents a recycling rate, $Q_{\text{out}} = \gamma\int_{\Omega_{\text{out}}}\phi\, dS$ is the total instantaneous uptake of ϕ through the Ω_{out} boundary and A_{in} is the area of the surface Ω_{in}.

Let the FVM mesh be comprised of N vertices, so that discretization produces N distinct

control volumes denoted $\{V_i\}_{i=1}^{N}$. Each V_k is enclosed by a surface S_i, which can be decomposed into the union of surfaces:

- S_i^f for any fluid-fluid surface,
- S_i^{in} for any surface belonging to the Ω_{in} boundary,
- S_i^{out} for any surface belonging to the Ω_{out} boundary,
- S_i^{a} for any surface belonging to the Ω_{bas} boundary,
- S_i^0 for any surface belonging to $\Omega_{\text{imp}} \cup \Omega_{\text{sym}}$.

Each of these surfaces can be further decomposed into the union of sets of edges e_i, such that S_i^f is the union of the set e_i^f and so forth. In the FVM, integration over the surface S_i is approximated via summation over the edges e_i. In these summations, we let r_M denote the r co-ordinate of the midpoint of the current edge, with Δr and Δz denoting the change in r and z co-ordinates over the length of the edge respectively.

A.1.1 Base case: fluid bulk

Consider a control volume V_i containing no source/sink and not adjacent to any boundary of our larger domain (i.e. $S_i \equiv S_i^f, e_i \equiv e_i^f$). Integration of the ADR equation over this volume yields

$$\int_{V_k} \frac{\partial \phi}{\partial t}\, dV = \int_{V_k} \nabla \cdot (\alpha \nabla \phi - \mathbf{u}\phi)\, dV \tag{A.1.1}$$

$$= \oint_{S_k} (\alpha \nabla \phi - \mathbf{u}\phi) \cdot \hat{\mathbf{n}}\, dS \tag{A.1.2}$$

Using the FVM discretisation, this becomes

$$\Delta V\left(\frac{\phi_i^{k+1}-\phi_i^k}{\Delta t}\right)=\pi\sum_{e_i^f} r_M\Bigg[\alpha\left(\left(\frac{\partial\phi^{k+1}}{\partial r}+\frac{\partial\phi^k}{\partial r}\right)\Delta z-\left(\frac{\partial\phi^{k+1}}{\partial z}+\frac{\partial\phi^k}{\partial z}\right)\Delta r\right) \tag{A.1.3}$$

$$-\left(u_r(\phi^{k+1}+\phi^k)\Delta z-u_z(\phi^{k+1}+\phi^k)\Delta r\right)\Bigg] \tag{A.1.4}$$

All $\phi, \nabla\phi$, and $\mathbf{u}$ terms on the right hand side of this equation are understood to be evaluated at the midpoint of the current edge (using interpolation of values from vertices in the mesh). For brevity, we define

$$\Upsilon^f := r_M\Bigg[\alpha\left(\left(\frac{\partial\phi^{k+1}}{\partial r}+\frac{\partial\phi^k}{\partial r}\right)\Delta z-\left(\frac{\partial\phi^{k+1}}{\partial z}+\frac{\partial\phi^k}{\partial z}\right)\Delta r\right)-\left(u_r(\phi^{k+1}+\phi^k)\Delta z-u_z(\phi^{k+1}+\phi^k)\Delta r\right)\Bigg], \tag{A.1.5}$$

so that the discretisation may be more succinctly written as

$$\Delta V\left(\frac{\phi_i^{k+1}-\phi_i^k}{\Delta t}\right)=\pi\sum_{e_i^f}\Upsilon^f. \tag{A.1.6}$$

A fluid-fluid surface S_i^f is present in every one of the CVs V_i, so the summation above will always be used.

A.1.2 Inclusion of sources and sinks

If the control volume V_i contains a nonzero source term ω, discretization of the governing equations must be adjusted accordingly

$$\int_{V_i} \frac{\partial \phi}{\partial t}\, dV = \int_{V_i} \nabla \cdot (\alpha \nabla \phi - \mathbf{u}\phi) + \omega \, dV \tag{A.1.7}$$

$$\Rightarrow \int_{V_i} \left(\frac{\partial \phi}{\partial t} - \omega \right) dV = \oint_{S_i} (\alpha \nabla \phi - \mathbf{u}\phi) \cdot \hat{\mathbf{n}} \, dS \tag{A.1.8}$$

$$\Rightarrow \Delta V \left(\frac{\phi_i^{k+1} - \phi_i^k}{\Delta t} - \omega \right) = \pi \sum_{e_i^f} \Upsilon^f \tag{A.1.9}$$

In the presence of a volumetric sink χ

$$\int_{V_i} \frac{\partial \phi}{\partial t}\, dV = \int_{V_i} \nabla \cdot (\alpha \nabla \phi - \mathbf{u}\phi) - \chi\phi \, dV \tag{A.1.10}$$

$$\Rightarrow \int_{V_i} \left(\frac{\partial \phi}{\partial t} + \chi\phi \right) dV = \oint_{S_i} (\alpha \nabla \phi - \mathbf{u}\phi) \cdot \hat{\mathbf{n}} \, dS \tag{A.1.11}$$

$$\Rightarrow \Delta V \left(\frac{\phi_i^{k+1} - \phi_i^k}{\Delta t} + \frac{\chi}{2}(\phi_i^{k+1} + \phi_i^k) \right) = \pi \sum_{e_i^f} \Upsilon^f \tag{A.1.12}$$

A.1.3 Inclusion of exocytosis / endocytosis

When part of the surface S_i contains a section of the boundary Ω_{out}, through there is prescribed flux $(\nabla\phi) \cdot \hat{\mathbf{n}} = -\frac{\gamma}{\alpha}\phi$, the FVM discretization deals with the different surface

types separately

$$\int_{V_i} \frac{\partial \phi}{\partial t}\, dV = \oint_{S_i} (\alpha \nabla \phi - \mathbf{u}\phi) \cdot \hat{\mathbf{n}}\, dS \tag{A.1.13}$$

$$= \int_{S_i^f} (\alpha \nabla \phi - \mathbf{u}\phi) \cdot \hat{\mathbf{n}}\, dS - \int_{S_i^{\text{out}}} \gamma \phi\, dS \tag{A.1.14}$$

$$\Rightarrow \Delta V \left(\frac{\phi_i^{k+1} - \phi_i^k}{\Delta t} \right) = \pi \left(\sum_{e_i^f} \Upsilon^f - \gamma \sum_{e_i^{\text{out}}} r_M (\phi^{k+1} + \phi^k) \sqrt{(\Delta z)^2 + (\Delta r)^2} \right) \tag{A.1.15}$$

Similarly if S_i contains a section of Ω_{in}, through which there is prescribed flux $(\nabla \phi) \cdot \hat{\mathbf{n}} = \frac{\zeta}{\alpha} \frac{Q_{\text{out}}}{A_{\text{in}}}$, it follows that

$$\int_{V_i} \frac{\partial \phi}{\partial t}\, dV = \oint_{S_i} (\alpha \nabla \phi - \mathbf{u}\phi) \cdot \hat{\mathbf{n}}\, dS \tag{A.1.16}$$

$$= \int_{S_i^f} (\alpha \nabla \phi - \mathbf{u}\phi) \cdot \hat{\mathbf{n}}\, dS + \frac{\zeta}{\alpha} \frac{Q_{\text{out}}}{A_{\text{in}}} \int_{S_i^{\text{in}}} dS \tag{A.1.17}$$

$$\Rightarrow \Delta V \left(\frac{\phi_i^{k+1} - \phi_i^k}{\Delta t} \right) = \pi \left(\sum_{e_i^f} \Upsilon^f + \frac{\zeta}{\alpha} \frac{Q_{\text{out}}}{A_{\text{in}}} \sum_{e_i^{\text{in}}} r_M \sqrt{(\Delta z)^2 + (\Delta r)^2} \right) \tag{A.1.18}$$

where Q_{out} is given by

$$Q_{\text{out}} = 2\pi\gamma \sum_{i=1}^{N} \sum_{e_i^{\text{out}}} r_M (\phi^{k+1} + \phi^k) \sqrt{(\Delta z)^2 + (\Delta r)^2}. \tag{A.1.19}$$

CHAPTER 3 APPENDICES

B.1 Regularized Stokeslets in cylindrical coordinates for ringlet evaluation

The expressions $S_{ij}^{\varepsilon}(\mathbf{x}_0, \mathbf{x}_n)$ for fluid point $\mathbf{x}_0 = (r_0, 0, z_0)$ and ring point $\mathbf{x}_n = (r_n, \theta, z_n)$ in cylindrical coordinates are given below

$$
\begin{aligned}
S_{11}^{\varepsilon} &= \frac{1}{\hat{r}_{\varepsilon}^3}\left[2(r_0 - r_n\cos\theta)^2 + (r_n\sin\theta)^2 + (z_0 - z_n)^2 + 2\varepsilon^2\right], \\
S_{12}^{\varepsilon} &= \frac{1}{\hat{r}_{\varepsilon}^3}\left[-(r_0 - r_n\cos\theta)(r_n\sin\theta)\right], \\
S_{13}^{\varepsilon} &= \frac{1}{\hat{r}_{\varepsilon}^3}\left[(r_0 - r_n\cos\theta)(z_0 - z_n)\right] \\
S_{21}^{\varepsilon} &= \frac{1}{\hat{r}_{\varepsilon}^3}\left[-(r_0 - r_n\cos\theta)(r_n\sin\theta)\right], \\
S_{22}^{\varepsilon} &= \frac{1}{\hat{r}_{\varepsilon}^3}\left[(r_0 - r_n\cos\theta)^2 + 2(r_n\sin\theta)^2 + (z_0 - z_n)^2 + 2\varepsilon^2\right], \\
S_{23}^{\varepsilon} &= \frac{1}{\hat{r}_{\varepsilon}^3}\left[-(r_n\sin\theta)(z_0 - z_n)\right], \\
S_{31}^{\varepsilon} &= \frac{1}{\hat{r}_{\varepsilon}^3}\left[(r_0 - r_n\cos\theta)(z_0 - z_n)\right] \\
S_{32}^{\varepsilon} &= \frac{1}{\hat{r}_{\varepsilon}^3}\left[-(r_n\sin\theta)(z_0 - z_n)\right], \\
S_{33}^{\varepsilon} &= \frac{1}{\hat{r}_{\varepsilon}^3}\left[(r_0 - r_n\cos\theta)^2 + (r_n\sin\theta)^2 + 2(z_0 - z_n)^2 + 2\varepsilon^2\right],
\end{aligned}
\tag{B.1.1}
$$

in which $\hat{r}_{\varepsilon} = ((r_0 - r_n\cos\theta)^2 + (r_n\sin\theta)^2 + (z_0 - z_n)^2 + \varepsilon^2)^{1/2}$.

B.2 Evaluating the behaviour of $R^{\varepsilon}_{\alpha\beta}$ as $r_n, r_0 \to 0$

To understand the behaviour of $R^{\varepsilon}_{\alpha\beta}$ as $r_n, r_0 \to 0$, it is easiest to consider $R^{\varepsilon}_{\alpha\beta}$ in the form

$$R^{\varepsilon}_{rr}(\mathbf{x}_0, \mathbf{x}_n) = r_n(-r_0 r_n I_0 + (2\tau - (z_0 - z_n)^2)I_1 - 3r_0 r_n I_2), \tag{B.2.1}$$

$$R^{\varepsilon}_{rz}(\mathbf{x}_0, \mathbf{x}_n) = r_n(z_0 - z_n)(r_0 I_0 - r_n I_1), \tag{B.2.2}$$

$$R^{\varepsilon}_{zr}(\mathbf{x}_0, \mathbf{x}_n) = r_n(z_0 - z_n)(-r_n I_0 + r_0 I_1), \tag{B.2.3}$$

$$R^{\varepsilon}_{zz}(\mathbf{x}_0, \mathbf{x}_n) = r_n((\tau + (z_0 - z_n)^2 + \varepsilon^2)I_0 - 2r_0 r_n I_1), \tag{B.2.4}$$

$$R^{\varepsilon}_{\theta\theta}(\mathbf{x}_0, \mathbf{x}_n) = r_n(r_0 r_n I_0 + (\tau + \varepsilon^2)I_1 - 3r_0 r_n I_2), \tag{B.2.5}$$

in which

$$I_0 = \frac{4k^3}{(4r_0 r_n)^{3/2}}\left(\frac{1}{1-k^2}E\right), \tag{B.2.6}$$

$$I_1 = \frac{4k^3}{(4r_0 r_n)^{3/2}}\left(\frac{2-k^2}{k^2(1-k^2)}E - \frac{2}{k^2}F\right), \tag{B.2.7}$$

$$I_2 = \frac{4k^3}{(4r_0 r_n)^{3/2}}\left(\frac{k^4 - 8k^2 + 8}{k^4(1-k^2)}E - \frac{4(2-k^2)}{k^4}F\right), \tag{B.2.8}$$

with $\tau = r_0^2 + r_n^2 + (z_0 - z_n)^2 + \varepsilon^2$ and $k^2 := 4r_0 r_n/(\tau + 2r_0 r_n)$. Evaluating $\lim_{k\to 0} I_n$ for each $n \in \{0, 1, 2\}$ and substituting back into Equations (B.2.1) – (B.2.5) yields the desired results for $\lim_{r_n \to 0} R^{\varepsilon}_{\alpha\beta}$ and $\lim_{r_0 \to 0} R^{\varepsilon}_{\alpha\beta}$.

The first step in evaluating these limits is to observe that from the definition of k, it follows that $k \to 0$ as either $r_0 \to 0$ or $r_n \to 0$ (or both). Further, noting that

$$\lim_{k\to 0} \frac{4k^3}{(4r_0 r_n)^{3/2}} = \lim_{k\to 0} \frac{4\left(\frac{4r_0 r_n}{\tau + 2r_0 r_n}\right)^{3/2}}{(4r_0 r_n)^{3/2}} = \frac{4}{\tau^{3/2}}, \tag{B.2.9}$$

in which the value of τ as $k \to 0$ depends on whether $r_0 \to 0$ or $r_n \to 0$ (or both), it is observed that I_0, I_1, I_2 contain common finite term outside of the larger brackets.

Evaluating the remaining parts of I_0, I_1, I_2 in the limit as $k \to 0$ requires employing the power series expansions of the complete elliptic integrals [59], such that

$$F(k) = \frac{\pi}{2}\left(1 + \frac{1}{4}k^2 + \frac{9}{64}k^4 + \dots\right), \tag{B.2.10}$$

$$E(k) = \frac{\pi}{2}\left(1 - \frac{1}{4}k^2 - \frac{9}{64}k^4 + \dots\right). \tag{B.2.11}$$

Letting $E \sim \pi/2$ it follows that

$$\lim_{k\to 0}\left(\frac{1}{1-k^2}E\right) = \frac{\pi}{2}. \tag{B.2.12}$$

Similarly, letting $E \sim \frac{\pi}{2}(1 - \frac{1}{4}k^2)$ and $F \sim \frac{\pi}{2}(1 + \frac{1}{4}k^2)$ it can be found that

$$\lim_{k\to 0}\left(\frac{2-k^2}{k^2(1-k^2)}E - \frac{2}{k^2}F\right) = 0. \tag{B.2.13}$$

Finally, using $E \sim \frac{\pi}{2}(1 - \frac{1}{4}k^2 - \frac{9}{64}k^4)$ and $F \sim \frac{\pi}{2}(1 + \frac{1}{4}k^2 + \frac{9}{64}k^4)$ yields

$$\lim_{k\to 0}\left(\frac{k^4 - 8k^2 + 8}{k^4(1-k^2)}E - \frac{4(2-k^2)}{k^4}F\right) = -\frac{\pi}{8}. \tag{B.2.14}$$

Compiling all of the above gives

$$\begin{aligned} &I_0 \to 2\pi/\tau^{3/2} \\ &I_1 \to 0 \qquad\qquad \text{as } k \to 0, \\ &I_2 \to -\pi/2\tau^{3/2} \end{aligned} \tag{B.2.15}$$

which upon substitution into the expressions for $R^{\varepsilon}_{\alpha\beta}$ yields

$$\lim_{r_n\to 0} R^{\varepsilon}_{\alpha\beta} \equiv 0, \tag{B.2.16}$$

$$\lim_{r_0\to 0} R^{\varepsilon}_{rr} = \lim_{r_0\to 0} R^{\varepsilon}_{rz} = \lim_{r_0\to 0} R^{\varepsilon}_{\theta\theta} = 0, \tag{B.2.17}$$

$$\lim_{r_0\to 0} R^{\varepsilon}_{zr} = -2\pi r_n^2(z_0 - z_n)/\tau^{3/2}, \tag{B.2.18}$$

$$\lim_{r_0\to 0} R^{\varepsilon}_{zz} = 2\pi r_n((\tau + (z_0 - z_n)^2 + \varepsilon^2))/\tau^{3/2}. \tag{B.2.19}$$

B.3 Evaluating the double layer potential

Recall the form of the double layer potential

$$(\mathrm{DLP})_i = \frac{1}{8\pi}\int_{\partial D} u_j(\mathbf{x}) T^{\varepsilon}_{ijk}(\mathbf{x}_0, \mathbf{x}) n_k(\mathbf{x})\, dS(\mathbf{x}), \tag{B.3.1}$$

in which the stress tensor T^{ε}_{ijk} is given by

$$\begin{aligned} T^{\varepsilon}_{ijk}(\mathbf{x}_0, \mathbf{x}) = -6\frac{(x_{0,i} - x_i)(x_{0,j} - x_j)(x_{0,k} - x_k)}{(|\mathbf{x}_0 - \mathbf{x}|^2 + \varepsilon^2)^{5/2}} \\ - 3\varepsilon^2 \frac{(x_{0,i} - x_i)\delta_{jk} + (x_{0,j} - x_j)\delta_{ik} + (x_{0,k} - x_k)\delta_{ij}}{(|\mathbf{x}_0 - \mathbf{x}|^2 + \varepsilon^2)^{5/2}}. \end{aligned} \tag{B.3.2}$$

As with the Stokeslet S^{ε}_{ij} in the SLP, the stress tensor T^{ε}_{ijk} can be expressed in cylindrical coordinates via

$$(x_{0,1} - x_1) = r_0 - r_n\cos\theta, \tag{B.3.3}$$

$$(x_{0,2} - x_2) = -r_n\sin\theta, \tag{B.3.4}$$

$$(x_{0,3} - x_3) = z_0 - z_n, \tag{B.3.5}$$

$$|\mathbf{x}_0 - \mathbf{x}|^2 = (r_0 - r_n\cos\theta)^2 + (r_n\sin\theta)^2 + (z_0 - z_n)^2. \tag{B.3.6}$$

and the Cartesian and cylindrical forms of the flow vector $\mathbf{u}$ are related via $u_j = \Theta_{j\beta} u_\beta$ in which

$$\Theta(\theta) = \begin{pmatrix} \cos\theta & -\sin\theta & 0 \\ \sin\theta & \cos\theta & 0 \\ 0 & 0 & 1 \end{pmatrix}, \tag{B.3.7}$$

Recalling that the azimuthal component of the normal to an axisymmetric body is zero, the transformation from polar to Cartesian coordinates is $n_i = \Psi_{i\alpha} n_\alpha$ where

$$\Psi(\theta) = \begin{pmatrix} \cos\theta & 0 & 0 \\ \sin\theta & 0 & 0 \\ 0 & 0 & 1 \end{pmatrix}. \tag{B.3.8}$$

Let

$$Q_{\alpha\beta\gamma} = r\delta_{\alpha i} \int_0^{2\pi} \Theta_{j\beta} T^{\varepsilon}_{ijk} \Psi_{k\gamma} \, d\theta, \tag{B.3.9}$$

such that

$$(\mathrm{DLP})_\alpha = \frac{1}{8\pi} \int_0^L Q_{\alpha\beta\gamma} u_\beta n_\gamma \, ds. \tag{B.3.10}$$

For fixed α, nonzero elements of $Q_{\alpha\beta\gamma}$ are given by

$$\begin{aligned}
Q_{\alpha 11} &= r_n \delta_{\alpha i} \textstyle\int_0^{2\pi} \left(T^{\varepsilon}_{i11} \cos^2\theta + T^{\varepsilon}_{i12} \sin\theta\cos\theta + T^{\varepsilon}_{i21} \sin\theta\cos\theta + T^{\varepsilon}_{i22} \sin^2\theta \right) d\theta, \\
Q_{\alpha 13} &= r_n \delta_{\alpha i} \textstyle\int_0^{2\pi} \left(T^{\varepsilon}_{i13} \cos\theta + T^{\varepsilon}_{i23} \sin\theta \right) d\theta, \\
Q_{\alpha 21} &= r_n \delta_{\alpha i} \textstyle\int_0^{2\pi} \left(-T^{\varepsilon}_{i11} \sin\theta\cos\theta - T^{\varepsilon}_{i12} \sin^2\theta + T^{\varepsilon}_{i21} \cos^2\theta + T^{\varepsilon}_{i22} \sin\theta\cos\theta \right) d\theta, \\
Q_{\alpha 23} &= r_n \delta_{\alpha i} \textstyle\int_0^{2\pi} \left(-T^{\varepsilon}_{i13} \sin\theta + T^{\varepsilon}_{i23} \cos\theta \right) d\theta, \\
Q_{\alpha 31} &= r_n \delta_{\alpha i} \textstyle\int_0^{2\pi} \left(T^{\varepsilon}_{i31} \cos\theta + T^{\varepsilon}_{i32} \sin\theta \right) d\theta, \\
Q_{\alpha 33} &= r_n \delta_{\alpha i} \textstyle\int_0^{2\pi} \left(T^{\varepsilon}_{i33} \right) d\theta.
\end{aligned} \tag{B.3.11}$$

such that each $Q_{\alpha\beta\gamma}$ is a linear sum of terms of the form

$$\langle\!\langle \bullet \rangle\!\rangle_{ijk} := r_n \int_0^{2\pi} T^{\varepsilon}_{ijk} \bullet \, d\theta. \tag{B.3.12}$$

Letting

$$J_{m,n} := r_n \int_0^{2\pi} \frac{\sin^m\theta\cos^n\theta}{(\tau - 2r_0r_n\cos\theta)^{5/2}}\,d\theta, \tag{B.3.13}$$

in which $J_{m,n} = 0$ for m odd, each of the necessary $\langle\!\langle \bullet \rangle\!\rangle_{ijk}$ can be written as:

$$\begin{aligned}
\langle\!\langle \cos^2\theta \rangle\!\rangle_{111} &= -(6r_0^3 + 9\varepsilon^2 r_0)J_{0,2} + (18r_0^2r_n + 9\varepsilon^2 r_n)J_{0,3} - 18r_0r_n^2J_{0,4} + 6r_n^3J_{0,5},\\
\langle\!\langle \sin\theta\cos\theta \rangle\!\rangle_{112} &= (3\varepsilon^2 r_n + 6r_0^2r_n)J_{2,1} - 12r_0r_n^2J_{2,2} + 6r_n^3J_{2,3},\\
\langle\!\langle \sin^2\theta \rangle\!\rangle_{122} &= -3\varepsilon^2 r_0J_{2,0} + 3\varepsilon^2 r_nJ_{2,1} - 6r_0r_n^2J_{4,0} + 6r_n^3J_{4,1},\\
\langle\!\langle \cos\theta \rangle\!\rangle_{113} &= -3(z_0 - z_n)((2r_0^2 + \varepsilon^2)J_{0,1} - 4r_0r_nJ_{0,2} + 2r_n^2J_{0,3}),\\
\langle\!\langle \sin\theta \rangle\!\rangle_{123} &= 6r_n(z_0 - z_n)(r_0J_{2,0} - r_nJ_{2,1}),\\
\langle\!\langle 1 \rangle\!\rangle_{133} &= (6(z_0 - z_n)^2 + 3\varepsilon^2)(-r_0J_{0,0} + r_nJ_{0,1}),
\end{aligned}$$

$$\begin{aligned}
\langle\!\langle \sin\theta\cos\theta \rangle\!\rangle_{211} &= (3\varepsilon^2 r_n + 6r_0^2r_n)J_{2,1} - 12r_0r_n^2J_{2,2} + 6r_n^3J_{2,3},\\
\langle\!\langle \sin^2\theta \rangle\!\rangle_{212} &= -3\varepsilon^2 r_0J_{2,0} + 3\varepsilon^2 r_nJ_{2,1} - 6r_0r_n^2J_{4,0} + 6r_n^3J_{4,1},\\
\langle\!\langle \cos^2\theta \rangle\!\rangle_{221} &= -3\varepsilon^2 r_0J_{0,2} + 3\varepsilon^2 r_nJ_{0,3} + 6r_n^3J_{2,3} - 6r_0r_n^2J_{2,2},\\
\langle\!\langle \sin\theta\cos\theta \rangle\!\rangle_{222} &= 9\varepsilon^2 r_nJ_{2,1} + 6r_n^3J_{4,1},\\
\langle\!\langle \sin\theta \rangle\!\rangle_{213} &= 6r_n(z_0 - z_n)(r_0J_{2,0} - r_nJ_{2,1}),\\
\langle\!\langle \cos\theta \rangle\!\rangle_{223} &= -3\varepsilon^2(z_0 - z_n)J_{0,1} - 6r_n^2(z_0 - z_n)J_{2,1},
\end{aligned}$$

$$\begin{aligned}
\langle\!\langle \cos^2\theta \rangle\!\rangle_{311} &= -3(z_0 - z_n)((2r_0^2 + \varepsilon^2)J_{0,2} - 4r_0r_nJ_{0,3} + 2r_n^2J_{0,4}),\\
\langle\!\langle \sin\theta\cos\theta \rangle\!\rangle_{312} &= 6r_0r_n(z_0 - z_n)J_{2,1} - 6r_n^2(z_0 - z_n)J_{2,2},\\
\langle\!\langle \sin^2\theta \rangle\!\rangle_{322} &= -3\varepsilon^2(z_0 - z_n)J_{2,0} - 6r_n^2(z_0 - z_n)J_{4,0},\\
\langle\!\langle \cos\theta \rangle\!\rangle_{313} &= (6(z_0 - z_n)^2 + 3\varepsilon^2)(-r_0J_{0,1} + r_nJ_{0,2}),\\
\langle\!\langle \sin\theta \rangle\!\rangle_{323} &= (6r_n(z_0 - z_n)^2 + 3r_n\varepsilon^2)J_{2,0},\\
\langle\!\langle 1 \rangle\!\rangle_{333} &= -(6(z_0 - z_n)^3 + 9\varepsilon^2(z_0 - z_n))J_{0,0}.
\end{aligned} \tag{B.3.14}$$

Using the double angle formulae for sin and cos we are able to express $J_{m,n}$ purely in terms of even powers of cos, such that

$$J_{m,n} = \lambda\cdot 2^m \int_0^{\frac{\pi}{2}} \frac{(2\cos^2\theta - 1)^n(1 - \cos^2\theta)^{m/2}\cos^m\theta}{(1 - k^2\cos^2\theta)^{5/2}}\,d\theta \quad \text{for } m \text{ even}, \tag{B.3.15}$$

where $\lambda = r_n(k/\sqrt{r_0 r_n})^5/8 = 4r_n(\sqrt{\tau + 2r_0 r_n})^{-5}$. Note that the upper limit of integration was first reduced by application of the double angle formulae, followed by the even parity of the resulting integrand about $\pi/2$. If we further define

$$C_m = \lambda \int_0^{\frac{\pi}{2}} \frac{\cos^{2m}\theta}{(1 - k^2\cos^2\theta)^{5/2}}\, d\theta,$$

then expanding Equation (B.3.15) for the relevant values of m, n yields

$$\begin{aligned}
J_{0,0} &= +C_0, \\
J_{0,1} &= -C_0 + 2C_1, \\
J_{0,2} &= +C_0 - 4C_1 + 4C_2, \\
J_{0,3} &= -C_0 + 6C_1 - 12C_2 + 8C_3, \\
J_{0,4} &= +C_0 - 8C_1 + 24C_2 - 32C_3 + 16C_4, \\
J_{0,5} &= -C_0 + 10C_1 - 40C_2 + 80C_3 - 80C_4 + 32C_5,
\end{aligned} \tag{B.3.16}$$

$$\begin{aligned}
J_{2,0} &= 4(+C_1 - C_2), \\
J_{2,1} &= 4(-C_1 + 3C_2 - 2C_3), \\
J_{2,2} &= 4(+C_1 - 5C_2 + 8C_3 - 4C_4), \\
J_{2,3} &= 4(-C_1 + 7C_2 - 18C_3 + 20C_4 - 8C_5),
\end{aligned}$$

$$\begin{aligned}
J_{4,0} &= 16(+C_2 - 2C_3 + C_4), \\
J_{4,1} &= 16(-C_2 + 4C_3 - 5C_4 + 2C_5),
\end{aligned}$$

in which the integrals C_m can be expressed in terms of complete elliptic integrals of the

first and second kind (F and E respectively) with elliptic modulus k as

$$
\begin{aligned}
C_0 &= \frac{\lambda}{3(1-k^2)}\left(-F + \frac{2(2-k^2)}{1-k^2}E\right), \\
C_1 &= \frac{\lambda}{3k^2(1-k^2)}\left(-F + \frac{1+k^2}{1-k^2}E\right), \\
C_2 &= \frac{\lambda}{3k^4(1-k^2)}\left((2-3k^2)F + \frac{2(2k^2-1)}{1-k^2}E\right), \\
C_3 &= \frac{\lambda}{3k^6(1-k^2)}\left((8-9k^2)F - \frac{3k^4-13k^2+8}{1-k^2}E\right), \\
C_4 &= \frac{\lambda}{3k^8(1-k^2)}\left((16-16k^2-k^4)F - \frac{2k^6+4k^4-24k^2+16}{1-k^2}E\right), \\
C_5 &= \frac{\lambda}{15k^{10}(1-k^2)}\left(128-120k^2-9k^4-4k^6)F - \frac{8k^8+11k^6+27k^4-184k^2+128}{1-k^2}E\right).
\end{aligned}
\tag{B.3.17}
$$

CHAPTER 4 APPENDICES

C.1 Materials and methods for experimental FRAP imaging

Fluorescence Recovery After Photobleaching experiments (and video capture) in Figures 4.17 – 4.19 were conducted by Dr Youssef Chebli and Prof Anja Geitmann of McGill University (Montreal, Canada). All subsequent image analysis was conducted by James Tyrrell with assistance from Dr Meurig Gallagher, University of Birmingham (Birmingham, UK).

Plant material

Pollen was collected directly after anthesis from a *Camellia japonica* plant grown in the greenhouse of the Montreal Botanical Garden. To minimize artefacts due to varying maturity of pollen grains, only batches collected during the same week were used for any given series of experiments. Pollen grains were then dehydrated over silica gel for 24 h and stored at −20 °C until use.

Pollen culture

Pollen grains were hydrated for 30 min and suspended in a modified Brewbaker and Kwack germination medium (100 µg ml^{-1} H_3BO_3, 300 µg ml^{-1} $Ca(NO_3)_2$, 100 µg ml^{-1} KNO_3,

200 µg ml^{-1} $MgSO_4$, 50 mg ml^{-1} sucrose). The pollen grain suspension was deposited in the channels of a 0.4 µm Ibidi® plates (µ-Slide VI 0.4, IbiTreat) and incubated at 22 °C for 90 min prior to membrane labeling.

Membrane Labeling

Membranes were fluorescently labeled by addition to the germination medium of FM4-64-FX (Molecular Probes, Invitrogen) to a final concentration of 1.60 µM. To image the endocytosis process, pollen tubes were labelled for 5 min prior to imaging.

Imaging and Fluorescence recovery after photobleaching

Confocal laser scanning imaging was performed with a Zeiss LSM710 AxioObserver system fitted with a Plan Apochromat 63x/1.4 oil objective. The FM4-64FX was excited with the 514 nm laser (maximal power 25 mW, output set at 3.5 %). The emitted photons were collected with tunable GaAsP PMT between 590 nm and 760 nm. Pinhole was set at 1 Airy Unit, detector gain at 740 and detector offset at 0.

A region covering the first 12 µm from the pollen tube tip was defined as the bleaching region of interest. Three images were taken before bleaching the ROI. Bleaching was performed with the 488 nm line of the argon laser used at maximal power (25 mW), output set 100 % for 10 iterations. After bleaching a series of images were acquired at different time intervals for at least 2 min.

C.2 Mapping experimental tube growth

The majority of the MATLAB code used in conducting this analysis was provided by Dr Meurig Gallagher, University of Birmingham, (Birmingham, UK).

In order to be able to quantify the speed of pollen tube growth for comparison with fluorescence intensity in the extreme APM, we developed new techniques for tracking the growth of the pollen tube across small time scales ($\mathcal{O}(s)$). Using a weighted form of Principal Component Analysis (PCA) where the weights correspond to fluorescence intensity, a spline is fitted to the boundary of the pollen tube for each frame in our FRAP video. This can be seen in Figure C.1a where the blue curve is the cubic polynomial interpolant for the location of the extreme apex (minimising the squared error in the x direction)[1]. The data to which this curve has been fitted can be seen in Figure C.1b. Starting from the first frame in our video, the first apical point is found by selecting the point in the apical region at which the absolute value of the second derivative of the boundary spline is minimised. The next apical point (for the second frame) is found by starting from an intermediary point on the second boundary spline that is closest to the first apical point. We then select the new apical point by choosing the point that minimises the second derivative of the boundary spline in a region 'sufficiently close' to the intermediate point. This iterative process is repeated for each frame, with the third apical point being selected based on the location of the second apical point and so on.

Using the apical points we have found, we are able to measure the growth speed of the tube between frames. Growth of the tube between one frame and the next is measured as the signed distance between the apical point of the first and the closest boundary point of the second. This is based on the assumption that growth in the apex occurs in the normal direction. The speed of growth is determined by dividing the growth distance by the time between frames. Results of this measurement can be seen in Figure C.2a. This data is smoothed in Figure C.2b by averaging the growth at each time point with growth during the two adjacent time points (one prior, one after) except for the data for the first and final timepoints which remain unchanged. This averaged growth data is used in our comparison with the fluorescence intensity of the extreme APM in Figure 4.20. We note that some of our data appears to show a shrinking of the tube with growth taking

[1]This is used purely for visualisation purposes in Figure C.1.

negative values. This is likely a result of the pollen tube shifting 'up or down' slightly in the plane of the $\approx 400\,\text{nm}$ thick horizontal slice that is visualized during the course of the confocal laser scanning microscopy experiments, with deviations away from the centre of the tube (where the apex is located and the tube extends furthest) mimicking the appearance of shrinking.

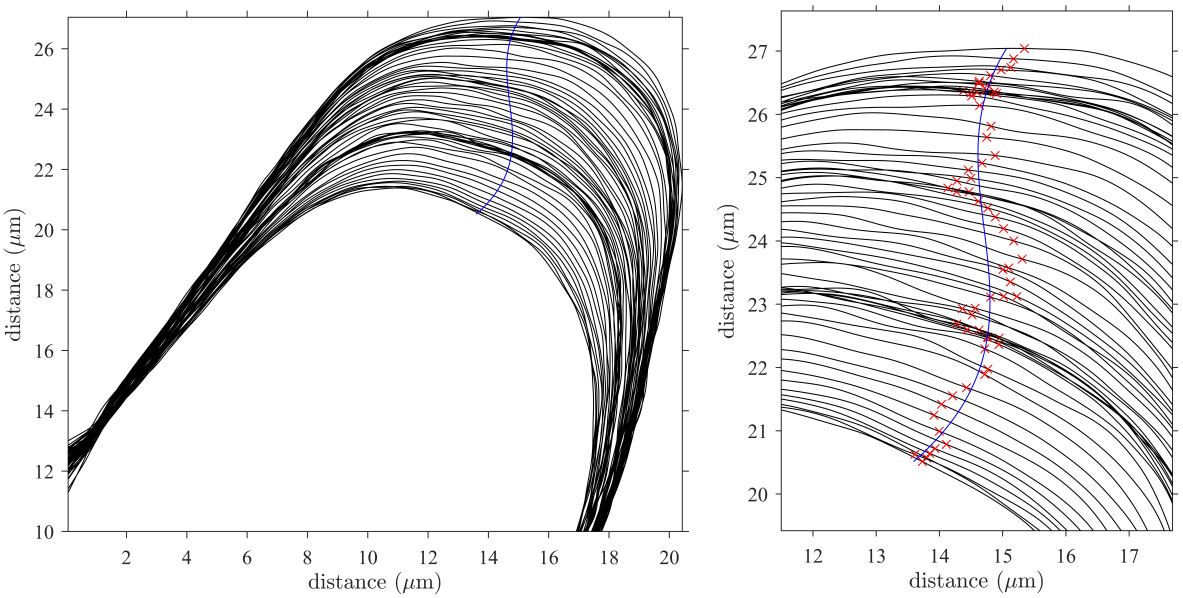

(a) **(b)**

Figure C.1: **(a)** An outline of the pollen tube for each frame in the FRAP video we analyze. The blue line is cubic polynomial interpolant for the location of the extreme apex, minimizing the squared error in the x direction (used purely for visualization). **(b)** A zoomed–in look at the location of apical points for each frame in the FRAP video.

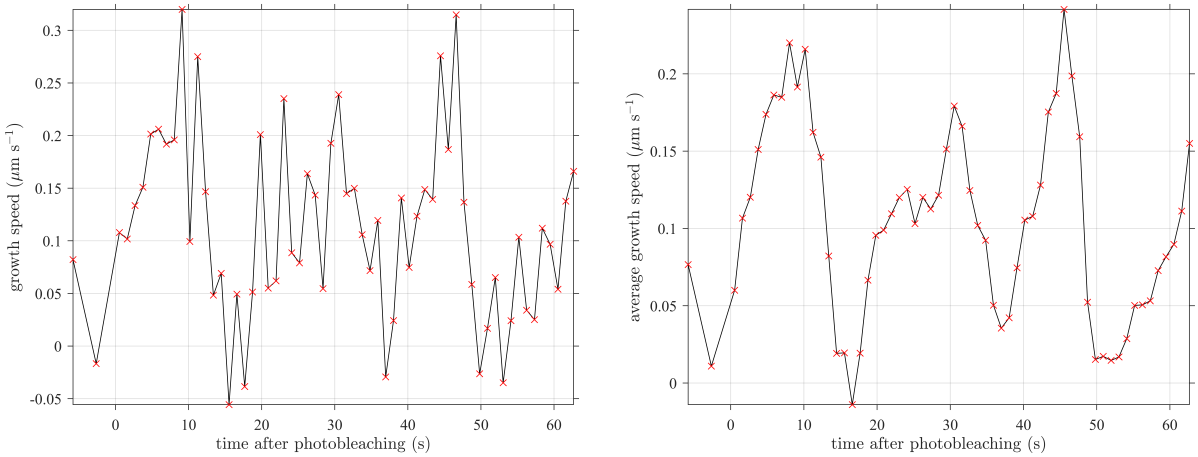

(a) **(b)**

Figure C.2: **(a)** Growth speed between frames in the FRAP video. **(b)** The same data smoothed by averaging over consecutive time points.

LIST OF REFERENCES

[1] Alberts, B., Johnson, A., Lewis, J., Raff, M., Roberts, K., and Walter, P. Molecular motors. In *Molecular Biology of the Cell*, fourth ed. Garland Science, 2002. Available from: https://www.ncbi.nlm.nih.gov/books/NBK26888/.

[2] Alves, C. J., and Silvestre, A. Density results using Stokeslets and a method of fundamental solutions for the Stokes equations. *Engineering Analysis with Boundary Elements 28*, 10 (2004), 1245–1252.

[3] Barrero-Gil, A. The method of fundamental solutions without fictitious boundary for solving Stokes problems. *Computers & Fluids 62* (2012), 86–90.

[4] Barrows, E. M. *Animal Behavior Desk Reference: A Dictionary of Animal Behavior, Ecology, and Evolution*, third ed. CRC Press, 2011.

[5] Bartnicki-García, S. Hyphal tip growth: outstanding questions. *Mycology Series 15* (2002), 29–58.

[6] Bartnicki-Garcia, S., Bracker, C. E., Gierz, G., López-Franco, R., and Lu, H. Mapping the growth of fungal hyphae: orthogonal cell wall expansion during tip growth and the role of turgor. *Biophysical Journal 79*, 5 (2000), 2382–2390.

[7] Baskin, T. I. On the alignment of cellulose microfibrils by cortical microtubules: a review and a model. *Protoplasma 215*, 1-4 (2001), 150–171.

[8] Beenakker, C. The effective viscosity of a concentrated suspension of spheres (and its relation to diffusion). *Physica A: Statistical Mechanics and its Applications 128*, 1-2 (1984), 48–81.

[9] Bingham, E. C. An investigation of the laws of plastic flow. *Bulletin of the Bureau of Standards 13* (1917), 309–352.

[10] Bingham, E. C. *Fluidity and plasticity*. McGraw-Hill Book Company Inc., New York, 1922.

[11] Blake, J. A spherical envelope approach to ciliary propulsion. *Journal of Fluid Mechanics 46*, 1 (1971), 199–208.

[12] Bove, J., Vaillancourt, B., Kroeger, J., Hepler, P. K., Wiseman, P. W., and Geitmann, A. Magnitude and direction of vesicle dynamics in growing pollen tubes using spatiotemporal image correlation spectroscopy and fluorescence recovery after photobleaching. *Plant Physiology 147*, 4 (2008), 1646–1658.

[13] Bryant, D. A., and Frigaard, N.-U. Prokaryotic photosynthesis and phototrophy illuminated. *Trends in microbiology 14*, 11 (2006), 488–496.

[14] Buchanan, B. B., Gruissem, W., and Jones, R. L. *Biochemistry and molecular biology of plants*, second ed. John Wiley & Sons, Hoboken, New Jersey, 2015.

[15] Burri, Jan T and Vogler, Hannes and Läubli, Nino F and Hu, Chengzhi and Grossniklaus, Ueli and Nelson, Bradley J. Feeling the force: how pollen tubes deal with obstacles. *New Phytologist 220*, 1 (2018), 187–195.

[16] Burström, H. *Encyclopedia of Plant Physiology*, vol. Fourth. Berlin: Springer–Verlag, 1961.

[17] Burström, H. Wishful thinking of turgor. *Nature 234*, 5330 (1971), 488.

[18] Čada, M., and Torrilhon, M. Compact third-order limiter functions for finite volume methods. *Journal of Computational Physics 228*, 11 (2009), 4118–4145.

[19] Campas, O., and Mahadevan, L. Shape and dynamics of tip-growing cells. *Current Biology 19*, 24 (2009), 2102–2107.

[20] Chavarría-Krauser, A., and Yejie, D. A model of plasma membrane flow and cytosis regulation in growing pollen tubes. *Journal of theoretical biology 285*, 1 (2011), 10–24.

[21] Chebli, Y., Kaneda, M., Zerzour, R., and Geitmann, A. The cell wall of the arabidopsis pollen tube—spatial distribution, recycling, and network formation of polysaccharides. *Plant Physiology 160*, 4 (2012), 1940–1955.

[22] Chebli, Y., Kroeger, J., and Geitmann, A. Transport logistics in pollen tubes. *Molecular Plant 6*, 4 (2013), 1037–1052.

[23] Chen, C., Young, D., Tsai, C., and Murugesan, K. The method of fundamental solutions for inverse 2D Stokes problems. *Computational Mechanics 37*, 1 (2005), 2–14.

[24] Chen, Z. J. Molecular mechanisms of polyploidy and hybrid vigor. *Trends in plant science 15*, 2 (2010), 57–71.

[25] Christensen, R. *Theory of viscoelasticity: an introduction*, second ed. Academic Press, Cambridge, Massachusetts, 1982.

[26] Chwang, A. T. Hydromechanics of low-Reynolds-number flow. Part 3. Motion of a spheroidal particle in quadratic flows. *Journal of Fluid Mechanics 72*, 1 (1975), 17–34.

[27] Chwang, A. T., and Wu, T. Y. Hydromechanics of low-Reynolds-number flow. Part 4. Translation of spheroids. *Journal of Fluid Mechanics 75*, 4 (1976), 677–689.

[28] Chwang, A. T., and Wu, T. Y.-T. Hydromechanics of low-Reynolds-number flow. Part 1. Rotation of axisymmetric prolate bodies. *Journal of Fluid Mechanics 63*, 3 (1974), 607–622.

[29] Chwang, A. T., and Wu, T. Y.-T. Hydromechanics of low-Reynolds-number flow. Part 2. Singularity method for Stokes flows. *Journal of Fluid Mechanics 67*, 4 (1975), 787–815.

[30] Cleland, R. Auxin and wall extensibility: Reversibility of auxin-induced wall-loosening process. *Science 160*, 3824 (1968), 192–194.

[31] Cortez, R. The method of regularized Stokeslets. *SIAM Journal on Scientific Computing 23*, 4 (2001), 1204–1225.

[32] Cortez, R. Regularized stokeslet segments. *Journal of Computational Physics 375* (2018), 783–796.

[33] Cortez, R., Fauci, L., and Medovikov, A. The method of regularized Stokeslets in three dimensions: analysis, validation, and application to helical swimming. *Physics of Fluids 17*, 3 (2005), 031504.

[34] Cosgrove, D. J. Linkage of wall extension with water and solute uptake. In *Physiology of Cell Expansion during Plant Growth (Symposium in Plant Physiology)* (Rockville, MD, 1987), D. J. Cosgrove and D. P. Knievel, Eds., American Society of Plant Physiologists, pp. 88–100.

[35] Cosgrove, D. J. Wall relaxation and the driving forces for cell expansive growth. *Plant physiology 84*, 3 (1987), 561–564.

[36] Cosgrove, D. J. Wall relaxation in growing stems: comparison of four species and assessment of measurement techniques. *Planta 171*, 2 (1987), 266–278.

[37] Cosgrove, D. J. Wall extensibility: its nature, measurement and relationship to

plant cell growth. *New Phytologist 124*, 1 (1993), 1–23.

[38] Cosgrove, D. J. Growth of the plant cell wall. *Nature reviews molecular cell biology 6*, 11 (2005), 850.

[39] Darwish, M., and Moukalled, F. TVD schemes for unstructured grids. *International Journal of heat and mass transfer 46*, 4 (2003), 599–611.

[40] De Win, A. H. N. *Quantitative analysis of organelle movements in pollen tubes.* PhD thesis, Radboud University, 1997.

[41] Dominguez, R., and Holmes, K. C. Actin structure and function. *Annual Review of Biophysics 40* (2011), 169–186.

[42] Dumais, J., Long, S. R., and Shaw, S. L. The mechanics of surface expansion anisotropy in medicago truncatula root hairs. *Plant physiology 136*, 2 (2004), 3266–3275.

[43] Dumais, J., Shaw, S. L., Steele, C. R., Long, S. R., and Ray, P. M. An anisotropic-viscoplastic model of plant cell morphogenesis by tip growth. *The International Journal of Developmental Biology 50* (2006), 209–222.

[44] Edelstein-Keshet, L., and Ermentrout, G. B. Models for spatial polymerization dynamics of rod-like polymers. *Journal of mathematical biology 40*, 1 (2000), 64–96.

[45] Engwirda, D. *Locally optimal Delaunay-refinement and optimisation-based mesh generation.* PhD thesis, University of Sydney, 2014.

[46] Fabricant, D. S., and Farnsworth, N. R. The value of plants used in traditional medicine for drug discovery. *Environmental health perspectives 109*, Suppl 1 (2001), 69.

[47] Fairweather, G., and Karageorghis, A. The method of fundamental solutions for elliptic boundary value problems. *Advances in Computational Mathematics 9*, 1-2 (1998), 69.

[48] Fallah, N. A cell vertex and cell centred finite volume method for plate bending analysis. *Computer methods in applied Mechanics and Engineering 193*, 33-35 (2004), 3457–3470.

[49] Fayant, P., Girlanda, O., Chebli, Y., Aubin, C.-É., Villemure, I., and Geitmann, A. Finite element model of polar growth in pollen tubes. *The Plant Cell 22*, 8 (2010), 2579–2593.

[50] Feijó, J. A., Sainhas, J., Holdaway-Clarke, T., Cordeiro, M. S., Kunkel, J. G., and Hepler, P. K. Cellular oscillations and the regulation of growth: the pollen tube paradigm. *Bioessays 23*, 1 (2001), 86–94.

[51] Fritsch, F. E., and Salisbury, S. E. J. *An introduction to the structure and reproduction of plants*. G. Bell and Sons, London, 1920.

[52] Fu, Y., Wu, G., and Yang, Z. Rop GTPase–dependent dynamics of tip-localized F-actin controls tip growth in pollen tubes. *The Journal of Cell Biology 152*, 5 (2001), 1019–1032.

[53] Gallagher, M. T., Choudhuri, D., and Smith, D. J. Sharp quadrature error bounds for the nearest-neighbor discretization of the regularized stokeslet boundary integral equation. *SIAM Journal on Scientific Computing* (2018).

[54] Geitmann, A., and Palanivelu, R. Fertilization requires communication: signal generation and perception during pollen tube guidance. *Floriculture and Ornamental Biotechnology 1*, 2 (2007), 77–89.

[55] Goriely, A., and Tabor, M. Biomechanical models of hyphal growth in actinomycetes. *Journal of theoretical biology 222*, 2 (2003), 211–218.

[56] Goriely, A., and Tabor, M. Self-similar tip growth in filamentary organisms. *Physical review letters 90*, 10 (2003), 108101.

[57] Goriely, A., and Tabor, M. Mathematical modeling of hyphal tip growth. *Fungal Biology Reviews 22*, 2 (2008), 77–83.

[58] Goriely, A., Tabor, M., and Tongen, A. A morpho-elastic model of hyphal tip growth in filamentous organisms. In *IUTAM Symposium on Cellular, Molecular and Tissue Mechanics* (2010), Springer, pp. 245–255.

[59] Gradshteyn, I. S., and Ryzhik, I. M. *Table of integrals, series, and products*. Academic Press, 2014.

[60] Green, P., Erickson, R., and Buggy, J. Metabolic and physical control of cell elongation rate: in vivo studies in nitella. *Plant Physiology 47*, 3 (1971), 423–430.

[61] Grefen, C., and Blatt, M. R. SNAREs—Molecular governors in signalling and development. *Current opinion in plant biology 11*, 6 (2008), 600–609.

[62] Guo, F., and McCubbin, A. G. The pollen-specific R-SNARE/longin Pi-VAMP726 mediates fusion of endo-and exocytic compartments in pollen tube tip growth. *Journal of experimental botany 63*, 8 (2012), 3083–3095.

[63] Hales, T. C. An overview of the kepler conjecture. *arXiv preprint math/9811071* (1998).

[64] Happel, J., and Brenner, H. *Low Reynolds number hydrodynamics: with special applications to particulate media*, vol. 1. Springer Science & Business Media, 2012.

[65] Harten, A. High resolution schemes for hyperbolic conservation laws. *Journal of computational physics 49*, 3 (1983), 357–393.

[66] Hejnowicz, Z., Heinemann, B., and Sievers, A. Tip growth: patterns of growth rate and stress in the chara rhizoid. *Zeitschrift für Pflanzenphysiologie 81*, 5 (1977), 409–424.

[67] Hill, R. *The mathematical theory of plasticity*. Oxford University Press, Oxford, 1950.

[68] Himschoot, Ellie and Beeckman, Tom and Friml, Jiří and Vanneste, Steffen. Calcium is an organizer of cell polarity in plants. *Biochimica et Biophysica Acta (BBA)-Molecular Cell Research 1853*, 9 (2015), 2168–2172.

[69] Huang, L., and Chwang, A. Hydromechanics of low-Reynolds-number flow. Part 6. Rotation of oblate bodies. *Journal of Engineering Mathematics 20*, 4 (1986), 307–322.

[70] Iwanami, Y. Protoplasmic movement in pollen grains and tubes. *Phytomorphology 6* (1956), 288–295.

[71] Jiang, Y., Wang, J., Xie, Y., Chen, N., and Huang, S. ADF10 shapes the overall organization of apical actin filaments by promoting their turnover and ordering in pollen tubes. *J Cell Sci* (2017), jcs–207738.

[72] jiro (MathWorks staff). grabit function (File Exchange). `https://uk.mathworks.com/matlabcentral/fileexchange/7173-grabit`. Accessed: 10/12/2018.

[73] Johnson, R. E., and Wu, T. Y. Hydromechanics of low-Reynolds-number flow. Part 5. Motion of a slender torus. *Journal of Fluid Mechanics 95*, 2 (1979), 263–277.

[74] Kalwarczyk, T., Tabaka, M., and Holyst, R. Biologistics—diffusion coefficients for complete proteome of Escherichia coli. *Bioinformatics 28*, 22 (2012), 2971–2978.

[75] Kelkar, V. S., and Sewell, R. T. *Fundamentals of the analysis and design of shell structures*. Prentice Hall, 1987.

[76] Kohno, T., and Shimmen, T. Accelerated sliding of pollen tube organelles along Characeae actin bundles regulated by Ca2+. *The Journal of cell biology 106*, 5 (1988), 1539–1543.

[77] Kroeger, J., and Geitmann, A. The pollen tube paradigm revisited. *Current opinion in plant biology 15*, 6 (2012), 618–624.

[78] Kroeger, J. H., Daher, F. B., Grant, M., and Geitmann, A. Microfilament orientation constrains vesicle flow and spatial distribution in growing pollen tubes. *Biophysical Journal 97*, 7 (2009), 1822–1831.

[79] Lamb, H. *Hydrodynamics*. Cambridge university press, 1993.

[80] Lauga, E., and Powers, T. R. The hydrodynamics of swimming microorganisms. *Reports on Progress in Physics 72*, 9 (2009), 096601.

[81] Lee, Y. J., Szumlanski, A., Nielsen, E., and Yang, Z. Rho-GTPase–dependent filamentous actin dynamics coordinate vesicle targeting and exocytosis during tip growth. *The Journal of cell biology 181*, 7 (2008), 1155–1168.

[82] Leonard, B. P. A stable and accurate convective modelling procedure based on quadratic upstream interpolation. *Computer methods in applied mechanics and engineering 19*, 1 (1979), 59–98.

[83] Leshansky, A., and Kenneth, O. Surface tank treading: Propulsion of Purcell's toroidal swimmer. *Physics of Fluids 20*, 6 (2008), 063104.

[84] Lindley, J. *The vegetable kingdom; or, The structure, classification, and uses of plants: illustrated upon the natural system*, vol. 1. Bradbury & Evans, London, 1853.

[85] Lockhart, J. A. An analysis of irreversible plant cell elongation. *Journal of theoretical biology 8*, 2 (1965), 264–275.

[86] Lovy-Wheeler, A., Wilsen, K. L., Baskin, T. I., and Hepler, P. K. Enhanced fixation reveals the apical cortical fringe of actin filaments as a consistent feature of the pollen tube. *Planta 221*, 1 (2005), 95–104.

[87] Malhó, R. *The pollen tube: a cellular and molecular perspective*. Springer-Verlag, Berlin, 2006.

[88] Maruyama, K., Kaibara, M., and Fukada, E. Rheology of F-actin I. Network of F-actin in solution. *Biochimica et Biophysica Acta (BBA)-Protein Structure 371*, 1 (1974), 20–29.

[89] McKenna, S. T., Kunkel, J. G., Bosch, M., Rounds, C. M., Vidali, L., Winship, L. J., and Hepler, P. K. Exocytosis precedes and predicts the increase in growth in oscillating pollen tubes. *The Plant Cell 21*, 10 (2009), 3026–3040.

[90] Michard, Erwan and Dias, Pedro and Feijó, José A. Tobacco pollen tubes as cellular models for ion dynamics: improved spatial and temporal resolution of extracellular flux and free cytosolic concentration of calcium and protons using pHluorin and YC3. 1 CaMeleon. *Sexual Plant Reproduction 21*, 3 (2008), 169–181.

[91] Mogilner, A., and Edelstein-Keshet, L. Regulation of actin dynamics in rapidly moving cells: a quantitative analysis. *Biophysical journal 83*, 3 (2002), 1237–1258.

[92] Morris, R. J., and Blyth, M. How water flow, geometry and material properties drive plant movements. *Journal of Experimental Botany* (2019).

[93] Nebenführ, A., and Dixit, R. Kinesins and myosins: molecular motors that coordinate cellular functions in plants. *Annual review of plant biology 69* (2018), 329–361.

[94] Ortega, J. K. Augmented growth equation for cell wall expansion. *Plant physiology 79*, 1 (1985), 318–320.

[95] Peaceman, D. W., and Rachford, Jr, H. H. The numerical solution of parabolic and elliptic differential equations. *Journal of the Society for Industrial and Applied Mathematics 3*, 1 (1955), 28–41.

[96] Phan-Thien, N., Tran-Cong, T., and Ramia, M. A boundary-element analysis of flagellar propulsion. *Journal of Fluid Mechanics 184* (1987), 533–549.

[97] Pozrikidis, C. *Boundary integral and singularity methods for linearized viscous flow*. Cambridge University Press, 1992.

[98] Purcell, E. M. Life at low Reynolds number. *American Journal of Physics 45*, 1 (1977), 3–11.

[99] Ramia, M., Tullock, D., and Phan-Thien, N. The role of hydrodynamic interaction in the locomotion of microorganisms. *Biophysical journal 65*, 2 (1993), 755–778.

[100] Ray, P. M., Green, P. B., and Cleland, R. Role of turgor in plant cell growth. *Nature 239* (1972), 163–164.

[101] Rayle, D. L., Haughton, P. M., and Cleland, R. An in vitro system that simulates plant cell extension growth. *Proceedings of the National Academy of Sciences 67*, 4 (1970), 1814–1817.

[102] Ridge, I., and Osborne, D. J. Role of peroxidase when hydroxyproline-rich protein in plant cell walls is increased by ethylene. *Nature New Biology 229*, 7 (1971), 205.

[103] Rojas, E. R., Hotton, S., and Dumais, J. Chemically mediated mechanical expansion of the pollen tube cell wall. *Biophysical journal 101*, 8 (2011), 1844–1853.

[104] Rubinow, S., and Keller, J. B. The transverse force on a spinning sphere moving in a viscous fluid. *Journal of Fluid Mechanics 11*, 3 (1961), 447–459.

[105] Schopfer, P. Biomechanics of plant growth. *American journal of botany 93*, 10 (2006), 1415–1425.

[106] Shum, H., Gaffney, E., and Smith, D. Modelling bacterial behaviour close to a no-slip plane boundary: the influence of bacterial geometry. *Proceedings of the Royal Society of London A 466* (2010), 1725–1748.

[107] Smith, D. J. A boundary element regularized Stokeslet method applied to cilia- and flagella-driven flow. *Proceedings of the Royal Society of London A 465*, 2112 (2009), 3605–3626.

[108] Smith, D. J. A nearest-neighbour discretisation of the regularized stokeslet boundary integral equation. *Journal of Computational Physics 358* (2018), 88–102.

[109] Steer, M. W., and Steer, J. M. Pollen tube tip growth. *New Phytologist 111*, 3 (1989), 323–358.

[110] Stokes, G. G. *On the effect of the internal friction of fluids on the motion of pendulums*, vol. 9. Pitt Press Cambridge, 1851.

[111] Swain, T. *Plants in the development of modern medicine: [Proceedings]*. Harvard Univ. Press, Cambridge, Massachusetts, 1972.

[112] Sweby, P. K. High resolution schemes using flux limiters for hyperbolic conservation laws. *SIAM journal on numerical analysis 21*, 5 (1984), 995–1011.

[113] Taylor, G. I. Analysis of the swimming of long and narrow animals. *Proc. R. Soc. Lond. A 214*, 1117 (1952), 158–183.

[114] Thaokar, R., Schiessel, H., and Kulic, I. Hydrodynamics of a rotating torus. *The European Physical Journal B 60*, 3 (2007), 325–336.

[115] Tominaga, M., Kojima, H., Yokota, E., Orii, H., Nakamori, R., Katayama, E., Anson, M., Shimmen, T., and Oiwa, K. Higher plant myosin XI moves processively on actin with 35 nm steps at high velocity. *The EMBO journal 22*, 6 (2003), 1263–1272.

[116] Ugural, A., and Fenster, S. *Advanced strength of materials*. Elsevier, New York, 1975.

[117] Ugural, A. C., and Ugural, A. C. *Stresses in plates and shells*, vol. 366. McGraw-Hill Boston, 1999.

[118] Vidali, L., and Hepler, P. K. Characterization and localization of profilin in pollen grains and tubes of lilium longiflorum. *Cell motility and the cytoskeleton 36*, 4 (1997), 323–338.

[119] Vidali, L., McKenna, S. T., and Hepler, P. K. Actin polymerization is essential for pollen tube growth. *Molecular Biology of the Cell 12*, 8 (2001), 2534–2545.

[120] Wang, X., Teng, Y., Wang, Q., Li, X., Sheng, X., Zheng, M., Šamaj, J., Baluška, F., and Lin, J. Imaging of dynamic secretory vesicles in living pollen tubes of Picea meyeri using evanescent wave microscopy. *Plant Physiology 141*, 4 (2006), 1591–1603.

[121] Wong, I., Gardel, M., Reichman, D., Weeks, E. R., Valentine, M., Bausch, A., and Weitz, D. A. Anomalous diffusion probes microstructure dynamics of entangled F-actin networks. *Physical Review Letters 92*, 17 (2004), 178101.

[122] Yee, H., Warming, R., and Harten, A. Implicit total variation diminishing (TVD) schemes for steady-state calculations. *Journal of Computational Physics 57*, 3 (1985), 327–360.

[123] Young, D., Jane, S., Fan, C., Murugesan, K., and Tsai, C. The method of fundamental solutions for 2D and 3D Stokes problems. *Journal of Computational Physics 211*, 1 (2006), 1–8.

[124] Zerzour, R., Kroeger, J., and Geitmann, A. Polar growth in pollen tubes is associated with spatially confined dynamic changes in cell mechanical properties. *Developmental biology 334*, 2 (2009), 437–446.

[125] Zonia, L., and Munnik, T. Life under pressure: hydrostatic pressure in cell growth and function. *Trends in plant science 12*, 3 (2007), 90–97.

[126] Zonia, L., and Munnik, T. Vesicle trafficking dynamics and visualization of zones of exocytosis and endocytosis in tobacco pollen tubes. *Journal of experimental botany 59*, 4 (2008), 861–873.